Author:
Lees, Robert M

Title:
Relationships Between Presynaptic Structural Plasticity and Mitochondrial Localisation in Rodent Cortical Axons

Relationships Between Presynaptic Structural Plasticity and Mitochondrial Localisation in Rodent Cortical Axons

Robert Michael Lees

A dissertation submitted to the University of Bristol in accordance with the requirements for award of the degree of PhD in the Faculty of Life Sciences

School of Physiology, Pharmacology and Neuroscience

September 2018

Word count: 45,000

Abstract

The addition and removal of synapses is fundamental to learning and memory formation in the adult mammalian neocortex. This experience-dependent structural plasticity of pre- and post-synaptic terminals changes neuronal circuit organisation. Structural plasticity of dendritic spines has been well-studied but the mechanisms driving presynaptic structural plasticity are not understood. Mitochondria are suitable candidates for regulation of presynaptic plasticity as they are small, fragmented organelles that can be positioned differentially to modulate individual terminals. They have been directly implicated in regulating presynaptic activity due to their roles in energy and calcium homeostasis. Based on the hypothesis that local mitochondria may influence synapse formation and/or loss, the studies presented here have investigated the relationship between axonal mitochondria and structural plasticity of presynaptic boutons. Light microscopy was used to track their formation and persistence in rodent neurons *in vitro* and *in vivo* alongside the trafficking and anchoring of mitochondria to assess their relationship to presynaptic structural plasticity. Electron microscopy techniques were also developed to obtain correlated spatial information that complemented the temporal dynamics of live light microscopy. Presynaptic terminals of cortical neurons were found to be highly dynamic, being lost and gained within hours *in vitro*, and days *in vivo*. The numbers of mitochondria and presynaptic terminals were strongly correlated *in vivo* due to local anchoring of mitochondria at approximately 40% of all terminals. The longevity of those terminals was also positively correlated with the presence of presynaptic mitochondria *in vivo*, but not *in vitro*. This suggests that, as boutons are formed, persist and become long-lived *in vivo,* they increasingly accumulate mitochondria to regulate their activity. Understanding these relationships is essential to unpicking the molecular mechanisms of learning, perception and memory formation in the neocortex as well as interpreting the aetiology of mitochondrial-related neurological diseases.

Acknowledgements

The completion of this thesis would not have been possible without the support and love from members of the Ashby lab, past and present. It has been a pleasure to work alongside you in a highly stimulating environment with some incredible brains (both fixed and live!). The Wolfson Bioimaging Facility has also provided me with advice and support to obtain the wonderful and inspiring images that I have taken over the years.

It goes without saying that the quality of my work would not be the same without the critical input of my supervisor Michael Ashby, who continues to baffle me with his depth and breadth of knowledge and his good spirit.

I would also like to thank my parents, Pauline and Kevin, for believing in me and reminding me that "All you can do is your best." My step father, Tony, for providing all manner of resources, for which I am truly grateful. And my sister, Rebecca, for always being ready with a G&T.

My time in Bristol would not have been complete without my closest friends and the community of PhD students at the University of Bristol. You have all provided love, fun and laughter along the way.

I am grateful for the funding granted by the Wellcome Trust and the opportunity to carry out the research that has contributed to this PhD thesis.

And last, but certainly not least, I would like to thank my partner and friend, Alice, who has been integral to the completion of this work. Thank you for putting a smile on my face.

Author’s declaration

I declare that the work in this dissertation was carried out in accordance with the requirements of the University's Regulations and Code of Practice for Research Degree Programmes and that it has not been submitted for any other academic award. Except where indicated by specific reference in the text, the work is the candidate's own work. Work done in collaboration with, or with the assistance of, others, is indicated as such. Any views expressed in the dissertation are those of the author.

SIGNED: ..... DATE: .....

Table of Contents

List of Figures

List of Abbreviations

#D ..... *# dimension(s)/(al)*

2P ..... *two-photon*

AAV ..... *adeno-associated virus*

ADP ..... *adenosine diphosphate*

AMPA ..... *α-amino-3-hydroxy-5-methyl-4-isoxazolepropionic acid*

ANOVA ..... *analysis of variance*

AOBS ..... *acousto-optical beam splitter*

APEX ..... *ascorbate peroxidase*

ATP ..... *adenosine triphosphate*

BP ..... *band pass*

BSA ..... *bovine serum albumin*

CCD ..... *charged coupled device*

cDNA ..... *complementary DNA*

CI ..... *confidence interval*

CLEM ..... *correlative light and electron microscopy*

CMV ..... *cytomegalovirus*

Cox8a ..... *cytochrome oxidase 8a subunit*

CV ..... *coefficient of variation*

DAB ..... *3,3′-Diaminobenzidine*

DAPI ..... *4′,6-diamidino-2-phenylindole*

(d)dH2O ..... *(double) distilled water*

DiI ..... *1,1′-dioctadecyl-3,3,3′3′-tetramethylindocarbocyanine perchlorate*

DISC1 ..... *disrupted in schizophrenia 1*

DIV ..... *days in vitro*

E18 ..... *embryonic day 18*

EGFP ..... *enhanced green fluorescent protein*

EM ..... *electron microscopy*

Em. ..... *emission wavelength*

EPB ..... *en passant bouton*

EPSP ..... *excitatory postsynaptic potential*

ER ..... *endoplasmic reticulum*

EtOH ..... *ethanol*

Ex. ..... *excitation wavelength*

FACS ..... *fluorescence-activated cell sorting*

FIB ..... *focussed ion beam*

FOV ..... *field of view*

GaAsP ..... *gallium arsenide phosphide*

GB ..... *gigabyte*

GECI ..... *genetically-encoded calcium indicator*

GFP ..... *green fluorescent protein*

HBSS ..... *Hank's buffered salt solution*

HEPES ..... *4-(2-hydroxyethyl)-1-piperazineethanesulfonic acid*

hSYN ..... *human synapsin*

JIP ..... *JNK-interacting proteins*

JNK ..... *c-Jun N-terminal kinases*

KIF5A ..... *kinesin family member 5A*

KS test ..... *Kolmogorov-Smirnov test*

LC8 ..... *dynein light chain 8*

LED ..... *light-emitting diode*

LKB1 ..... *liver kinase B1*

LM ..... *light microscopy*

LTD ..... *long-term depression*

LTP ..... *long-term potentiation*

M1/M2 ..... *primary/secondary motor cortex*

MB ..... *megabyte*

MOC ..... *Mander's overlap coefficient*

MCU ..... *mitochondrial calcium uniporter*

MFF ..... *mitochondrial fission factor*

microCT ..... *micro computerised tomography*

Miro1 ..... *mitochondrial rho GTPase 1*

MP ..... *multiphoton*

mtDNA ..... *mitochondrial DNA*

NA ..... *numerical aperture*

NADH ..... *reduced nicotinamide adenine dinucleotide*

NIRB ..... *near infrared branding*

NMDA ..... *N-Methyl-D-aspartic acid*

NUAK1 ..... *adenosine monophosphate-related kinase-related protein kinase 5*

OCT ..... *optimal cutting temperature*

OPA1 ..... *optic atrophy 1 a.k.a. dynamin-like 120 kDa (kilodalton) protein*

OXPHOS ..... *oxidative phosphorylation*

P2A ..... *porcine teschovirus-1 2A*

PBS ..... *phosphate-buffered saline*

PFA ..... *paraformaldehyde*

pH ..... *acidity/basicity measurement unit*

PH ..... *proportional hazards*

PMT ..... *photomultiplier tube*

PSD-95 ..... *postsynaptic density protein 95*

PTV ..... *piccolo-bassoon transport vesicle*

RAM ..... *random access memory*

ROI ..... *region of interest*

rpm ..... *revolutions per minute*

RT ..... *room temperature*

SBF ..... *serial block-face*

SD..... *standard deviation*

SDS ..... *sodium dodecyl sulfate*

SEM..... *scanning electron microscope/y*

shRNA..... *short hairpin ribonucleic acid*

SNARE..... *soluble N-ethylmaleimide-sensitive factor attachment protein associated receptor*

ssTEM ..... *serial section transmission electron microscopy*

STV..... *synaptic vesicle protein transport vesicle*

Syn1a-GFP..... *synapsin1a-GFP*

Syp-GFP..... *synaptophysin-GFP*

TB ..... *terminaux bouton*

TCH..... *thiocarbohydrazide*

TEM ..... *transmission electron microscopy*

Trak1/2 ..... *trafficking kinesin protein 1/2*

VA-044 ..... *2,2'-Azobis[2-(2-imidazolin-2-yl)propane]dihydrochloride*

VGluT1..... *vesicular glutamate transporter 1*

CHAPTER 1 INTRODUCTION

1.1 Mammalian neocortex

The mammalian brain is an organ of detailed functional and structural complexity. The outer region of the brain—the neocortex—is involved in perception, complex behaviour, learning, and memory formation (Bear et al. 2015, Fu and Zuo 2011, Holtmaat and Caroni 2016). The neocortex can be crudely split in to functional areas that receive, send and integrate specific pieces of information about perception, e.g. somatosensation (Figure 1.1A; Amunts and Zilles, 2015). These functional areas are organised laterally across the surface of the brain and each area can be further divided in to layers in the axial dimension (Figure 1.1B, C). Each layer comprises of a mixture of cell types including neurons—cells that transmit and integrate signals during neural activity—and glia—cells that are important for supporting neuronal function through structural support, nutrient provision, debris clean-up and insulation of conducting fibres (Bear et al., 2015). Neocortical layers are distinguished in structure and function by cell-type composition (including different neuronal cell types) and connectivity with other layers and areas (Figure 1.1C; Amunts and Zilles, 2015). The neocortex is thought to carry out its function by integrating, storing and transmitting information across neocortical layers and between neocortical areas (Douglas and Martin, 2004). Typically, the thalamus projects in to layer 4 of sensory areas and neurons in layer 4 then project up to layer 2/3

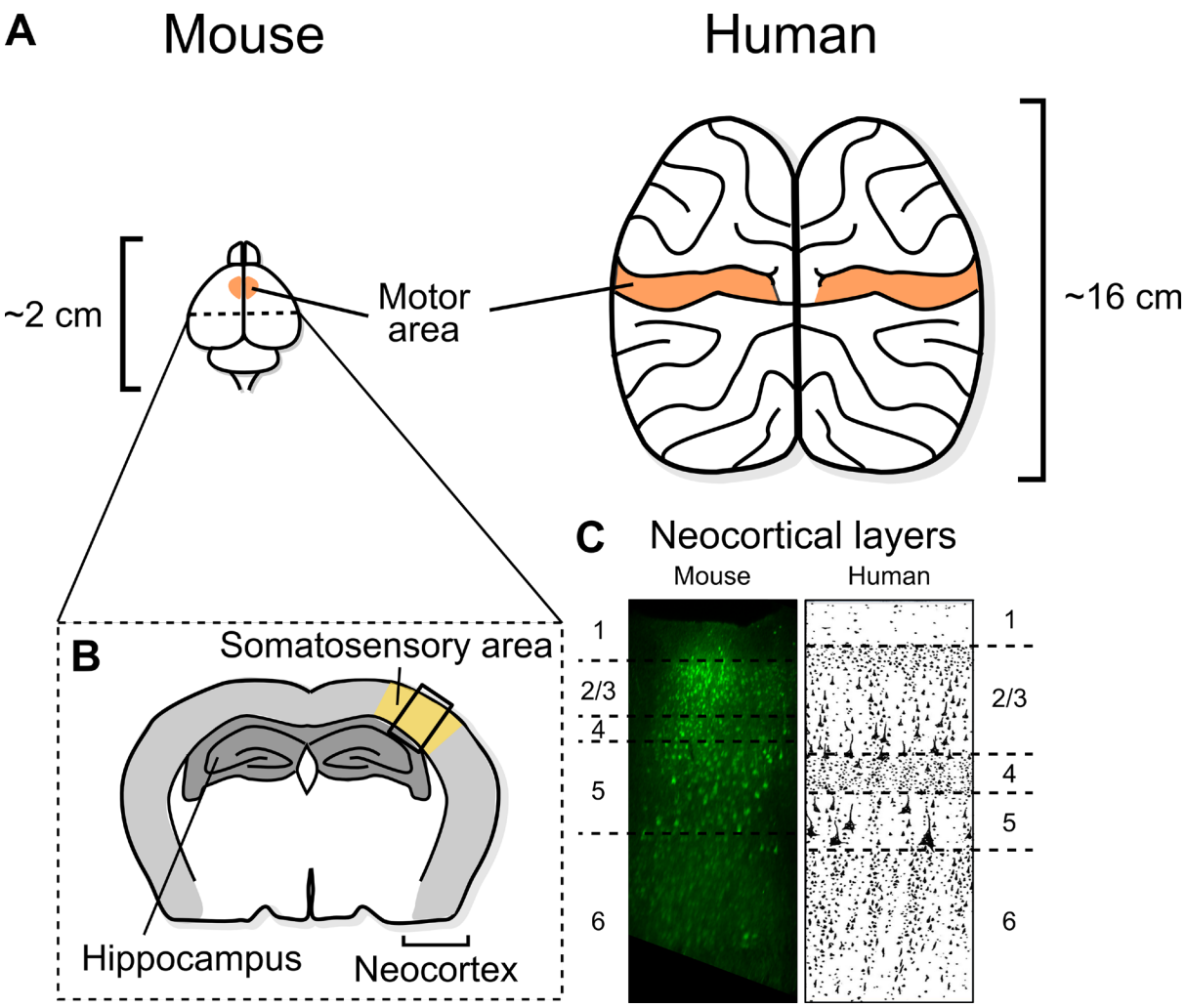

Figure 1.1. Mammalian neocortical cytoarchitecture. (**A**): Top-down view of the mouse and human brain. The mammalian neocortex is highly folded in humans compared to mice and can be divided laterally in to functional areas, such as the motor area (indicated). (**B**): Cross-section of the mouse brain shows the neocortex (*light grey*) with the hippocampus (*dark grey*) situated underneath. Another functional area—the somatosensory area—is indicated. (**C**): The neocortex is typically split in to 6 layers based on cytoarchitecture. Cross-sections of neocortex (e.g. *black box* in B) with sparse cellular labelling shows layer 1 with no cell bodies, layer 2/3 with small pyramidal cells, layer 4 with small cell bodies, layer 5 with large pyramidal cells and layer 6 with a variety of smaller cell bodies. Drawing of stained human neocortex edited from Vogt and Vogt (1919).

pyramidal neurons—these are excitatory neurons named after their pyramid-like cell body (Amunts and Zilles, 2015). Layer 2/3 pyramidal neurons synapse with each other and make cortico-cortical connections with surrounding areas. Layer 5 and 6 are mainly output layers to subcortical structures, including the brain stem and spinal cord, but layer 5 pyramidal cells can also make cortico-cortical projections (Oswald et al., 2013).

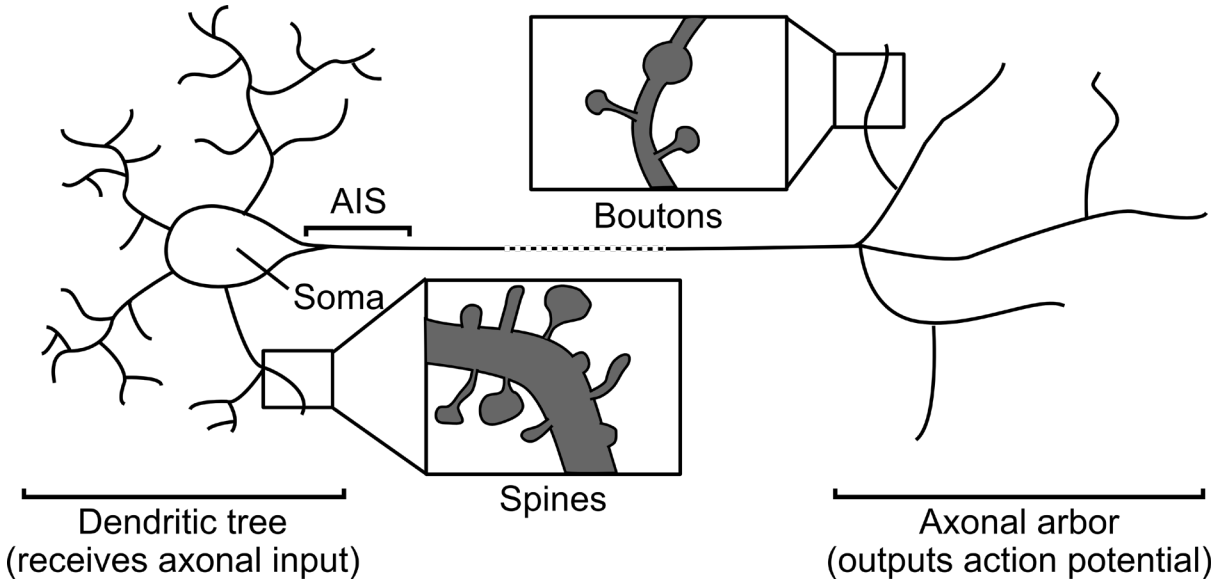

Figure 1.2. Typical structure of a neuron. A drawing of a typical neuron with many branched dendrites (dendritic tree) emanating from the cell body (soma), which receive axonal input from other neurons. Special structures on dendrites (spines) are the postsynaptic component of excitatory synaptic connections. The axon initial segment (AIS) is where the action potential is initiated once the membrane potential reaches a threshold voltage. A single, long axon extends from the soma, with sparse branching. Axonal boutons are the presynaptic component of synaptic connections.

1.2 Synaptic neurotransmission

Transmission of information in the neocortex between neurons is mainly carried out across synapses (synaptic neurotransmission). Each neuron has a typical structure including a single axon and multiple dendrites (Figure 1.2). The axon is a long, thin process that extends from the neuronal cell body and whose role is to send signals onwards to other neurons. The dendrites also extend from the cell body, but are thicker, tapered and highly branched in comparison. Dendrites receive signals from the axons of other cells and integrate them to be sent on via the axon (London and Hausser, 2005). These two types of subcellular structure—axons and dendrites, also known as the neuropil—occupy the majority of the neocortical volume (~60%; Chklovskii et al. 2002).

At excitatory synapses, which promote excitability in the postsynaptic cell, presynaptic axonal terminals—also known as axonal *boutons*, a French characterisation of their swollen button-like appearance along the axon—release chemical neurotransmitter on to postsynaptic

dendritic spines. Boutons and spines are structural specialisations that allow localised signalling from one neuron to another (Figure 1.2).

The fundamentals of neurotransmission are centralised around the cellular membrane potential, which is the difference in voltage across the plasma membrane (Bear et al., 2015). In a neuron, if the membrane potential is depolarised beyond a threshold voltage an action potential (fast conduction of signal down the axon) is generated by opening of voltage-gated ion channels.

At rest, an assortment of ion channels and pumps maintain the membrane potential below the action potential threshold, fighting against other mechanisms that hyperpolarise or depolarise the membrane intermittently. One of these mechanisms is synaptic neurotransmission, which begins when membrane depolarisation of the presynaptic neuron elicits the release of chemical neurotransmitter by synaptic vesicle fusion (Bear et al., 2015). The neurotransmitter is released in to the synaptic cleft where it binds to neurotransmitter receptors on the synaptically-coupled neuron (Figure 1.3). Some of these neurotransmitter receptors may be ligand-gated ion channels that open to change the membrane potential of the postsynaptic neuron. Inhibitory synapses act to hyperpolarise the postsynaptic membrane potential, whereas excitatory synapses act to depolarise it. If excitation dominates at a particular point in time and depolarisation of the plasma membrane near the axon (axon initial segment) is sufficient, an action potential will be initiated (Bear et al., 2015). A plethora of spatial input configurations are possible along the neuron (at the dendrites, soma or axons) that can integrate spatially and temporally to output many possibilities in terms of frequency, duration and interval of depolarisation (London and Hausser, 2005). In the neocortex, a single neuron may be connected by thousands of others through pre- and post-synaptic connections (Pakkenberg et al., 2003), resulting in dense, intermingled microcircuits that are thought to underlie neocortical function (Petreanu et al, 2009).

1.3 Synaptic plasticity

One of the key attributes of neurons in neocortical microcircuits is synaptic plasticity. Synaptic plasticity can manifest in several forms, mainly altering the strength or frequency of

neurotransmission at one or many synapses. Synaptic plasticity changes how a synapse influences the membrane potential of a postsynaptic neuron during activity. Therefore, it is thought to be important for learning and memory formation by providing capacity for change in microcircuit activity (Martin et al, 2000). Further still, new synapses can be gained—or pre-existing synapses eliminated—in a type of synaptic plasticity termed *structural synaptic plasticity*, which will be discussed in greater detail later in this chapter.

1.4 Presynaptic terminal

The presynaptic terminal is populated by synaptic vesicles, which are uniform 40 nm vesicles filled with chemical neurotransmitter (Figure 1.3). Three pools of synaptic vesicles have been identified based on their localisation and protein composition: the reserve, ready-releasable and the recycling pool. The ready-releasable pool is organised by active zone proteins such as Piccolo and Bassoon to dock them at the plasma membrane (Bear et al., 2015). They are released upon receipt of an action potential via SNARE-mediated fusion (Chicka et al., 2008; Brose et al., 1992). Subsequently, endocytosis of plasma membrane adjacent to the release site helps to reform the vesicle pool via the recycling pool (Saheki and De Camilli, 2012). The reserve pool of vesicles is not mobilised until sustained levels of stimulation are received at the presynaptic terminal, mediated by Synapsin (Kuromi and Kidokoro 2000, Verstegen et al. 2014).

Calcium is a master regulator of many processes in cell biology, and neurotransmission is no exception (Sudhof, 2012). Depolarisation of the presynaptic membrane (typically triggered by an action potential) leads to voltage-gated calcium channels opening and subsequently a large transient rise in calcium concentration. This rise in calcium concentration is responsible for triggering synaptic vesicle fusion with the plasma membrane during neurotransmission.

However, the connection between membrane depolarisation and neurotransmitter release is not completely reliable, meaning that the probability of release given an action potential is usually less than 100% (del Castillo and Katz, 1954). Plasticity mechanisms can affect presynaptic neurotransmitter release to increase or decrease the probability of release at individual synapses (Regehr, 2012). For example, the size of a calcium transient upon

depolarisation at the presynaptic terminal affects the probability of release. Calcium stores, such as the endoplasmic reticulum (ER) and mitochondria, exist throughout the cell and at the presynaptic terminal. The ER is thought to be involved in modulation of presynaptic release at central synapses through calcium-dependent interaction with the plasma membrane (de Juan-Sanz et al. 2017). Mitochondria are also thought to regulate calcium concentration at presynaptic terminals (Vaccaro et al., 2017; Marland et al., 2016; Kwon et al., 2016), which will be discussed in detail later in this chapter. Other determinants of the probability of release include the number of docked synaptic vesicles and size of the active zone (area of neurotransmitter release), but not necessarily the vesicle pool size (Branco et al. 2010; Holderith et al. 2012; Rollenhagen et al. 2015).

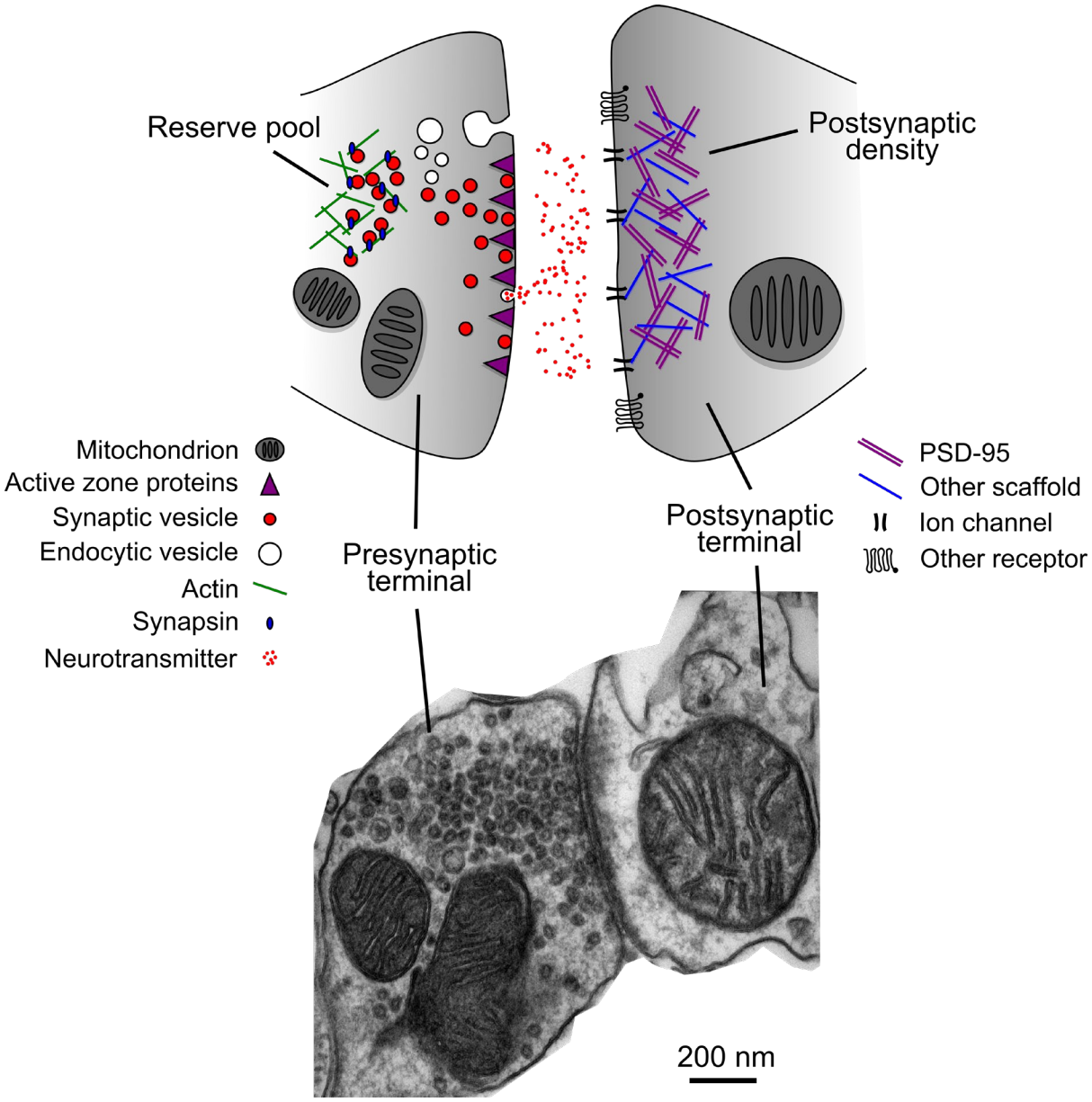

Figure 1.3. Synaptic structure. A schematic of synaptic structure (top) and an electron micrograph of a synaptic terminal in mouse neocortex (bottom). The presynaptic terminal is packed with 40 nm synaptic vesicles, loaded with chemical neurotransmitter. These vesicles can be functionally split in to three pools, the ready-releasable pool (docked to the membrane), the recycling pool (endocytic recycling) and the reserve pool (bound by Actin and Synapsin). Active zone proteins (Piccolo and Bassoon) are found at the membrane opposing the postsynaptic terminal for docking synaptic vesicles. Mitochondria are also frequently found in presynaptic boutons. The postsynaptic terminal has a dense proteinaceous region near the membrane (postsynaptic density) where scaffolding proteins hold ionotropic neurotransmitter receptors (ion channels) and other receptors (e.g. metabotropic G-protein coupled receptors). Mitochondria are very unlikely to be found in dendritic spines but are commonly found in the dendritic shaft.

1.5 Postsynaptic terminal

Postsynaptic terminals, which are mostly on dendritic spines for excitatory synapses (Nimchinsky et al. 2002), receive signals from presynaptic terminals in the form of chemical neurotransmitter (Figure 1.3). Ionotropic neurotransmitter receptors (e.g. AMPA and NMDA) on the surface of the postsynaptic membrane are ligand-gated ion channels that open upon neurotransmitter binding to cause a change in the membrane potential (Traynelis et al., 2010). Ultimately for excitatory synapses, an excitatory postsynaptic potential (EPSP) results. If enough inputs are made in a close spatiotemporal pattern (i.e. multiple spines on the same dendritic branch within a few milliseconds), a larger EPSP will be made. Eventually large enough EPSPs cause the depolarisation of the soma and axon initial segment past threshold, firing an action potential down the axon. The postsynaptic terminal—whether it be the dendritic shaft, a dendritic spine or even the axon or somatic membrane—is therefore very important for computation in neocortical microcircuits (London and Hausser, 2005). Mixtures of inhibitory and excitatory synapses may occur on different subcellular compartments of the neuron, sometimes even occurring on the same dendritic spine (Villa et al. 2016). The integration of signals from these synapses in space and time, depending on the circuits they are involved in, produces differential responses from the neuron (London and Hausser, 2005).

As with presynaptic terminals, there are plasticity mechanisms that can increase or decrease a spine's response to stimulation. These mainly involve either changes in neurotransmitter receptor activity (Lee et al., 2003) or availability (through changes in spine structure; Takahashi et al., 2003; Bosch and Hayashi, 2012) on the postsynaptic membrane. Long-term increases or decreases in the synaptic strength are called long-term potentiation (LTP; Bliss and Collingridge, 1993) or long-term depression (LTD; Collingridge et al., 2010), respectively. These mechanisms of plasticity provide an additional layer of regulation at individual synapses, and similarly to presynaptic plasticity, are thought to underlie learning and memory formation in the neocortex (Martin et al., 2000; Bear and Kirkwood, 1993).

Spines involved in excitatory synapses are assembled by recruitment of actin machinery to form the structure, and scaffolding proteins for receptor insertion (Bosch and Hayashi, 2012). One of these scaffolding proteins is PSD-95 (postsynaptic density protein 95) and is often used

to identify excitatory postsynaptic terminals (Figure 1.3, Chen et al. 2011). The structure of the postsynaptic spine is thought to allow it to compartmentalise electrical activity and calcium concentration changes (Yuste, 2013; Yuste et al. 2000). Compartmentalisation between adjacent spines may allow for the precise regulation of calcium-dependent plasticity at individual spines (Malenka et al., 1988), despite being in close proximity to each other.

1.6 Synaptic structure-function relationship

Synaptic structure and function are inextricably linked. For presynaptic terminals, the size of the active zone is proportional to the number of synaptic vesicles docked there and the probability of neurotransmitter release (Holderith et al. 2012; Branco et al. 2010). Presynaptic bouton, active zone and synaptic vesicle pool sizes are also correlated to the size of the postsynaptic density and spine (Meyer et al., 2014; Rollenhagen et al. 2015; Smith et al. 2016; Kasthuri et al, 2015), which dictates the number of neurotransmitter receptors (Bosch and Hayashi, 2012). Hence, the structural size of an axonal bouton or dendritic spine is indicative of synaptic efficacy (Holderith et al. 2012, Meyer et al., 2014).

Axonal boutons can have varying structure, typically either *en passant*—bilateral swellings along the axonal shaft—or *terminaux*—terminals at the end of branches that are <5 μm (Figure 1.2). Boutons can also adopt intermediate structures, but less commonly (Morimoto et al., 2018). The differences between *en passant* and *terminaux* boutons are not known (Anderson and Martin, 2001) and will be discussed further in Chapter 3.

A single axonal bouton may have more than one postsynaptic partner due to separate release sites. These multi-synaptic boutons occur at rates of ~14–18% at excitatory boutons of the mouse neocortex (Knott et al., 2006; Kasthuri et al., 2015), and are thought to be associated with increased spine dynamics in comparison to single-synaptic boutons due to competition between partnering spines (Reilly et al., 2011). Swellings along the axonal backbone can also be non-synaptic, lacking synaptic vesicles, active zones and synaptic contacts, but this is uncommon (10–15% in rat hippocampus; Shepherd and Harris 1998; Smith et al. 2016).

Structural plasticity may be related to synaptic efficacy; smaller boutons, with potentially lower synaptic efficacy (Welzel et al. 2011, Meyer et al. 2014), are less stable than larger boutons in the neocortex *in vivo* (Ash et al. 2018) and in *Xenopus* retinal ganglion cells (Ruthazer et al. 2006). Additionally, it has been shown that weaker synapses are more readily lost when targeted for LTD than stronger ones (Wiegert and Oertner, 2013).

1.7 Synaptogenesis

How the location of synapse formation along the axon is determined is not well understood. Okabe et al. (2001) show that physical contact sites between the axon and dendrite lead to spine formation and clustering of both PSD-95 and Synaptophysin. Additionally, Sabo et al. (2006) show that specific sites exist where synaptic vesicle protein transport vesicles (STVs) consistently pause; subsequently, presynaptic terminals form at these sites upon postsynaptic contact. It is also thought that complementary proteins on the pre- and post-synaptic membranes drive synapse formation upon contact and aid in specificity of contacts between different cell types or subcellular locations (Schroeder and Wit, 2018). Many different adhesion proteins have been identified that can anchor the pre- and post-synaptic membranes together (Missler et al., 2012), resulting in lots of combinations for selective contacts.

The temporal order of synaptic assembly is also not well understood. The formation of dendritic spines is thought to come before synaptogenesis in the adult neocortex (Knott et al. 2006). Synaptic contacts with nascent spines are not found until they are at least a few days old *in vivo* (Blazquez-Llorca et al. 2015; Knott et al., 2006), with most new spines contacting pre-existing boutons (Knott et al., 2006), which is also true after LTP *ex vivo* (Smith et al. 2016). Supporting this, spatially-restricted glutamate release in acute brain slices can induce spine formation (Kwon and Sabatini, 2011), suggesting that presynaptic terminals of excitatory synapses can induce spine formation by neurotransmitter release. A retrograde signal (nitric oxide) from the postsynaptic terminal back to the presynaptic terminal has also been suggested to occur upon activation of NMDA receptors (Nikonenko et al. 2003). Further support for reciprocal postsynaptic signalling comes from Meyer et al. (2014) where they show that artificially increasing spine size also induced matching presynaptic structural change if the increased spine size was persistent.

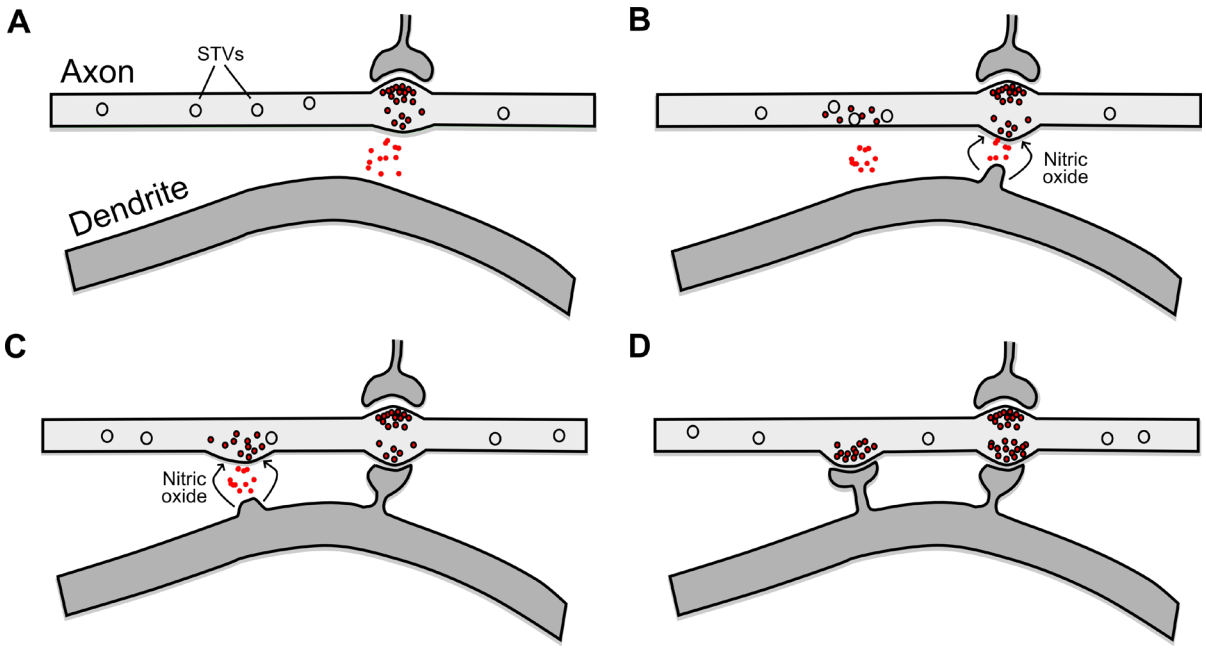

Figure 1.4. Mechanisms of synaptogenesis. (**A**): A pre-existing bouton with a single synapse releases neurotransmitter near to another dendrite. (**B**): The dendrite forms a protrusion and releases a reciprocal signal (nitric oxide) to induce structural change in the presynaptic terminal. A set of synaptic vesicle protein transport vesicles (STVs) pause at a pre-defined site on the axon and neurotransmitter is released. (**C**): The pre-existing bouton now possesses two mature dendritic spines, making it a multi-synaptic bouton. The nascent bouton receives a reciprocal signal from the immature dendritic spine for further structural alterations. (**D**): A mature synapse forms between the newly-formed bouton and dendritic spine.

These findings point towards a model where pre-existing presynaptic boutons signal for spine formation and spines reciprocate with signalling for presynaptic terminal growth, although the role of new boutons in *de novo* synapse formation is underexplored (Figure 1.4).

1.8 Presynaptic structural plasticity

Synaptic structural plasticity of neocortical circuits is thought to be fundamental for learning and memory formation (Holtmaat and Svoboda, 2009). Structural plasticity in the neocortex was discovered using cranial window implantation and two-photon microscopy (Lendvai et al. 2000; further detail provided in Chapter 3). Using this technique, it is possible to track pre- and post-synaptic structure over time to correlate external stimuli and behaviour to structural changes (Holtmaat et al., 2009).

Presynaptic structural plasticity can take many forms: bouton shrinkage or enlargement; *de novo* formation or elimination; or the remodelling of an entire axonal branch (Gogolla et al. 2007). Structural plasticity is not limited to periods of development, structural changes in boutons can be seen throughout the lifetime of mice (Grillo et al. 2013, Mostany et al., 2013). Shrinkage and enlargement of terminals is thought to relate to the strength of the synaptic connections (Holderith et al. 2012), whereas the entire gain or loss of axonal boutons may increase the number of configurations for synaptic connectivity (Holtmaat and Svoboda 2009).

1.8.1 Bouton turnover in the mammalian neocortex

Structural presynaptic plasticity in the neocortex seems to be conserved in at least two divergent species of mammals, mouse and macaque monkeys (Stettler et al. 2006; Majewska et al. 2006; De Paola et al. 2006; Grillo et al. 2013; Qiao et al. 2015; Mostany et al. 2013; Holtmaat and Svoboda 2009). The density of boutons along pyramidal cell axons in the adult mammalian neocortex is consistent over time due to a balance between bouton loss and gain (Stettler et al. 2006; De Paola et al. 2006; Grillo et al. 2013). Interestingly, gained boutons are not necessarily all formed equally. Most newly-formed boutons are quickly lost again in mouse motor and somatosensory cortex (70% within 1 week), with a small but significant proportion being stable for very long periods (>1 month; Qiao at al. 2015). Fewer pre-existing boutons are lost in comparison, and in this way the longer a bouton exists the less likely it is to be lost (Ash et al., 2018; Qiao et al., 2015).

The importance of a single bouton being persistent in a network has been questioned, as size continuously varies (Minerbi et al., 2009), and so the idea that a persistent bouton is a stable synaptic connection is disputed. However, new and persistent boutons that are reconstructed with the aid of electron microscopy almost always have postsynaptic partners (De Paola et al., 2006; Grillo et al., 2013). This indicates that short-term (weekly) structural plasticity is functionally relevant, but substantial changes to neural processing probably only occur through coordinated plasticity of multiple synaptic connections in the same circuit.

1.8.2 Experience-dependent presynaptic structural plasticity

Although bouton density is stable during normal behaviour (Grillo et al., 2013), studies show that perturbing sensory stimulation changes the density and turnover of boutons in the mouse brain. The changes that occur can be positive or negative depending on the cell type and cortical area.

In the barrel cortex (responsible for sensory input from the whiskers in rodents), plucking of a whisker results in increased bouton formation on axons of excitatory neurons innervating the associated area, compared to axons outside (Marik et al. 2010). In a separate study of whisker trimming, excitatory axons in areas surrounding the deprived region have ~60% larger boutons and synaptic contact zones (Cheetham et al. 2014). Marik et al. (2010) also found that inhibitory neurons innervating the deprived area have increased bouton loss, suggesting different plasticity responses for inhibitory and excitatory neurons during sensory perturbation.

For pyramidal neurons of layer 2/3 primary visual cortex, monocular retinal lesions or enucleation (removal of an eye) result in an almost doubling of excitatory bouton loss, but no change in bouton gain (Smit-Rigter et al. 2016, Sammons et al. 2018). Remaining bouton sizes are reduced in variability in Sammons et al. (2018), which is thought to increase the capacity for reorganising the circuit by allowing for more bidirectional plasticity. Other studies show no change in excitatory synapse number after eye suturing, a different sensory intervention (Villa et al., 2016, Frantz et al., 2016). These conflicting results may suggest that damage (lesion/enucleation)—rather than a lack of stimulus (suturing)—is inducing the structural plasticity.

For inhibitory axons of layer 2/3 pyramidal neurons in visual cortex, bouton survival and density reduce by ~20% immediately following monocular lesions (Keck et al. 2011). Similarly, with eye suturing, a ~10% reduction in dynamic inhibitory synapses is seen (Villa et al., 2016). As in somatosensory cortex, these results support the idea that there are differences in excitatory and inhibitory dynamics during sensory perturbation of vision.

In sensory neurons of the olfactory bulb, occlusion of a nasal passage results in ~50% decreased bouton turnover (loss and gain; Cheetham et al. 2016). These neurons directly receive odour signals; therefore, this may be an example of reduced structural plasticity directly resulting from loss of sensory stimulus and activity.

In cases where mice are stimulated using a natural environment, both excitatory and inhibitory synaptic density increase in the same area of the somatosensory cortex (Landers et al., 2011). Other studies in animals that are exposed to enriched environments show increased expression of synaptic proteins across the brain and an increased number of boutons per neuron in occipital cortex and hippocampus (Nithianantharajah et al. 2004; Sirevaag and Greenough, 1987, Briones et al. 2004, Briones et al. 2005). However, Qiao et al. (2015) did not find a significant change in bouton turnover in layer 5 pyramidal neurons of somatosensory cortex with sensory enrichment. They used a moderate form of enrichment consisting of single housing in a small cage with hanging beads (Qiao et al., 2015), in comparison to the other studies, which use multiple housing in large cages and a variety of textures and shapes. Standard protocols have been published that would reduce the possibility of enrichment variation affecting results in the future (Sztainberg and Chen, 2010; Slater and Cao, 2015).

These results support the theory that bouton turnover is experience-dependent; however, different sensory perturbations lead to different trajectories for excitatory or inhibitory bouton turnover. Enriching sensation can increase general bouton density and deprivation appears to reduce inhibitory tone, but excitatory boutons are affected differentially by deprivation in somatosensory and visual cortices. Different plasticity responses to sensory deprivation between these two areas might be explained by higher use of somatosensation than vision in mouse behaviour, which is mostly nocturnal (Krubitzer et al., 2011).

1.8.3 Learning-related presynaptic structural plasticity

Presynaptic structural changes during and after training in behavioural tasks are also correlated to learning in mice (Holtmaat and Caroni, 2016). After motor training, bouton elimination doubles on axons projecting to layer 1 of the motor cortex compared to a period of rest, despite having similar levels of bouton gain (Ash et al. 2018). The structural plasticity

during learning is almost entirely due to loss and gain of small boutons, drawing a parallel with the idea that small dendritic spines are learning spines (Kasai et al., 2003). While investigating rule learning in the orbifrontal cortex, Johnson et al. (2016) found increased bouton turnover in animals trained with an odour task. Further to this, animals undergoing more trials of exploration and therefore potential error had greater bouton loss and those undergoing exploitation of learned rules had greater bouton gain. These studies indicate that structural plasticity is involved in learning and memory formation processes in the neocortex of mice. Furthermore, the loss of boutons may be related to error and gain of boutons to reinforced success. More evidence for experience-dependent and learning-related structural changes will be discussed later in this chapter with relation to postsynaptic dendritic spines.

1.8.4 Presynaptic structural plasticity changes with age and cell-type

As well as experience-dependent changes in presynaptic structure, there are differences in bouton properties between age groups of mice and between different areas of the mouse brain.

Aging is related to cognitive decline in mice and humans (Grillo et al., 2013; Hedden and Gabrieli, 2004), which may be caused by a reduction in learning-related structural plasticity. Bouton density in juvenile mice (<1-month-old) starts at almost half of that in aged mice (>20-months-old) and subsequently increases in the first 8 months before reaching a plateau (Mostany et al. 2013; Grillo et al. 2013). The degree of bouton turnover is similar throughout life, with a slight net gain of boutons resulting in a higher density at old age (Mostany et al. 2013; Qiao et al. 2015). Studies have also shown that average bouton size either remains constant or increases slightly with age, mainly due to an increase in large boutons (Mostany et al. 2013; Grillo et al. 2013). While Mostany et al. (2013) show increased stabilisation of *en passant* boutons with age, Grillo et al. (2013) suggests old mice have less stable *en passant* boutons, which correlates with cognitive decline. These studies show that structural plasticity is altered during aging and destabilisation of boutons is related to cognitive decline; however, no underlying mechanism has been suggested.

Different cell types can display differential synaptic dynamics. In three cell types of the mouse somatosensory cortex, bouton survival over 1 month varied from 30% to 90% (De Paola et al.

2006). The composition of bouton types is also different among these cell types, some are majority *terminaux* boutons, whereas others are rich in *en passant* boutons. A different study of one of the cell types (Morimoto et al. 2018) also measured a similar survival as De Paola et al. (2006). In the same study, Morimoto et al. (2018) found that bouton turnover on catecholaminergic axons—thought to originate from subcortical regions—is much higher than that of pyramidal neurons projecting to the same area. Very high turnover of axonal boutons is seen in the olfactory bulb of mice where a high proportion of boutons can turnover in hours (10–20% in 3 hours; Cheetham et al. 2016). In Cheetham et al. (2016) the different genetic identities of olfactory neurons (immature and mature) also differed in their bouton turnover rates. These studies support the idea of cell-type specificity in structural plasticity, which could be determined by genetic identity, brain area and connectivity.

Further evidence that connectivity controls presynaptic structural plasticity comes from saturated EM-based reconstructions of the neocortex (Kasthuri et al., 2015). Similar synaptic ultrastructure is seen at sets of synapses between the same two cells, indicating that activity at synaptic connections may be driving synaptic structure. Additionally, the expression of various trans-synaptic adhesion proteins in different regions occupied by the same axon may lead to differential synaptic stability in each region (Schroeder and de Wit, 2018). Evidence from the cerebellum where axons ascend to synapse on Purkinje cells shows branch-specific differences in bouton turnover (Nishiyama et al. 2007), which could be due to differences in postsynaptic adhesion proteins.

1.9 Postsynaptic structural plasticity

A great deal more is known about the structural plasticity of postsynaptic dendritic spines than presynaptic axonal boutons (Fu and Zuo, 2011). Persistently enlarged dendritic spine sizes are correlated with bouton sizes at the ultrastructural level (Meyer et al. 2014), indicating that spine and bouton structural plasticity are linked. Therefore, it is important to understand the role of postsynaptic structural plasticity in experience-dependent and learning-related plasticity in the neocortex and correlate it to presynaptic structural plasticity.

1.9.1 Spine turnover in the mammalian neocortex

Spine density is ~3–4 times higher than bouton density on the same layer 5 pyramidal neurons in somatosensory cortex (Mostany et al., 2013). Spine density rises on these cells as mice age due to an increase in stability, similar to changes in presynaptic terminal density (Mostany et al. 2013). Majewska et al. (2006) showed that dendritic spine turnover of layer 5 pyramidal neurons in different areas of the cortex is consistent over time (80–90% persistence over 1–3 weeks). The 1-week turnover is not a third of the 3-week turnover, indicating that, similarly to axonal boutons (Qiao et al. 2015), newly-formed spines are quickly lost in comparison to pre-existing spines. Although spine dynamics follow a similar trajectory to bouton dynamics over time, spine turnover of layer 5 pyramidal neurons was 2–3 times that of bouton turnover for the layer 2/3 and 5 pyramidal neurons that they are thought to synapse with (Mostany et al. 2013; Trachtenberg et al. 2002). This indicates that dendritic spines are sampling synaptic partners at a higher rate than axonal boutons and agrees with studies showing that new spines form on pre-existing boutons, forming multi-synaptic sites (Smith et al., 2016; Knott et al., 2006, Reilly et al., 2011).

Differences in postsynaptic structural plasticity between male and female mice have also been identified. Basal density and turnover do not differ between the two sexes, but sensory-evoked changes in turnover for female mice depend on their stage in the estrous cycle (Alexander et al., 2018). This is important to note for the design of experiments depending on experience-dependent or learning-related modulation of structural plasticity.

1.9.2 Experience-dependent postsynaptic structural plasticity

As with presynaptic terminals, dendritic spine structural dynamics differ with changes in experience. In layer 4 somatosensory cortex, whisker stimulation for 24 hours results in increased spine density and numbers of inhibitory and excitatory synapses on spines (Knott et al., 2002). This reverts back to basal levels after 4 days for excitatory but not inhibitory synapses. On layer 2/3 and layer 5 pyramidal cells of somatosensory cortex, spine density is increased by ~30% for mice with enriched environments and spine survival is also reduced due to elevated turnover (Jung and Herms, 2014). Sensory deprivation by whisker trimming in adult mice did not change spine density in the barrel cortex in the 4 days immediately

following trimming. However, it did result in the decreased lifetime and increased turnover of dendritic spines (Trachtenberg et al. 2002).

In the visual cortex, Hofer et al. (2009) found that monocular deprivation (eye suturing) resulted in increased spine density due to more spine formation, but a second deprivation did not alter structural dynamics (or revert the density back to basal levels). Keck et al. (2011) showed that, similarly to inhibitory boutons in visual cortex, monocular lesions can lead to a decrease in inhibitory spine density and survival by 15-20%. These results show that, similarly to axonal boutons, spine dynamics are altered by changes in sensory experience, potentially increasing turnover to sample more synaptic partners under both enrichment and deprivation and reducing inhibitory tone upon deprivation.

1.9.3 Learning-related postsynaptic structural plasticity

Postsynaptic structural changes related to learning and memory formation are thought to be correlated to performance, as well as occurring during the learning phase (Fu and Zuo, 2011). The increased density of spines seen in Hofer et al. (2009), which persisted during the second monocular deprivation, was linked to faster onset of functional plasticity. This may be an indication that structural changes create a lasting memory for later improved performance. Similarly, spine turnover rate prior to learning was positively correlated with performance in a contextual fear freezing task (Frank et al. 2018). Areas of spine turnover before learning were hotspots for clustered spine formation during training, suggesting that pre-learning turnover levels allow for more sampling of the synaptic space during learning and speed up the formation of new connections. Persistence of gained spines in the barrel cortex during a whisker-dependent task were shown to be specific to that task and not just the act of learning, as they did not occur in a separate whisker-independent task (Kuhlman et al., 2014). Both pre-existing and newly-formed spines were more persistent after whisker-dependent training. Yang et al. (2014) showed a subcellular difference in structural plasticity rates during motor training, where spine formation outweighed elimination in a branch-specific manner. Interestingly, those spines formed during learning were destabilised if the task was reversed, but not if the task was repeated in the normal manner, suggesting overwriting of the memory trace through spine loss. Changes in spine size have also been associated with learning. In a

motor grabbing task, the area of the motor cortex associated with the training had increased spine widths coupled to higher electrophysiological response (Harms et al. 2008). These results show that postsynaptic structural plasticity prior to learning may be indicative of performance, and changes during learning occur in a specific manner, potentially leaving a lasting structural trace.

It is clear from these studies in the mammalian neocortex that a synapse's function is related to its structure, and that the pre- and post-synaptic terminals are highly dynamic throughout life, indicating changes in synaptic strength and connectivity. The results from longitudinal *in vivo* imaging experiments have also elucidated the importance of structural plasticity in perception, learning and memory formation (Figure 1.5). However, the intrinsic mechanisms that influence structural synaptic plasticity remain to be determined.

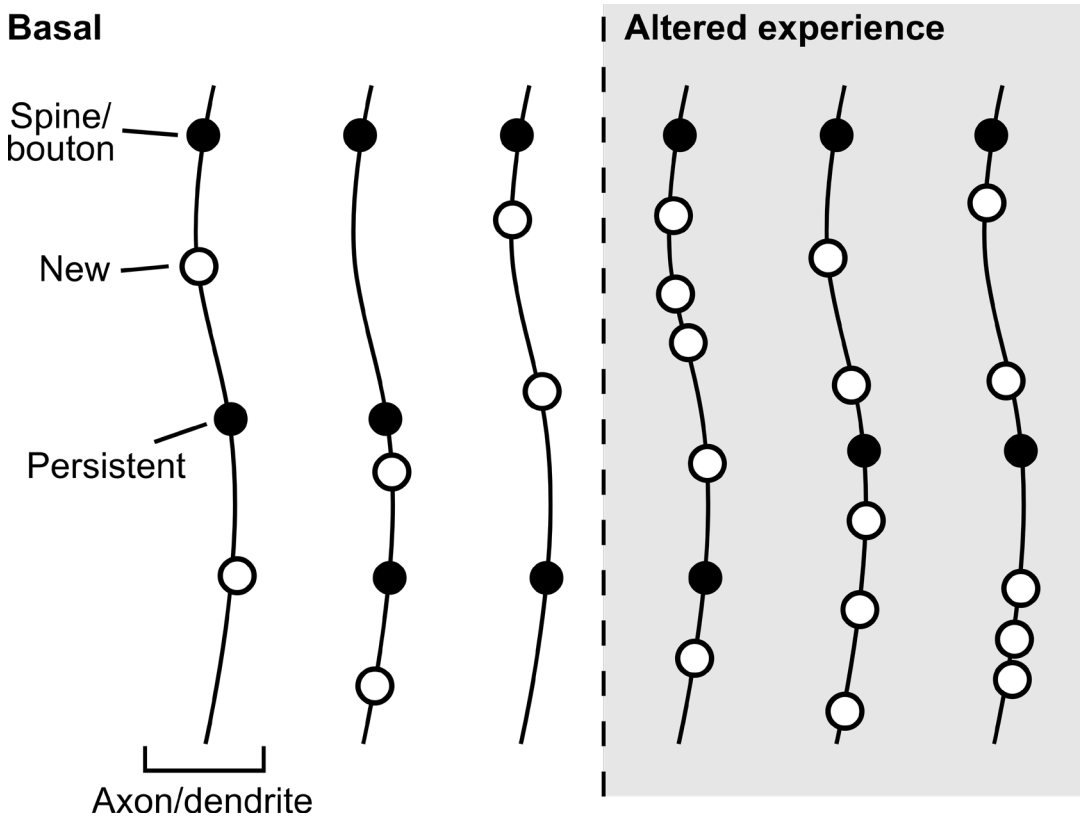

Figure 1.5. Experience-dependent structural synaptic plasticity. Schematic of axonal and dendritic structural changes during altered experience. Synaptic structures are lost and gained at a relatively low level during normal behaviour. New structures are quickly lost again, and rarely persist to become long-lived, whereas the majority of pre-existing structures are long-lived. Upon altered experience (both deprivation and enrichment) density and turnover are typically increased, which is thought to provide a greater capacity for circuit reorganisation. Dendritic spines are found at a higher density than axonal boutons, and also have higher turnover.

1.10 Mitochondria in a neuronal context

Mitochondria will be introduced in this section before their function is considered in the context of the presynaptic terminal in *section 1.11*.

1.10.1 ATP synthesis

It is estimated that 41% of the adenosine triphosphate (ATP) consumed in the cerebral cortex is used for synaptic neurotransmission (Harris et al. 2012). Postsynaptic mechanisms that utilise ATP are mainly involved in membrane potential maintenance through ion pumps, whilst presynaptic mechanisms include maintaining internal calcium concentration, generating axon potentials and motor protein trafficking. The source of ATP in neurons is either from glycolysis or mitochondrial metabolism in the neuron (Hall et al., 2012). However, the mechanism by which glucose is utilised, either by a lactate shuttle from astrocytes or directly through neuronal glycolysis, is debated (Magistretti and Allaman, 2015; Diaz-Garcia et al., 2017). Most recently, it has been suggested that during high metabolic demand, neurons briefly shift to glycolysis as their main source of ATP (Diaz-Garcia et al., 2017), but this remains controversial (Hall et al., 2012).

Mitochondrial metabolism generates ATP through oxidative phosphorylation (OXPHOS), which is carried out within the confines of the mitochondrial membranes (Figure 1.6). For this to occur, multiple protein complexes along the inner mitochondrial membrane act to produce a proton gradient across the membrane from the breakdown of NADH and electron transport (Figure 1.6; Alberts et al., 2014). Ultimately, ADP (adenosine diphosphate) is converted to ATP via phosphorylation at the ATP synthase, whose operation is dependent on the mitochondrial membrane potential established by the proton gradient (Bagkos et al., 2014).

1.10.2 Mitochondrial calcium sequestration

The large mitochondrial membrane potential required to efficiently synthesise ATP (Bagkos et al., 2014) creates a driving force for the accumulation of calcium in the mitochondrial matrix (Rizzuto et al., 2012). Calcium is transported across the outer mitochondrial membrane via the voltage-dependent anion channel (VDAC1; Gincel et al., 2001). The mitochondrial calcium uniporter (MCU) is the primary calcium transporter used to sequester calcium inside the

mitochondrial matrix (De Stefani et al., 2011). The MCU only opens at high calcium concentrations dependent on the regulatory subunits mitochondrial calcium uptake 1 and 2 (MICU1/2; Patron et al., 2014). MICU2 acts to inhibit MCU at low calcium concentrations to prevent the energetic sink of shuttling calcium, and MICU1 promotes MCU calcium uptake at high concentrations (Patron et al., 2014). The result is that when cytosolic calcium concentration sharply rises (relevant at presynaptic terminals), the MCU opens to sequester calcium (Figure 1.6). It has been postulated that a high concentration of calcium inside the mitochondrial matrix is linked to an increased rate of ATP synthesis (Chouhan et al. 2012, Jouaville et al. 1999, Gunter and Sheu 2009, Denton and McCormack, 1980).

1.10.3 Other biochemical pathways involving mitochondria

Mitochondria are also involved in a variety of other less well-studied processes, such as lipid metabolism (Tyurina et al. 2014) and lipid and ion exchange occurring at organelle contact sites (Figure 1.6; Murley and Nunnari, 2016). Surprisingly, mitochondria have also been implicated in direct neurotransmitter release in taste buds (Romanov et al., 2018). The interacting and essential functions of mitochondria have often made it difficult to tease apart their role in specific cellular processes.

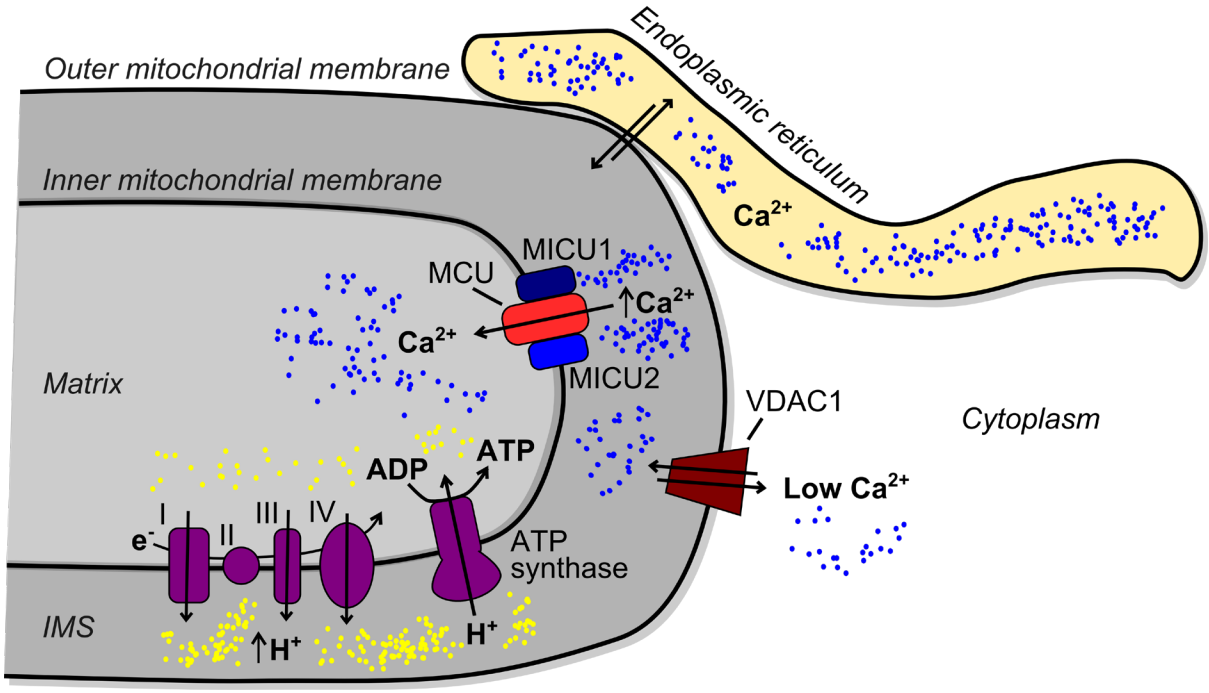

Figure 1.6. Mitochondrial function in ATP synthesis and calcium homeostasis. The endoplasmic reticulum is the largest store of calcium in cells and often interacts with mitochondria at contact sites, exchanging lipids and ions. Mitochondria accumulate calcium in the intermembrane space (IMS) via import through the voltage-dependent anion channel (VDAC1), which acts at low calcium concentrations. High concentrations of calcium open the mitochondrial calcium uniporter (MCU) due to regulation by mitochondrial calcium uptake 1 (MICU1) and disinhibition by mitochondrial calcium uptake 2 (MICU2). This results in calcium accumulation inside the mitochondrial matrix. The mitochondrial membrane potential across the inner mitochondrial membrane (IMM) is maintained by transmembrane proton pumps—the electron transport chain protein complexes I, III and VI. Ultimately, adenosine diphosphate (ADP) is phosphorylated to adenosine triphosphate (ATP) by the ATP synthase, dependent on the proton gradient established over the IMM.

1.10.4 Mitochondrial trafficking

The long, thin and convoluted morphology of dendrites and particularly axons make the provision of mitochondria to these areas a difficult task (Misgeld and Schwarz, 2017). Mitochondria are discontinuous in neuronal processes in comparison to their reticular form in the soma (Cagalinec et al., 2013; Alberts et al., 2014). They are highly fragmented in axons and much less so in dendrites, similarly mitochondria occupy less of the overall area in axons compared to dendrites (Lewis et al., 2018; Figure 1.7). The small size of individual mitochondria in axons may mean that they can be effectively trafficked to presynaptic sites, which are many centimetres to metres away from the soma in human neurons (Misgeld and Schwarz, 2017).

Mitochondria are trafficked anterogradely along microtubules via kinesin motor proteins (KIF5A specifically) using Trak1/2 adaptor proteins (Loss and Stephenson, 2017; van Spronsen et al., 2013; Brickley and Stephenson, 2011; Stowers et al., 2002) that bind to Miro1 (mitochondrial Rho GTPase 1) on the mitochondrial surface (Saotome et al., 2008; Figure 1.7). Indeed, Miro1 knockout has been shown to alter the distribution of mitochondria in peripheral nerve axons and produce deficits in transportation (Nguyen et al. 2014). However, Miro1 knockout mice still possess mitochondria in distal axons of the central nervous system due to the persistence of some mitochondrial motility (Lopez-Domenech et al., 2016; Lopez-Domenech et al., 2018). Retrograde transport of mitochondria is mediated by the dynein/dynactin complex and is less well-studied than anterograde transport (van Spronsen et al. 2013, Drerup et al. 2017).

Most studies of mitochondrial motility in neurons have been carried out in primary cortical and hippocampal cultures from embryonic rodents. These showed that, in a period of 2–10 minutes, 20–40% of the mitochondria in the field of view were mobile, the rest being stationary (Sun et al., 2013; Chang et al., 2011; MacAskill et al., 2009; Ligon and Steward, 2000). However, further interrogation of developing neurons *in vitro* and more recently *in vivo* has led to the realisation that mitochondrial motility reduces throughout development (Faits et al. 2016; Smit-Rigter et al. 2016; Loss and Stephenson, 2017) despite mitochondrial function—namely membrane potential and calcium sequestration—remaining at similar levels (Chang and Reynolds, 2006). In the visual cortex of anaesthetised adult mice (3–4 months old), the mitochondrial motility rates in axons are on average 1% over a 2-minute period (Smit-Rigter et al. 2016). Mitochondrial motility was not found to be much higher in awake animals (Lewis et al. 2016), suggesting low activity during anaesthesia was not responsible for the low motility rates. These findings indicate that a developmental or maturation process is driving the reduction in mitochondrial trafficking over time in the central nervous system.

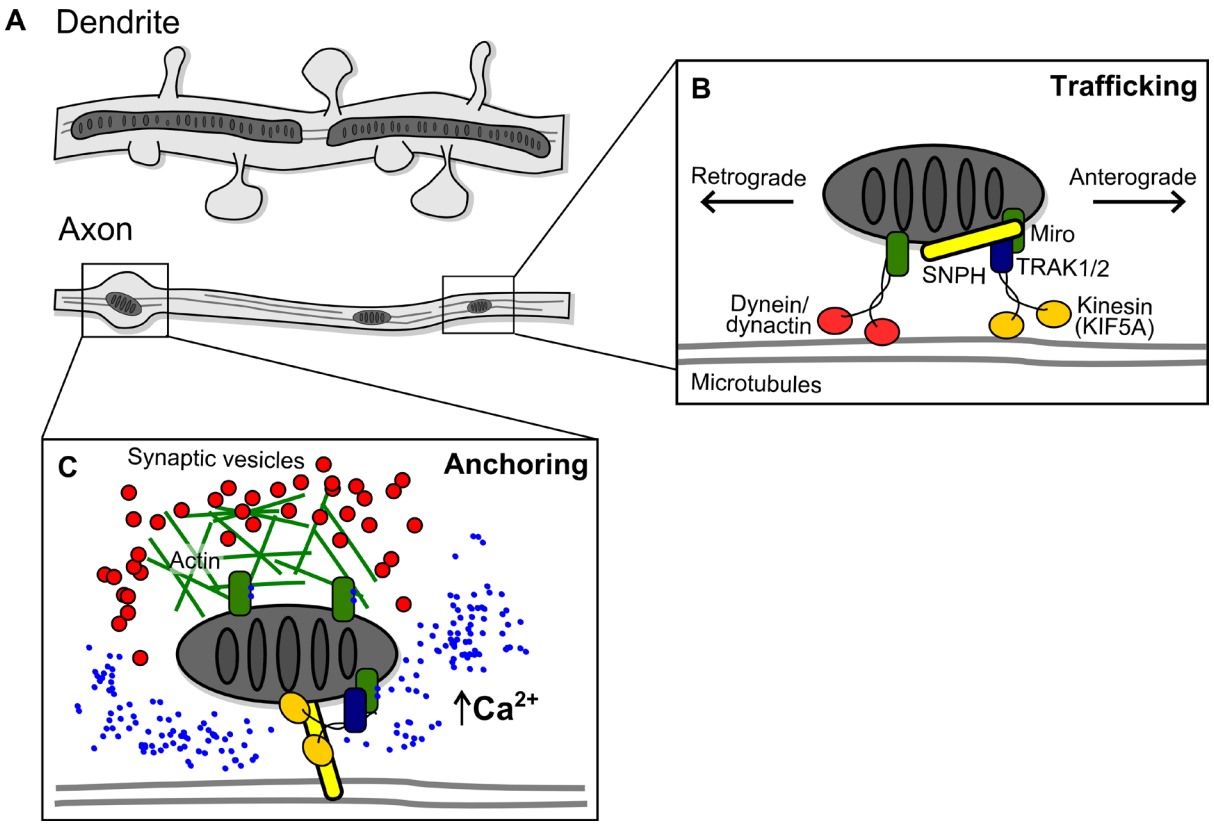

Figure 1.7. Mitochondrial trafficking and anchoring. (**A**): Mitochondria are discontinuous in neuronal processes, covering a larger area in dendrites than in axons. Mitochondrial trafficking occurs in both axons and dendrites facilitated by microtubules. (**B**): In axons, anterograde trafficking is mediated by mitochondrial Rho GTPase (Miro) and the trafficking kinesin proteins (TRAK1/2) attached to kinesin motor KIF5A. Syntaphilin (SNPH) is an anchoring protein found localised to mitochondria that is not bound to microtubules during trafficking. Retrograde trafficking of mitochondria is mediated by the dynein-dynactin complex and Miro. (**C**): Anchoring of mitochondria occurs in a calcium-dependent fashion, where calcium binds to Miro and subsequently Kinesin is no longer able to function, potentially due to binding by SNPH. SNPH is thought to anchor mitochondria to microtubules directly. Positioning of mitochondria may be further mediated by Actin and Miro.

1.10.5 Mitochondrial anchoring

Calcium is thought to regulate mitochondrial motility in neurons. An increased concentration of cytosolic or mitochondrial matrix calcium results in immobilisation of mitochondria via Miro1 and MCU (Guo et al., 2005; Saotome et al. 2008, MacAskill at al. 2009; Wang and Schwarz, 2009; Chang et al. 2011; Nguyen et al. 2014; Figure 1.7). Other mechanisms of mitochondrial immobilisation have also been proposed that may work in parallel with Miro1. Syntaphilin is a protein that is localised to the axon and specifically found on mitochondria, immobilising them and not other cargoes (Kang et al. 2008). This may be mediated through binding to Miro1 and KIF5A to prevent further motor procession (Chen and Sheng, 2013).

Indeed, altering syntaphilin levels has been used to reduce axonal damage in mouse models of neurodegenerative and neurological injury by increasing mitochondrial motility (Joshi et al., 2015; Ohno et al. 2014; Zhou et al. 2016). Other proteins, such as DISC1 (disrupted in schizophrenia 1), LC8 (dynein light chain 8), LKB1 (liver kinase B1) and NUAK1 (also known as ARK5: adenosine monophosphate-related kinase (AMPK)-related protein kinase 5) are thought to mediate the Miro-dependent trafficking or Syntaphilin-dependent anchoring of mitochondria (Norkett et al. 2016; Park et al. 2016, Chen et al. 2009; Courchet et al., 2013).

Microtubule motors are the fastest method of transporting mitochondria from the neuronal cell body, but more fine precision may be needed to anchor mitochondria at presynaptic terminals. Mitochondria are suggested to evenly distribute along axons *in vitro* by pausing in spaces devoid of other mitochondria, potentially due to increased ADP levels (Miller and Sheetz, 2004; Mironov, 2007). A thin axon packed with organelles may also lead to pausing or stopping of mitochondria due to steric hindrance at presynaptic terminals, particularly *en passant* boutons (Che et al. 2016). Actin also appears to play a role in keeping mitochondria close to synapses (Perkins et al., 2010; Lee and Peng, 2006), potentially also mediated by Miro (Lopez-Domenech et al., 2018; Oeding et al., 2018).

1.10.6 Mitochondrial homeostasis

Mitochondria are not all equal, they can differ in their functional capacity due to several factors including: membrane potential, respiratory capacity and matrix calcium concentration (Chang et al. 2011; Graham et al. 2017; Cserep et al. 2018; Lee and Peng, 2006; Misgeld and Schwarz, 2017). It is thought that mitochondria maintain functionality by undergoing fusion and fission to allow for mixing of matrix content, mtDNA and membrane proteins (Youle and van der Bliek, 2012). In axons, fission also tightly regulates mitochondrial size to keep them under 1 μm in length, mediated by MFF (mitochondrial fission factor; Lewis et al. 2018).

Depolarisation of mitochondria, an indication of poor mitochondrial health, leads to degradation by mitophagy, the mitochondrial-specific autophagic pathway (Narendra et al. 2008; Miller and Sheetz, 2004). Shedding of syntaphilin via mitochondrially-derived vesicles is thought to allow dysfunctional mitochondria to be trafficked retrogradely to the cell body

for mitophagy (Lin et al. 2017). However, mitophagy can also occur in distal axons as a response to damage, but not under normal physiological conditions (Ashrafi et al. 2014; Sung et al. 2016). Subsequently, mitochondrial biogenesis is thought to occur in the cell body to replace dysfunctional mitochondria, but recent evidence suggests it can also occur in distal axons (Laar et al. 2018, Hafner et al. 2018).

1.11 The role of presynaptic mitochondria

1.11.1 Mitochondrial enrichment correlates with presynaptic function

One of the first discoveries of mitochondria at the presynaptic terminal was over half a century ago, when characterisation of cortical axonal boutons was being completed using electron microscopy (Palay, 1956; Gray, 1959). Mitochondria were thought to be sustaining the energetic requirements of synapses but were less frequently found in cortical presynaptic terminals compared to cerebellar cortex and medulla oblongata (Palay, 1956). This finding still holds true today where between 20% and 50% of terminals on cortical neurons possess a mitochondrion less than 2 μm away (Kasthuri et al 2015; Chavan et al. 2015; Smit-Rigter 2016; Dufour et al., 2014); whereas, in thalamic axons that innervate the sensory cortex mitochondrial enrichment at presynaptic boutons is much higher, sometimes approaching 100% (Bopp et al. 2017, Rollenhagen et al. 2015, Rodriguez-Moreno et al. 2018). It is suggested that mitochondria are more readily found at thalamocortical synapses because they are few in number but highly important in driving the cortex, increasing the need for high efficacy. The distribution of mitochondria close to boutons in the cortex is neither a result of random positioning nor of spatial constraints in the axon (Smit-Rigter et al., 2016; Smith et al., 2016), suggesting that they are actively anchored there.

Mitochondrial ultrastructure and positioning at presynaptic terminals are correlated to synaptic strength and efficacy (Figure 1.8). Sizes of the postsynaptic density, active zone, docked and non-docked vesicle pools are positively correlated with mitochondrial presence (Kasthuri et al. 2015; Smith et al. 2016; Cserep et al. 2018). Larger, multi-synaptic boutons also have a higher probability (~2/3) of mitochondrial occupancy than smaller single-synaptic boutons (1/4; Smith et al. 2016; Rollenhagen et al. 2015).

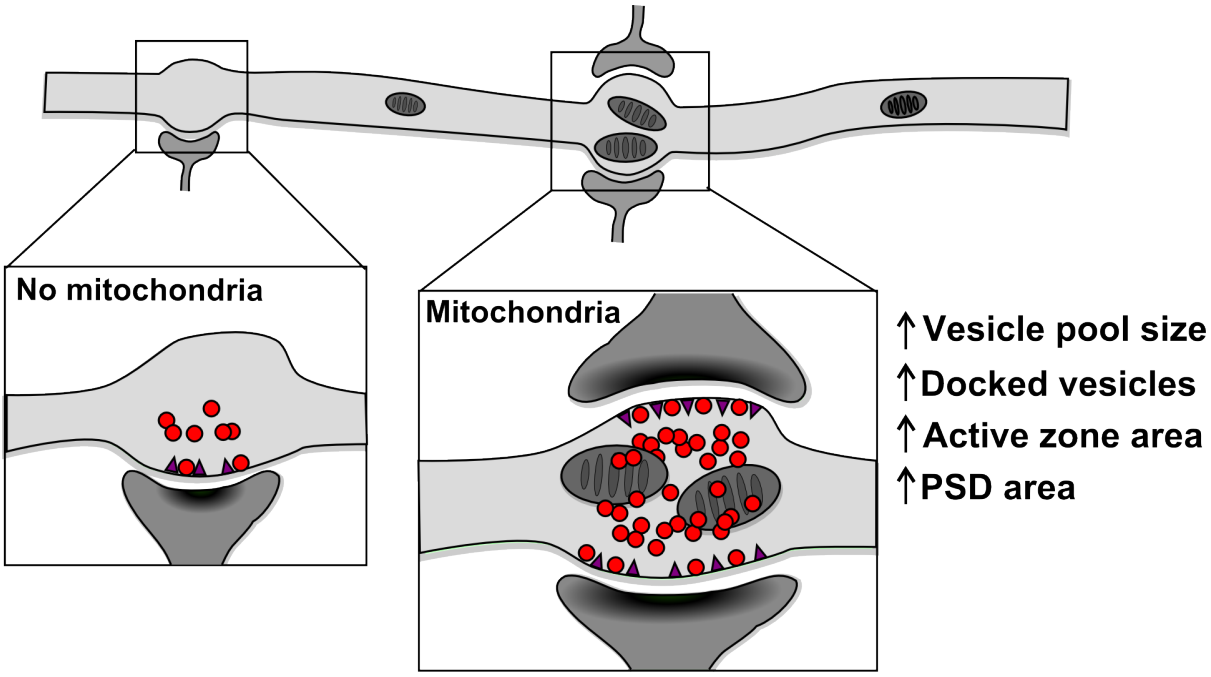

Figure 1.8. Correlation between presynaptic mitochondria and synaptic ultrastructure. Compared to synapses without mitochondria, the presence of mitochondria is correlated to increased vesicle pool size, number of docked vesicles, active zone area and postsynaptic density (PSD) area. Mitochondria are also more likely to be found at multi-synaptic boutons.

1.11.2 Mitochondrial functionality is elevated at presynaptic terminals

Mitochondrial function appears to be regulated by synaptic activity; upon stimulation, the capacity for mitochondrial ATP production is elevated via increased mitochondrial matrix pH, inner membrane potential and NADPH levels (Chouhan et al. 2012; Gazit et al. 2016). This is thought to be a mechanism that matches metabolic output to demand during presynaptic activity. Indeed, presynaptic mitochondrial ultrastructure is altered at central synapses to decrease size, increase crista junctions and orient cristae towards active zones in comparison to extrasynaptic mitochondria (Perkins et al. 2010, Smith et al. 2016; Graham et al. 2017; Cserep et al. 2018). This is important because mitochondrial shape is thought to be related to function (Ahmad et al., 2013). Functional differences between synaptic and extrasynaptic mitochondria have also been identified by proteomic screens, such as increased expression of respiratory chain proteins or higher membrane potential (Graham et al. 2017; Cserep et al. 2018; Lee and Peng, 2006).

1.11.3 Mitochondrial ATP provision sustains presynaptic neurotransmission

It has been estimated that 28% of the energy budget for neurons is taken up by presynaptic mechanisms and the remaining 72% by postsynaptic mechanisms (Hall et al. 2012). This could explain the abundance of mitochondria in dendrites, often extending continuously along them, compared to the lower density of mitochondria in axons (Lewis et al. 2018, Li et al., 2004).

Although ATP has been shown to diffuse between presynaptic terminals and may be at high concentrations basally through glycolysis (Pathak et al, 2015; Chavan et al., 2015; Sobieski et al., 2017), it is thought that increased levels of neuronal activity can not be sustained without local mitochondrial OXPHOS (Sobieski et al., 2017; Rangaraju et al., 2014; Hall et al., 2012; Verstreken et al., 2005). Specifically, presynaptic activity requires high levels of ATP for vesicle cycling (Rangaraju et al. 2014; Pathak et al. 2015; Zhou and Liu, 2015; Ivannikov et al., 2013). Indeed, the movement of mitochondria past presynaptic sites has been linked to ATP-dependent variability in presynaptic release by altering vesicle cycling rates (Sun et al. 2013). Sustainment of neurotransmission has been associated with increased presynaptic structural stability (Wiegert and Oertner, 2013), and evidence from Smit-Rigter et al. (2016) suggests that the presence of a presynaptic mitochondrion reduces structural loss of a bouton. These results suggest presynaptic mitochondrial presence is positively correlated to synaptic efficacy and presynaptic functional and structural stability.

When studying processes involved in energetic homeostasis *in vitro* it is important to consider the metabolic environment the cells are in. Glucose concentrations used *in vitro* are up to 10 times higher than any physiologically-relevant level (Silver and Erecinska, 1994). This may lead to an over-reliance on glycolysis by neurons due to the abundant levels of glucose, and reduced viability and metabolic responsiveness (Kleman et al. 2008). Other problems occur with oxygen supply, where neuronal cell culture oxygen levels may be reaching hypoxic levels (Bambrick et al., 2011), lowering capacity for oxidative phosphorylation. Irregularities in the ultrastructure of mitochondria have also been seen in neuronal culture under normal culture conditions (Robert et al., 2012). These findings are of concern as they may affect results

regarding mitochondrial function in cultured neurons and their generalisation to *in vivo* models.

1.11.4 Mitochondrial calcium sequestration dampens presynaptic activity

Calcium uptake by mitochondria at presynaptic terminals has been directly observed, leading to reduced cytosolic calcium and subsequent presynaptic release (Lewis et al. 2018, Vaccaro et al. 2017). Functionally, a decreased cytosolic calcium concentration is less likely to evoke presynaptic release because of reduced activation of calcium-sensitive release machinery (Brose et al. 1992; Chicka et al. 2008). It is thought that calcium sequestration via MCU leads to a dampened initial presynaptic release probability by keeping the calcium concentration low, and subsequently sustains presynaptic release through delayed release of calcium from the mitochondrial matrix (David and Barrett, 2000; Billups and Forsythe, 2002; Kwon et al. 2016). In this way, mitochondria are potentially involved in different forms of presynaptic plasticity (Tang and Zucker, 1997; David and Barrett, 2003; Vaccaro et al. 2017). Indeed, a decreased density of mitochondria in axons leads to increased short-term synaptic facilitation during trains of repeated, high frequency action potentials (Kang et al., 2008), which is thought to be driven by the build-up of residual calcium leading to increased probability of release. However, at presynaptic terminals of retinal bipolar neurons, mitochondria are postulated to be energy providers for plasma membrane calcium pumps, rather than being the main players in calcium clearance (Zenisek and Matthews, 2000).

Contradictory evidence shows that removal of MCU activity does not change the rate of synaptic vesicle exocytosis as expected, but increases the rate of endocytosis, and overexpression of MCU did the reverse (Marland et al. 2016). The results from this study suggest that calcium accumulation in the cytosol regulates endocytosis, which is dampened in the presence of presynaptic mitochondria. This corroborates with Smith et al. (2016) where the presence of mitochondria resulted in reduced vesicle pool sizes at rat hippocampal presynaptic terminals after LTP, presumably because of decreased endocytosis. However increased basal calcium did not correlate with effects on endo- or exo-cytosis at neuromuscular junctions devoid of mitochondria in *Drosophila melanogaster* (Verstreken et al. 2005).

1.11.5 Mitochondrial localisation changes during activity and plasticity

Mitochondria in rat hippocampal axons are highly likely to be found at presynaptic boutons *in vivo* (80%; Smith et al. 2016), whereas in mouse sensory cortex the probability is much lower (50%; Smit-Rigter et al. 2016). Mitochondrial positioning in axons is dynamic, only 40–50% remain in the same position over 4 days *in vivo* and *in vitro* and mitochondria are more stable at presynaptic compared to non-presynaptic sites (Obashi and Okabe, 2013; Smit-Rigter et al. 2016; Chang et al., 2006). Pharmacologically limiting activity through addition of tetrodotoxin—which prevents action potentials—sometimes decreases mitochondrial colocalisation with boutons; however, causing overactivity through veratridine—which inhibits re-polarisation of the membrane—or picrotoxin—which is an inhibitory neurotransmitter receptor antagonist—does robustly increase colocalisation, suggesting an activity-dependent homeostatic mechanism (Vaccaro et al. 2017; Obashi and Okabe, 2013; Chang et al. 2006; Chen et al., 2013; Figure 1.9). On the other hand, mitochondrial anchoring in excitatory axons or dendrites does not appear to be affected by activity changes *in vivo* (Smit-Rigter et al., 2016; Faits et al., 2016). Evidence for a relationship between mitochondrial availability, synaptic plasticity and sensory enrichment can be found in studies where mitochondrial presence at synapses was significantly increased in those animals with enriched environments and higher synaptic density per neuron (Briones et al., 2005; Sirevaag and Greenough, 1987). These studies suggest that mitochondrial anchoring is responsive to presynaptic activity, where increased activity leads to a higher probability of mitochondrial presence, which may regulate neurotransmission.

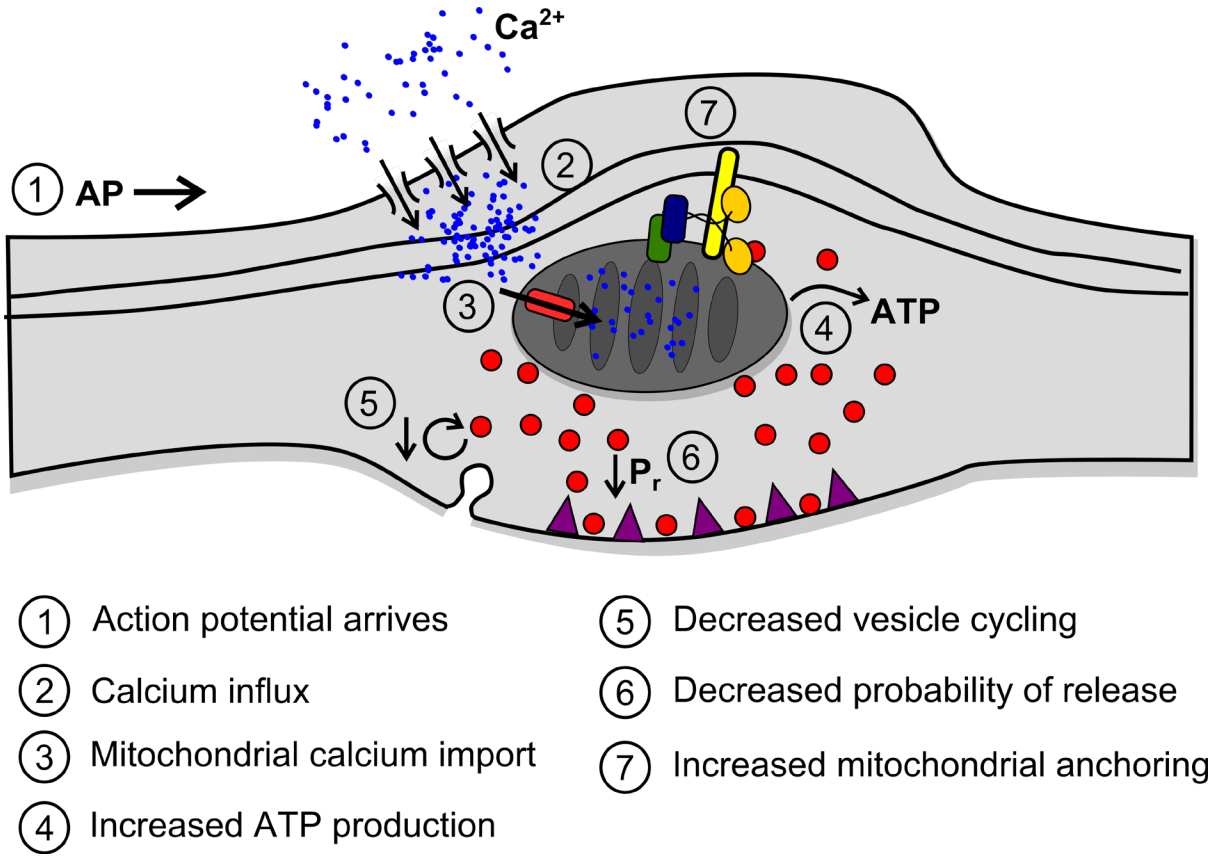

Figure 1.9. Homeostatic mitochondrial mechanisms at the presynaptic terminal. Schematic of the effect of mitochondrial presence on synaptic function. Mitochondria decrease the calcium rise that occurs after an action potential arrives, because of MCU activation. Elevated calcium concentrations in the mitochondrial matrix increase ATP production. The probability of release and synaptic vesicle cycling is reduced due to calcium sequestration by mitochondria. Furthermore, synaptic activity increases mitochondrial anchoring to elicit these effects.

1.11.6 Mitochondria at axonal branch points

Mitochondria are also thought to be important at axonal branch points. This is relevant because presynaptic sites appear to be prerequisites for axonal branch points (Meyer and Smith, 2006; Courchet et al., 2013). Translation sites along the axon are the initiators of axonal branching, but only when mitochondria are stationary and respiring at these sites (Spillane et al., 2013; Courchet et al., 2013). Further to this, stabilisation and activity of presynaptic terminals, potentially through mitochondria, is thought to aid axonal branching and arborisation in development (Ruthazer et al. 2006; Lewis et al. 2018). These studies point to the importance of mitochondria in development for gross circuit formation and remodelling.

1.12 Mitochondria in neurological disease

Mitochondria are important for neuronal physiology, as described in previous sections. Logically, mitochondria are also implicated in a host of neurological diseases, both directly and indirectly (Devine and Kittler, 2018). Direct involvement of mitochondrial proteins includes: Charcot-Marie Tooth neuropathy type 2A (Zuchner et al., 2004) through the protein Mitofusion-2; Friedreich Ataxia (Shidara and Hollenbeck, 2010) through Frataxin deficiency and associated failure in mitochondrial transport and ATP production; and dominant optic neuropathy (Sarzi et al., 2016) through OPA1. Indirect involvement in neurodegenerative disease progression has also been suggested (Sheng and Cai, 2012); in certain dementias, accumulation of mutant tau and amyloid beta is thought to affect axonal transport (Kanaan et al., 2011; Calkins and Reddy, 2011), which would directly affect mitochondrial distribution and homeostasis in axons. For example, increased amyloid beta on synaptic mitochondria causes deficits in mitochondrial function (Du et al., 2010). Pathogenic tau has been linked to changes in anterograde fast axonal transport that is required to traffic mitochondria to presynaptic terminals in axons (Kanaan et al., 2011). These results may help to explain the synaptic loss observed in Alzheimer's disease when coupled with the knowledge that mitochondria sustain neurotransmission and structural plasticity (Sobieski et al., 2017; Smit-Rigter et al., 2016). Parkinson's disease is also related to mitochondrial deficiencies, where neurons appear to increase mitochondrial biogeneis and the presence of mitochondria at synaptic sites in a compensatory mechanism (Reeve et al., 2018). Importantly, a large proportion of the effects are on mitochondrial transport, suggesting that positioning of mitochondria is affected in these diseases. Further understanding of how mitochondrial positioning is related to neuronal function would be beneficial to understand the progression of particular neurological diseases linked to mitochondrial dysfunction and find therapeutic targets.

1.13 Aims

Changes in synaptic strength and connectivity in the mammalian neocortex involve presynaptic structural plasticity, which is closely linked to perception, learning and memory formation. Mitochondria are found at a subset of presynaptic terminals via active mechanisms and regulate neurotransmitter release homeostatically. Ultimately, their presence is correlated with elevated synaptic efficacy and potentially increased synaptic stability. This leads to the hypothesis that mitochondrial presence at a presynaptic terminal is positively related to presynaptic structural stability, which would have implications for the understanding of neocortical plasticity and neurological disease.

The aims of this thesis are:

- To determine the relationship between mitochondrial presence and presynaptic terminal lifetime in mammalian cultured neurons
- To determine the relationship between mitochondrial presence and presynaptic age and longevity in mammalian neocortex *in vivo*
- To develop correlative two-photon and serial block-face scanning electron microscopy for the relocation and characterisation of individual axonal boutons imaged *in vivo*

CHAPTER 2 RELATIONSHIP BETWEEN PRESYNAPTIC TERMINAL LIFETIME AND MITOCHONDRIAL LOCALISATION IN CULTURED RAT NEURONS

This chapter involved collaborative work. Kevin Wilkinson, Ashley Evans, Philip Rubin, Dan Rocca, Sonam Gurung, Alex Fletcher-Jones, Vanilla Shi, Caroline Binda, Michaela Heimann, Paul Bishop and Ellen Braksator carried out harvesting, dissection and dissociation of rat brains. Culturing was carried out independently after the dissociation step.

2.1 Introduction

Changes in connectivity between neurons in the mammalian neocortex are involved in perception, learning and memory formation (Holtmaat and Caroni, 2016; Fu et al., 2011; Holtmaat and Svoboda, 2009), involving the loss and gain of both presynaptic (Johnson et al., 2016) and postsynaptic terminals (Frank et al., 2018). Therefore, correct regulation of presynaptic terminal lifetime and hence the tenacity of synaptic connections is essential for the function of neocortical networks. However, the molecular mechanisms that influence presynaptic terminal lifetime are not well understood.

Presynaptic terminal formation involves the recruitment of essential protein machinery to create a functional synaptic connection. Presynaptic terminals are thought to be assembled

from two distinct types of transport vesicle containing either active zone or synaptic vesicle proteins. These are the Piccolo-Bassoon transport vesicle (PTV) and the synaptic vesicle protein transport vesicle (STV; Bury and Sabo, 2011), respectively. PTVs and STVs are transported along the axon on microtubules until a signal is received to offload them at presynaptic sites, potentially through JNK (c-Jun N-terminal kinases) and JIPs (JNK-interacting proteins; McAllister, 2007), resulting in accumulation of presynaptic proteins over time (Ruthazer et al., 2006). Tracking of these presynaptic protein accumulations can be used to estimate the lifetime of terminals.

Presynaptic proteins are involved in the organisation and mobilisation of synaptic vesicles for neurotransmission. Synapsin, a synaptic vesicle protein found on STVs, is a switch that mobilises reserve pool vesicles to the ready-releasable pool upon phosphorylation (Orenbuch et al., 2012). Synaptophysin is another synaptic vesicle protein found on STVs thought to be involved in regulating endocytosis of synaptic vesicles (Kwon and Chapman, 2011). Piccolo and Bassoon are proteins found on PTVs involved in function of the active zone, the area of the terminal involved in neurotransmitter release (Gundelfinger et al., 2016). These large active zone proteins have a variety of binding sites to create the protein complexes required for vesicle fusion. Each of the presynaptic proteins mentioned have been used in studies as markers of presynaptic terminals through immunocytochemistry or expression of a fluorescent protein conjugate (Courchet et al., 2013; Chang et al., 2006; Fletcher et al, 1991, Okabe et al., 2001, Meyer and Smith, 2006), which are useful for assessment of presynaptic terminal lifetime.

The formation and stabilisation of presynaptic terminals and establishment of synaptic connections (along with maintenance of synaptic efficacy) may be regulated by local energy availability or calcium homeostasis involving mitochondria (Harris et al., 2012; Hall et al., 2012; Lee and Peng, 2006). Axonal mitochondria can mobilise (MacAskill and Kittler, 2010) and are found preferentially at presynaptic terminals (Smit-Rigter et al., 2016, Obashi and Okabe, 2013) where their ATP production and calcium sequestration regulate synaptic efficacy (Vaccaro et al., 2017; Smith et al., 2016; Lewis et al. 2018; Rangaraju et al., 2014). However, mitochondria are not found at every presynaptic terminal *in vivo* and in neuronal

culture (Smit-Rigter et al.., 2016; Obashi and Okabe, 2013; Smith et al., 2016). These studies lead to the hypothesis that presynaptic terminal lifetime is increased in the presence of mitochondria due to mitochondrial support of synaptic efficacy. Indeed, it has been shown that increased efficacy and size of a presynaptic terminal is correlated with a longer lifetime (Ash et al., 2018; Wiegert and Oertner, 2013; Ruthazer et al., 2006). Some direct evidence also exists to suggest that the localisation of mitochondria at presynaptic terminals is beneficial for their survival *in vivo* (Smit-Rigter et al., 2016).

Mammalian neuronal culture provides favourable genetic and optical experimental access to study this. However, most studies in culture assessing mitochondrial localisation in combination with presynaptic terminal lifetime have either not quantified terminal lifetime, or don't have enough information due to short imaging durations (<30 minutes; Chang et al., 2006) or long intervals between timepoints (1 day; Obashi and Okabe, 2013). Results suggest that some presynaptic terminals are highly stable (over 4 days; Obashi and Okabe, 2013) in neuronal culture, but there are also highly dynamic terminals (Okabe et al., 2001; Hopf et al., 2004).

Neuronal cultures have been compared to the developing brain. As the cultured neurons grow, they extend neurites and make synaptic connections. However, the order with which they make these connections is not driven by any developmental or sensory cues as it is *in vivo*. Despite this, activity in cultured neurons shares many similarities to that of a developed system (Mazzoni et al., 2007). Very few presynaptic terminals form in culture until 7 or 14 days *in vitro* (DIV; Ichikawa et al., 1993), after which presynaptic terminal density per neuron continues to increase, peaking at 28 DIV. This correlates with maturation in the network activity of cortical cultures (Chiappalone et al., 2006; Moutaux et al., 2018). At the same time, axonal mitochondrial motility is reducing, increasing both the percentage of mitochondria that are stationary and the proportion found at presynaptic terminals (Lewis et al., 2016, Loss and Stephenson, 2017). However, the effect of neuronal development in culture on presynaptic terminal lifetime is unknown.

The aim of this study was to determine the lifetime of presynaptic terminals in rat cortical cultures at different ages, the degree to which mitochondria colocalise with them and the relationship between mitochondrial presence and presynaptic terminal lifetime.

2.1.1 Key findings

- Synapsin1a was a poor marker for presynaptic terminals in fixed rat cortical cultures due to differential colocalisation with other presynaptic markers in individual axons.
- Synapsin1a was potentially a poor marker for estimation of putative presynaptic terminal lifetimes in live-cell imaging due to its dispersion during neuronal activity.
- Putative presynaptic terminal lifetimes were not significantly different with maturation of rat cortical neurons from 14 to 21 days *in vitro* in preliminary experiments.
- Correlation between the duration of mitochondrial colocalisation and putative presynaptic terminal lifetime was very weak in rat cortical cultures in preliminary experiments.

2.2 Materials

- α-synaptophysin mouse mAb (Merck Millipore; 573822-50UL)
- α-bassoon mouse mAb (Cell Signaling Technolgy; 6897S)
- α-PSD-95 mouse mAb (UC Davis NeuroMab; clone K28/43)
- α-synapsin rabbit mAb (Abcam; ab64581)
- α-GFP chicken polyAb (Abcam; ab13970)
- α-mouse or α-rabbit Cy2, Cy3 and Cy5-conjugated antibodies (Abcam)
- Goat anti-chicken Alexa-488 conjugated antibody (ThermoFisher Scientific; A-11039)
- 25 mm Ø No. 1.5 glass coverslips (Fisher Scientific; 50-121-5161)
- 1M nitric acid
- Plastic 35 mm Ø dishes (Sigma Aldrich; CLS430588)
- 35 mm Ø dishes with 14 mm Ø, No. 1.5 glass coverslip inserts (MatTek Corp.; P35G-1.5-14-C)

- Poly-L-Lysine substrate (Sigma Aldrich; P4707)
- Neurobasal A culture medium (Thermo Fisher Scientific; 10888022)
- GlutaMAX (Thermo Fisher Scientific; 35050061)
- Horse serum
- B27 supplement (Thermo Fisher Scientific; A3582801)
- Lipofectamine 2000 (Thermo Fisher Scientific; 11668019)
- Mitotracker Deep Red FM (Thermo Fisher Scientific; M22426)
- Methanol
- PFA
- Glycine
- BSA
- Fluoromount-G (Thermo Fisher Scientific; 00-4959-52)
- Glass microscope slides

2.3 Methods

2.3.1 Antibodies and DNA constructs

Primary antibodies used for immunocytochemistry were α-synaptophysin (1:400 dilution), α-bassoon (1:400), α-PSD-95 (1:250), α-synapsin (1:250), α-GFP (1:200). Secondary α-mouse or α-rabbit Cy3 and Cy5-conjugated antibodies (1:400) or Alexa-488 (1:400) were used where appropriate.

The following constructs were used in transfections: DsRed2-Mito under a CMV promoter (cytomegalovirus; DsRed2 conjugated to a Cox8a mitochondrial targeting sequence, pUC vector, gift from Guo Chun), Synapsin1a-GFP under a CMV (cytomegalovirus) promoter (pEGFP vector, gift from Tim Craig). Synaptophysin-GFP under a CMV promoter (pEGFP vector, gift from Kevin Wilkinson).

2.3.2 Preparing coverslips and plating cells

For fixed immunofluorescence, 25 mm Ø No. 1.5 glass coverslips were cleaned by incubation with 1M nitric acid. Coverslips were submerged in nitric acid inside a large glass beaker that was sealed with foil and placed on a shaking platform overnight. Coverslips were briefly

washed three times with dH_2O and then again for 3 x 30 min to remove any residual nitric acid. Then the coverslips were incubated on a shaking platform for 2 hours in 70% EtOH inside a parafilm-sealed 15 cm petri dish. The remaining cleaning steps were done inside a cell culture hood. The coverslips were cleaned 3 x 30 min in sterile dH_2O and placed in plastic 35 mm Ø dishes. For live-cell imaging, sterile 35 mm Ø dishes with 14 mm Ø, No. 1.5 glass coverslip inserts (MatTek), were cleaned with sterile water. Both glass coverslips and glass-bottomed dishes were coated in Poly-L-Lysine substrate (1 mg/ml), then left in an incubator at 37°C overnight for the substrate to adhere to the glass. The dishes or coverslips were washed twice with sterile water to remove surplus substrate and then 2 ml of warmed plating media (Neurobasal A culture medium with 1% GlutaMAX, 5% horse serum, 2% B27 supplement) was added before the dissociated cells were seeded.

Cortical cells were counted using a hemocytometer to obtain the concentration of cells in the dissociation medium. A seeding density of 75,000-150,000 cells was used on coverslips for immunocytochemistry purposes and a higher seeding density of 200,000 was used on dishes with coverslip inserts for live-cell imaging purposes.

2.3.3 Primary neuronal cell culture

Cells were cultured in a homeostatic incubator for 6-16 hours at 37°C, 5% CO_2 in plating media to allow the cells to adhere to the substrate. CO_2 is required to maintain the pH of the buffer in the Neurobasal medium. Afterwards, media was either titrated to feeding media (1 mL replaced daily for ~3 days) or completely exchanged with 2.5 ml feeding media (Neurobasal A culture medium with 1% GlutaMAX, 2% B27 supplement) to prevent further glial proliferation. Where necessary, Neurobasal A culture media without phenol red (pH indicator) was used for live-cell imaging experiments to reduce background contamination of the signal. Every 7 days cells were fed with 0.5 ml feeding media to counteract any evaporation occurring during incubation.

2.3.4 Transfection of DNA constructs and Mitotracker incubation

Cells were transferred to 1 mL of fresh, warmed feeding media and the conditioned media from the cells was kept in an incubator at 37°C, 5% CO_2. Transfection using Lipofectamine

2000 (Thermo Fisher Scientific) was carried out according to the manufacturer's instructions. 1 μg of each construct was added to 1.5 μl of Lipofectamine and cells left for 1.5 hours. Afterwards, the transfection mix was replaced by the original conditioned media and cells were kept at 37°C, 5% CO_2 for at least 4 days prior to imaging or fixation. Where required, cells were incubated in 2 mL of 100 nM Mitotracker Deep Red FM in fresh feeding media for 30 min at 37°C, 5% CO_2 then washed with 1x PBS before fixation.

2.3.5 Immunocytochemistry

For staining of cultures on 25 mm coverslips, coverslips were briefly and gently washed with warm 1x PBS to remove residual media and debris. Then cells were incubated with 1 mL of warm 4% PFA for 12-15 min. Alternatively, cells were fixed and permeabilised by incubation with 100% ice-cold methanol for 4 min on ice. After PFA fixation, cells were washed with PBS three times and quenched with 100 mM glycine and then washed three times with PBS again. Afterwards, permeabilization was carried out using 100% ice-cold methanol. PFA-fixed and methanol-fixed cells were then immediately washed with 1x PBS twice and non-specific binding was blocked by incubation in 4% bovine serum albumin (BSA) in 1x PBS. Afterwards, coverslips were inverted on to drops of primary antibody diluted in 4% BSA in 1x PBS (concentrations in *Antibodies and DNA constructs* section) and incubated for at least 40 min at RT (room temperature). Primary antibody was washed off with 1x PBS (3 x 5 min) and the coverslips were then inverted on to drops of secondary antibody diluted in 4% BSA in 1x PBS and incubated for 40 min at RT. Finally, the secondary antibody was washed off (3 x 5 min wash with 1x PBS) and the coverslips were mounted using 40 μL of Fluoromount-G (containing DAPI nuclear stain) on a glass microscope slide.

Alternatively, for post-hoc staining of cells in dishes, the same protocol was used, but antibody was pipetted on to the glass insert of a gridded glass-bottomed dish. Finally, a 14 mm Ø coverslip was mounted on top of the insert using Fluoromount-G.

2.3.6 Imaging

For live-cell imaging and some fixed-cell immunofluorescence imaging, an inverted widefield microscope (Leica DMI6000 inverted) was used with Leica LAS X software, a homeostatic

chamber, Mercury lamp and CCD camera (Leica DFC365FX monochrome). Filter sets were assigned for the following fluorophores: DAPI (Ex. 350/50, dichroic mirror 400, Em. BP 460/50), A488/Cy2/GFP (Ex.: 480/40, 505 nm dichroic mirror, Em. BP 527/30), Cy3/DsRed2 (Ex. 560/40, 595 nm dichroic mirror, Em. BP 645/76), Cy5/Mitotracker Deep Red FM (Ex. 620/60, 660 nm dichroic mirror, Em. BP 700/38). Objective lenses used: 5x dry 0.15 NA (numerical aperture), 40x oil immersion 1.25 NA and 100x oil immersion 1.4 NA. Parameters were set the same for imaging of all repeated experiments.

For live-cell imaging, the homeostatic chamber was set at 37°C and a sealed stage insert with a gas inlet was used to maintain 5% CO_2. Timelapse images were typically acquired overnight (~6-12 h) and the motorised stage was used for multipoint acquisition (Mark and Find tool, Leica LAS X). Three-dimensional (3D) stacks of 3-5 μm (0.5 μm z-steps) were obtained at each ROI due to the undulating axons not sitting in one imaging plane. Time intervals were between 10-20 min to minimise photobleaching of the fluorophores. Adaptive focus control (Leica LAS X) was also used to correct the drift in focal plane over time due to temperature or mechanical fluctuations during imaging.

Regions of interest (ROI) for live-cell imaging were chosen based on several criteria: identification of an axon, i.e. long, thin, straight and maintaining constant width; expression of both fluorescent constructs; few overlapping transfected axons to contaminate structure colocalisation analysis; originating cell body was more than 100 μm away to ensure the dynamics are not representative of the axon initial segment; limited expression throughout the cell body and dendrites in comparison to the axon (not highly overexpressing).

For post-hoc immunostaining, glass-bottomed dishes were used with a coordinate finder grid. Brightfield images were taken at the end of live-cell imaging to note the locations of time-lapse images on the finder grid. Subsequently, the coordinate on the grid was relocated after fixation and staining.

For further fixed-cell immunofluorescence imaging, a confocal microscope (Leica SPE single channel) with Leica LAS X software was used with 405, 488 and 532 nm solid-state lasers and adjustable emission filters. Objective lenses used: 40x oil immersion 1.3 NA and 63x oil

immersion 1.3 NA. Confocal microscopy was used to check colocalisation in dense samples, as it has a greater axial resolution.

2.3.7 Image analysis

Image processing of live-cell imaging was carried out using the FIJI package for ImageJ (version 2.0.0-rc-43/1.51a, Schindelin et al., 2012). Macros were created to allow automated processing of images, carrying out the following functions: 1) cropping in the z-axis using the Make Substack plugin. 2) MultiStackReg plugin to correct x- and y-axis drift from temperature or mechanical fluctuations during imaging. 3) Extended Depth of Field plugin, which obtains the most in-focus signal from each kernel of a 3D stack and reconstructs a 'focused' 2D image. 4) Straightening of the traced axons of interest using the segmented line tool and Straighten plugin. 5) Auto thresholding of DsRed2-Mito and Synapsin1a-GFP channels by the Auto Threshold plugin using the MaxEntropy algorithm (Kapur et al., 1985).

Tracking of putative presynaptic terminal puncta was carried out using TrackMate plugin (Tinevez et al., 2017; v2.8.1) for ImageJ. The plugin defines spots of 1 μm Ø around Synapsin1a-GFP puncta using a laplace of gaussian algorithm in each frame. Spots were tracked through the time course based on user-defined parameters. A linking-distance of 1 μm and gap-closing duration of 2 frames were used, meaning spots had to be within 1 μm in either of the subsequent two timepoints (<40 min interval). For lifetime analysis, only putative presynaptic terminals formed and lost within the time course were measured to accurately estimate lifetimes. DsRed2-Mito signal above the threshold (MaxEntropy) was converted to a binary image and the presence of this marker inside each spot was measured through the TrackMate plugin "Multi-channel spot mean intensity analyser". Any overlapping signal from mitochondria was classed as colocalisation with a putative terminal.

Colocalisation between structures labelled with transfection (e.g. Syn1a-GFP) or incubation (e.g. Mitotracker) and immunolabelled structures was carried out using the Coloc 2 plugin for ImageJ. The signal from the structure of interest was manually thresholded to exclude unnecessary parts of the image (i.e. those that do not contain the axon of interest). Coverslips stained with only the secondary antibody were used to set an appropriate threshold to control

for non-specific binding and background fluorescence levels. Subsequently, a binary mask was made using the manual threshold. The mask was applied to both channels and each channel had an auto threshold applied to remove background signal. Mander's correlation coefficient for signal overlap was used to determine the degree of colocalisation between the structures of interest and different immunolabelled puncta (Mander's et al., 1993). Costes' significance was used to determine the probability of the same colocalisation when signals were smoothed (using kernel accounting for size of calculated microscope PSF) and scrambled (Costes et al., 2004). A Costes' significance level of >95% was used as a cut-off in this study.

2.3.8 Statistics

MATLAB was used for statistical tests. A two-sample Kolmogorov-Smirnov test was used to compare non-normal distributions to test the null hypothesis that they were from the same distribution. An alpha value of 0.05 was the threshold for statistical significance in this study. Spearman's rank correlation was used to test the monotonic relationship between two variables where the variables had non-normal distributions.

2.4 Results

2.4.1 Mitochondrial localisation to presynaptic terminals

It is known that mitochondria are found at ~40% of presynaptic terminals in neuronal culture as well as *in vivo* (Vaccaro et al., 2017; Chavan et al., 2015; Smit-Rigter et al., 2016). Here, cortical cultures were made from embryonic rat pups to assess the basal colocalisation of presynaptic terminals and mitochondria. Mitochondria were labelled with Mitotracker and presynaptic terminals stained using immunofluorescence with antibodies for Synaptophysin, a synaptic vesicle protein, and Bassoon, an active zone cytomatrix protein. The large number of closely-apposed neurites found in dense cultures did not allow the identification of individual axons to assess colocalisation (Figure 2.1). Therefore, cultures were made sparser, lowering the seeding density from 200,000 per 25 mm coverslip to 75,000. Decreasing the density of cells made it less ambiguous when trying to determine if different fluorescent structures were originating from the same cell (Figures 2.2 and 2.3). Regions of interest containing axons were chosen based on the morphology of the cell (see *Methods*).

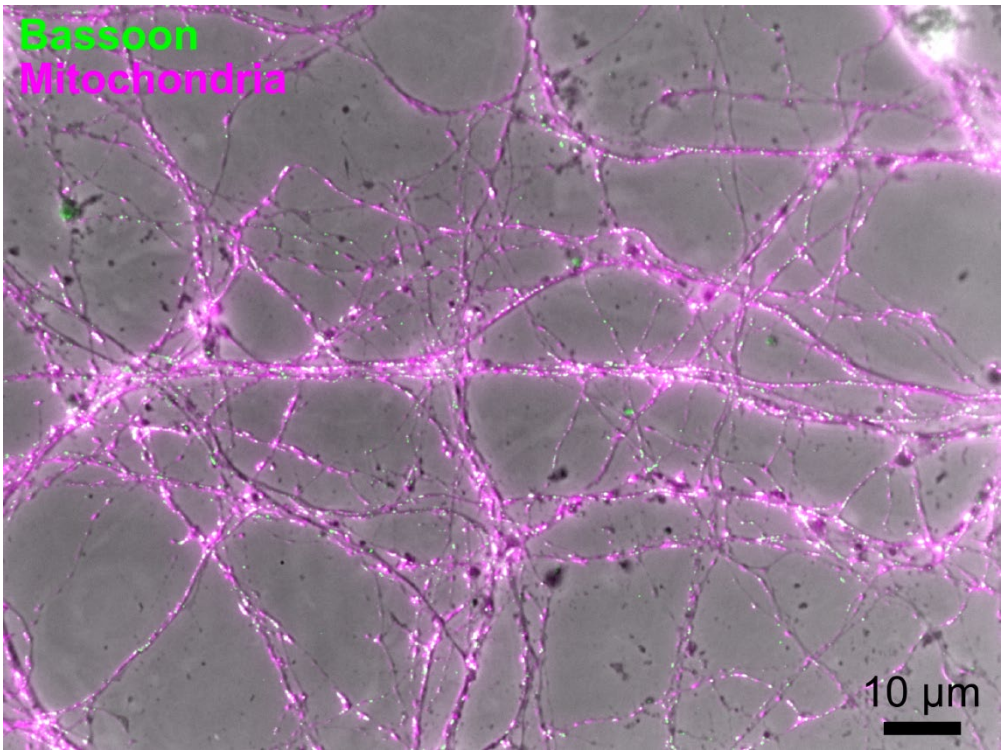

Figure 2.1. Staining of all mitochondria within dense neurites was not conducive to the measurement of colocalisation. Representative widefield image of a region of interest in a rat primary cortical culture. Mitochondria (magenta) were labelled with Mitotracker dye and Bassoon (a presynaptic cytomatrix protein; green) was immunostained. Fluorescence signal was overlaid on a phase contrast image of the cellular structure showing complete coverage of the cells in the region with staining. The staining and culture were too dense to determine colocalisation within a single cell.

Synaptophysin staining appeared as ~1 µm puncta, presumably pools of synaptic vesicles or STVs, spread evenly throughout the axon (~5-10 µm intervals; Figure 2.2). Mitochondrial staining appeared interconnected by thin strips of membrane, with intermittent regions of swelling, these regions were slightly larger and less evenly spread and of a higher density than Synaptophysin puncta (length ~2µm at ~2-5 µm intervals; Figures 2.2 and 2.3). Bassoon staining resulted in much smaller puncta at a higher density throughout the axon (~0.5 µm at 1-2 µm intervals).

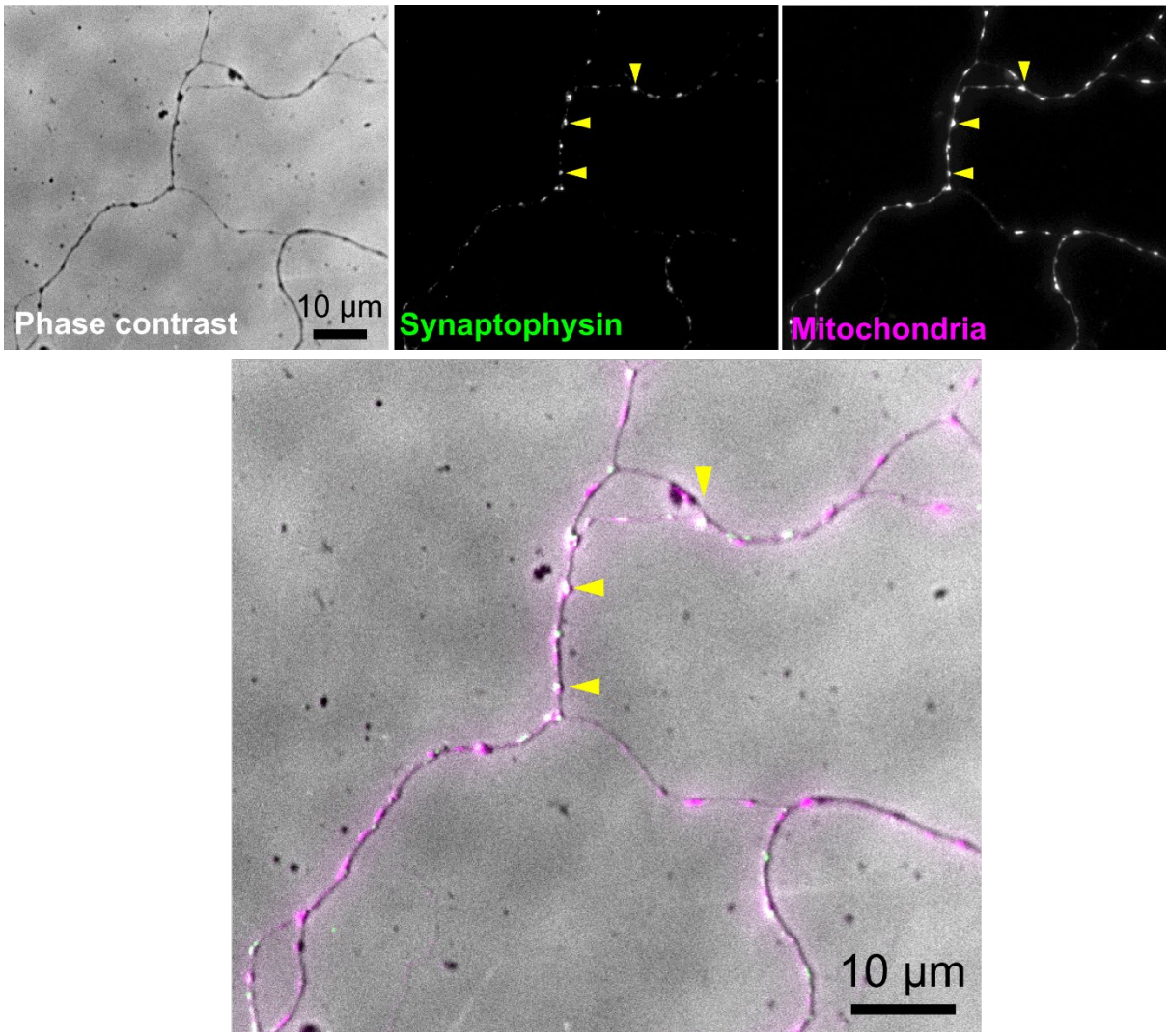

Figure 2.2 Mitochondria were partially colocalised with the synaptic vesicle marker Synaptophysin. Representative widefield images of individual axons with relatively few crossings allowed for more reliable colocalisation analysis. Axons were easily identifiable as long, thin neurites, maintaining constant thickness (not tapering), with sparse branching. Synaptophysin (a synaptic vesicle protein) and mitochondria were stained using immunostaining and Mitotracker, respectively. Examples of colocalisation between intense puncta in both channels is shown (*yellow arrowhead*). Mander's overlap coefficient (MOC) = 0.34, n = 7 regions, 1 culture.

Colocalisation was measured using the Mander's overlap coefficient (MOC), which is a measure of signal overlap between two labels, producing a coefficient for each label with respect to the other (see *Methods*). The reported MOCs indicate the proportion of presynaptic signal that overlaps with mitochondrial signal. There was an MOC of 0.34 for colocalisation of mitochondria and Synaptophysin (n = 7 regions, 1 culture; Figure 2.2). This equates to 34% of the presynaptic signal overlapping with signal from the mitochondria. Colocalisation was stronger between mitochondria and Bassoon (MOC = 0.62, n = 2 regions, 1 culture; Figure 2.3).

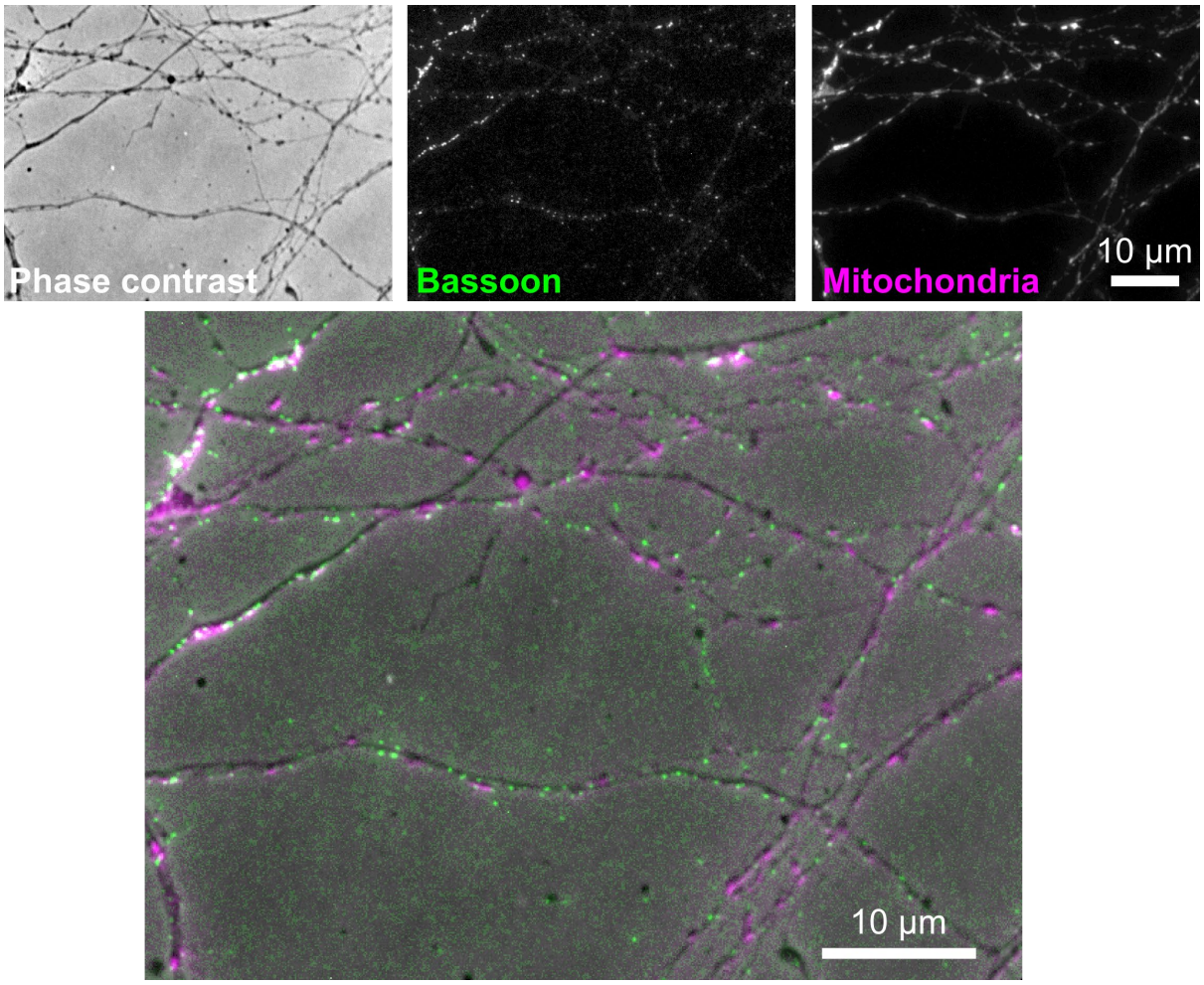

Figure 2.3 Mitochondria were partially colocalised with the active zone marker Bassoon. Representative widefield images of individual axons with relatively few crossings allowed for more reliable colocalisation analysis. Axons were easily identifiable as long, thin neurites, maintaining constant thickness (not tapering), with sparse branching. Bassoon (presynaptic cytomatrix protein) and mitochondria were stained using immunostaining and Mitotracker, respectively. MOC = 0.62, n = 2 regions, 1 culture. Brightness and contrast were adjusted in the phase contrast image for the composite (*bottom*).

The use of dyes and antibodies resulted in all mitochondria and relevant presynaptic proteins being labelled. Despite lower cellular density, colocalisation measurements were still potentially unreliable as axons often wrapped around dendrites and ran alongside each other.

To further decrease the density of labelling, neurons were transfected with DNA constructs encoding fluorescently-tagged presynaptic or mitochondrial proteins. Transfection efficiency in neurons is low (~1-5%; Karra and Dahm, 2010), allowing isolation of single cells and their long axons. A DNA construct expressing Synapsin1a-GFP (Syn1a-GFP) was used to label

presynaptic terminals and the mitochondrially-targeted DsRed2-Mito was used to label mitochondria.

2.4.2 Validation of Synapsin1a-GFP and Synaptophysin-GFP as presynaptic terminal markers

Overexpression of labelled Synapsin1a protein (Syn1a-GFP) might have misrepresented the underlying endogenous distribution. Therefore, validation was carried out by immunostaining for other presynaptic markers to determine if the Syn1a-GFP construct was labelling presynaptic structures as expected. The majority of Syn1a-GFP puncta would have needed to be at presynaptic terminals (>80%), so that the conclusions from any analysis using the marker were reliable. MOC was again used to estimate the degree of overlap between the fluorescent signals, reported MOCs are for the proportion of Syn1a-GFP signal overlapping with the other presynaptic markers.

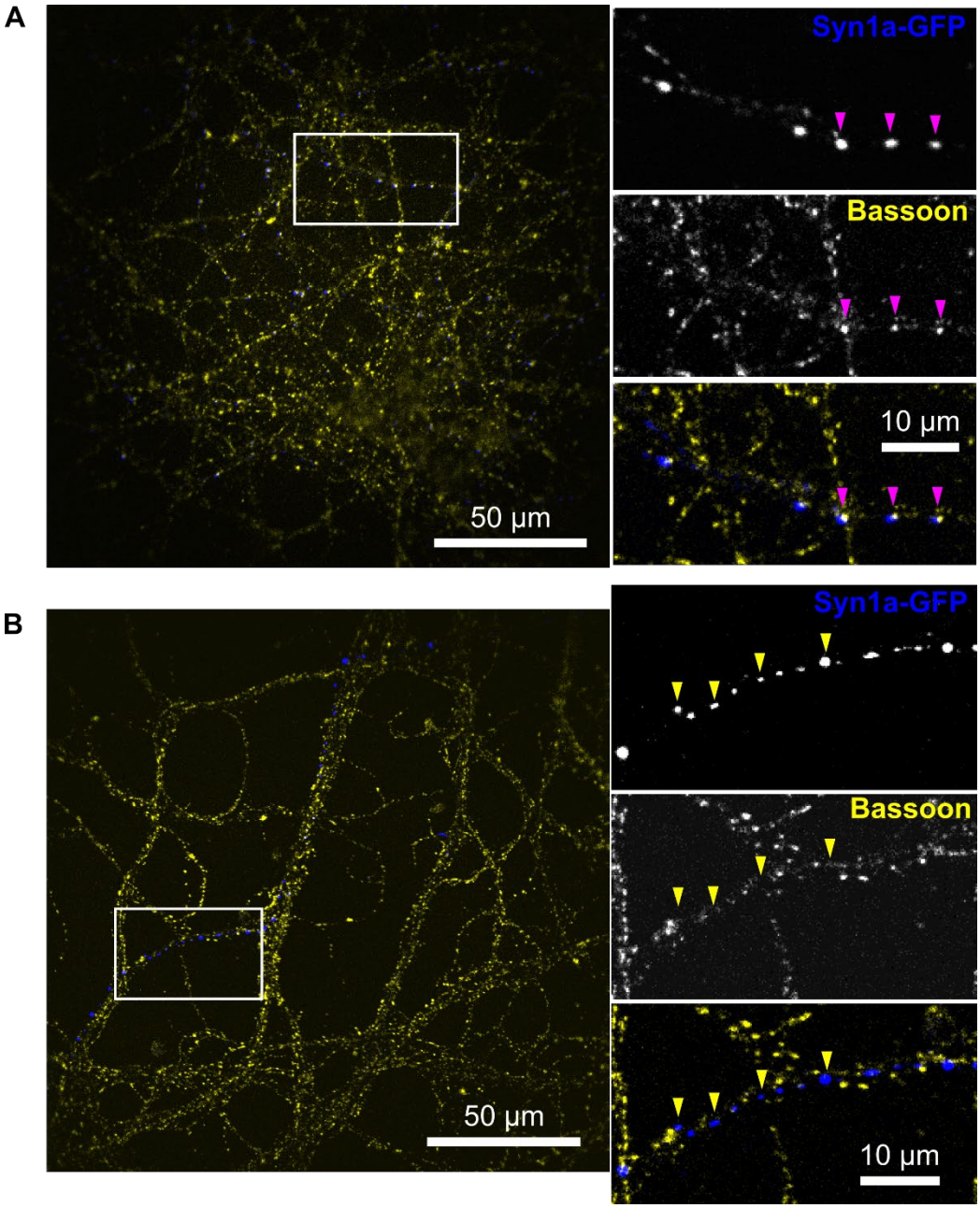

Figure 2.4 Differential colocalisation of Synapsin1a-GFP with endogenous Bassoon in individual axons. (**A** and **B**): Representative confocal images of individual axons expressing Synapsin1a-GFP (Syn1a-GFP; *blue*) along with immunostained Bassoon (presynaptic cytomatrix protein; *yellow*). Puncta appear as "beads-on-a-string", typical of axonal en passant terminals. Some axons showed very good overlap between Syn1a-GFP puncta and Bassoon (*magenta arrowheads*; A). However, other axons showed puncta that appeared to be negatively correlated with Bassoon (*yellow arrowhead*; B). MOC = 0.44, n = 9 regions, 3 cultures, methanol fixation. MOC = 0.66, n = 4 regions, 1 culture, PFA fixation.

Bassoon or Synaptophysin were used to label endogenous presynaptic sites. Colocalisation between either of the two markers and Syn1a-GFP was low with either of two different fixation protocols (methanol-only or PFA-methanol fixation). Two different fixation protocols were used in case one caused loss of the antibody epitope on the proteins targeted for immunostaining (Schnell et al., 2012). For methanol fixation, MOC was 0.44 for Syn1a-GFP and Bassoon (n = 9 regions, 3 cultures; Figure 2.4). For methanol fixation and staining of Synaptophysin, the MOC was 0.39 (n = 23 regions, 4 cultures; Figure 2.5). For PFA fixation, Syn1a-GFP with Bassoon resulted in an MOC of 0.66 (n = 4 regions, 1 culture; Figure 2.4) and with Synaptophysin an MOC of 0.21 (n = 3 regions, 1 culture; Figure 2.5). Colocalisation in some axons was very good (Figures 2.4A and 2.5A), while in other axons it was very poor (Figures 2.4B and 2.5B), which was not represented in the MOCs. Secondary antibody controls showed very little non-specific binding when compared to samples with primary antibody present (Figure 2.6), although this did not explain the lack of colocalisation in whole axons. These results questioned the reliability of using overexpression of Syn1a-GFP to label mature presynaptic terminals (i.e. consisting of a complement of presynaptic proteins). The Synapsin1a DNA sequence of the Syn1a-GFP construct was correct, showing a 100% match with rat Synapsin1a, determined by a FASTA database search.

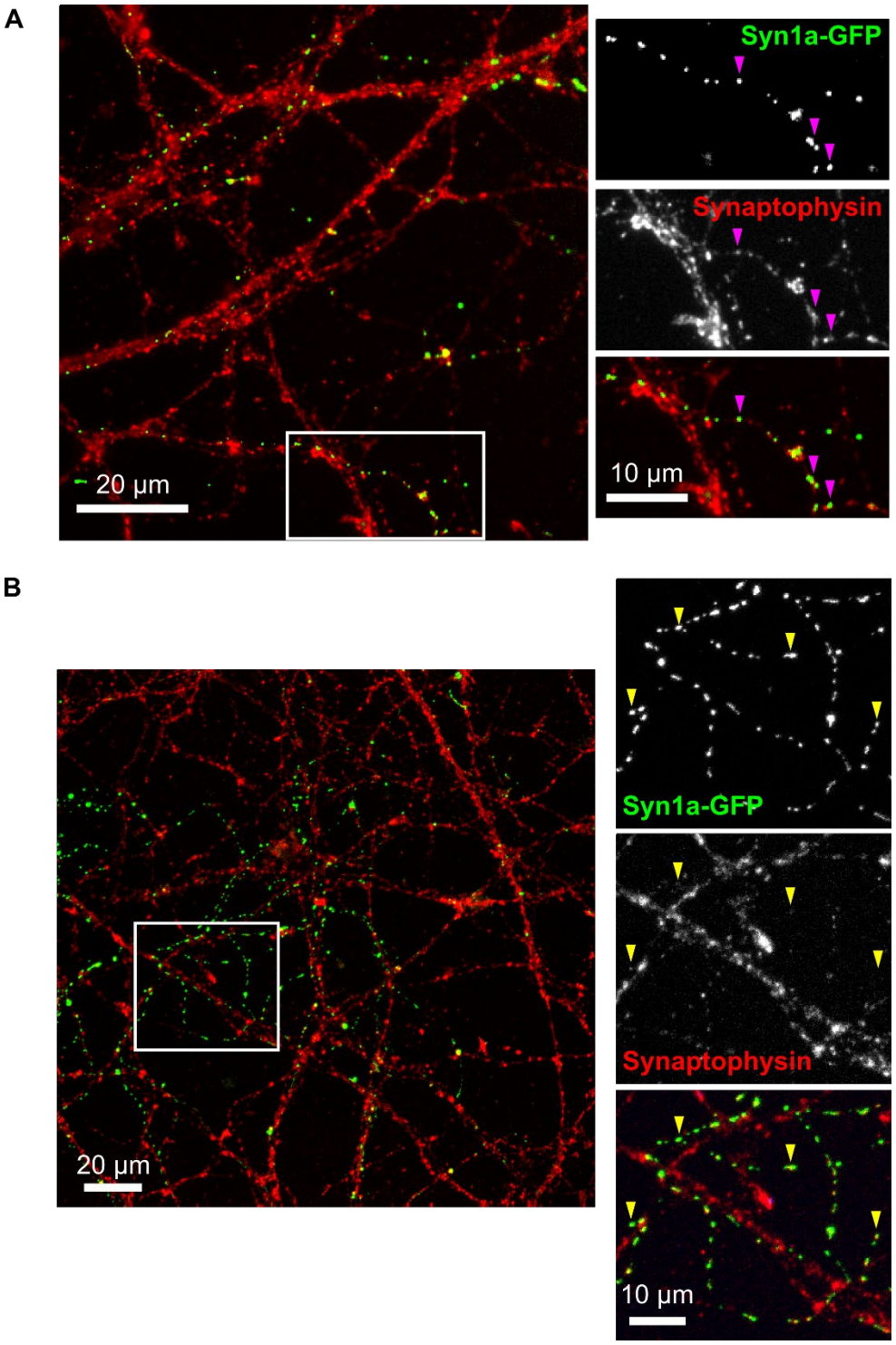

Figure 2.5 Differential colocalisation of Synapsin1a-GFP with endogenous Synaptophysin in individual axons. (**A** and **B**): Representative confocal images of individual axons expressing Synapsin1a-GFP (Syn1a-GFP; *green*) along with immunostained Synaptophysin (synaptic vesicle protein; red). Puncta appear as "beads-on-a-string", typical of axonal *en passant* terminals. Some axons showed very good overlap between Syn1a-GFP puncta and Synaptophysin (*magenta arrowheads*; A). However, other axons showed puncta that appeared to be negatively correlated with Synaptophysin (*yellow arrowhead*; B). MOC = 0.39, n = 23 regions, 4 cultures, methanol fixation. MOC = 0.21, n = 3 regions, 1 culture, PFA fixation.

Fixation could have quenched the signal from Syn1a-GFP (Schnell et al., 2012), leaving only highly overexpressed signal that may have been mislocalised. Low-levels of Syn1a-GFP signal could be more representative of the endogenous expression profile of Synapsin1a. Therefore, signal from Syn1a-GFP was amplified by immunostaining for GFP. This resulted in an apparent increase in signal from axons in the background (Figure 2.7). This method increased low-level expression but did not provide a way of distinguishing those axons with low expression from high expression.

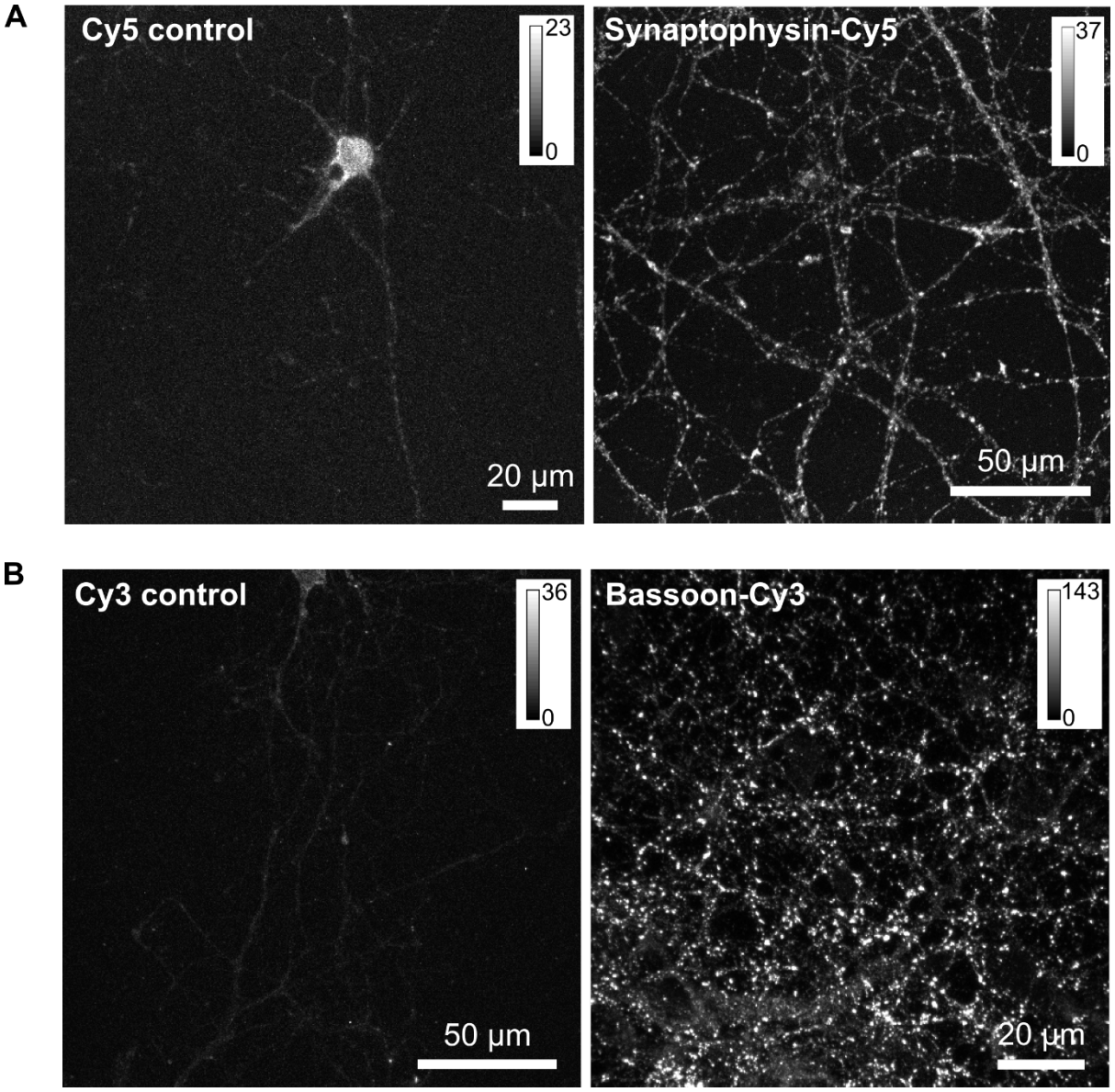

Figure 2.6 Background and non-specific binding were low for Cy3 and Cy5 secondary antibodies. (**A** and **B**): Cultures that were transfected with Syn1a-GFP were fixed and stained with no primary antibody, only Cy5 (A) or Cy3 (B) secondary antibody. Representative confocal images are shown of secondary controls (left) next to images of primary antibody treated cultures using the same settings (right). Note the differences in the calibration bars. The contamination from background and non-specific binding of the secondary antibodies was very low.

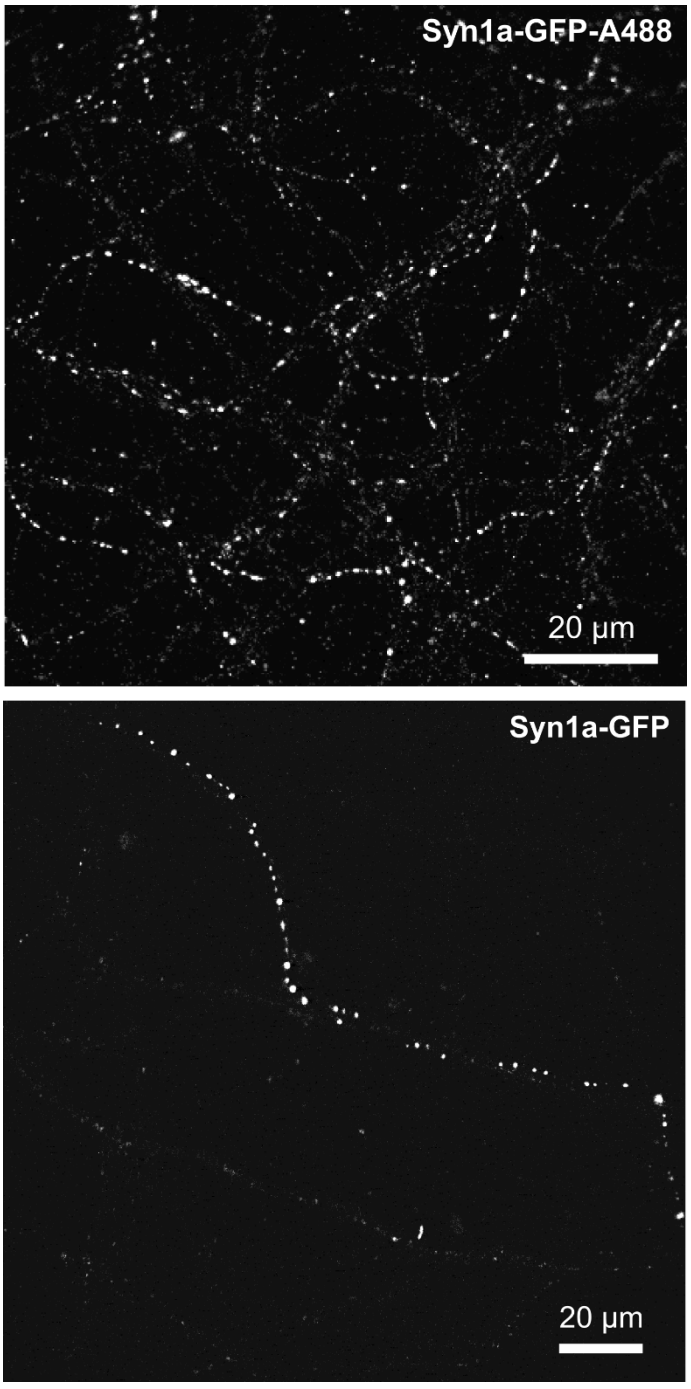

Figure 2.7 Amplification of weak or quenched Synapsin1a-GFP signal using immunostaining. (*Top*) representative confocal image of Synapsin1a-GFP puncta that were immunostained with an anti-GFP antibody. Comparison to a non-stained culture (*bottom*) shows that background axons that are just visible in the non-stained culture may be amplified to higher levels using an anti-GFP antibody. This would aid identification of axons with more endogenous levels of expression to determine if Syn1a-GFP puncta were localising to presynaptic terminals.

To further address whether Syn1a-GFP signal was being quenched through fixation, live-cell imaging of Syn1a-GFP signal that was supposedly not quenched (Figure 2.8A) was followed by subsequent fixation and post-hoc immunostaining of presynaptic proteins (Figure 2.8B). This method was attempt successfully, however there was a discrepancy between the live-cell and fixed puncta, potentially due to the time between imaging and fixation. Despite this, colocalisation between the Synapsin1 antibody and Syn1a-GFP was poor, suggesting the GFP was occluding the antibody epitope on Syn1a-GFP.

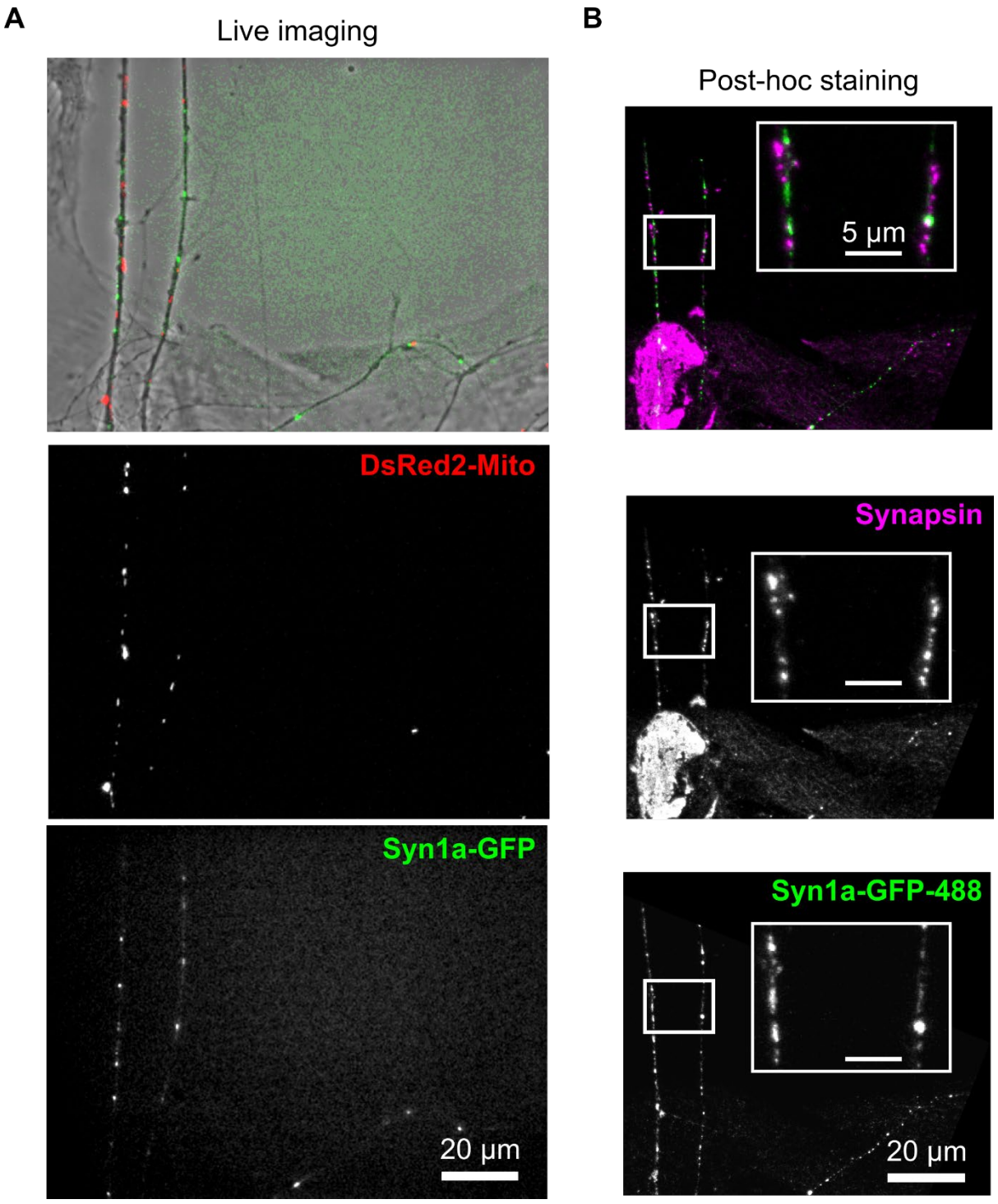

Figure 2.8 Post-hoc staining was used to interrogate colocalisation of transfected Synapsin1a-GFP. (**A**): Representative widefield fluorescence images from live-cell imaging of two axons expressing DsRed2-Mito and Syn1a-GFP. The final image from a 12-hour timelapse is shown. (**B**): Representative confocal images of the axons shown in (A) after fixation, mounting and immunostaining of Synapsin1. There was an artefact in the channel for Synapsin1 immunostain (*middle*). Differences in Syn1a-GFP between (A) and (B) were probably the result of the relatively long time between final live image and fixation (up to 2 hours). Due to the time between the images, no effort was made to correlate the puncta in (A) with (B). This figure is representative of only a single culture.

These results suggested Syn1a-GFP was a poor presynaptic marker in rat cortical cultures. Therefore, Synaptophysin-GFP (Syp-GFP) was synthesised to assess the localisation in comparison to Syn1a-GFP. Synaptophysin is a synaptic vesicle marker commonly used for live-cell imaging (Okabe et al., 2001; Meyer and Smith, 2006; Chang et al., 2006), which labels the entire vesicle pool rather than just the reserve pool, as with Synapsin1a. Syp-GFP appeared punctate when fixed in neurons, similarly to Syn1a-GFP. However, the colocalisation with endogenous Bassoon and Synaptophysin was no better than Syn1a-GFP (MOC: 0.28 and 0.39 respectively, n = 9 and 5 regions, from 1 culture each; Figures 2.9 and 2.10). Again, particular axons had very poor colocalisation, whereas other axons had good colocalisation between Syp-GFP and presynaptic markers. Localisation in relation to the postsynaptic protein PSD-95 was also assessed qualitatively. Syp-GFP puncta did appear to oppose sites of intense PSD-95 puncta, suggesting some Syp-GFP puncta were also at sites with postsynaptic partners (Figure 2.11).

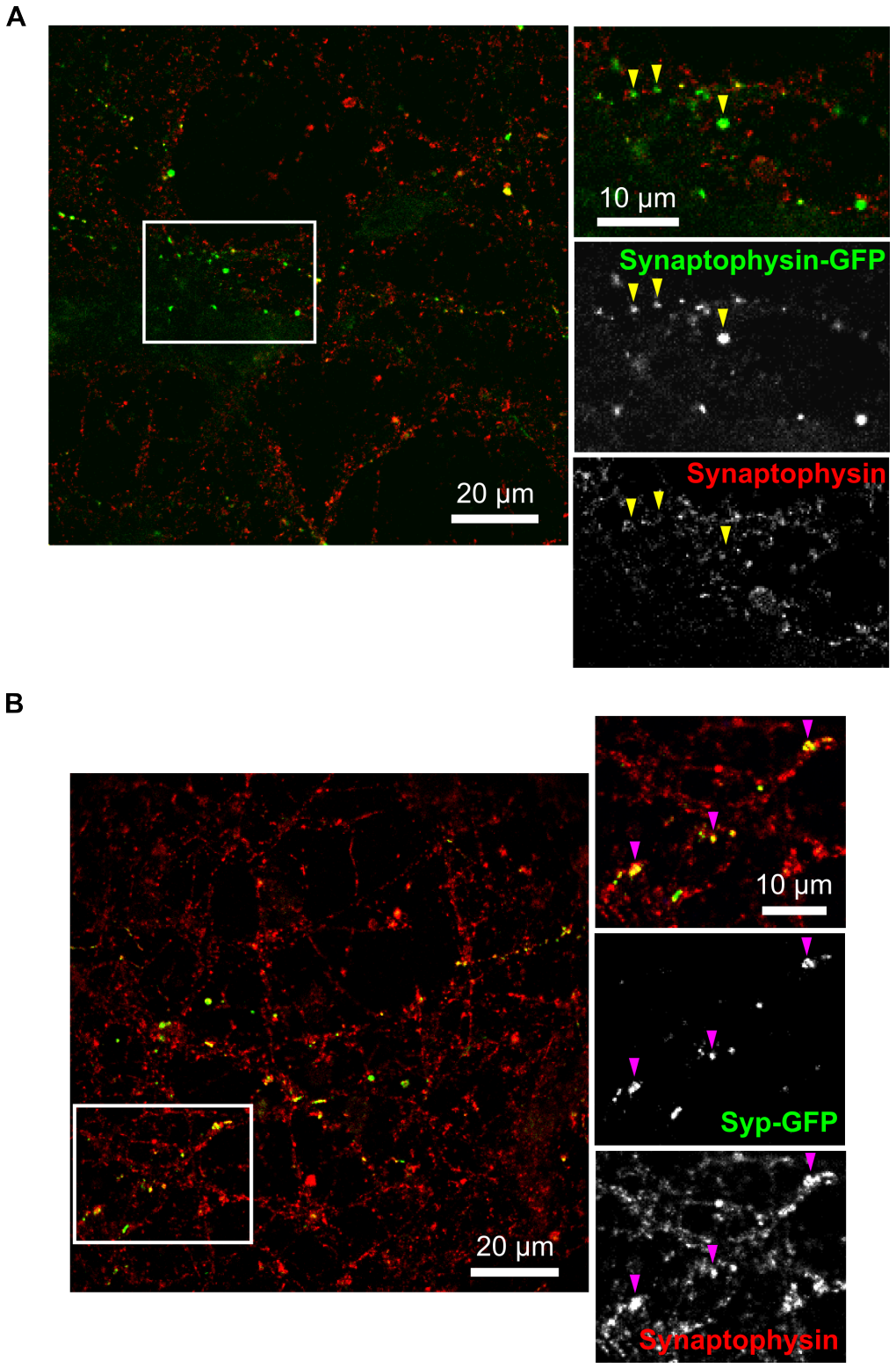

Figure 2.9 Differential colocalisation of Synaptophysin-GFP with endogenous Synaptophysin. (**A** and **B**): Representative confocal images of Synaptophysin-GFP (Syp-GFP) colocalisation with immunolabelled endogenous Synaptophysin. Synaptophysin-GFP was poorly colocalised along some axons (A; *yellow arrowheads*) and strongly along others (B; *magenta arrowheads*). MOC = 0.39, n = 5 regions, 1 culture.

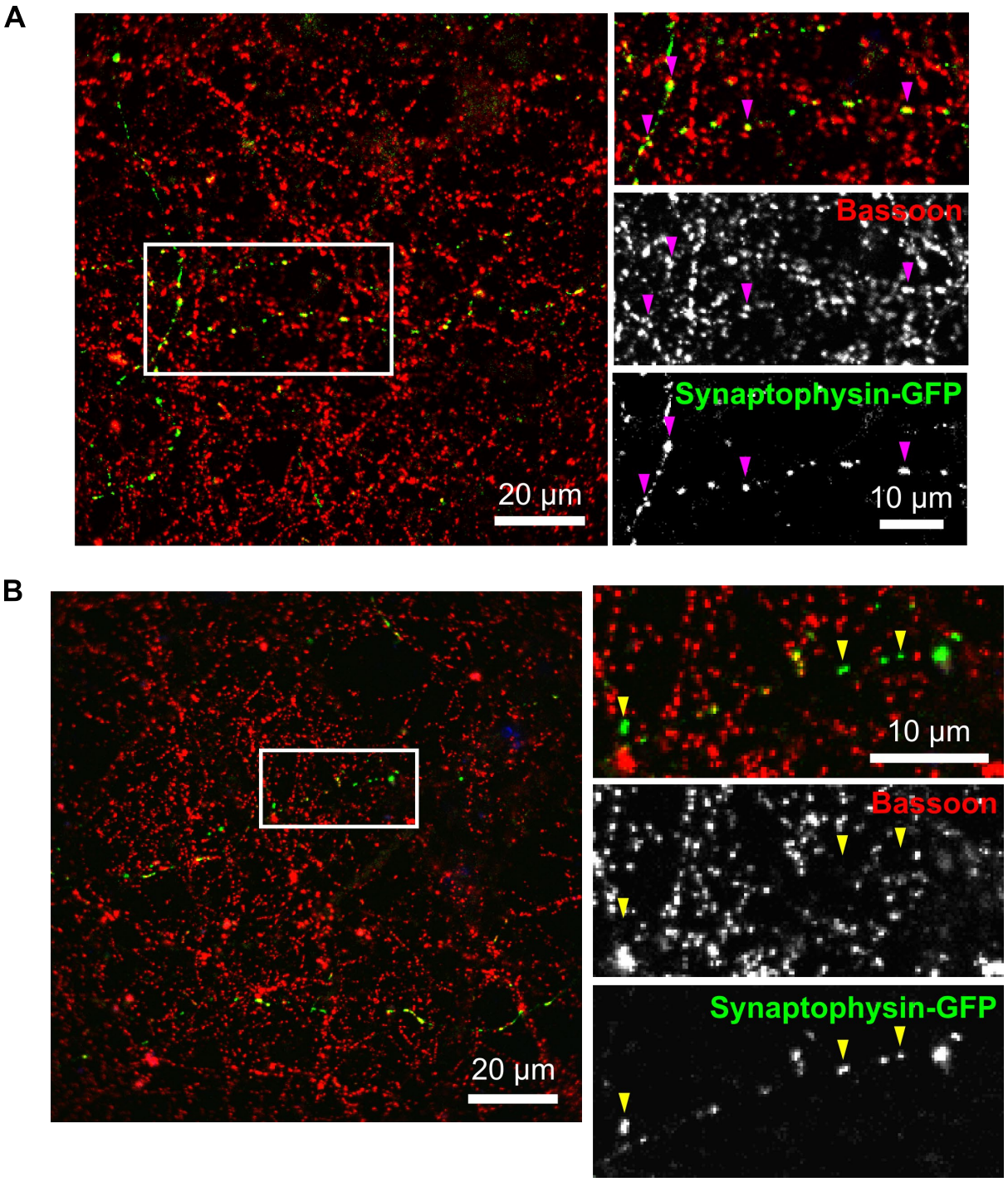

Figure 2.10 Differential colocalisation of Synaptophysin-GFP with endogenous Bassoon. (**A** and **B**): Representative confocal images of Synaptophysin-GFP (Syp-GFP) colocalisation with immunolabelled endogenous Bassoon. Synaptophysin-GFP was poorly colocalised along some axons (A; *magenta arrowheads*) and strongly along others (B; *yellow arrowheads*). MOC = 0.28, n = 9 regions, 1 culture.

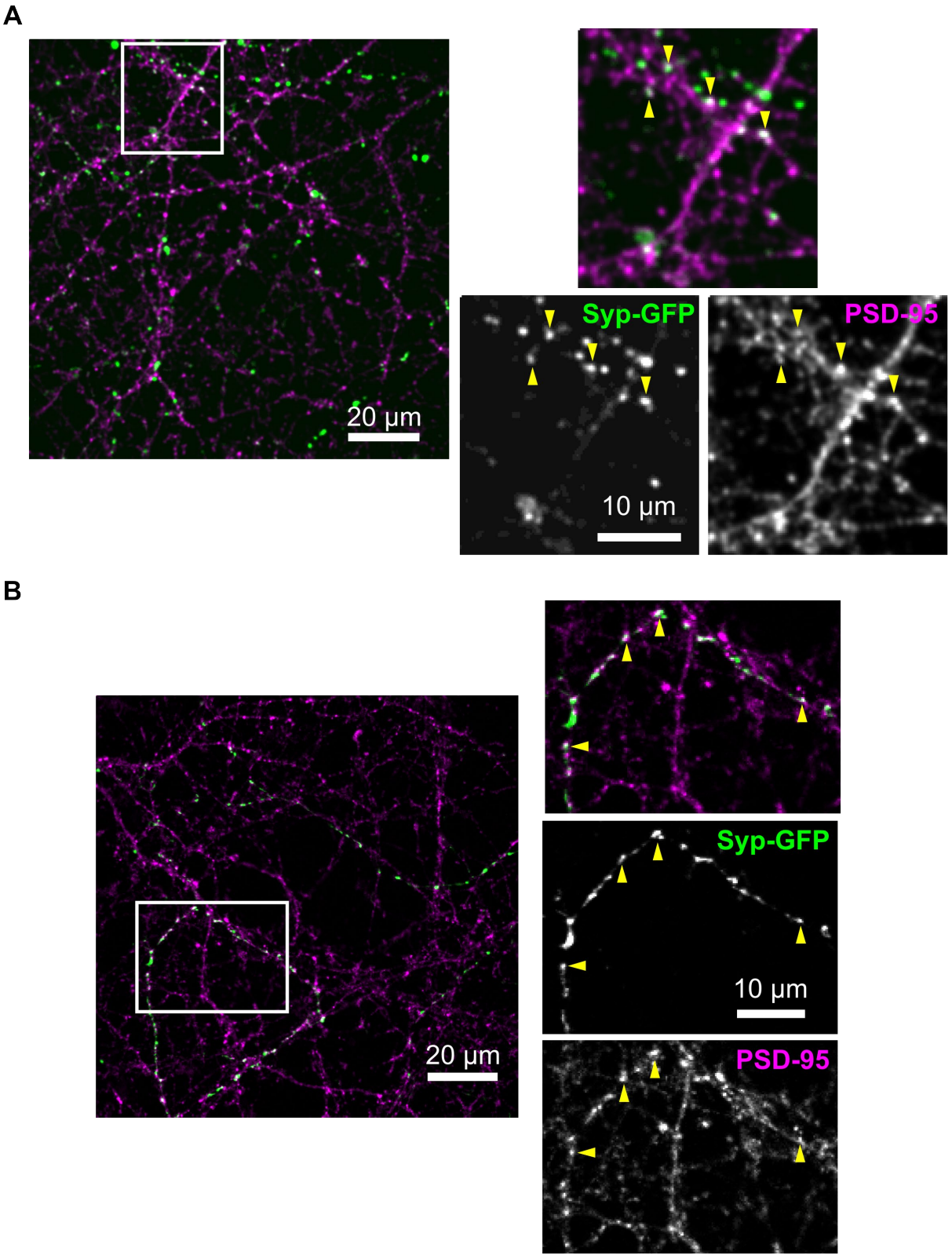

Figure 2.11 Synaptophysin-GFP was opposed to PSD-95 puncta in some cases. (**A** and **B**): Example confocal images of individual axons transfected with Syp-GFP in cultures co-stained for the postsynaptic protein, PSD-95. Opposition of Syp-GFP with PSD-95 puncta is indicated (yellow arrowheads) implying their involvement in a synaptic contact. N = 2 regions, 1 culture.

2.4.3 Determining the lifetimes of putative presynaptic terminals

Live-cell imaging of Syn1a-GFP was carried out to determine the lifetime of putative presynaptic terminals in neuronal culture. Syn1a-GFP was transfected in to cortical neurons at either DIV 10 or 17 and imaged 4 days later (Figure 2.12). Different ages were used because synaptic connections were still maturing at this stage in culture and the lifetimes of presynaptic terminals may have been affected by this maturation (Chiappalone et al., 2006; Ichikawa et al., 1993). Initial observations showed that Syn1a-GFP puncta were dynamic, moving anterogradely and retrogradely along the axon at both ages, sometimes dispersing and returning to the same sites (Figure 2.14). Time-lapse imaging was carried out in an incubated imaging chamber (37^{o}C, 5% CO_2) over 6-12 hours with 10-20 minute intervals. The lifetime of putative presynaptic terminals was measured as the duration that each Syn1a-GFP punctum remained stable. Stable Syn1a-GFP puncta were those that remained within 1 μm of their position and were allowed to disappear for one frame in every two to account for the dispersion of Synapsin1a that is sometimes seen (Chi et al., 2001; see *Methods*). The lifetimes of putative terminals that were either present before the start of time-lapse imaging or those that persisted after the last time point could not be estimated accurately, and so these terminals were not included in the analysis. The distribution of putative presynaptic terminal lifetimes at DIV 14 and 21 were not significantly different (two-sample Kolmogorov-Smirnov test: $k = 0.046$, $p = 0.923$, median lifetime of 30 min for both; Figure 2.15).

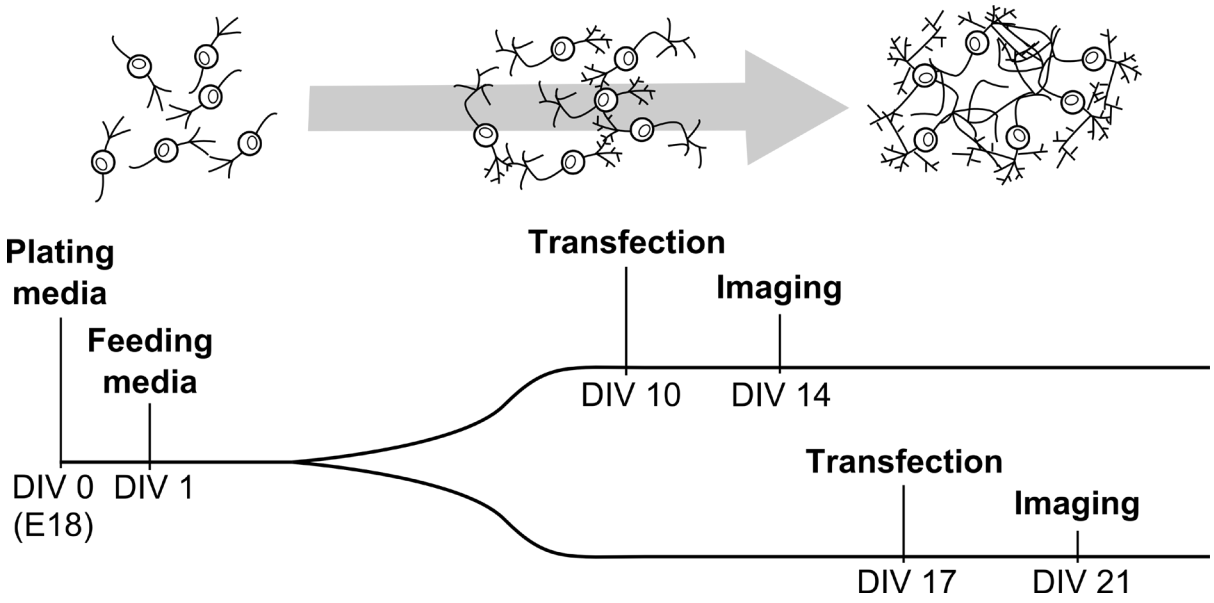

Figure 2.12 Treatment and imaging timeline for cultures used in live-cell imaging. The cortex of embryonic (E18) rat brains were dissected and the cells dissociated and plated (DIV 0). As cultures aged, neurons extended processes to form synaptic connections. Plating media was exchanged for feeding media within 16 hours (DIV 1), to prevent further glial proliferation. Cultures were transfected four days prior to imaging, young cultures were transfected at DIV 10 and imaged at DIV 14, whereas older cultures were transfected at DIV 17 and imaged at DIV 21.

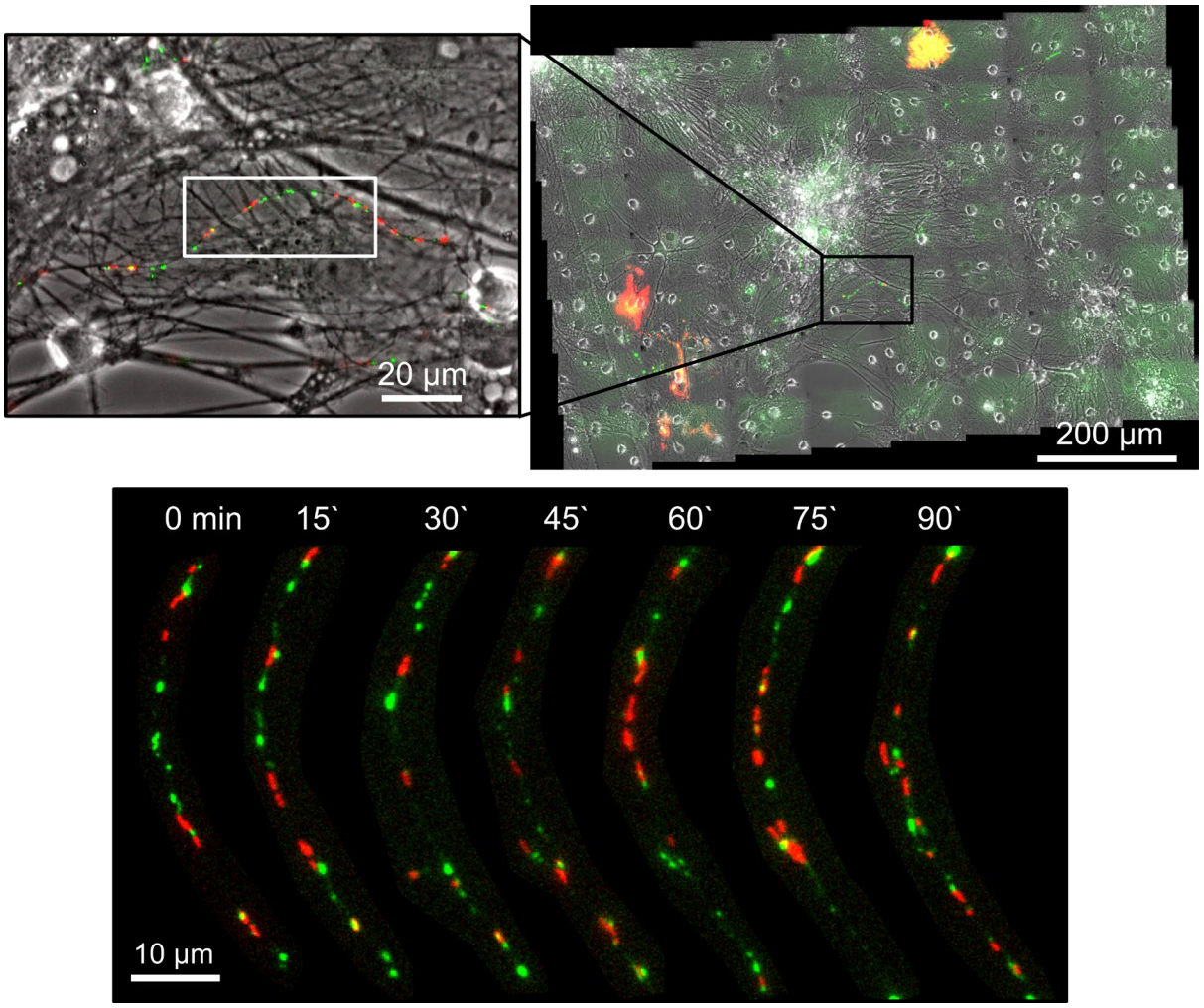

Figure 2.13 Dynamic movement of Syn1a-GFP and DsRed2-Mito. Very sparse transfection resulted in isolation of transfected cells for uncontaminated imaging. Mosaic phase contrast image of a mature culture is shown (DIV 14; *top-right*) with widefield fluorescence overlay of DsRed2-Mito (*red*) and Syn1a-GFP (*green*). A section of the axon was chosen to show the dynamics of these proteins over time (*bottom*) at 15 min intervals. Very few stable puncta persist on the axon of either label.

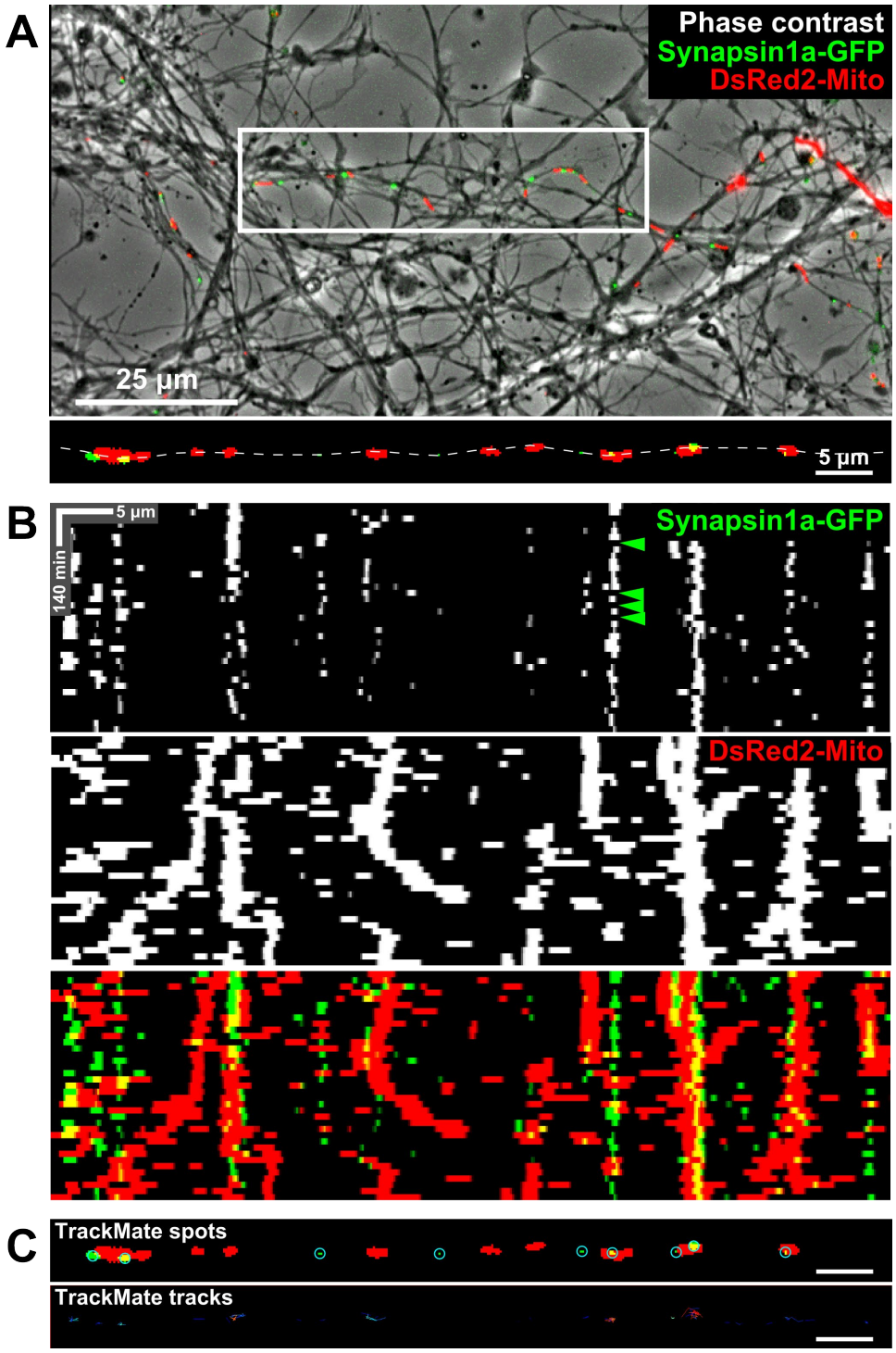

Figure 2.14 Putative presynaptic terminals and mitochondria were tracked and colocalisation assessed at each timepoint. (**A**): (Top) representative phase contrast image from time-lapse imaging overlaid with signal from Synapsin1a-GFP and DsRed2-Mito taken using a widefield fluorescence microscope. (Bottom) cropped and straightened axon from the white box (top) with binarised Synapsin1a-GFP and DsRed2-Mito signal. (**B**): Illustrative kymograph (made using dashed white line in A) showing the binarised signal for Synapsin1a-GFP and DsRed2-Mito. Synapsin1a-GFP puncta would disperse and localise back to the same regions over time (green arrowheads). (**C**): Spots with 1 µm diameter drawn around Synapsin1a-GFP puncta (top) from the TrackMate plugin for ImageJ. Puncta that moved very little (< 1 µm) and were present within 2 frames (< 40 min, green arrowheads in B, allowing for dispersion and reclustering) were tracked using the same plugin (bottom).

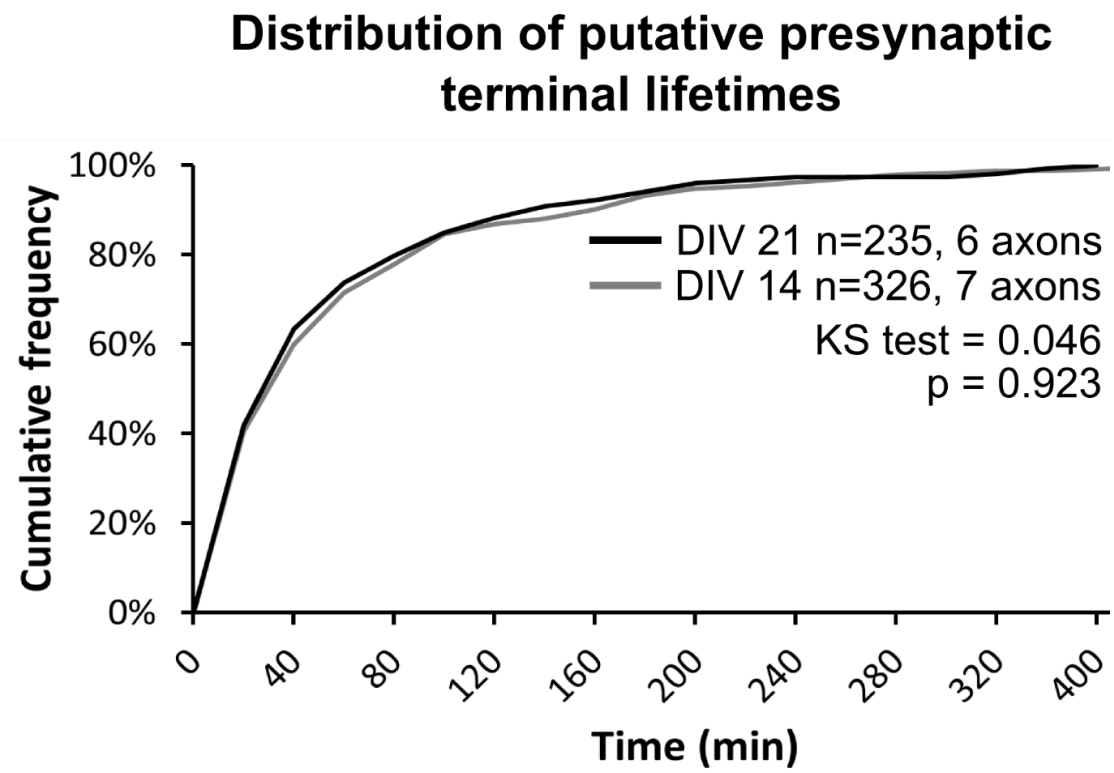

Figure 2.15 Distributions of the lifetimes of putative presynaptic terminals did not differ between DIV 14 and DIV 21. Live-cell imaging of Synapsin1a-GFP puncta in axons was carried out at 10 or 20-minute intervals for 6 hours. Only puncta that were formed and lost within the imaging time course were included to give an accurate estimation of their lifetime. N = 235 terminals, 6 axons for DIV 21, n = 326 terminals, 7 axons for DIV 14.

2.4.4 The relationship between mitochondrial colocalisation and putative presynaptic terminal lifetime

Live-cell imaging was also used to address the relationship between mitochondrial colocalisation and putative presynaptic terminal lifetime at DIV 14 and DIV 21 (Figure 2.14). DsRed2-Mito was expressed alongside Syn1a-GFP, and the proportion of time mitochondria were colocalised with putative presynaptic terminals was measured. Mitochondrial colocalisation was scored if the mitochondrial signal overlapped within a 0.5 μm radius of the Syn1a-GFP puncta centre (Figure 2.14C; see Methods). The proportion of time mitochondria were colocalised represented the strength of association between mitochondria and each terminal. The relationship between terminal lifetime and mitochondrial colocalisation was variable, some terminals with short lifetimes (1 hour) were always associated with a mitochondrion, whereas others with long lifetimes (>6 hours) were almost never associated with a mitochondrion. However, as a population, there was a very weak significant positive correlation at both ages between the proportion of time colocalised with mitochondria and putative presynaptic terminal lifetime (Spearman's rho: $R_s = 0.16$, $p = 0.0174$, DIV 21, $R_s = 0.12$, $p = 0.0254$, DIV 14; Figure 2.16).

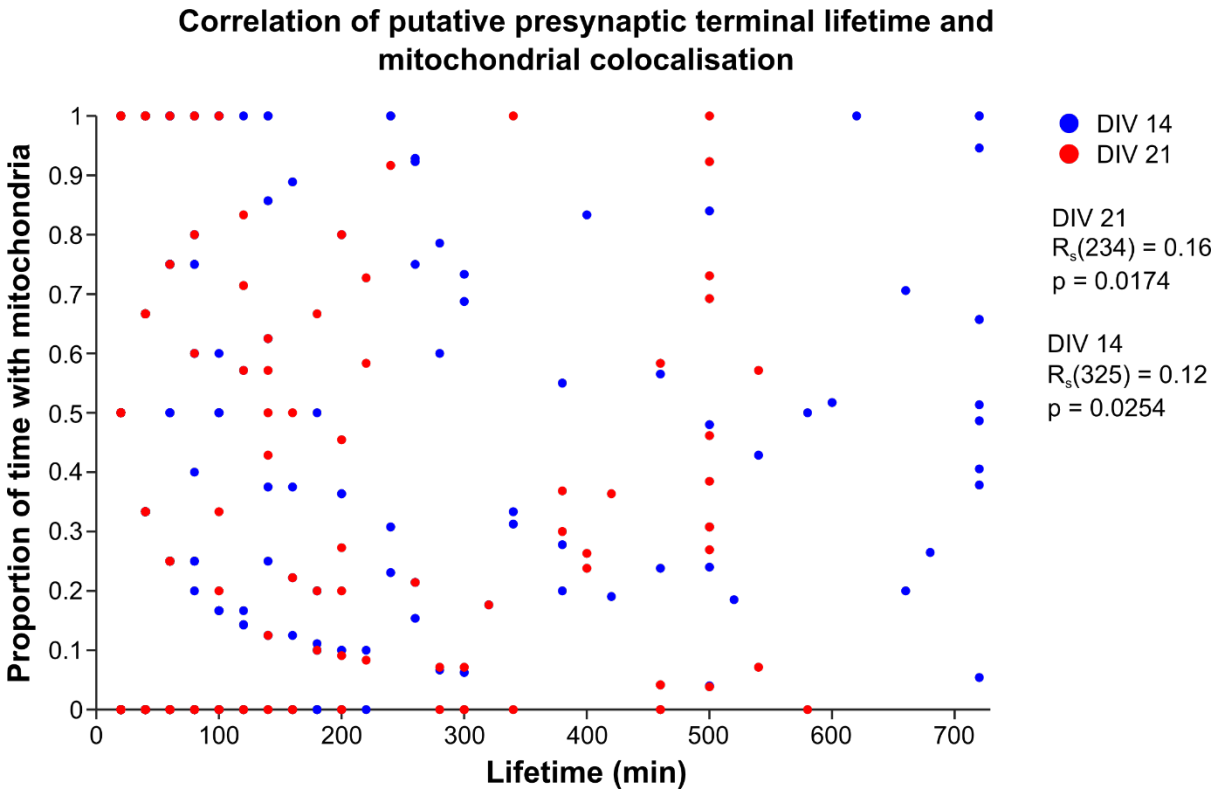

Figure 2.16 Duration of mitochondrial colocalisation was very weakly correlated to putative presynaptic terminal lifetime. The proportion of time that mitochondria were localised to putative presynaptic terminals was plotted against their lifetime (blue = DIV 14 and red = DIV 21). Spearman's rho correlation was done to calculate a non-linear correlation.

2.5 Discussion

In this study, preliminary experiments assessed the relationship between mitochondrial colocalisation and putative presynaptic terminal lifetime in neurons of rat cortical cultures.

Initial attempts to determine the basal colocalisation between mitochondria and presynaptic terminals were not satisfactory. Although mitochondrial colocalisation with endogenous presynaptic terminal markers was shown (Figures 2.1, 2.2 and 2.3), the isolation of individual cells for colocalisation analysis was problematic. The results would have been useful to compare to *in vivo* models (Chavan et al., 2015; Smit-Rigter et al., 2016; Kasthuri et al., 2015) and other studies using primary cultures (Obashi and Okabe, 2013; Courchet et al., 2013; Lewis et al., 2016). Those studies showed similarities between the two models, with ~40% of terminals containing mitochondria in cortical axons. In future, sparse expression of reliable fluorescently-tagged presynaptic and mitochondrial proteins would provide optically isolated axons for colocalisation analysis in fixed cells.

Putative presynaptic terminal lifetimes did not differ as neuronal cultures matured. The lifetime distributions were similar between axons of DIV 14 and DIV 21 neurons (median 30 minutes; Figure 2.15). This is the first time that the stability of terminals has been compared at different ages of neuronal cultures. It was already known that as neurons mature *in vitro*, mitochondrial motility decreases, and mitochondria occupy presynaptic terminals at a higher rate (Lewis et al., 2016; Moutaux et al., 2018; Loss and Stephenson, 2017). The theory that mitochondria act to stabilise presynaptic terminals via regulation of calcium and ATP (Vaccaro et al., 2017; Rangaraju et al., 2014; Sobieski et al, 2017; Smit-Rigter et al., 2016) would suggest that terminals should increase in stability with age in culture (due to increased presynaptic mitochondria), which was not the case here.

Previously, presynaptic terminal stability had been assessed *in vivo* and in cultured hippocampal neurons (De Paola et al., 2006; Okabe and Obashi et al., 2013; Ruthazer et al., 2006; Meyer and Smith, 2006). Developing zebrafish had highly mobile Synaptophysin clusters in axons of the optic tectum, with median lifetimes of ~30 minutes (Meyer and Smith, 2006), similar to the lifetimes of Syn1a-GFP puncta in this study. On the other hand, terminals

of cultured mouse hippocampal neurons were very persistent in culture when observed over long periods of time (VAMP2-EGFP puncta stable for 4 days at 1-day intervals; Obashi and Okabe, 2013), although no assessment of their dynamics was made at the scale of minutes or hours. It could have been that presynaptic proteins were dynamic over short periods, but presynaptic sites were stable over long periods, akin to STV pause sites seen in Sabo et al. (2006). If this was the case, 1-day intervals in Okabe and Obashi (2013) may have captured what seemed to be highly stable synaptic sites, but the dynamism occurring within that interval was not observed. Alternatively, the high dynamism of Synapsin1a-GFP puncta seen here may have been due to its dispersion and reclustering during neuronal activity (Chi et al, 2001; Tang et al., 2015), which is not seen with Synaptophysin or VAMP2, reducing the suitability of Synapsin1a as a marker for the measurement of terminal lifetime in live-cell imaging. Therefore, an important question to ask is: what is a good presynaptic marker for the study of terminal stability?

Functional presynaptic terminals are formed from multiple proteins (Goda and Davis, 2003). The synaptic vesicle protein Synapsin1a was chosen here as its function was well known (Verstegen et al., 2014; Orenbuch et al., 2012; Fornasiero et al., 2012) and it had been used previously as a presynaptic terminal marker in neuronal cultures (Fletcher et al., 1991; Hopf et al., 2002; Courchet et al., 2013; Tang et al., 2015). However, colocalisation in fixed cells between Syn1a-GFP and other presynaptic markers was between 21% and 66% (Figures 2.4 and 2.5). Poor colocalisation did not seem to be a problem with the Syn1a-GFP signal, as amplification did not improve colocalisation qualitatively (Figures 2.7 and 2.8). Interestingly, some Syn1a-GFP-positive axons did not appear to stain for either Bassoon or Synaptophysin at all (Figures 2.4 and 2.5), which would suggest that some neurons were not expressing either of those essential synaptic proteins, a highly unlikely phenomenon. Synaptophysin-GFP was used as an alternative presynaptic marker but showed a similar colocalisation profile to Syn1a-GFP: good colocalisation in some axons and poor colocalisation in others (Figures 2.9 and 2.10).

In future, to validate markers for functional presynaptic terminals, FM dyes should be used (Gaffield and Betz, 2006). FM dyes can be washed on to cultured neurons, where they are

endocytosed and accumulated in the lumen of synaptic vesicles. The intensity of the dye along the axon indicates the level of endo- and exo-cytosis occurring. Colocalisation of a presynaptic marker of choice and these sites of dye uptake would confirm the presence of a functional presynaptic terminal.

The duration of mitochondrial colocalisation with putative presynaptic terminals was very weakly correlated to terminal lifetimes (Figure 2.16). This weak correlation may have been due to the chance of colocalisation with presynaptic terminals as a function of time, rather than the relationship between mitochondrial colocalisation and terminal lifetime. Mitochondria can redistribute along the axon and so, as terminals age, the probability of finding a mitochondrion at a terminal increases, although this was not quantified.

The pausing of mitochondria in kymographs nearby presynaptic terminals fitted well with the mechanistic understanding of the interaction (Figure 2.14B). A large number of studies have identified the mechanism of mitochondrial localisation at presynaptic terminals to be calcium-dependent through the proteins Miro1 and Syntaphilin (Vaccaro et al., 2017, Sun et al., 2013; Chen and Sheng, 2013). Activity and calcium influx at active presynaptic terminals were thought to anchor mitochondria via these mechanisms. Supporting this, Obashi and Okabe (2013) showed that larger presynaptic terminals (presumably with higher Ca^{2+} influx) could capture mitochondria for longer.

It was noticed that mitochondria would sit adjacent to putative terminals in live-cell imaging, rather than within the 1 μm diameter required for colocalisation during analysis. The maximal distance from which a mitochondrion can influence presynaptic function is not entirely clear (Pathak et al., 2015; Smith et al., 2016). Depending on the level of activity, ATP may be used up more quickly requiring mitochondria to be closer to the terminal (Sobieski et al., 2017), although there may be upregulation of ATP production with activity to balance this (Chouhan et al., 2012; Gazit et al., 2016). Alternatively, calcium regulation of presynaptic release may require mitochondria to be positioned close to the release site (Vaccaro et al., 2017; Sun et al., 2013). These small distances are beyond the resolution of fluorescence imaging used in this study, so a very short distance of 1 μm (close to the optical resolution) was chosen to define co-localisation between mitochondria and presynaptic markers. A gradual decrease in

mitochondrial influence on presynaptic terminals has been seen up to 3 μm away from the vesicle pool in ultrastructural studies (Smith et al., 2016). This could be taken in to account during any future analysis to assess the influence of mitochondria at greater distances from the presynaptic terminal, including those seen sitting adjacently in live-cell images.

In vivo studies of mammalian cortex have shown that presynaptic terminals are frequently turned over, at a rate of ~10% every week (Stettler et al., 2006, Grillo et al., 2013; Mostany et al., 2013; De Paola et al., 2006; Ash et al., 2018). However, the measurements taken in this study suggested turnover may be far higher *in vitro*. There are clearly some very significant differences between these experimental situations that might underlie the differing presynaptic stability. Presynaptic turnover *in vivo* is thought to be experience-dependent and underlie learning and memory formation (Holtmaat and Svoboda, 2009). Using an *in vitro* model does not recapitulate any of the sensory inputs occurring during experience-dependent turnover, however, spontaneous activity is occurring at the ages looked at in this study (Moutaux et al., 2018; Biffi et al., 2013). Spontaneous activity is thought to be highly important for neuronal development, particularly the formation of synaptic contacts (Andreae and Burrone, 2018). It may be that spontaneous activity was driving this high turnover of putative presynaptic terminals in neuronal culture, which could be addressed with pharmacological inhibition during time-lapse imaging in future.

Neuronal culture is beneficial for optical access, genetic and environmental manipulations. However, when assessing relationships with mitochondria, which potentially regulate synaptic efficacy through ATP production and calcium sequestration, the energetic environment is important. Glucose concentrations in this and many other studies were 25 mM in Neurobasal A culture medium, substantially higher than any physiological concentration found in mammalian brain or blood (Silver and Erecinska, 1994). Glucose levels also change significantly over time, due to media evaporating (Kleman et al., 2008). This changing energetic environment for neurons may shift ATP production from mitochondria to glycolysis during stress (Jang et al., 2016).

Overall, these preliminary results provide promise to improve the success of future experiments, including the choice of presynaptic terminal marker and methodology for time-lapse colocalisation analysis.

CHAPTER 3 RELATIONSHIPS BETWEEN PRESYNAPTIC TERMINAL DYNAMICS AND MITOCHONDRIAL LOCALISATION IN LONG-RANGE AXONS OF MOUSE NEOCORTEX

3.1 Introduction

In the mammalian brain, structural changes of pre- and post-synaptic terminals can be tracked over short and long durations (hours to years). The results have given unprecedented insight into the link between structural plasticity and the processes of perception, learning and memory formation (Holtmaat and Caroni, 2016). However, the molecular mechanisms of structural plasticity, particularly of the presynaptic terminal, are not well understood.

Structural tracking *in vivo* is carried out using a cranial window for optical access, genetic strategies for labelling cells, and two-photon microscopy to acquire images. Cranial windows involve surgical implantation of a glass coverslip over the top of an exposed part of the brain (Holtmaat et al. 2009) or thinning of the skull to less than 50 μm in thickness (Yang et al. 2010). Specific populations of neurons are labelled *in vivo* according to their genetic identity through spatially-restricted viral injection (Bedbrook et al. 2018), transgenic animals (Feng et al., 2000) or DNA electroporation of embryonic neurons (Lewis et al., 2018). To track axonal and

dendritic structural changes, cytosolic fluorescent protein is expressed in neurons of interest. Subsequently, two-photon microscopy is used to acquire structural images over time (Svoboda and Yasuda 2006; Holtmaat et al. 2009).

Problems with imaging in tissue involve the scattering of excitation and emission light. Two-photon microscopy is used due to its benefits in this area over other fluorescent imaging techniques (Zipfel et al. 2003). Two-photon (2P) microscopy involves the use of longer wavelength (lower energy) photons to excite the fluorophore by arrival of two photons simultaneously (Zipfel et al., 2003). Compared to confocal microscopy, this reduces light scattering to increase imaging depths. Other advantages include: restriction of the excitation volume (depending on the NA of the objective) due to the low likelihood of 2P excitation; reduced damage to the tissue due to lower energy photons (near infrared); and increased sensitivity of emission light detection as all photons contain signal of interest (no out-of-focus light).

Defining a structure as synaptic requires that the ground truth correlation between light microscopy structure and a functional synapse is known. Previous studies of presynaptic terminals have identified criteria in light microscopy that correlate with functional synaptic ultrastructure in electron microscopy (Grillo et al., 2013; Gala et al. 2017; Bass et al. 2017; Drawitsch et al., 2018). Through this correlation it was possible to determine, with high confidence, that a bouton with 2x the intensity of the axonal backbone was a presynaptic terminal (100% of boutons relocated; Grillo et al., 2013). Automated methods can use this threshold to attempt to identify all of the presynaptic terminals on a given axon (Song et al., 2016; Bass et al., 2017). Unfortunately, manual intervention is still required for these techniques to avoid false positives and negatives. These automated methods are also not suitable for the unique structure of *terminaux* boutons, which make up a large proportion of some cell-types (De Paola et al., 2006). Other studies have taken a probabilistic approach to bouton identification due to fluctuations in image quality over time (Gala et al. 2017). Ultimately, manual analysis of 2P images prevails today based on strict criteria until faithful automated techniques can be used (Qiao et al., 2015; Johnson et al., 2016; Frantz et al., 2016; Ash et al. 2018; Sammons et al. 2018; Morimoto et al. 2018).

Bouton structure is not homogeneous; there are two distinct terminal structures in the neocortex: *en passant* and *terminaux*. They are formed along the axon shaft or at the end of protrusions, respectively. The reason for differences in these structures is unknown, but Anderson and Martin (2001) showed that it is not due to differences in their postsynaptic targets (e.g. dendritic spine versus dendritic shaft). The reach of a *terminaux* bouton is much greater than an *en passant* bouton, suggesting that *terminaux* bouton turnover is a mechanism for greater reorganisation of neuronal circuits (Gogolla et al. 2007). Differences in *terminaux* and *en passant* bouton turnover have been identified (Stettler et al., 2006; De Paola et al., 2006). However, the difference is most likely the result of differential turnover between cell-types, as *en passant* and *terminaux* boutons on the same axon have similar survival (De Paola et al., 2006).

Terminaux boutons share a similarity in structure to dendritic spines, whose structure has been postulated to allow for compartmentalisation of calcium that may spatially limit Ca^{2+}-dependent signalling mechanisms to the individual spine (Yuste et al., 2000). This suggests that *terminaux* boutons may also be involved in compartmentalisation of biochemistry. However, the thin axonal regions between *en passant* boutons may also be useful for compartmentalisation (Shepherd and Harris, 1998), once again casting doubt on how *terminaux* and *en passant* boutons are distinguished.

Presynaptic structural plasticity is experience-dependent and occurs throughout the life of mice and macaques (Mostany et al., 2013; Grillo et al., 2013; Stettler et al., 2006). Basal turnover in the neocortex is thought to be cell-type and circuit specific, increasing during development until mice reach 3 – 5 months of age (De Paola et al., 2006; Mostany et al., 2013). Turnover rates range from 5 to 10% over 4 days to 4 weeks (Ash et al., 2018; Grillo et al., 2013; Qiao et al., 2015; Sammons et al., 2018). The pre-existing population of boutons has 2-3 times higher rate of survival than newly-formed boutons (Ash et al., 2018; Qiao et al., 2015). Despite the wealth of information pertaining to presynaptic structural plasticity *in vivo*, the molecular mechanisms underlying bouton survival and turnover are not well understood, with only a few candidates identified (Ash et al., 2018; Frantz et al., 2014; Akbik et al., 2013).

Mitochondria are regulators of synaptic efficacy through calcium sequestration and ATP production (Devine and Kittler, 2018); but mitochondria are not present at the majority of presynaptic terminals of neocortical neurons that have been studied (60-70%; Kasthuri et al., 2015; Smit-Rigter et al., 2016). Mitochondria are also dynamic, and can re-distribute throughout the axon at an estimated rate of 50% every 4 days (Lewis et al., 2016; Smit-Rigter et al., 2016). Smit-Rigter et al., also provided evidence that increased bouton survival is linked to mitochondrial presence. However, it is not known how the maturity of boutons (newly-formed or pre-existing) affects this relationship.

In this study, pyramidal neurons of the mouse motor cortex were labelled using an adeno-associated virus to monitor presynaptic structural plasticity. This method was used to target a subset of cells to reduce the spread and variety of labelled cells seen in other studies (De Paola et al., 2006; Lewis et al., 2018). Cortico-cortical axonal projections from the motor cortex emanate mostly from upper layer 5 and layer 2/3 (Oswald et al., 2013), one of the areas they project to is the somatosensory cortex, specifically layer 1 and more weakly to layer 5/6 (Petreanu et al., 2009). The connection is thought to be modulating the somatosensory cortex during whisking, potentially feeding information back about whisker location when determining object location (Petreanu et al., 2012; Veinante and Deschenes, 2003), thought to be essential for navigation by active touch. The aim of this study was to determine if relationships exist between presynaptic terminal turnover, terminal age and the distribution of mitochondria in this specific long-range axonal projection.

3.1.1 Key findings

- Axonal bouton and mitochondrial dynamics can be tracked in specific neuronal projections using viral strategies and *in vivo* two-photon imaging
- Bouton and mitochondrial densities remained consistent over >1 month in long-range motor-somatosensory projections
- Bouton and mitochondrial densities were strongly correlated
- The size of the dynamic fraction of boutons was not related to regional mitochondrial density along an axonal segment

- Mitochondrial positioning was biased towards presynaptic boutons, with a stronger presence at EPBs than TBs
- Probability of mitochondrial presence increased with bouton age
- Newly-formed boutons were quickly lost in their first week, but less so with mitochondria present
- Pre-existing boutons were twice as likely to be lost without mitochondria present, which was more representative for EPBs than TBs

3.2 Materials

- Foraging food
- α-GFP chicken polyAb (Abcam; ab13970)
- Goat anti-chicken Alexa-488 conjugated antibody (ThermoFisher Scientific; A-11039)
- Dexamethasone
- Rimadyl
- Isoflurane
- Chlorohexidine
- Lubrithal/lacrilube
- Stereotaxic frame
- Surgery tools
- Cotton wool buds
- Cortex buffer chemicals
- Microcapillary
- VetBond glue
- Gelfoam
- Glass coverslip 5 mm
- Dental cement (DePuy)
- Stainless steel bar
- Screw (for bar)
- Scalpel
- Euthatal

- PBS
- PFA
- Perfusion-fixation apparatus
- 31-gauge needle
- DiI
- Acrylamide
- VA-044
- ETC
- X-CLARITY chamber + mounting medium
- Triton X-100
- Agarose (low MP)
- Sucrose
- Glass microscope slides
- No. 1.5 coverslips
- Fluoromount-G w/ DAPI
- Horse serum

3.3 Methods

All procedures involving animals were carried out adhering to the Animals (Scientific Procedures) Act 1986 as outlined by the Home Office, UK and approved by the University of Bristol Animal Welfare and Ethics Review Board.

3.3.1 Animal housing, husbandry and enrichment

Adult (2.5 month) C57Bl/6 male mice were housed individually. This was due to concerns for the safety of animals and integrity of the implant during fighting in groups, especially in males (Kappel et al., 2017). The likelihood of loss of the implant by over-grooming (between animals) or fighting was eliminated through individual housing.

All animals were kept in large cages, with extra enrichment consisting of tunnels, wheels, textures and foraging food. The extra enrichment and space were used to increase the experience-dependent turnover of presynaptic terminals to identify more events of terminal formation in imaging experiments and therefore use less animals (Landers et al., 2011; Nithianantharajah et al., 2004; Briones et al., 2004).

Animals were on a 12 hour light-dark cycle and cleaned weekly. Animals were not directly handled by the tail, instead cardboard or plastic tubes were used to transport them to reduce anxiety (Hurst and West, 2010). Male animals were used for all observations and experiments.

3.3.2 Antibodies and viral DNA constructs

Chicken α-GFP (1:5000 dilution) was used as a primary antibody for immunohistochemistry with an α-chicken Alexa488-conjugated secondary (1:1000).

The virus used for intracranial injection was a hybrid recombinant adeno-associated virus of serotype 2/1 expressing a bi-cistronic vector (AAV2/1-hSYN-EGFP-P2A-Cox8a-TagRFP; Figure 3.1A). This serotype was designed to increase neuronal tropism (McFarland et al., 2009). The human synapsin promoter (hSYN) was used to limit expression to neuronal cells. Cytosolic enhanced green fluorescent protein (EGFP) was separated by a P2A peptide from mitochondrially-targeted tagRFP (red fluorescent protein; fused to amino acids 1-29 of Cox8a

subunit of cytochrome oxidase) localised to the inner mitochondrial membrane. The P2A peptide is a self-cleaving peptide of the 2A family from porcine teschovirus, that has a high cleaving efficiency (Kim et al., 2011). Additionally, Woodchuck Hepatitis Virus Posttranscriptional Regulatory Element was used to increase protein expression (Zuffery et al., 1999).

3.3.3 Surgery

Aseptic technique was used to limit the possibility of infection, guidelines were followed as outlined by the Laboratory Animal Science Association (http://www.lasa.co.uk/wp-content/uploads/2017/04/Aseptic-surgery-final.pdf). To reduce stress, animals were allowed at least one week to acclimatise to unfamiliar environments after relocation before the commencement of experiments. Intraperitoneal injections of analgesic and anti-inflammatory drugs (dexamethasone at 4 mg mL^{-1} kg^{-1} and rimadyl at 0.5 mg mL^{-1} kg^{-1}) were given pre-operatively to reduce pain and inflammation.

3.3.3.1 Pre-operation

Adult (2.5 months old) male C57BL/6 mice were anaesthetised using gaseous isoflurane at 3-4% for induction and 1-2% to sustain anaesthesia, carried by 1.5 L/min O_2. Gaseous isoflurane has a benefit over injectable anaesthetics as it can be easily regulated and quickly altered to keep the animal at a similar level of anaesthesia throughout surgery. Animals were weighed before surgery to monitor weight gain post-operation, as a measure of recovery.

Animals were shaven around the scalp, especially behind the ears and between the eyes. Antiseptic solution (5% chlorohexidine) was applied using gauze to disinfect the skin area surrounding the incision site to reduce bacterial contamination of the surgical site. A sterile drape was also placed over the animal to avoid transfer of material between the fur and surgical area. The internal body temperature was kept at 37°C throughout surgery by a homeothermic controller connected to a rectal probe and heat mat. Lacrilube or lubrithal was used to coat the animal's eyes to prevent them drying during surgery. Illumination was provided by cool swan neck lamps (which do not produce excessive heat), alongside a ring of

LEDs on a stereo microscope. The stereo microscope was used for all parts of the surgery after scalp incision.

3.3.3.2 Intracranial viral injection

Animals were placed in a stereotaxic frame and head-fixed using blunt-ended ear bars. The scalp was grasped using blunt forceps and removed in a single cut with curved scissors. The periosteum was gently rubbed away with sterile cotton wool buds soaked in cortex buffer (125 mM NaCl, 5 mM KCl, 10 mM Glucose, 10 mM HEPES, 2 mM CaCl2, 2 mM MgSO4 in dH2O, pH 7.4), taking care not to allow loose hair to enter the incision site. Subsequently, the skull bone was kept moist throughout surgery with cortex buffer.

Prior to measuring the injection site, the skull anterior-posterior axis tilt was adjusted until the Lambda and Bregma landmarks were within 0.5 mm depth of each other. A screw (0-80 UNF thread, 1/16 inch length) was implanted in the left parietal skull bone to anchor the implant to the skull; a small dent was made to guide the screw in place using a motorised precision hand drill. The screw was lightly (but securely) tightened to the skull, leaving a gap under the screw head for glue application later. The intracranial injection site was measured +0.7 mm lateral (always to the right) and +1.0 mm anterior from Bregma, as these coordinates corresponded to the primary/secondary motor cortex (Lein et al., 2007; Petreanu et al., 2012). A small (~0.5 mm Ø) burr hole was made in the skull using a high-speed motorised hand drill. For viral injections, a glass capillary was pulled in to a micropipette with a long, pointed tip. The end of the micropipette was bevelled on a whetstone to sharpen it further (Roome and Kuhn, 2014). Virus was injected intracranially using a Hamilton syringe and motorised pump at a rate of 100 nL/min. A volume of 300 nL was injected at depths of 300 μm (first) and 700 μm (second) from the pial surface to spread it across all cortical layers (Figures 3.4-6). Virus was allowed to spread for 3 min before moving the micropipette. The viral titre used in surgeries was in the range of 1-2 x 10^{13} particles mL^{-1} in cortex buffer, lower titres produced more consistently low densities of expression, which was useful for isolating individual axon structure during imaging.

3.3.3.3 Cranial window implantation

After viral injection, a thin layer of VetBond™ glue was spread across the skull, to the skin edges, avoiding the right parietal skull bone where the cranial window was to be implanted. The skin was pushed back on the right side to create enough space for the glue to get underneath the lip of the coverslip when it was glued in place later. The craniectomy was outlined with a dotted pen line roughly starting at the anterior and medial border of the right parietal skull bone, with a diameter of ~3-4 mm spreading posteriorly/laterally. A motorised hand drill was used to carefully drill away the outline. Drilling was done intermittently to ensure the skull did not get too hot and the skull was kept slightly moist with cortex buffer to make the drilling as consistent as possible (Holtmaat et al., 2009). A pair of fine forceps were used to prise up the skull fragment when only a small layer of bone was remaining around the edges of the craniectomy. The skull fragment was gently lifted up-and-away from the brain surface, ensuring the dura remained undamaged.

The exposed area was gently but thoroughly cleaned for 2–3 minutes using dental gelfoam soaked in cortex buffer to remove any bone fragments and blood from the surface of the brain. A 5 mm Ø glass coverslip was placed over the craniectomy on top of a small volume of cortex buffer, with an overhanging lip for the glue to adhere to. A blunt cocktail stick was used in the stereotaxic apparatus to apply pressure on the coverslip and allow the use of both hands for glue and cement application. The window was held in place with reasonable force to prevent the glue getting in to the skull cavity. VetBond™ glue was applied around the lip of the coverslip, taking care not to contaminate the top surface of the coverslip.

Quick-drying dental cement mix (DePuy w/ gentamycin) was used to apply a ~1 mm thick layer of cement over the top of the edges of the coverslip as well as up to the edges of the skin incision. A stainless-steel bar (10 x 3 x 1 mm) was placed over the left hemisphere as close to the window as possible while leaving enough space for microscope objective access during subsequent imaging. The bar was used for securing the head during repeated microscopy imaging sessions. The animal was then allowed to recover from anaesthesia on a heat mat before being placed in a clean cage to reduce the chance of infection.

3.3.3.4 Post-operation

Animals were monitored closely for 5 days following surgery, including daily weighing to check for body weight change of >10% from pre-operation levels. Animals were left for 3–4 weeks before imaging to allow for any inflammation to clear under the window and for viral expression to increase.

3.3.4 Histology

Histology was carried out to map the locations and projection patterns of labelled cells and the cranial window site to assess consistency in surgery.

3.3.4.1 Transcardial perfusion fixation

Following the end of an imaging paradigm, mice were administered a dose of 70–100 μL of Euthatal (200 mg/ml sodium pentobarbital) intraperitoneally to achieve terminal anaesthesia. When the animal was deeply anaesthetised, exsanguination was performed, and the animal was transcardially perfused with 5 mL of filter-sterilised 0.01 M PBS to flush out any remaining blood, reducing background fluorescence during imaging. This was followed by infusion of 20–30 mL of 4% paraformaldehyde (PFA) in 0.01 M PBS to fix the tissue.

The cranial window implant was peeled away from the skull and, when required, a 31-gauge needle was dipped in DiI and placed in to the window site to dye the area for later reference. The brain was then dissected out and post-fixed in 4% PFA in 0.01 M PBS at 4°C until required (no longer than 2 months).

3.3.4.2 Tissue clearing

Tissue clearing was used to achieve optical clarity throughout the whole brain and therefore gain an intact view of labelled projections (Lee et al., 2016). For tissue clearing, the brain was post-fixed for 24 hours in 4% PFA followed by overnight incubation in hydrogel solution (4% w/v acrylamide without bis-acrylamide, 1% w/v VA-044 initiator in 0.01 M PBS) at 4°C. Oxygen was removed from the solution by degasification using pure nitrogen bubbling through the solution (providing some agitation). Degasification was carried out because the polymerisation process relied on free radical production, which was most efficient in the absence of oxygen (Lee et al., 2016). The solution was then sealed with parafilm to prevent

oxygenation of the solution. Polymerisation of the hydrogel was carried out at 37°C in a water bath for ~3 hours. The polymerised hydrogel was washed from the brain surface using RT electrophoretic tissue clearing solution (ETC; 4% SDS and 200 mM boric acid) and the brain was then mounted inside the X-CLARITY electrophoresis chamber.

The X-CLARITY machine was used according to the manufacturer's instructions (Logos Biosystems). Parameters were set to 1.2–1.5 A, 37°C, 30–50 revolutions per minute, 50 V (default). Higher pump speeds were used to decrease overheating of the solution. The brain colour/clarity was checked every 2–3 hours until the brain turned white and slightly translucent, the brain did not appear clear until it was placed in refractive index-matched medium (X-CLARITY mounting solution). The brain was washed in 0.01 M PBS containing 0.1% Triton X-100 to remove excess ETC and kept at RT.

3.3.4.3 Tissue sectioning

For histological sectioning, brains were embedded in 2% agarose (in distilled H_2O), trimmed to the region of interest and two series of 50 μm-thick sections were cut in 0.01 M PBS on a Leica vibratome. Alternatively, brains were incubated in a 30% sucrose solution (w/v) for up to 1 week for substitution of water to protect from freeze-fracture. The brains were then sectioned using a freezing microtome in optimal cutting temperature (OCT) solution. 50-μm sections were stored at 4°C in 0.01 M PBS for up to 4 days or indefinitely on glass slides at -20°C, after which they were either immunostained or directly mounted on glass microscope slides with No. 1.5 coverslips using Fluoromount-G (containing DAPI nuclear stain).

3.3.4.4 Tissue immunostaining

The immunostaining protocol for tissue sections was carried out entirely at RT. Sections were washed with 0.01 M PBS (3 x 15 minutes) and permeabilised with 50% ethanol for 30 min. After, the tissue was washed with 0.01 M PBS (3 x 15 minutes) and incubated with the primary antibody in 0.01 M PBS, 0.3% Triton-X 100, 5% horse serum for 24 hours on a rocker. The primary antibody was washed off with 0.01 M PBS (3 x 15 minutes) and the tissue was incubated with the appropriate secondary antibody diluted in 0.01 M PBS, 0.3% Triton-X 100, 2% horse serum for 4 hours on a rocker. Finally, the tissue sections were washed in 0.01 M

PBS (3 x 15 minutes) and mounted with Fluoromount-G (containing DAPI nuclear stain) on glass microscope slides with No. 1.5 coverslips.

3.3.5 Imaging

3.3.5.1 Tissue sections

Imaging of whole tissue sections was carried out on a widefield microscope (Leica DMI6000) with a mercury lamp and CCD camera (Leica DFC365FX monochrome) using Leica LAS X software. Filter sets were assigned for the following fluorophores: DAPI (Ex. 350/50 nm, 400 nm dichroic mirror, Em. BP 460/50 nm), A488/EGFP (Ex.: 480/40 nm, 505 nm dichroic mirror, Em. BP 527/30 nm), TagRFP (Ex. 620/60, 660 nm dichroic mirror, Em. BP 700/38). Objective lenses used: 5x dry 0.15 NA and 20x dry 0.4 NA. Parameters were changed depending on the tissue being imaged, so that the entire dynamic range was used. This avoided saturation in areas of high expression, while still capturing dim axonal projections. Whole slides or tissue sections were imaged using a motorised stage and the tilescan function of Leica LAS X software. Brightfield and DAPI signal of coronal or sagittal tissue sections were compared to the Paxinos Mouse Brain Atlas (Franklin and Paxinos, 2008) or Allen Mouse Brain Atlas (Lein et al., 2007) as a reference to map the positions of viral injections and window sites.

3.3.5.2 Cleared tissue

The cleared tissue was immersed in a small volume (5–10 mL) of mounting medium (X-CLARITY mounting solution) inside a 50 mL Falcon tube for at least 2 hours before mounting. Cleared tissue was mounted in the centre of a circular wall of blu-tac inside the lid of a 35 mm dish to create a water-tight well. The well was filled partially with fresh X-CLARITY mounting medium and the chamber was sealed on top with a 35 mm coverslip pressed in to the blu-tac. The chamber was filled from a small inlet in the blu-tac using a 200 μL pipette and the inlet was sealed by squeezing the blu-tac back together.

Cleared tissue was imaged using a Leica SP8 AOBS confocal laser scanning microscope attached to a Leica DM6000 upright epifluorescence microscope with a Ti-Sapphire laser (MaiTai DeepSee; tuneable from 680-1300 nm) and a fixed-wavelength 1040 nm laser. Two hybrid GaAsP detectors were used with a BP 525/50 nm filter for EGFP and BP 630/75 nm for

tagRFP. Objectives lenses used: 10x water-immersion 0.3 NA and 25x water-immersion 0.95 NA. Large z-stack mosaic images (5 μm steps for ~1 mm) were acquired using the tilescan function in Leica LAS X software. The laser intensity was attenuated at shallower imaging depths to maintain signal-to-noise ratio.

3.3.5.3 *In vivo* imaging

For *in vivo* imaging, a customised Scientifica upright microscope was used along with a motorised stage to aid precise movement in coordinate space for relocation of regions of interest (ROIs). Epifluorescence capabilities (Xenon lamp and filter carousel) were used for low resolution mapping of expression across the window to guide two-photon imaging. Two MaiTai Ti-Sapphire tuneable lasers (Spectra Physics; tuneable from 680–1040 nm) were used and attenuation of laser power was controlled through either a Pockel's cell or half-wave plate. Two-photon excitation wavelengths for imaging were typically 920 nm (EGFP) and 1040 nm (TagRFP; Figure 3.2). Laser lines were combined using a polarising beamsplitter cube in reverse, and combined power never exceeded 60 mW average power as read from power meter at the sample. Acquisition was controlled by ScanImage software (Pologruto et al., 2003; version 5.1) and Micromanager software (Edelstein et al., 2014; version 1.4). Objective lenses used: 4x dry 0.15 NA, 10x water-immersion 0.6 NA and 60x water-immersion 1.1 NA. Emission filter sets used for PMTs were BP 620/60 nm for tagRFP and BP 525/50 nm for EGFP. The stage was fitted with a micromanipulator for precise head fixation in every repeated imaging session, allowing for efficient relocation of ROIs.

During *in vivo* imaging, mice were anaesthetised by gaseous isoflurane anaesthetic (1–2% carried by 1.5 L/min O_2) and breathing was monitored to judge depth of anaesthesia. Breathing was kept in the range of 80-100 beats per minute by eye. Internal body temperature was kept at 37°C by a homeostatic controller with rectal temperature probe and heat mat. Lacrilube or lubrithal were used to prevent drying of the animal's eyes. The animal was head-fixed by a single screw between a bar in the micromanipulator and the implanted head bar. The head was rotated by the micromanipulator until the cranial window was flat, decreasing light refraction by the glass coverslip. The angle was recorded for obtaining the same position in repeated sessions.

Epifluorescence imaging was used with a low magnification objective to locate expression in axonal projections under the window from virally-infected cells. For each mouse, a large blood vessel bifurcation was chosen using reflected light and set as the origin for recording coordinates of ROIs. Two-photon imaging was used to locate ROIs based on the following criteria: sparse labelling, to reduce background and contamination from crossing axons; distinctive axonal structures, for easy relocation; distance from other ROIs, to prevent sampling the same axon twice.

Z-stacks of 20–50 μm were acquired at each ROI with a step size of 1 μm (60x, 1.1 NA objective). Images were acquired with 3x frame averaging, 1 us pixel dwell time at 1024 x 1024 pixels and a field of view of 76 x 76 μm, resulting in a final pixel size of 74 nm. Signal was matched between sessions by adjusting laser power because of differences in window quality between imaging sessions, which would alter the signal-to-noise ratio. Up to 7 ROIs were chosen per animal and each imaging session was kept under 2 hours. After imaging, the animal recovered on a heat mat before being returned to its cage.

Axons were tracked for up to 35 days after the initial session, for a total of 9 sessions (ethical limit) or until the cranial window was no longer optically clear (Figure 3.7).

3.3.6 Image analysis

3.3.6.1 Image processing

Image processing of *in vivo* imaging was carried out using the FIJI package for ImageJ (Schindelin et al., 2012; version 2.0.0-rc-43/1.51a) and a custom ImageJ macro. The macro allowed for automated processing of images for each ROI, carrying out the following functions: (1) alignment of the EGFP signal within a single z-stack to correct drift and application of the transformation to the TagRFP channel using the MultiStackReg registration plugin, (2) matching of z-stack sizes between timepoints by addition of blank slices, (3) alignment of z-stacks between timepoints in the x and y axes using maximum z-projections and the MultiStackReg plugin, (4) alignment of z-stacks in the z-axis using an edited version of the Correct 3D Drift plugin to only include the z-axis transformation. This resulted in a 5-dimensional (5D - XYZCT) stack of each ROI aligned to within 5 μm in x, y and z for both

channels across all timepoints. For presentation in figures only, images had brightness and contrast adjusted and a median filter (74 nm kernel) applied.

3.3.6.2 Data quantification

Axonal segments were traced using the segmented line tool with spline as part of a custom ImageJ macro script. Tracing was completed on a two-dimensional summed intensity projection of the z slices containing the axon of interest. Traces were used to estimate axonal segment length for analysis. After tracing at each timepoint, a minimum volume that encompassed the axon across all the timepoints was cropped from the original 5D stack. Every axon and region were uniquely labelled for easier indexing and handling of the data. Between 1 and 12 axonal segments were chosen from each ROI. Factors used to choose axonal segments were: good signal-to-noise (subjective measure by analyst), few crossing axons and existence in all timepoints.

Identification and indexing of presynaptic terminals and mitochondria were carried out manually on each cropped axonal segment using a custom ImageJ macro script and the multi-point tool. A gaussian blur (sigma = 2 pixels, 154 nm) was used to smooth the signal and presynaptic terminals were scored subjectively, using the local intensity profile as a guide (Figure 3.9). The position of each object (bouton or mitochondrion) was estimated from a point placed by the analyst.

Boutons were tracked across imaging sessions from the first timepoint they were identified. Boutons in separate timepoints were linked if they were in the same place relative to fiducial markers, including any crossing axons, kinked structure or other persistent boutons. Any bouton that was lost from the field of view for one timepoint (through a shift in alignment in x or y axes) was excluded entirely. All boutons were scored independently of the mitochondrial signal.

En passant boutons (EPBs) are larger in volume than the axon backbone and therefore have higher intensity relative to the backbone due to increased numbers of fluorescent molecules (cytosolic EGFP; Figure 3.10, 3.8). An EPB had to have contiguous pixels in the x-, y- and z-axes to ensure it was not the result of noise. The intensity profile of an EPB needed to include

sharp edges (relatively steep curve either side of peak) to exclude gentle changes in the axonal thickness. If the peak of an EPB was twice that of the local axon backbone (1.5 μm either side of the bouton) at any timepoint, the bouton was scored as being present (Figure 3.10). A bouton was scored as lost if it was below 1.3 times the local axon backbone. These criteria have been shown to be faithful indicators of synapse presence in correlative light and electron microscopy studies (Grillo et al., 2013; Song et al., 2016).

Terminaux boutons were scored as unilateral protrusions from the axon backbone with a bulbous appearance and sometimes consisted of a resolved thin neck that extended for less than 5 μm. Those extending for longer than 5 μm were considered to be axonal branches (Grillo et al., 2013).

A small proportion of boutons changed bouton type (*en passant* or *terminaux*) over the time series and so those boutons were classified based on their predominant type.

Mitochondria were identified as discrete objects 2x above the global median background signal (Figure 3.10), with contiguous pixels in the x-, y- and z-axes and steep edges to their intensity profile. The axonal EGFP signal was used to verify that each mitochondrion was inside the axon only after it was scored.

3.3.6.3 Data analysis

The final dataset was obtained from 12 animals in three different batches of littermates (Figure 3.7). A total of 51 ROIs and 306 axons were tracked for this study. The total number of mitochondria counted across all timepoints was 11,264 along with 4,892 unique boutons. Mitochondria were not tracked and indexed due to their ability to move between timepoints.

A small proportion of ROIs were first imaged at days one and two, rather than day zero. Most ROIs and animals were tracked for the entire imaging time series (Figure 3.7). However, some regions dropped out because of bone regrowth or dural thickening that obstructed the cranial window.

Some data were excluded from the final dataset. Any ROI that was too dim for accurate axon tracing (subjectively based on analyst experience) within the first four timepoints was not tracked. Axons were removed when the signal-to-noise in a session was low enough that the scorer could not be confident in bouton scoring. One animal that had only 2 axons tracked was also removed.

Relative ROI positions were calculated using a custom ImageJ macro. They were calculated using the relative x and y coordinates from the origin and the offset between the origin and the window centre (Figure 3.9).

Initial data analysis for mitochondrial and bouton measurements was completed using custom scripts in MATLAB. Large multivariate data tables were created, and new variables computed. Data was prepared and exported for statistical testing where appropriate in other software packages (see *Statistics* below).

Mitochondria were classified as being present at a bouton if the distance between their centroids (defined by a point placed by the analyst) was less than or equal to 1.5 μm. The distance of 1.5 μm was biologically-relevant because previously in the hippocampus a distance-dependent relationship had been seen up to 3 μm away using electron microscopy (Smith et al., 2016). A dichotomous variable (present or not) was chosen rather than a continuous variable (μm from nearest mitochondrion) because the axonal segment was a small sample of the axonal arbor and the true distance to the nearest mitochondria from each bouton could not be accurately measured, especially for boutons at the edge of the field of view.

Randomisation of bouton or mitochondrion positions was carried out to test the probability of obtaining the real distribution by chance. Randomisation was completed on a one-dimensional (1D) projection of the axon (Figure 3.20A). Axons were first plotted in two dimensions (2D) in MATLAB using interpolation from segmented line coordinates recorded in ImageJ. The length of the axon was then estimated using Euclidean distances and split in to segments of 74 nm in 1D, the original pixel size of the 2P images. The objects of interest were plotted to the closest segment of the 1D axon based on where they were in the 2D image.

This was calculated using the nearest neighbour of all the axon coordinates to the single set of object coordinates. The position of TBs and mitochondria inside TBs was poorly estimated by this procedure whereas other mitochondria and EPBs, which resided within the axon backbone, were very well estimated. Either mitochondria or boutons were then removed and randomly re-plotted along the axon without being placed closer than 1 μm together. Intervals of at least 1 μm were chosen to attempt to match the resolution limit with which two objects could be resolved using the 2P microscope in this study (Figure 3.18). This was repeated 1000 times for each axon and the range plotted, similar to Smit-Rigter et al. (2016).

Bouton or mitochondrial densities were plotted as the number per 10 μm because these values were more intuitive then per μm. Loss and gain densities were the number of boutons lost or gained within the time interval normalised to the axon length. The dynamic fraction of boutons was calculated as the proportion of unique boutons that were either lost or gained. Specifically, the sum of gains and losses divided by the total number of unique boutons across the two timepoints: (gained + lost)/(gained + $total_{time1}$).

3.3.7 Statistics

A priori power calculations were performed in G*Power software (Faul et al., 2007) to calculate the number of newly-formed boutons (New_{early}; Figure 3.22) required to detect a 10% difference in survival between two mitochondrial conditions. This calculation resulted in an estimate of 450 newly-formed boutons. The number of animals required to achieve this was estimated from pilot studies to be 10-15 animals. In this study, 21 animals were used, 15 were imaged and 12 produced high quality data that was included (see exclusion criteria in *Data analysis*).

Statistics were calculated using appropriate software for the complexity of the test. MATLAB (release 2016a), GraphPad Prism 7 and SPSS were used.

If the distribution of data was non-normal, as assessed by the Shapiro-Wilk test, attempts were first made to restore normality by transformation. Transformation retained relative differences in the data but changed the shape of the distribution of values to fit the assumptions of parametric tests. Depending on the degree of skewness, different

transformations were used. The square root was taken for slightly positive skews, and $\log_{10}$ taken for stronger positive skews. If no transformation could restore normality, the data was run through a less informative non-parametric test.

The length of axonal segments analysed in this study (Figure 3.11) resulted in artificially low bouton and mitochondrial densities when zero mitochondria or boutons were present. These outliers were removed to return the distributions back to normality for parametric tests.

Error bars were either standard deviation (SD) for normally-distributed data, inter-quartile range for non-normal data, 95% confidence intervals for proportions or the range for the distributions of nearest neighbour distances in Figure 3.20. Statistical significance was set at $p < 0.05$. Confidence intervals for proportions were calculated using the formula for single samples. The z value for a 95% coverage of a gaussian distribution is 1.96. Therefore, the CI is $+/- z*\text{sqrt}(\text{prop}_1*(1-\text{prop}_1)/N)$, where prop_1 is the proportion, z is 1.96, N is the number of samples in the population.

Only axons present in all relevant timepoints were analysed for repeated measures statistical tests to match group sizes. To avoid pseudoreplication, samples were not pooled together from repeated measures for comparisons of e.g. proportions, instead the first timepoint was taken for comparisons.

One-way repeated measures ANOVA was used to compare means across groups/time. The Friedman test was used for comparing distributions of non-normally distributed repeated measures data. The independent t-test was used to compare means of two independent groups of normally distributed data. The Mann Whitney U test was conducted to compare distributions between two independent groups of non-normally distributed data. A two-sample Kolmogorov-Smirnov test was used to determine if two distributions could be sampled from the same distribution.

Correlations were tested using either Pearson's for normally distributed and linearly correlated data, or Spearman's for non-normal, monotonic data. Trend lines were only plotted in normally distributed data that assumed a linear correlation. A Gaussian mixture model was

used to calculate posterior probabilities (0 to 1) of axons being in groups based on EPB and TB densities. This was based on an assumed number of gaussian components defined by the user. Axons that fell under the threshold of 0.7 probability for both groups were not assigned a group.

The Chi-square test of independence or Fisher's exact test were used to compare proportions between two independent groups. Fisher's exact test was used when N numbers were below 200 for at least one group. Cochran's Q test was used as a test for trend in proportions over time for repeated measures data.

Kaplan-Meier curves were created for survival analysis, based on time-to-event data. For bouton survival, this was the time from first observation until the bouton was no longer observed. Boutons that were no longer observed due to reasons other than loss were classed as "censored". A log rank (Mantel-Cox) test was used to compare survival of two independent populations where the survival curves did not cross. The Cox proportional hazards regression test was used with time-varying covariates to determine if covariates (mitochondrial presence) influenced survival (Therneau et al., 2018).

3.4 Results

3.4.1 Targeting and characterising the motor-somatosensory axonal projection

To enable visualisation of axon structure and resident axonal mitochondria, cytosolic EGFP and mitochondrially-targeted TagRFP were expressed in motor cortical neurons by infection with a custom AAV (Figure 3.1A, B). Expression of the bicistronic construct was driven by a human Synapsin promoter, which is only active in neurons. Furthermore, the serotype used (AAV 2/1) is highly neurotropic. Therefore, the infection strategy was predicted to drive expression in motor cortical neurons that project long-range axons into somatosensory cortex (Petreanu et al., 2009), where they could be imaged through a cranial window. Two-photon *in vivo* imaging was carried out in anesthetised animals using two near-infrared lasers set to 920 nm (EGFP) and 1040 nm (TagRFP) for simultaneous excitation of both fluorescent proteins. Detection using spectrally separated filters resulted in very little (< 3.5%) overlap between the two PMT channels (Figure 3.2).

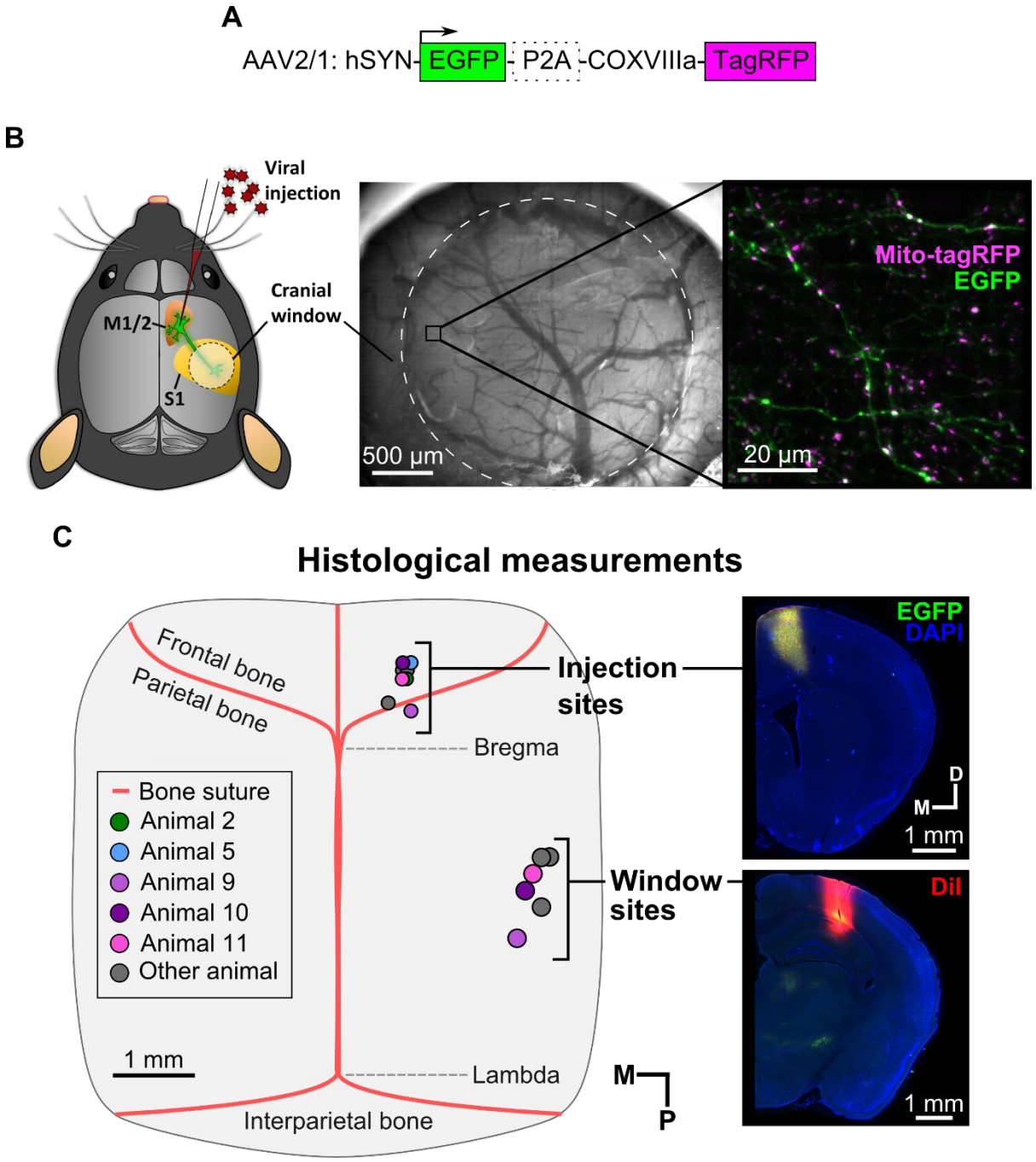

Figure 3.1 Intracranial viral injection and cranial window implantation. (**A**): Bicistronic adeno-associated virus (*AAV2/1*) used for labelling neurons. Human synapsin promoter (*hSYN*) limited expression of cytosolic enhanced green fluorescent protein (*EGFP*) and mitochondrially-targeted red fluorescent protein (*COXVIIIa-TagRFP)* to neurons. EGFP and COXVIIIa-TagRFP were separated by porcine teschovirus 2A peptide (*P2A*) that cleaved after translation. (**B**): (*Left*) virus injected in to the motor cortex (M1/M2) and axonal projections visualised in the somatosensory cortex (S1) through an implanted cranial window (*dashed circle*). (*Centre*) reflected light from the brain surface showing vasculature (*dashed circle* = skull outline). (*Right*) example of a region visualised using two-photon microscopy. (**C**): (*Left*) estimated positions of viral injection sites and window centres on the skull surface. Different animals are identified by colours (*other animal* = pilot animal). (*Right*) example histological widefield fluorescence images of coronal brain sections showing an estimated injection site (*top*) and window centre (*bottom*). M = medial, P = posterior, D = dorsal.

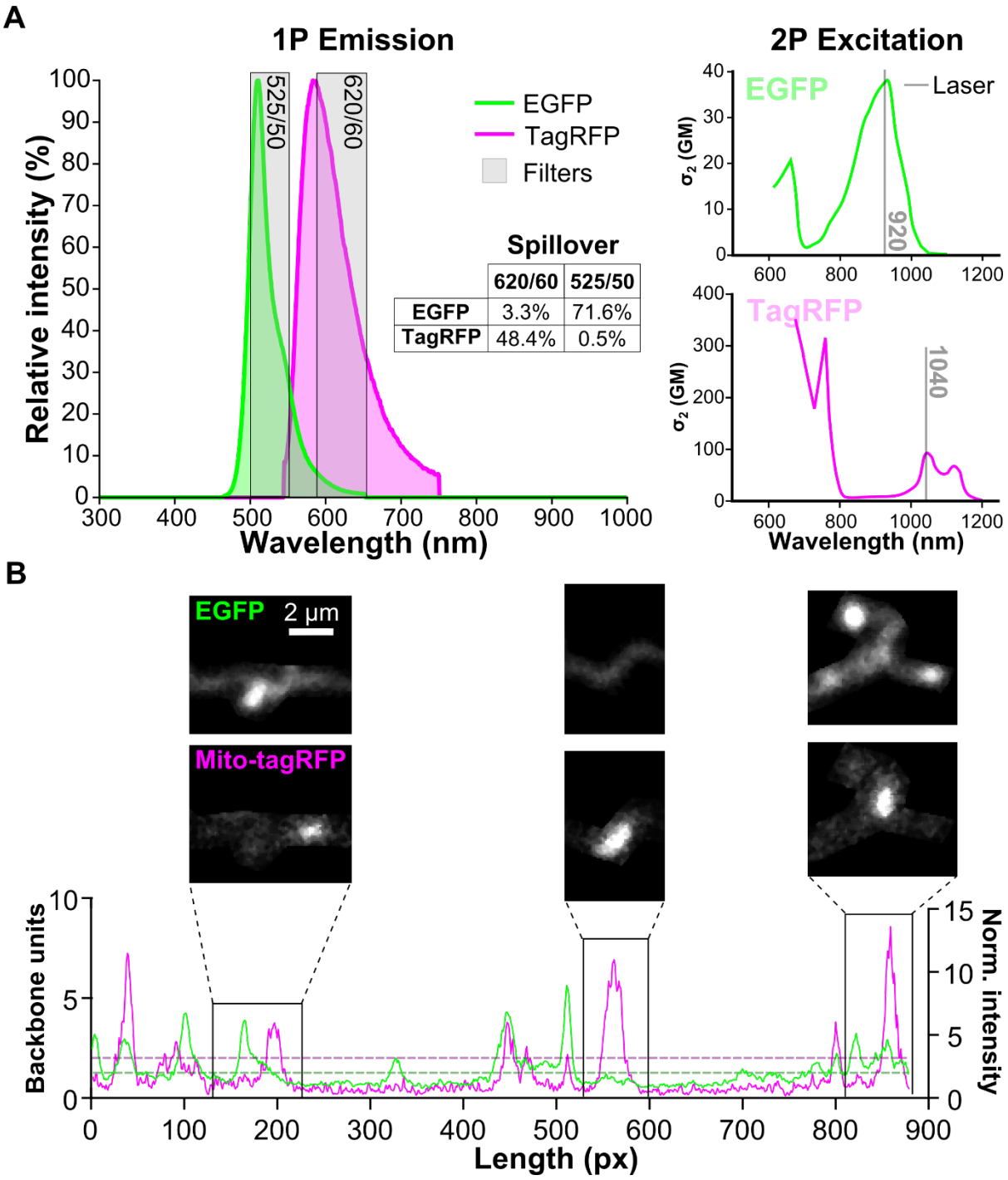

Figure 3.2 Simultaneous dual-colour two-photon imaging. (**A**): (*Left*) one-photon (1P) emission spectra of EGFP and TagRFP fluorescent proteins showing spectral overlap. The bandpass of the PMT filters are shown with the grey boxes. Filters were chosen to prevent bleedthrough from each of the fluorescent proteins in to the wrong channel. The proportion of intensity spillover is indicated in the table. (*Right*) two-photon (2P) excitation spectra for EGFP and TagRFP. Two Ti:Saph lasers were used to excite at local peaks in the infrared part of the excitation spectrum for each fluorophore, indicated by vertical lines and wavelengths indicated in nm. (**B**): (*Bottom*) intensity profiles are plotted from the EGFP signal (*green*) in backbone units using a local median threshold (left axis) and the TagRFP signal (*magenta*) in normalised intensity units using a global median filter (right axis). (*Top*) Crops of an axon from a sum-projected 2P image with a gaussian blur filter (sigma of 2 pixels, 148 nm) showing a lack of correlation and bleedthrough between the two channels.

Pilot studies were carried out on six animals to optimise infection/expression and imaging strategy, and assess presynaptic bouton turnover rates, which were undocumented in these long-range axons. Stereotaxic coordinates for viral injections were measured from pilot experiments and standardised for all future experiments (Figure 3.1C). A final injection site of +0.7 mm lateral (right-hand side) and +1.0 mm anterior of Bregma was used to target the primary and secondary motor cortices (M1/M2). Different titres of viral particles were used to alter multiplicity of infection (viral particles per cell). The density of labelled axons in layer 1 of the somatosensory cortex was assessed using empirical judgement of density in two-photon images taken through the cranial window of each animal (Figure 3.3). A viral titre of 1×10^{13} particles/mL was settled upon as it resulted in 5–10 axons with suitable expression in each volume of images (76 x 76 x 30 μm) that would be used throughout the study to capture regions of interest (see *Methods* section for further information).

Window site coordinates were estimated post-hoc from histology using a needle coated in DiI that was pierced through the window centre (Figure 3.1C). The cranial windows covered most of the right parietal bone of the skull with a diameter of 3–4 mm. The area of the brain under the window was mainly primary somatosensory cortex as well as some areas of parietal and primary visual cortex.

Histology was carried out to assess the architecture of the projections emanating from the motor cortex. Cells were labelled across all layers of the motor cortex with cortical and subcortical projection patterns (Figures 3.4 and 3.5). The cortico-cortical projections were of interest to us in this study (Oswald et al., 2013). Histological analysis of whole, cleared brain showed that cortico-cortical projections appeared to emerge from layer 5/6 and traverse above the white matter, separate from the subcortical projections (Figure 3.6). Relatively sparse axonal arbors also lay through layer 1 and layer 2/3, but were not as strong as the layer 5 signal (Figure 3.7). Layer 5/6 projections sent collaterals dorsally once they reached somatosensory cortex and appeared to vastly outweigh any signal from layer 1 projections (Figures 3.4 and 3.5). These projections were therefore characterised as long-range (3–4 mm estimated length) motor-somatosensory cortical projections.

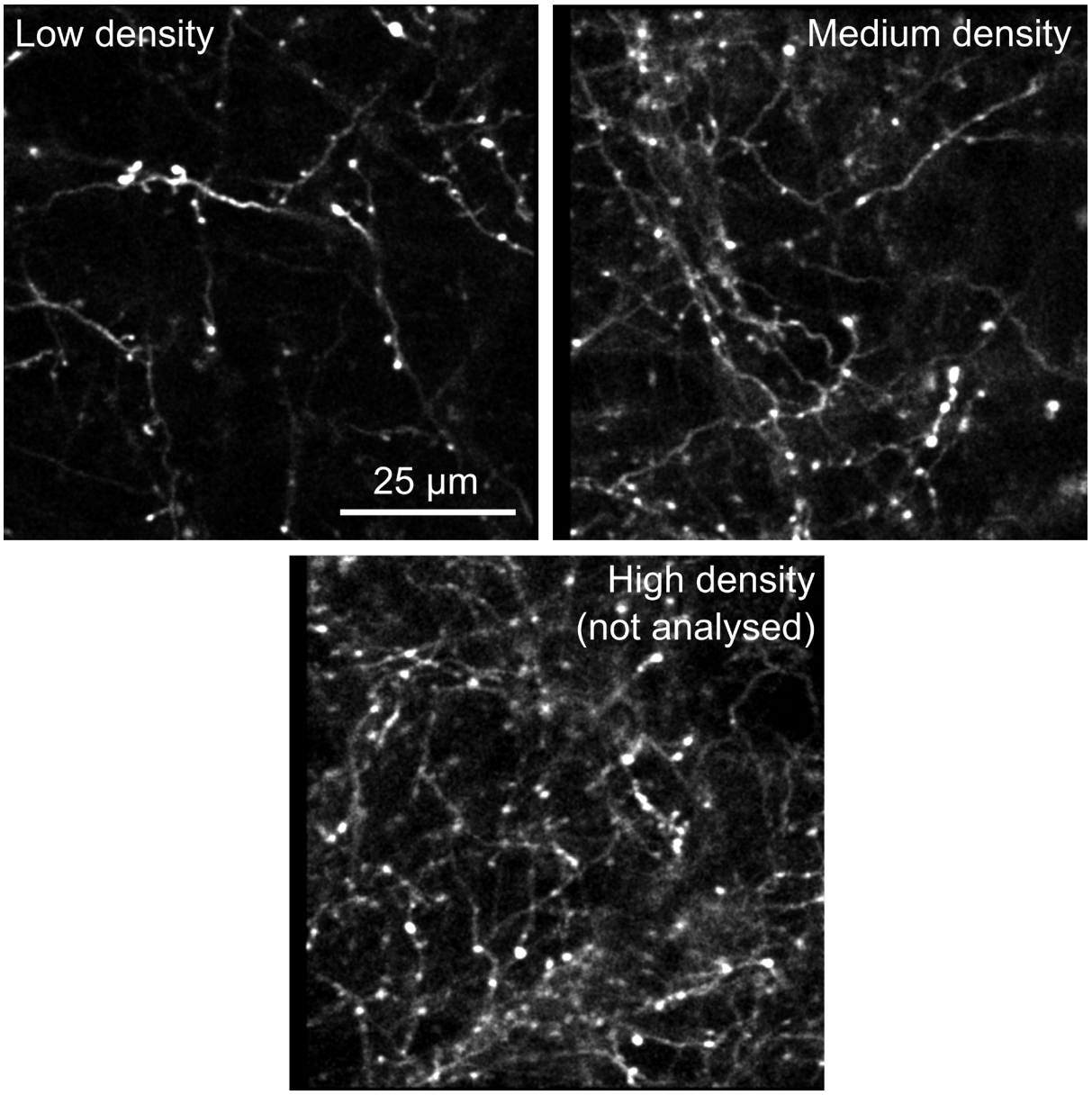

Figure 3.3 Empirical judgement of density. Three example two-photon images of a slice from a z-stack in virally-labelled axons. The least dense field of view (FOV) would yield the most segmentable axons, whereas the most dense FOV results in impossible segmentation and analysis.

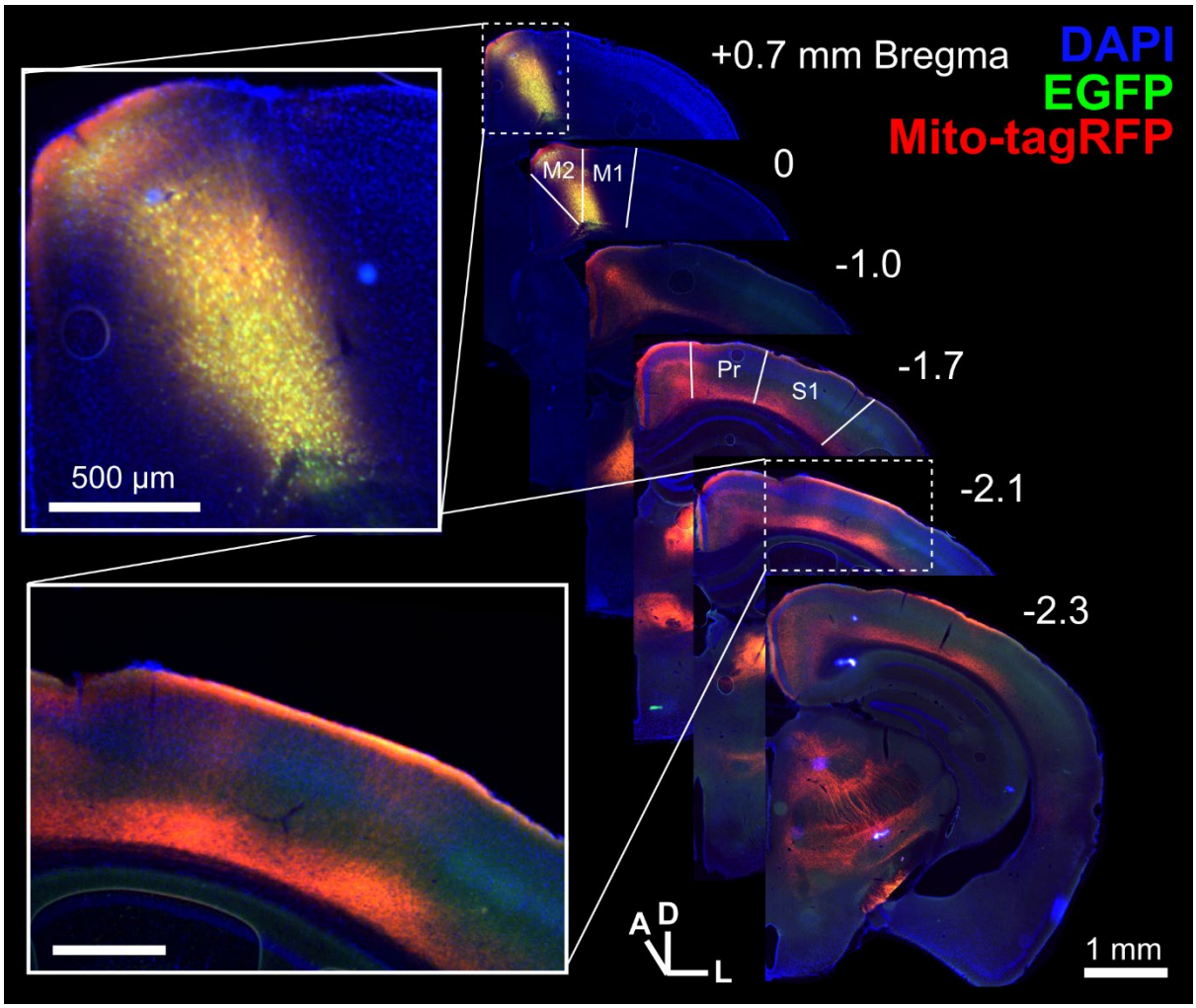

Figure 3.4 Coronal histology of motor cortex projection architecture. Representative widefield fluorescence images of 50 µm coronal sections showed a strong projection from primary and secondary motor cortex (M1/M2) to primary somatosensory cortex (S1) and parietal cortex (Pr) as well as subcortical projections. EGFP signal in axons appeared weak due to quenching and background fluorescence in the same channel. TagRFP that was localised to the mitochondria was used to determine the projection pattern. (*Insets*) zoom of estimated injection site centre showing labelling of cells across all layers (*top*) and zoom of estimated window site (notice slight swelling) showing layer 6 collaterals projecting to layer 1. A = anterior, D = dorsal, L = lateral.

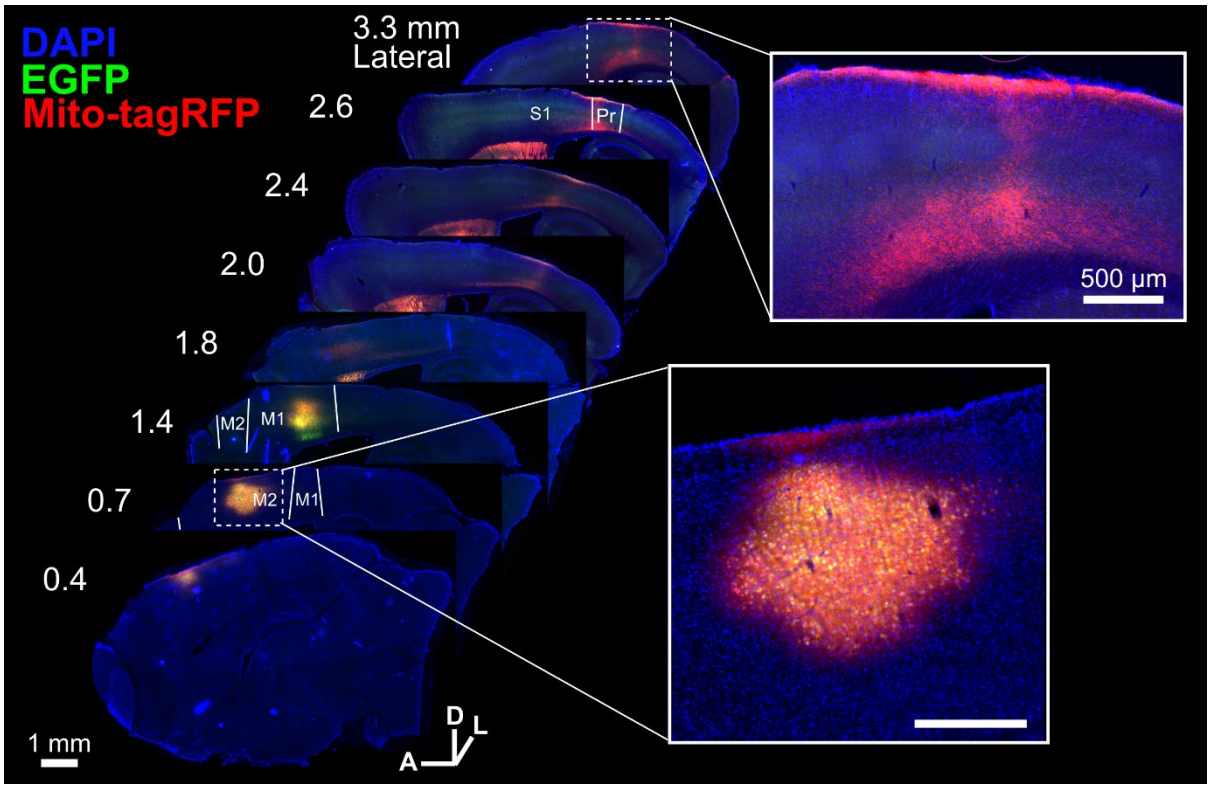

Figure 3.5 Sagittal histology of motor cortex projection architecture. Representative widefield fluorescence images of 50 µm sagittal sections showed a strong projection from primary and secondary motor cortex (M1/M2) to primary somatosensory cortex (S1) and parietal cortex (Pr). The projection can be seen to run along layer 6 of the cortex, above the white matter, until turning dorsally to arborise in layer 1 in the more lateral sections. (*Insets*) zoom of estimated window site showing strong mito-tagRFP signal in layer 1 (*top*) and zoom of estimated injection site showing labelled cells in motor cortex, notice that the injection site is cut at an angle. A = anterior, D = dorsal, L = lateral.

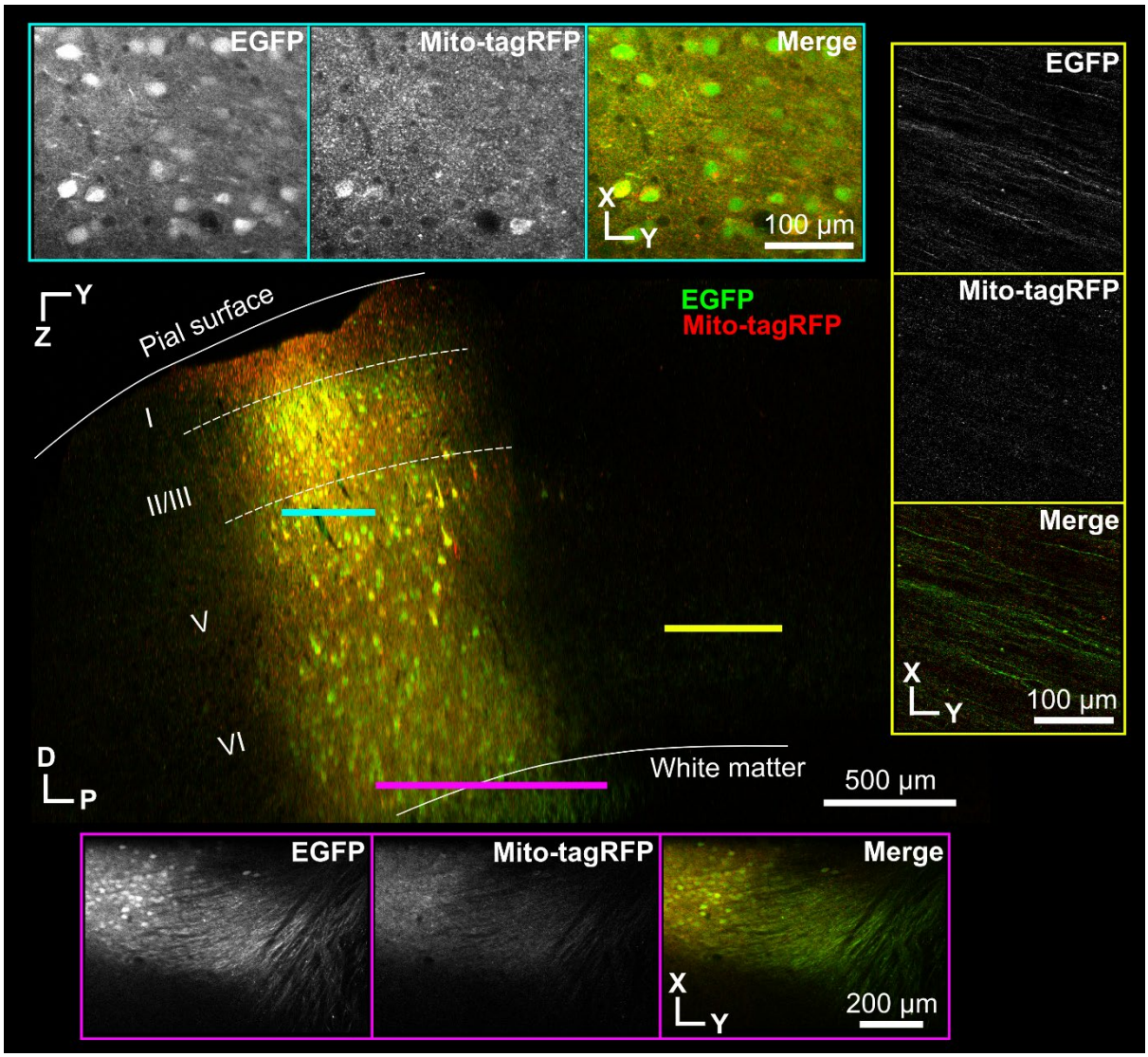

Figure 3.6 Analysis of projection architecture from cleared brain tissue. Two-photon image re-sectioned in the sagittal plane from an intact cleared whole brain showing cells labelled throughout the cortical layers (numerals) of the motor cortex and their axonal projections. Coloured lines indicate where the cross-sections from the insets are taken. (*Insets*) cells in the injection site express both EGFP and mito-tagRFP (*top*, *cyan*). Axons that emanated from the lower layers of the cortex project down in to the white matter (*bottom*, *magenta*). A relatively sparse projection from layer V and VI project posteriorly, far above the white matter (*right*, *yellow*). D = dorsal, P = posterior.

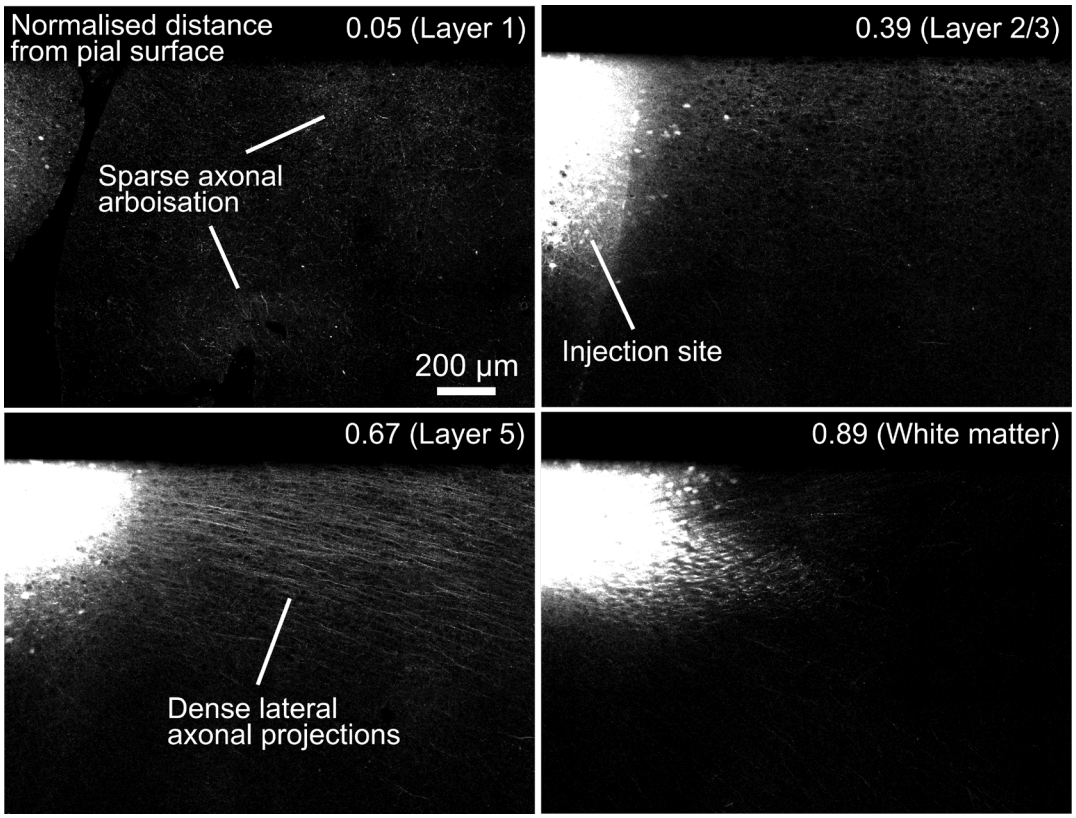

Figure 3.7 Projection pattern from labelled cells in motor cortex. Two-photon images through motor cortex in cleared brain tissue. (*Top-left*): Layer 1 sparse axonal arborisations did not look directed towards somatosensory cortex. (*Top-right*): Sparse arborisations in layer 2/3 seen at the top of the image. (*Bottom-left*): Very intense striations from layer 5 indicating a strong projection heading towards somatosensory cortex. (*Bottom-right*): At the bottom of the labelled cells, axons delve in to the white matter**.** The normalised distance from the pial surface was used to measure the depth and infer cortical layers.

3.4.2 Experimental design and data collection

To measure the dynamics of their structural plasticity, superficial axonal projections were tracked at daily and weekly intervals over the course of one month (Figure 3.7B, C, D and 3.8). Changes in the number and position of presynaptic terminals (boutons) and mitochondria were recorded, as well as the longevity of individual boutons. Previous studies showed that newly-formed boutons of pyramidal neurons in the neocortex have a low survival rate (Grillo et al., 2013; Qiao et al., 2015; Ash et al., 2018). Since structural plasticity of this axonal projection had not been previously documented, a pilot study of six animals was used to measure the rate of new bouton formation and survival. The results provided estimates for the effect size used in *a priori* statistical power calculations of the main study, which looked at effects of mitochondrial colocalisation on bouton longevity (see *Methods*).

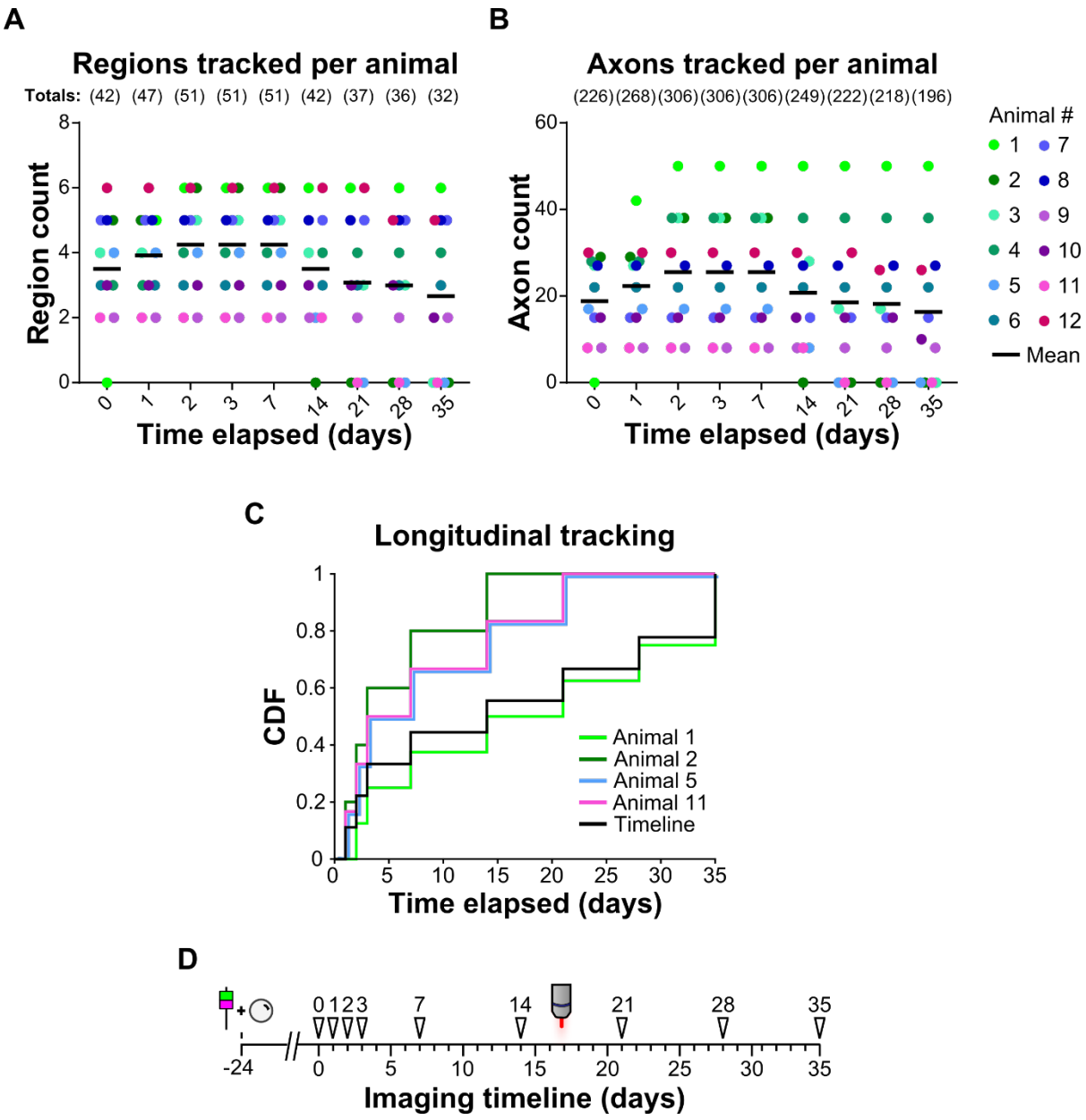

Figure 3.7 Distribution of data and longitudinal tracking. (**A** and **B**): Number of regions (A) and axons (B) tracked per animal (coloured dots; see legend) at each time point. Totals are indicated for each timepoint in brackets above the graphs. The mean for each time point is indicated with a black horizontal line. (**C**): Cumulative distribution function (CDF) for the imaging time course of each animal. Most animals are within the imaging paradigm timeline (*black line*; D). Some animals deviate from this line, e.g. they were first imaged later than day 0 (e.g. animal 1) or were not imaged at later time points (e.g. animal 2). (**D**): Viral intracranial injection and cranial window implantation were carried out 24 days prior to commencement of imaging. From day 0 to 3, animals were imaged with 24 h intervals to identify newly-formed boutons. From day 7-35, animals were imaged with 7-day intervals to track long-term stability of boutons.

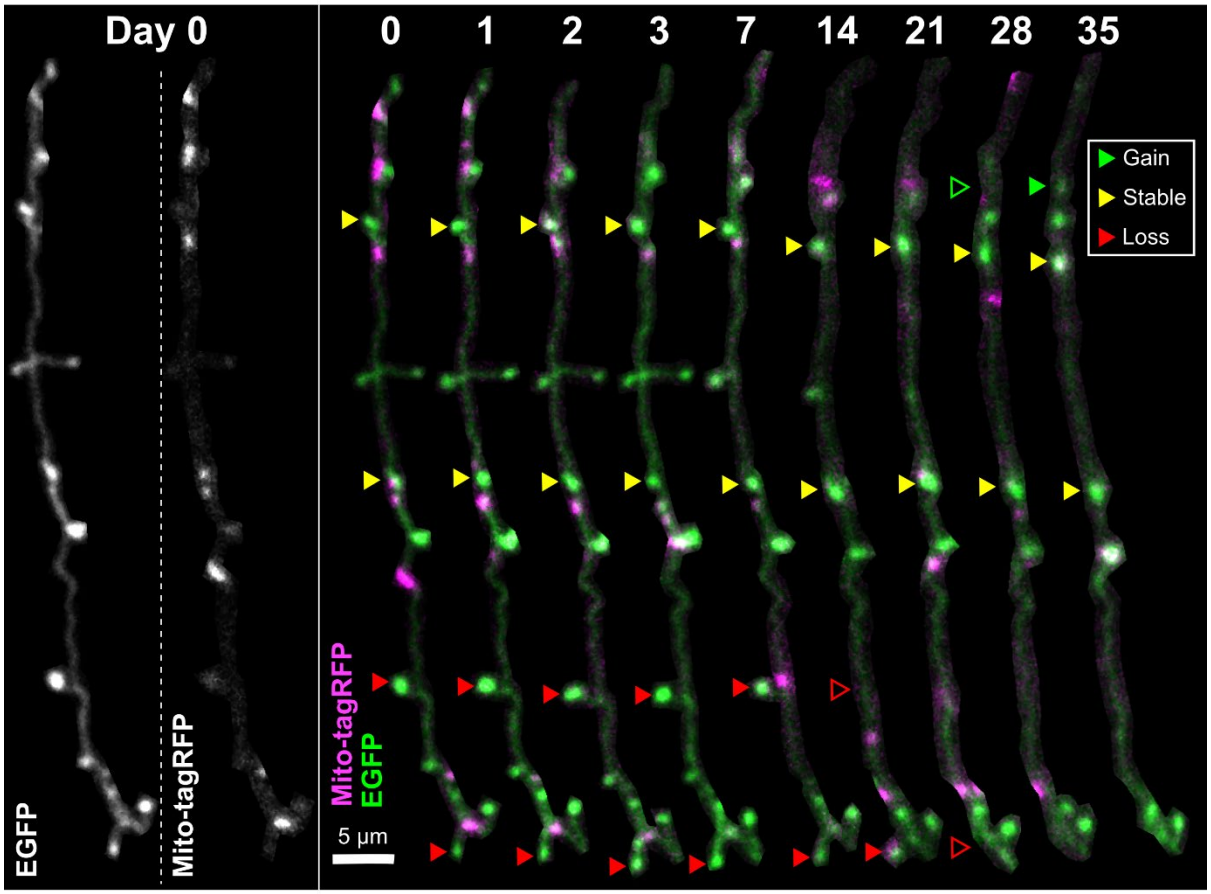

Figure 3.8 Longitudinal tracking of axonal structure and mitochondrial positioning. Example two-photon images from a single axon tracked for daily and weekly intervals over 35 days (time points indicating above). Both axon structure (EGFP) and mitochondria (Mito-TagRFP) were tracked. Some dynamics have been indicated. Red arrowhead = loss, green arrowhead = gain, yellow arrowhead = stable. Images have been cropped and edited with a median filter to lower noise and increase contrast for presentation.

A total of 12 animals were used in the main study, over three different batches of littermates from a wildtype genetic background (C57Bl/6). Between two and seven regions were chosen for each animal, resulting in between 8 and 54 axons in total for each animal (Figure 3.7A, B). Regions were chosen based on EGFP expression level, density of axons in the field of view and distance from other regions to get a diverse sample with easily identifiable axonal structures (Figures 3.9). Subsequently, repeated image stacks of the region over time were registered and aligned to allow tracking of the same structures over time (see *Methods*). The axonal segments chosen for analysis were based on criteria such as the level of expression and number of crossing axons, factors which affect the ability to trace the axon reliably.

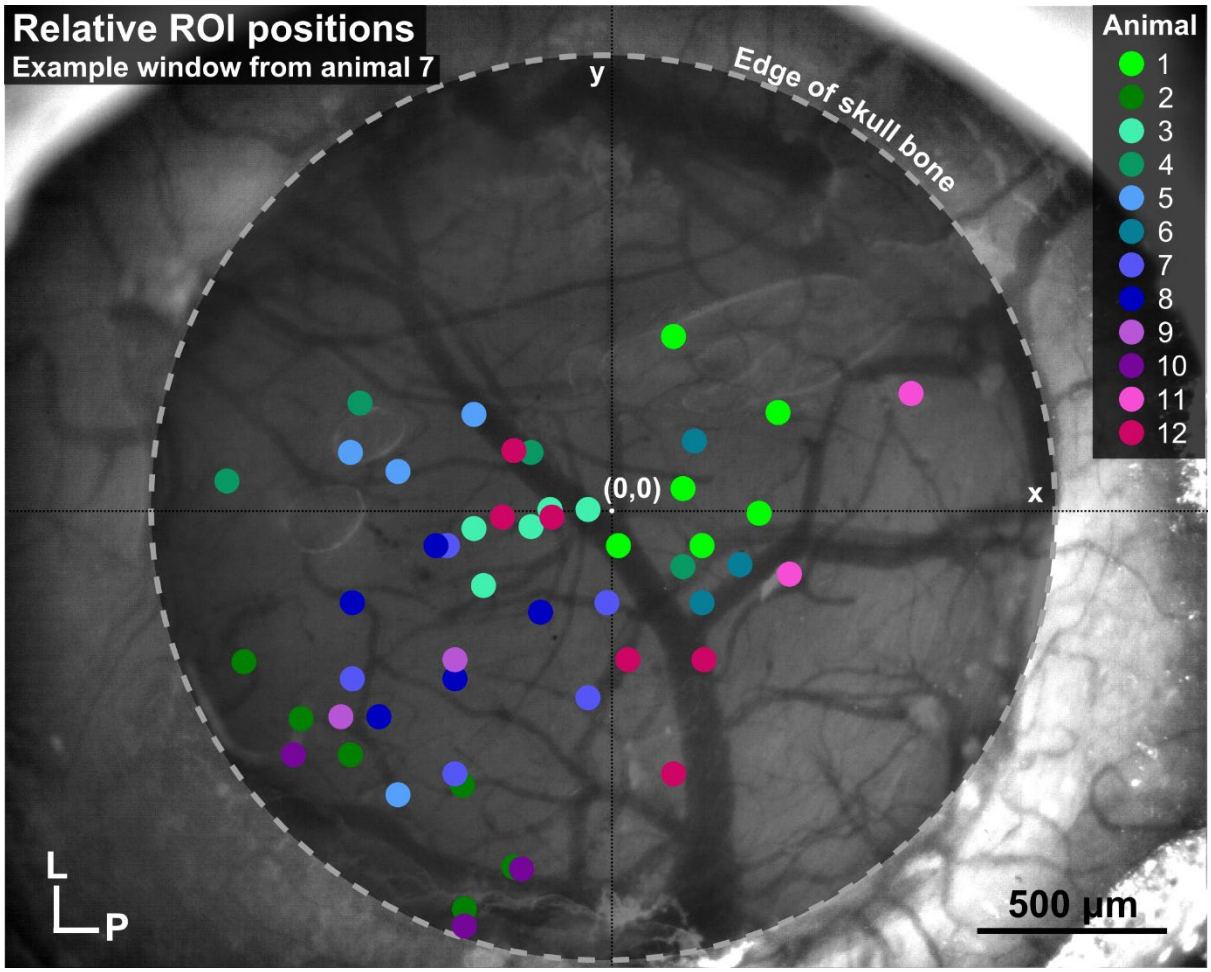

Figure 3.9 Relative positions of all regions captured. A representative brightfield image of a cranial window from animal 7 is shown with estimated region positions plotted from all animals in the imaging study. Positions were calculated using the offset between the origin point for the region coordinates and the centre of the window. Each animal is plotted in a separate colour (see legend). L = lateral, P = posterior.

Boutons and mitochondria were quantified from two-photon images manually using strict criteria (see *Methods* section; Figure 3.10). The field of view for images was 76 x 76 µm and so axonal segments were relatively small samples of the overall axonal arbor. The minimum axonal segment length was 31.4 µm and the maximum was 116.5 µm, with the mean being 72 µm +/- 15 (SD; Figure 3.11). The total number of axons tracked was 306, with 4,892 unique boutons and 11,264 mitochondria. The mitochondria were not indexed and tracked as they were mobile and could undergo fusion and fission (Youle and van der Bliek, 2012), which resulted in reduced individuality.

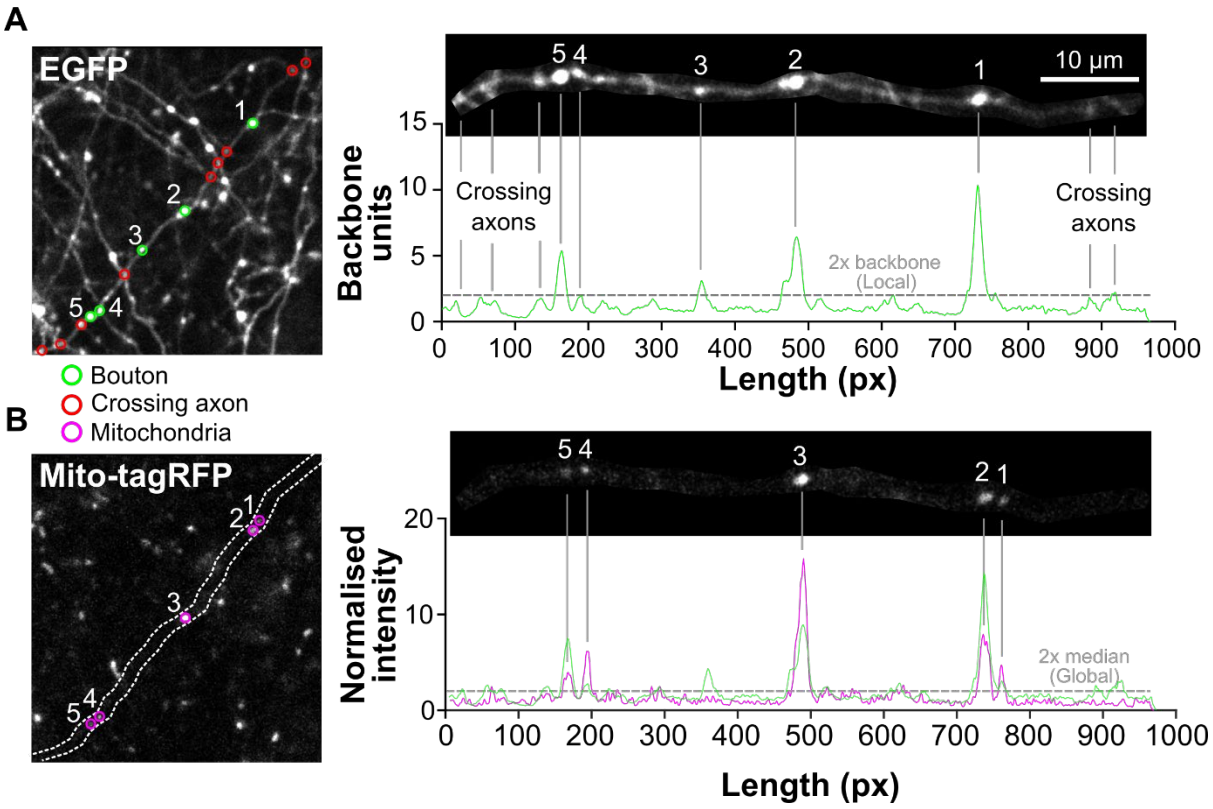

Figure 3.10 Identification of axonal boutons and mitochondria. (**A**): (*Left*) sum projection of an example EGFP two-photon stack around an axon of interest. Boutons and crossing axons are indicated (see key). (*Right*) an intensity profile is used to illustrate the identification of boutons based on the EGFP intensity crossing a 3 µm local median threshold (*dotted line*), measured in axon backbone units. Crossing axons are difficult to distinguish in an intensity profile, but relatively easy in a 3D image stack. (**B**): (*Left*) similarly, the sum projection of the tagRFP channel is shown, with mitochondria identified and the axon backbone approximately demarcated (*dotted lines*). (*Right*) identification of mitochondria was done based on TagRFP intensity crossing a threshold of 2x the global median. Manual counting of boutons and mitochondria was done using ImageJ and intensities inspected using the cursor. The EGFP channel was checked after identification to ensure mitochondria were within the axon of interest.

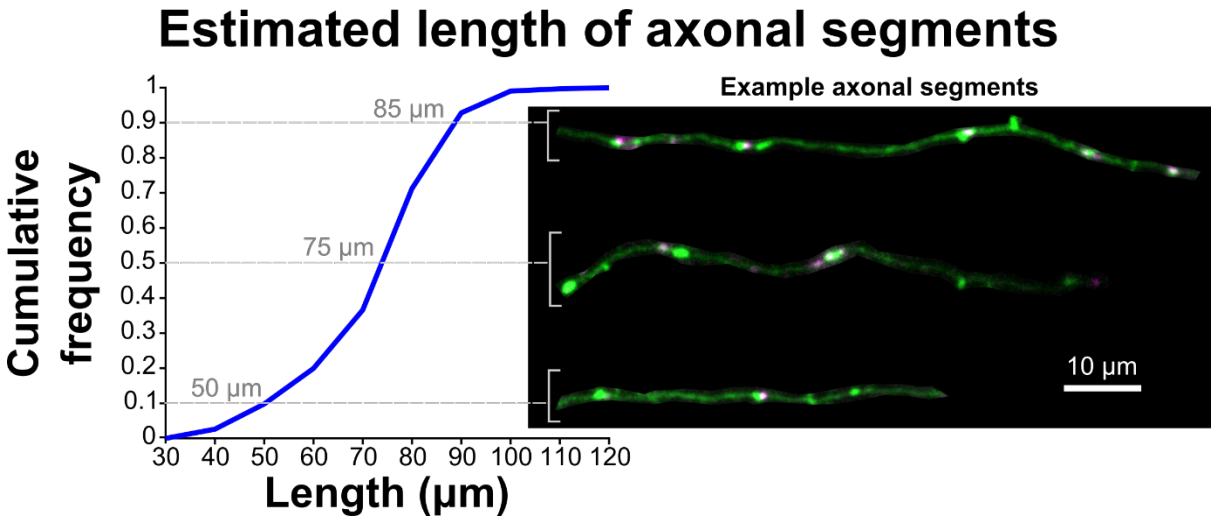

Figure 3.11 Distribution of axon segment lengths. Axonal segments were a small proportion of the whole axon. The length of each axon was calculated from a 2D line drawn by hand. The cumulative distribution of axonal segment lengths is shown here. Example two-photon images of axons are shown (*right*) that are representative of 90% of the overall pool of axons (n = 306), from 50 to 85 µm (*bottom to top*). Two-photon images have been cropped and a gaussian blur (sigma = 2 pixels, 148 nm) applied for presentation only.

3.4.3 Axonal bouton density variability

In previous studies of axonal structural plasticity, presynaptic bouton density remained remarkably consistent across time in a variety of cell types (De Paola et al., 2006; Majewska et al., 2006; Grillo et al., 2013; Stettler et al., 2006; Qiao et al., 2015; Mostany et al., 2013). The number of boutons per unit length was measured across time for axons present at all timepoints. As a population, all of the axons and animals in this study had a mean bouton density of 1.1 +/- 0.4 (SD) per 10 µm (Figure 3.12A), equivalent to 1 bouton every 9 +/- 3 µm. The mean bouton density of the population varied by a very small, but significant amount across time (one-way repeated measures ANOVA; $F(4.4, 593.1) = 3.413$, $p = 0.007$; Figure 3.12A). Pairwise comparisons revealed a significant dip of 0.12 per 10 µm at 35 days relative to days 0 and 3 (Bonferroni post-hoc test, $p = 0.032$ and 0.011 respectively; Figure 3.12A). This was equivalent to a loss of 1 bouton per 83 µm of axon. The effect size (Cohen's d) was very small (11%), meaning the difference in means was small in comparison to the variation.

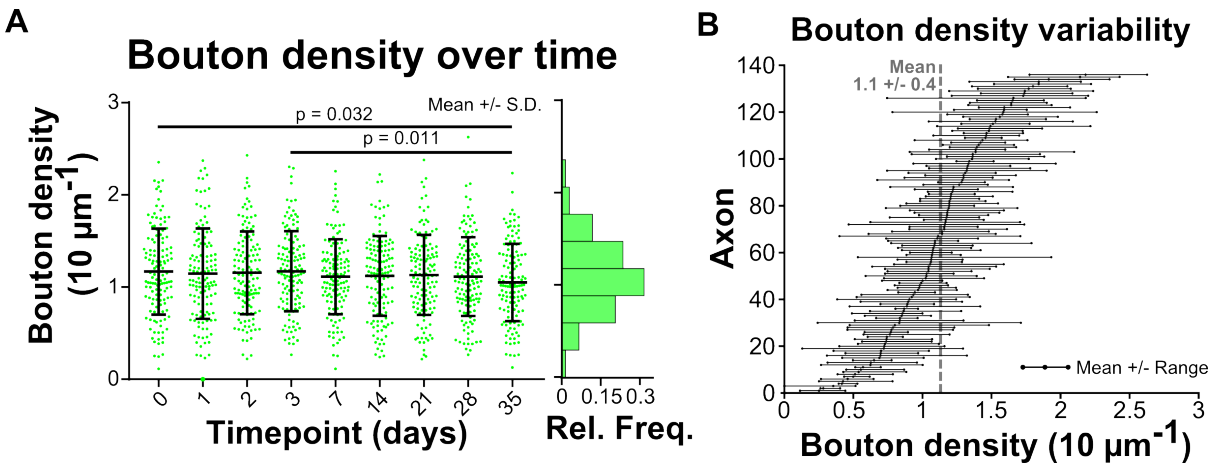

Figure 3.12 Bouton density was mostly consistent across time. (**A**): The population of axons that were present for all time points (n = 136 axons) had their bouton density plotted at each timepoint (*green dots*). The relative frequency of all bouton densities is plotted (*right*). (**B**): Each axon that was present in every time point had their mean bouton density plotted (*central mark*) and the range indicated (*horizontal line*). The axons were sorted by their mean bouton densities.

Within individual axons the variability in bouton density was also relatively low (Figure 3.12B), including axons from the whole range of mean bouton densities.

3.4.4 Axonal mitochondrial density variability

Mitochondria can mobilise in the axons of adult mice (Smit-Rigter et al., 2016; Lewis et al., 2016), unlike boutons. Therefore, the mitochondrial density was measured to compare the variability to bouton density. The number of mitochondria per unit length were measured across time for axons present at all timepoints. The mean mitochondrial density in axonal segments was 0.7 +/- 0.2 (SD) per 10 µm (Figure 3.13A), equivalent to 1 mitochondrion every 14 +/- 4 µm. The mean mitochondrial density of the population also varied by a small amount over time (one-way repeated measures ANOVA: $F(6.5, 825.6) = 6.716$, $p < 0.0005$; Figure 3.13A). Pairwise comparisons revealed a significant dip of between 0.09 and 0.13 per 10 µm at timepoints 3 and 4 (Figure 3.13A). This was equivalent to a difference of 1 mitochondrion per 77 and 111 µm of axon (Bonferroni post-hoc test: $p = 0.044$ to < 0.0005). The effect size (Cohen's d) was small (30-40%).

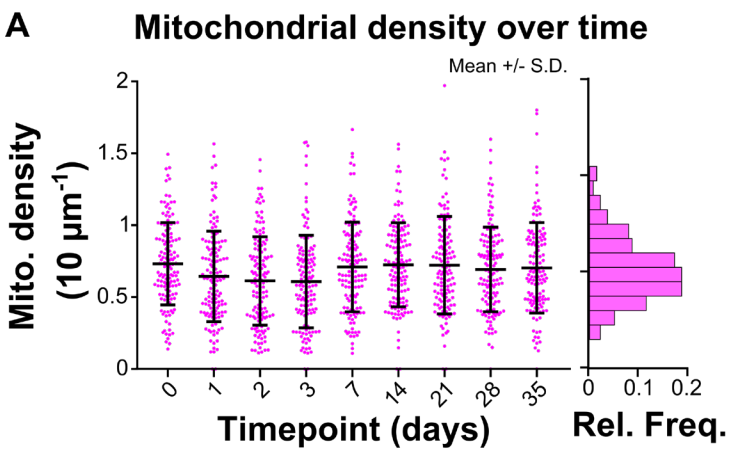

Comparison	p-value
Day 3 to day 0	<0.0005
3 to 5	0.007
3 to 6	<0.0005
3 to 7	0.002
3 to 9	0.044
4 to 1	0.001
4 to 5	0.006
4 to 6	<0.0005
4 to 7	0.005

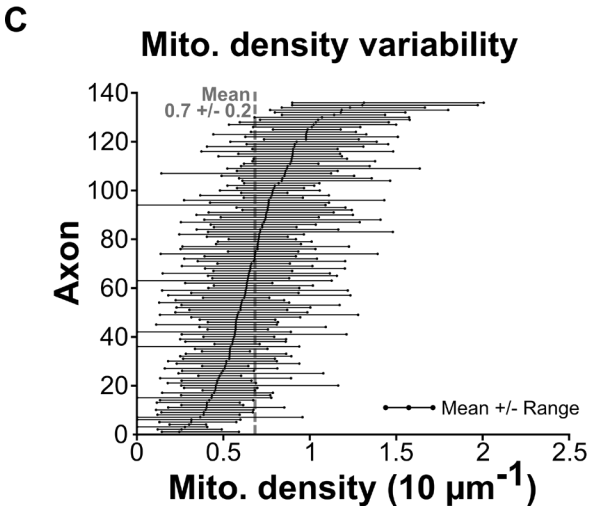

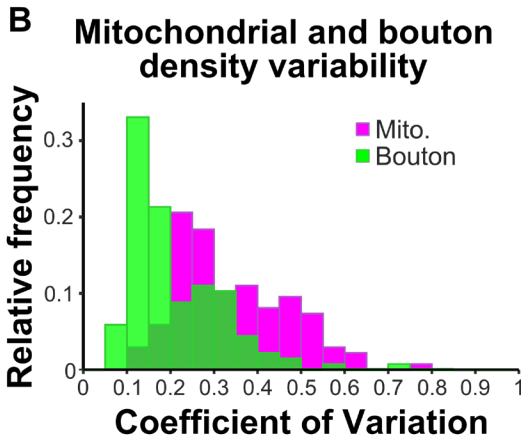

Figure 3.13 Mitochondrial density was more variable than bouton density. (**A**): The population of axons that were present for all time points (n = 136 axons) had their mitochondrial density plotted at each timepoint (*magenta dots*). The relative frequency of all mitochondrial densities is plotted (*centre*). The p-values for comparisons between timepoints are listed in the table. (**B**): The coefficient of variation of the densities was calculated for each axon across time and the distribution of these values was plotted for bouton densities and mitochondrial densities for comparison. (**C**): Each axon present in every time point had their mean mitochondrial density plotted (central mark) and the range indicated (horizontal line). The axons were sorted by their mean mitochondrial densities.

Within individual axons, the variability of mitochondrial density was considerably higher than bouton density (Figure 3.12C and 3.13C). The median coefficient of variation (CV; calculated as SD divided by the mean) was 0.31, meaning the variation in mitochondrial density over time for the average individual axon was only 31% of their mean mitochondrial density (Figure 3.13B). The distribution of CVs was non-normal, so some axons did have a much higher variation in mito density over time (Figure 3.13B); comparatively, the median coefficient of variation was 0.17 for bouton density.

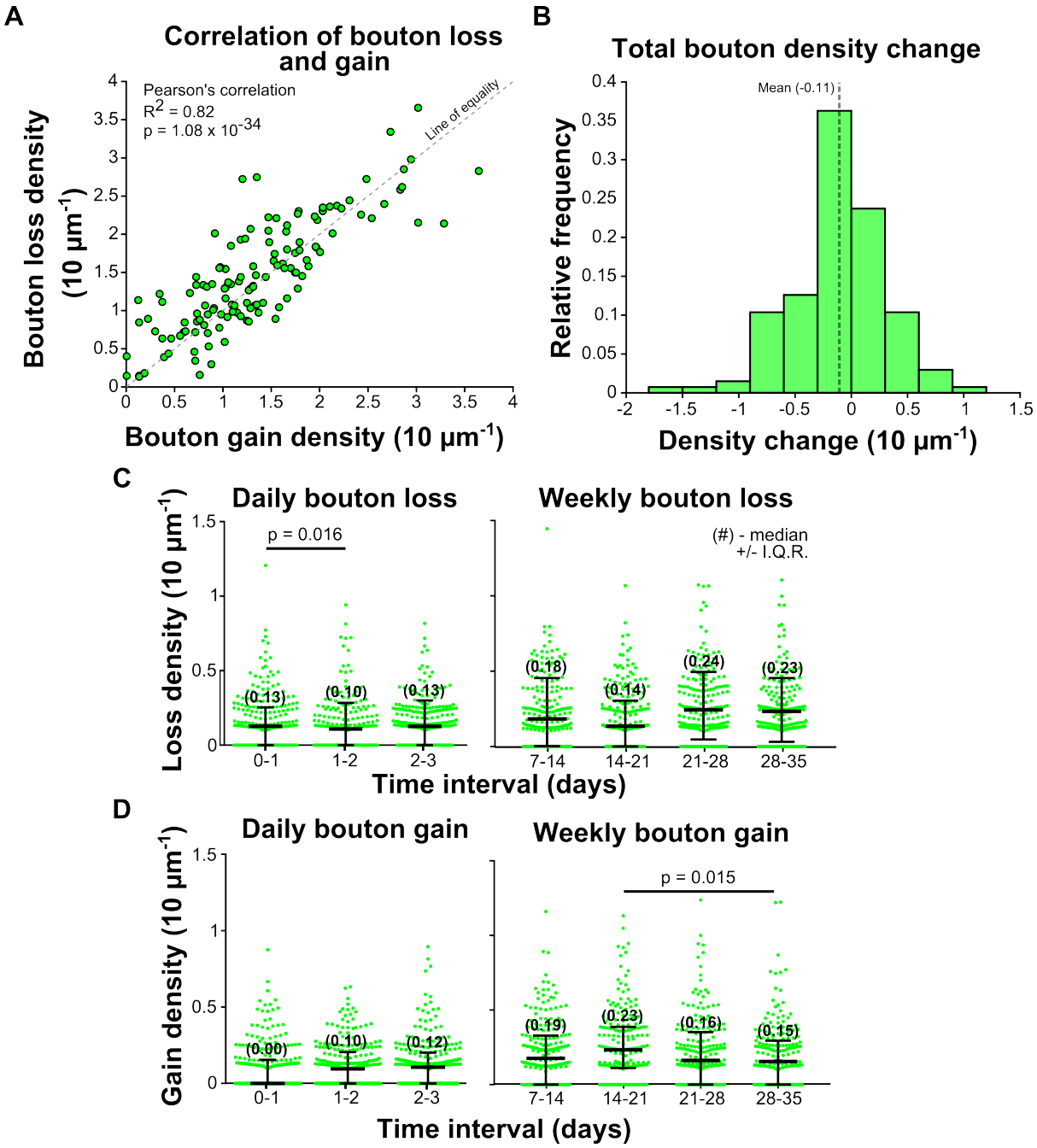

Figure 3.14 Bouton loss and gain was matched across time. (**A**): Axons present in all timepoints (n= 135) had their total number of boutons lost or gained over the entire time course plotted against each other. The numbers were plotted as a density to normalise for axon length differences. The line of equality is shown with a dashed line. (**B**): Bouton loss and gain was summed for each axon (n = 135) and the distribution of total change in density was plotted. The mean is indicated with the dashed vertical line. (**C** and **D**): Bouton loss (C) and gain (D) were further broken down in to daily (n = 248) and weekly (n= 206) time intervals and compared across time for all axons present. Median (in brackets) and inter-quartile range are plotted.

3.4.5 Bouton gain and loss

The degree of bouton gain and loss on individual axons was expected to be matched across time, as the bouton density remained relatively constant (Figure 3.12A). The sum of the bouton gains and the sum of bouton losses (per unit length) were compared for axons present in all timepoints and found to be strongly correlated (Pearson's correlation: $R^2 = 0.82$, $p = 1.08 \times 10^{-34}$; Figure 3.14A). The distribution of bouton density changes for all axons over the entire study was centred close to zero, with a mean of -0.11 per 10 μm (Figure 3.14B).

Bouton gain and loss were compared across time, to show how the number of boutons was varying across short (daily) and long (weekly) time intervals. Many axonal segments had a gain or loss density of zero due to the limited sampling of the entire length of axon (Figure 3.14C, D). As a result, the data was severely non-normal (Shapiro-Wilk test for normality: $p < 0.0005$), with a large break between zero and the next smallest value. Therefore, the non-parametric Friedman test was used for repeated measures to compare distributions. This was done across the daily and weekly intervals.

Median daily bouton gain was 0.00, 0.10 and 0.12 per 10 μm respectively for daily intervals 1, 2 and 3, and median bouton loss was 0.13, 0.10 and 0.13 per 10 μm (Figure 3.14C, D). There was a significant difference in the distributions of daily bouton losses, but not for daily bouton gains (Friedman test: loss, $X^2(2) = 9.492$, $p = 0.009$; gain, $X^2(2) = 2.222$, $p = 0.329$). Pairwise comparisons post-hoc revealed that there was a significant difference between bouton loss in intervals 1 (days 0–1) and 2 (days 1–2; Bonferroni post-hoc test: $p = 0.016$; Figure 3.14C).

Median weekly bouton gain was 0.19, 0.23, 0.16, 0.15 per 10 μm respectively for weekly intervals 1, 2, 3 and 4 (Fig 3.14C, D). Median bouton loss was 0.18, 0.14, 0.24, 0.23 per 10 μm. There was no difference detected in the distributions of weekly bouton losses, but there was for bouton gains (Friedman test: loss, $X^2(3) = 11.341$, $p = 0.010$; gain, $X^2(3) = 7.378$, $p = 0.061$). Pairwise comparisons post-hoc revealed there was a significant difference between bouton gain in intervals 7 (days 14–21) and 9 (days 28–35; Bonferroni post-hoc comparison: $p = 0.015$; Figure 3.14D). Altogether, even though there were differences detected, it was not the result of a compound trend over time but did explain the small significant drop in bouton density at timepoint 9 (Figure 3.12A).

3.4.6 Classification of axon types

The axons sampled in this study were presumed to be from a similar population of pyramidal neurons in layer 5 of the motor cortex (Figure 3.6; Oswald et al., 2013). Previously, cell types have been classified from axonal morphology alone, including the density of *en passant* and *terminaux* boutons (De Paola et al., 2016). Here, axons were separated based on their density of boutons or mitochondria, or their density of bouton types (*en passant* and *terminaux*) to see if distinctly different populations existed, which would affect the generalisation of any further analyses. The distribution of bouton or mitochondrial densities appeared normal and did not exhibit separate groups of axons with particularly high or low bouton or mitochondrial density (Figures 3.12A and 3.13A).

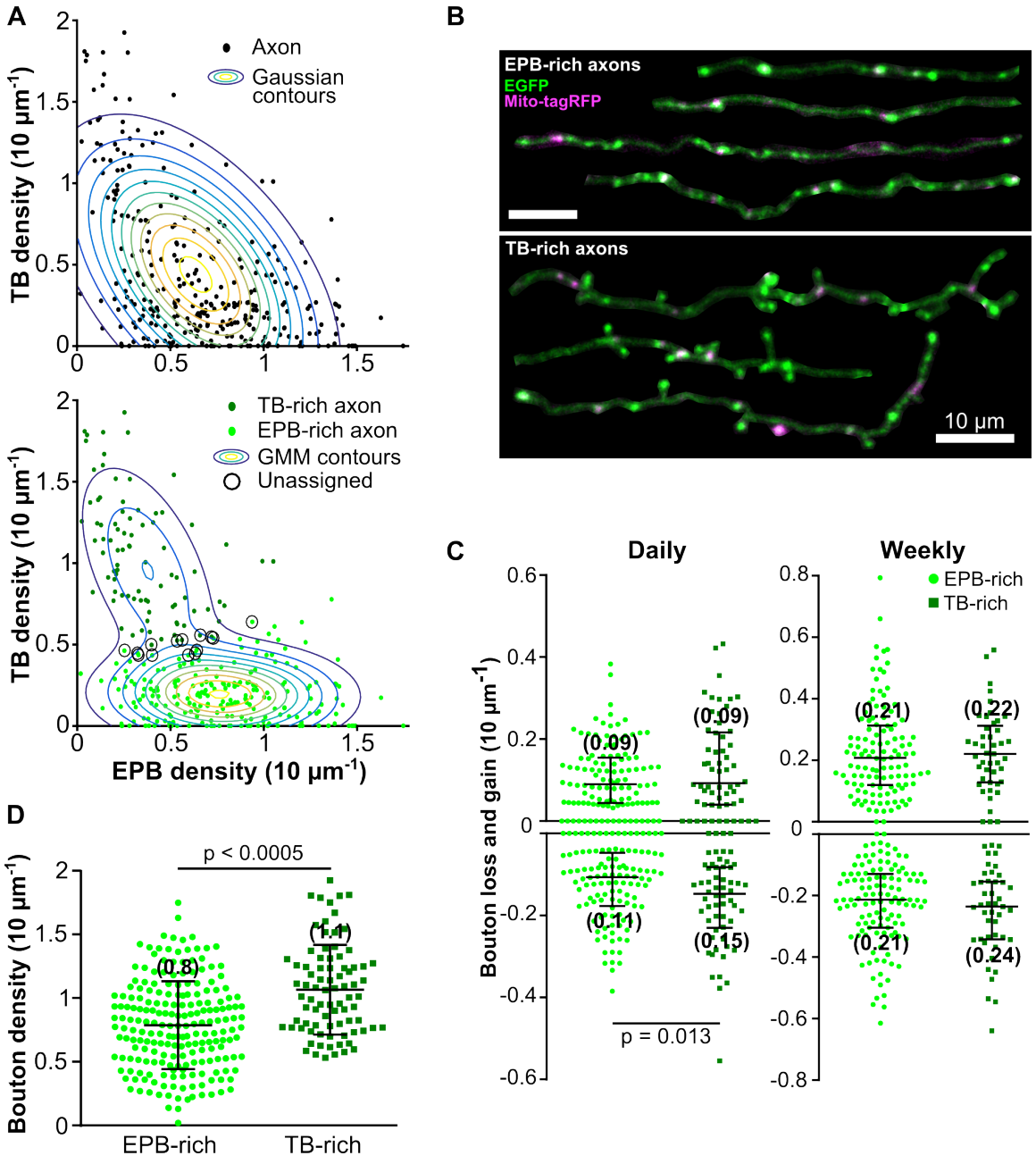

Figure 3.15 Axons grouped by bouton type did not differ in turnover. (**A**): Mean EPB and TB densities over time were calculated for each axon (n= 306) and plotted. A single-component Gaussian distribution did not adequately explain the distribution of EPB and TB densities on individual axons. Therefore, a Gaussian mixture model (GMM) was run to determine probabilities of each axon being in a group (TB-rich or EPB-rich). Axons were assigned a group if the probability was above a threshold of 0.6. Unassigned axons are indicated (black circles). (**B**): Example two-photon images of axons from the EPB-rich (top) and TB-rich (bottom) groups. Axons have been cropped and a gaussian filter (sigma = 2 pixel, 154 nm) applied for presentation only. (**C**): The number of boutons lost and gained across daily and weekly intervals were compared between the two axon groups (Daily n = 116 (EPB) and 58 (TB); Weekly n = 118 (EPB) and 45 (TB)). Loss and gain were plotted as a density to normalise for axon length. Median (in brackets) +/- inter-quartile range. (**D**): The mean density of boutons on axons in each group was calculated across time and the means of the population compared (EPB, n = 203; TB, n = 83). Mean +/- standard deviation.

Two distinct bouton classes exist for presynaptic terminals, *en passant* boutons (EPBs) and *terminaux* boutons (TBs), distinguished by their structure (see *Methods* for classifications; De Paola et al., 2006; Grillo et al., 2013). The two bouton classes are thought to differ in their function or postsynaptic partners, but no distinctions have yet been found (Anderson and Martin, 2001). Here, a Gaussian mixture model based on EPB and TB density in each axon was used to identify possible distinct axonal subpopulations. A single gaussian did not adequately explain the variation seen in the scatter of average EPB and TB densities for each axon (Figure 15A). Therefore, a two-component model was used to separate the population in to two groups, labelled EPB-rich and TB-rich (Figure 3.15A, B). Interestingly, the maximum combined bouton density of all the axons seemed to be 2 per 10 μm, as shown by the lack of summed bouton densities above that point (Figure 3.15A). There was a significant difference in the bouton densities of these axon types (independent t-test: $t(289) = 6.09$, $p < 0.0005$, 0.3 +/- 0.1 um^{-1} (95% CI) difference; EPB-rich 0.8 per 10 μm, TB-rich 1.1 per 10 μm mean density; Figure 3.15D).

Bouton loss and gain was compared between EPB-rich and TB-rich axon types to see if composition of bouton type was related to dynamics. Only daily bouton loss for TB-rich axonal segments was significantly higher than EPB-rich axonal segments (median bouton loss: TB-rich 0.15 per 10 μm, EPB-rich 0.11 per 10 μm; Mann Whitney U test: 4,144, $p = 0.013$; Figure 3.15C), daily bouton gain and weekly bouton loss and gain were not significantly different between EPB-rich and TB-rich axonal segments. Overall, although there appeared to be two groups of axons based on the composition of EPB and TB densities, their bouton dynamics did not differ consistently; therefore, they were grouped together for further analysis of mitochondrial effects on bouton dynamics.

3.4.7 Relationship between regional bouton and mitochondrial densities

Mitochondrial positioning and function are thought to be related to presynaptic function and plasticity (Smit-Rigter et al., 2016; Smith et al., 2016; Hall et al., 2012; Lewis et al., 2018; Rangaraju et al., 2014). Bouton and mitochondrial densities along an axonal segment may be correlated to ensure the correct supply of mitochondria per bouton. To test this, the mean mitochondrial and bouton densities were measured for axons present at every timepoint.

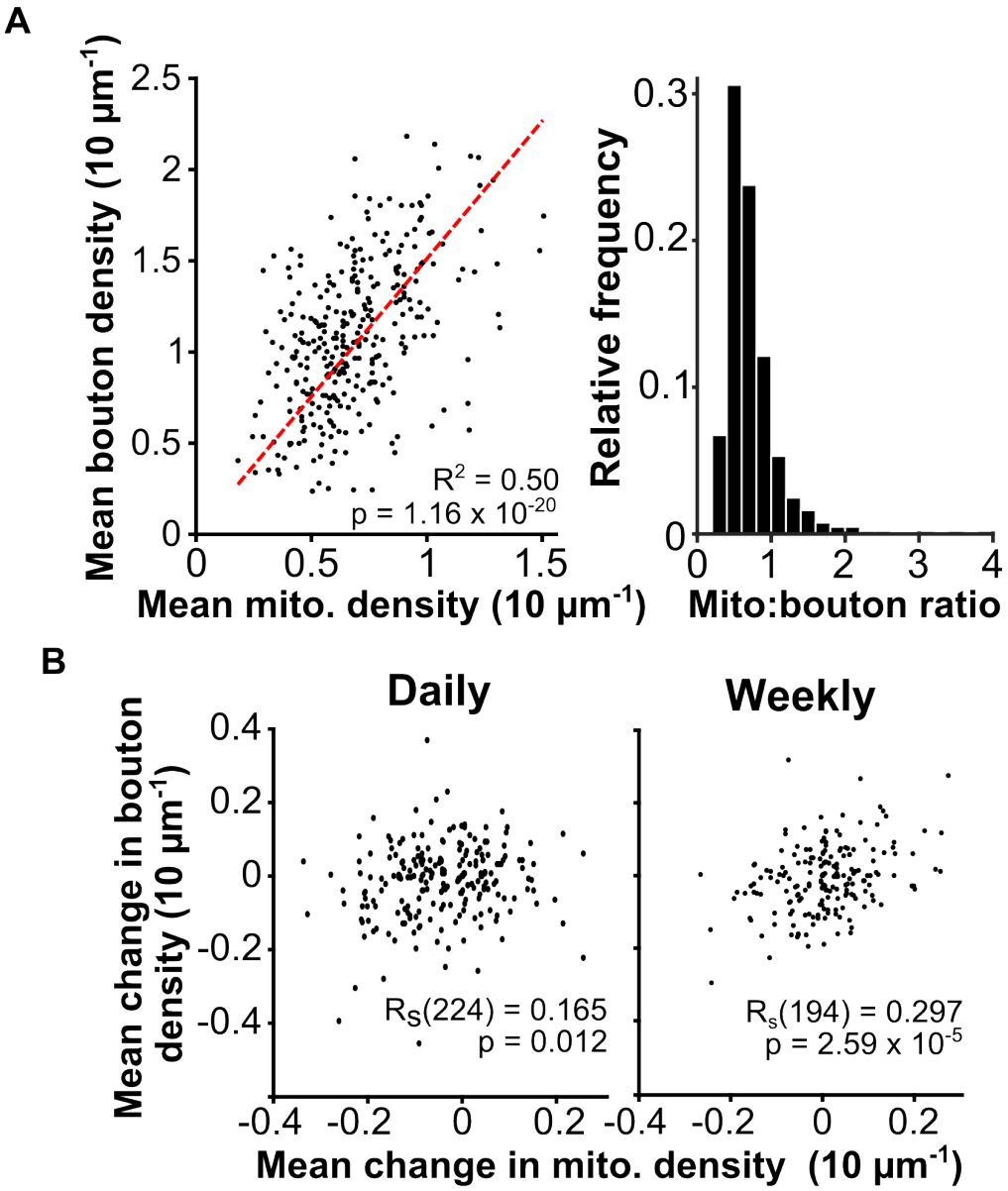

Figure 3.16 Mitochondrial and bouton densities were correlated. (**A**): (*Left*) mean mitochondrial and bouton densities across time were calculated for each axon and plotted against each other (*red dashed line* = regression line). (*Right*) The number of mitochondria to the number of boutons was calculated (*mito:bouton ratio*) for each axon at each timepoint and the distribution plotted as a histogram. (**B**): Mean changes in bouton and mitochondrial densities were calculated for each axon across daily (*left*) intervals or weekly (*right*) intervals. Regression lines not plotted because test was for non-linear correlation.

Indeed, average mitochondrial and bouton densities over time were strongly correlated for individual axons (Pearson's correlation: $R^2(304) = 0.5$, $p = 1.16 \times 10^{-20}$; Figure 3.16A). This resulted in a median mitochondrion-to-bouton ratio along axonal segments of 3:5 (0.6; Figure 3.16A).

The change in bouton and mitochondrial densities over time was also assessed. Daily changes in mitochondrial density were only weakly matched with bouton density. However, weekly changes of the two densities were more strongly matched (Spearman's correlation: daily, $R_s(224) = 0.165$, $p = 0.012$; weekly, $R_s(194) = 0.297$, $p = 2.59 \times 10^{-5}$; Figure 3.16B). These results suggested that mitochondrial and bouton densities were correlated in axons and were better matched over longer time periods (weekly versus daily).

3.4.8 Relationship between regional mitochondrial density and bouton turnover

The number of boutons that were lost or gained as a fraction of the total (dynamic bouton fraction, see *Methods* section) may have been related to energetic requirements. Therefore, the number of mitochondria available regionally (in an axonal segment) was compared against bouton dynamics. However, neither mitochondrial density nor mitochondrion-to-bouton ratio appeared to be correlated with the dynamic bouton fraction in this population of axons (Figure 3.17A, B). Only the relationship between mitochondrion-to-bouton ratio and daily dynamic bouton fraction was weakly correlated (Spearman's correlation: $R_S(225) = 0.183$, $p = 0.006$). This relationship did not hold up at weekly intervals (Figure 3.17A). This suggests that bouton turnover rates are not related to overall mitochondrial density regionally.

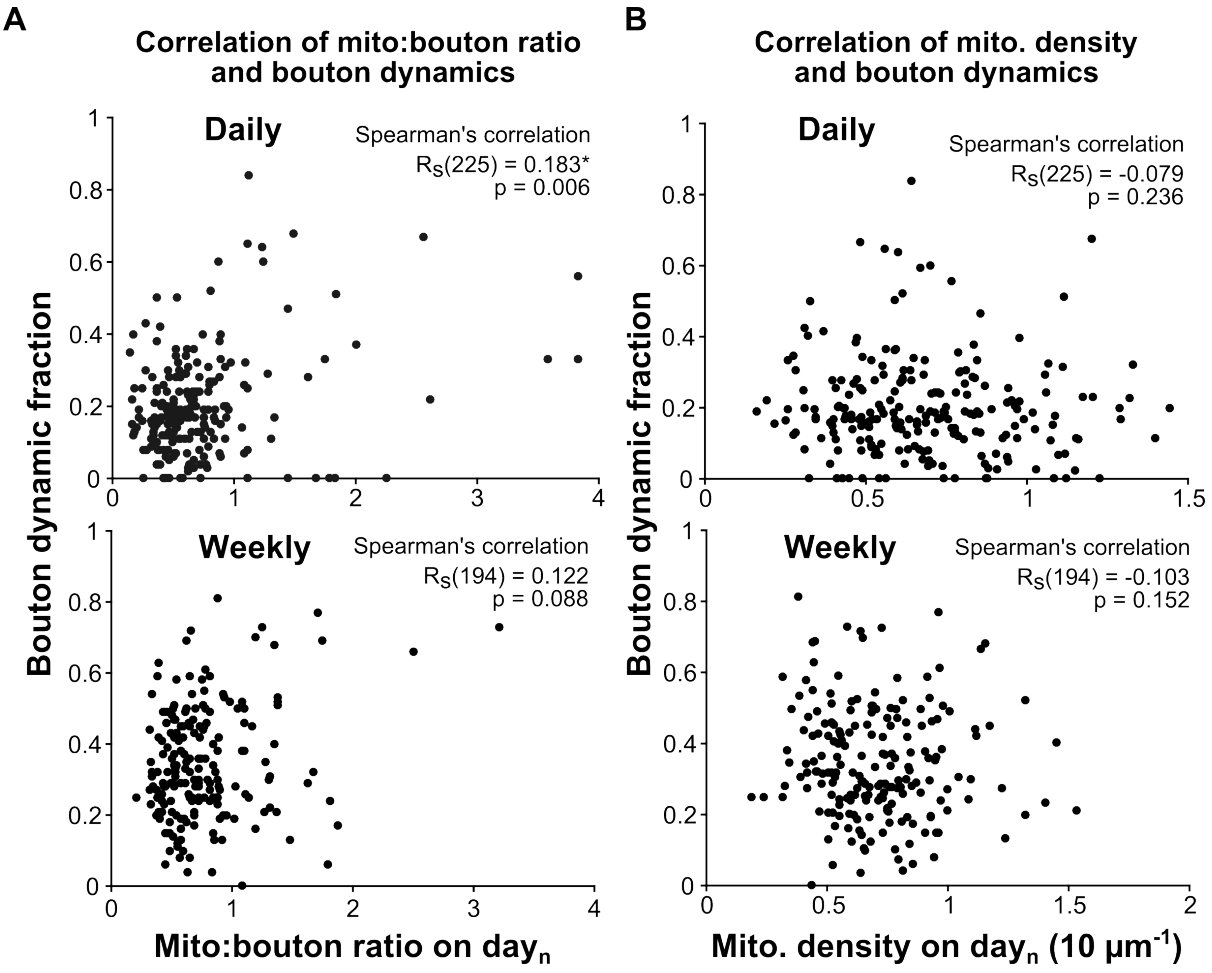

Figure 3.17 Size of bouton dynamic fraction was not related to number of mitochondria. Bouton dynamic fraction is the fraction of boutons that are dynamic in the time interval (daily or weekly). (**A** and **B**): Mitochondrion to bouton ratio (Mito:bouton; A) or mitochondrial density (Mito. density; B) was measured on day_n for correlation with the dynamic fraction between day_n and day_{n+1} (daily) or day_n and day_{n+7} (weekly). * = $p < 0.01$.

3.4.9 Local positioning of axonal mitochondria relative to presynaptic boutons

The lack of a consistent relationship between regional mitochondrial density and bouton dynamics (Figure 3.17) suggested there may be a more local relationship between mitochondria and boutons. The spatial distribution of mitochondria relative to individual boutons was assessed to test this relationship. Previous literature has suggested a distance-dependent effect of mitochondria on bouton function up to 3 μm away (edge-to-edge distance from mitochondrion to vesicle pool; Smith et al., 2016). Constraints in 2P imaging resolution (Figure 3.18), combined with this knowledge, led to a distance threshold of 1.5 μm (centroid-to-centroid) being chosen to indicate a mitochondrion was "present" at a bouton (see *Methods*).

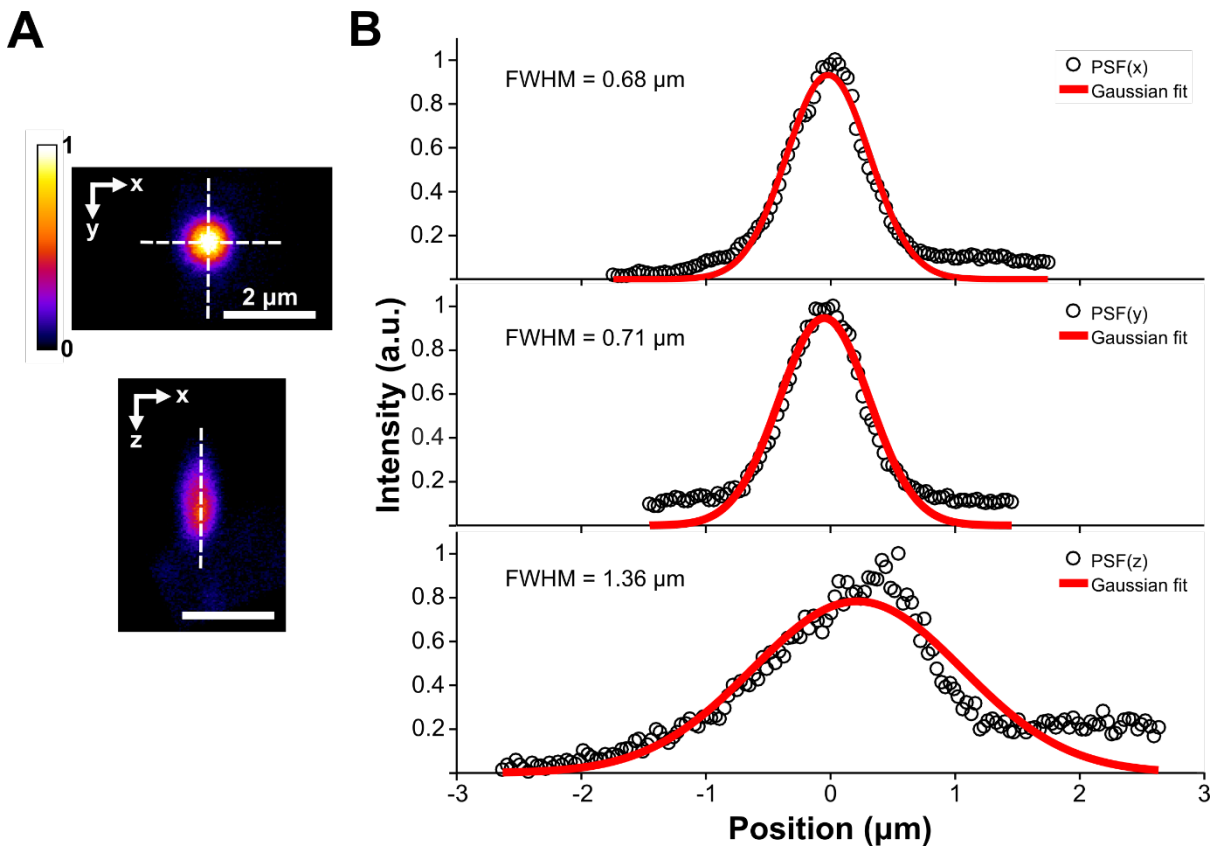

Figure 3.18 Experimental point spread function. (**A**): Sub-resolution (200 nm) fluorescent beads were imaged in 3D to obtain point spread functions (PSF) at 910 nm. Images were over-sampled at 100 nm axially and 37 nm laterally. Images of 10 beads were subsequently aligned, averaged and intensity profiles plotted along the x, y and z axes. Calibration bar in arbitrary units (a.u.). (**B**): Intensity profile plots of averaged, aligned bead images. Gaussian curves were fitted in MATLAB and the full-width half-maximum (FWHM) was calculated. Lateral resolution was estimated to be 700 nm and axial resolution 1.4 um. Some drift occurred initially in the z-axis, so axial resolution may be poorly estimated.

The fraction of mitochondria present at axonal boutons was between 57% and 62% over time (Figure 3.19A), and the fraction of boutons with mitochondria present was between 37% and 45% (Figure 3.19B). It was important to determine whether this colocalisation could be explained by chance alone, based on their relative densities. The distances between each bouton and its nearest mitochondrion (and each mitochondrion and its nearest bouton) were calculated (Figure 3.20B, C). To compare real distributions with chance levels, positions of boutons were randomised along each axonal segment while mitochondrial positions were kept constant and nearest distances were recalculated (Figure 3.20A). The same procedure

was repeated, but with randomised mitochondrial positions and fixed bouton positions (see *Methods* for more details). The randomisation procedure relied on moving bouton or mitochondrion positions in one dimension along the axon backbone, however positions of TBs were approximated best in two dimensions (as they stick out from the backbone). They were therefore approximated in one dimension by projecting them on to the backbone with a linear translation to the nearest axon backbone position for this randomisation (Figure 3.20A; see next paragraph for split of EPB and TB). The randomisation of positions resulted in greater distances between the mitochondria and boutons (median bouton-to-nearest mitochondrion: real, 2.2 μm; randomised, 4.5 μm; median mitochondrion-to-nearest bouton: real, 0.9 μm, randomised, 3.5 μm). The distribution of the real nearest neighbour distances was different from that of randomised positioning when comparing mitochondria-to-nearest bouton (Figure 3.20B; two-sample Kolmogorov-Smirnov test: $p < 0.0005$) or bouton-to-nearest mitochondria (Figure 3.20C; two-sample Kolmogorov-Smirnov test: $p < 0.0005$). Randomising did not keep the distributions of inter-mitochondrial or inter-bouton distances similar to the real data; therefore, the positions of the mitochondria were also separately mirrored on the axon to maintain inter-mitochondrial distance, and subsequently plotted (Fig 3.20B; *green dotted line*). Randomised positioning changed the proportion of boutons with mitochondria present from 35-45% to 20-25% (Figure 3.20D). Therefore, the positioning of mitochondria close to boutons was not due to chance.

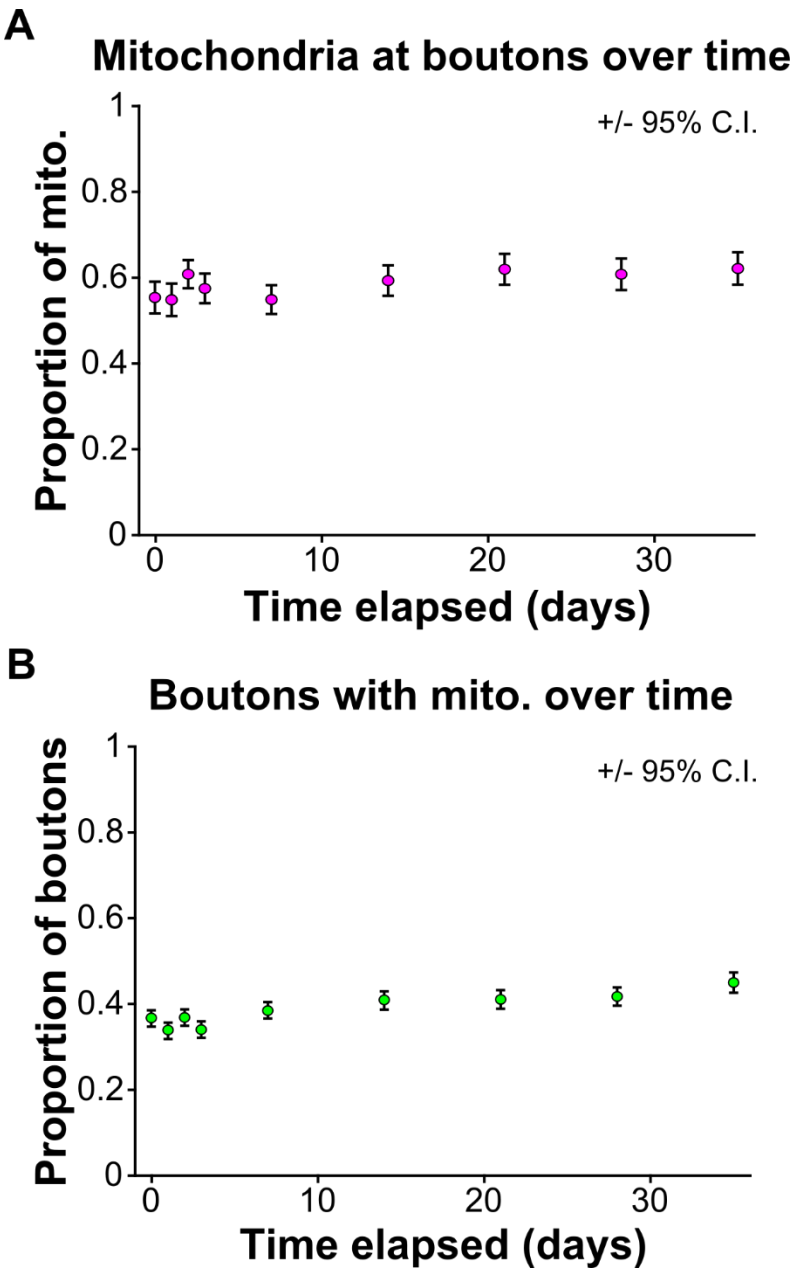

Figure 3.19 Bouton and mitochondrial colocalisation over time. The entire population of boutons and mitochondria were assessed for their colocalisation with each other. (**A** and **B**): The entire population of mitochondria (A) or boutons (B) were assessed for colocalisation with each other at every individual time point. Colocalisation was classed as being 1.5 µm or closer.

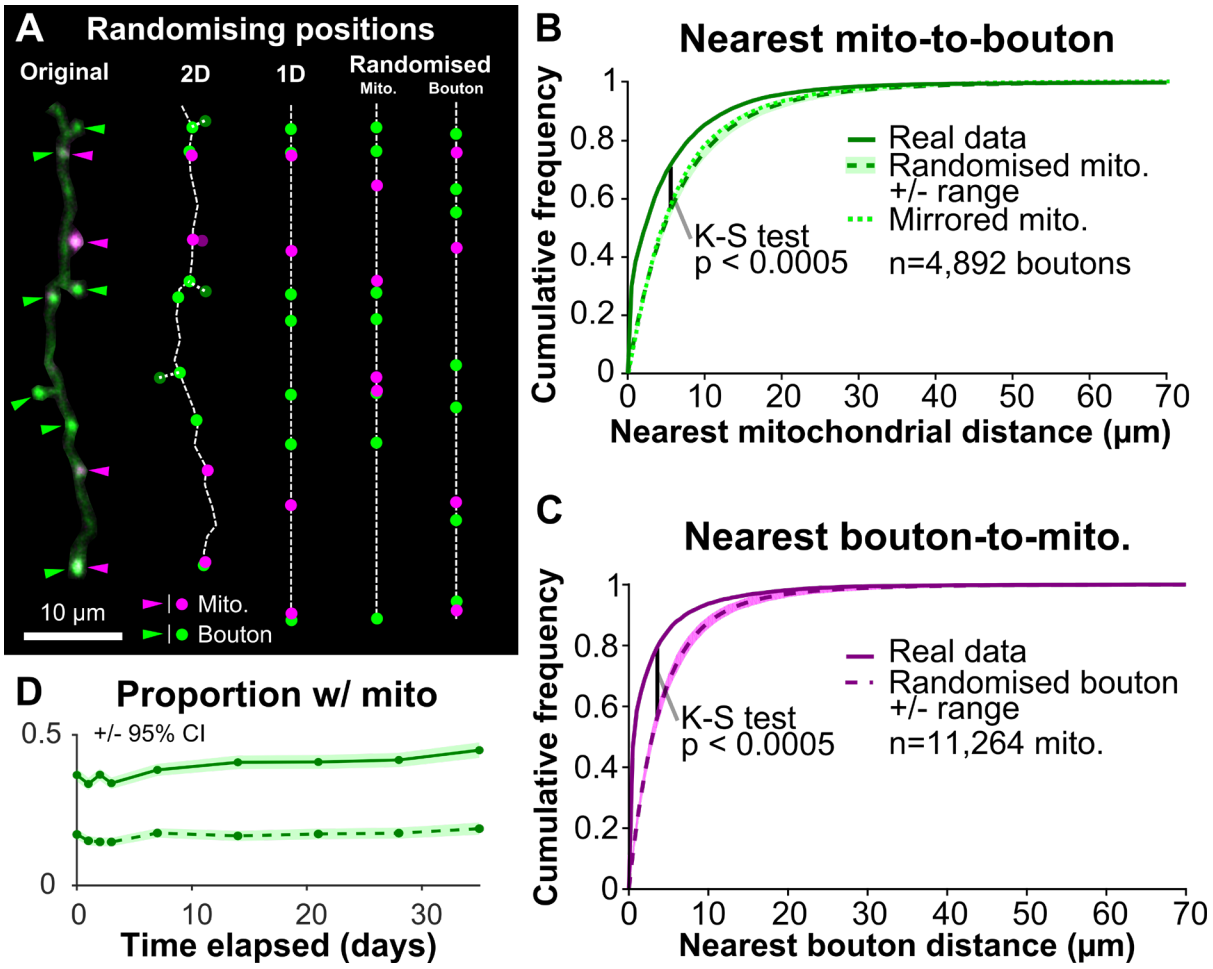

Figure 3.20 Distances between mitochondria and boutons are the results of non-random spatial distributions. (**A**): Example of randomisation process for one axon. (*Original*) Representative image of an axon from *in vivo* two-photon imaging with mitochondria and boutons indicated using arrowheads. (*2D*) The axon was interpolated and a 2D representation of the axon was created (*dashed line*) with all boutons and mitochondria (*circles*) plotted on the axon backbone. (*1D*) The axon was then collapsed to one dimension. (*Randomised*) The positions of either mitochondria or boutons were then randomised, and distances recalculated. The randomisation was repeated 1000 times to get the range of distributions plotted in (B) and (C). (**B**): The distance from each bouton to its nearest mitochondrion was measured and the cumulative distribution of distances plotted (*solid line*). The same calculations were done for randomised positioning of mitochondria, 1000 times (*dashed line*). Comparison between the two distributions was done using a two-sample Kolmogorov-Smirnov (*K-S*) test. Additionally, the positions of mitochondria were mirrored on the axon to maintain inter-mitochondrial distance and nearest neighbour distances plotted (*dotted line*). (**C**): The distance from each mitochondrion to the nearest bouton was also measured. Randomisation and analysis was repeated as in (B). (**D**): The proportion of all boutons with mitochondria 1.5 µm or less away was plotted for each time point for both the real data (*solid line*) and randomised data (*dashed line*).

As the structures of an EPB and TB are dissimilar, they may differ in their ability to anchor mitochondria. To assess this, the presence of mitochondria at each bouton class was determined. The presence of mitochondria near the heads of TBs (expected site of synaptic contact) was greatly reduced in comparison to EPBs (Chi-square test: $X^2(1)$: 67.64, $p < 0.0001$; mitochondrial presence: 45% EPBs, 28% TBs; Figure 3.21A). However, mitochondria were often located in the axon backbone near to the base of a TB protrusion, and this was not significantly different in comparison to EPBs (Chi-square test: $X^2(1)$: 1.735, $p = 0.1878$; mitochondrial presence: 40%; "TB 1D" in Figure 3.21A, B). Random positioning of mitochondria also affected this relationship, suggesting it also did not occur by chance ("TB 1D rand." in Figure 3.21A). Overall, EPBs were 60% more likely to have mitochondria near to their putative synaptic contact than TBs, but this difference was reduced to 12% from the base of a TB.

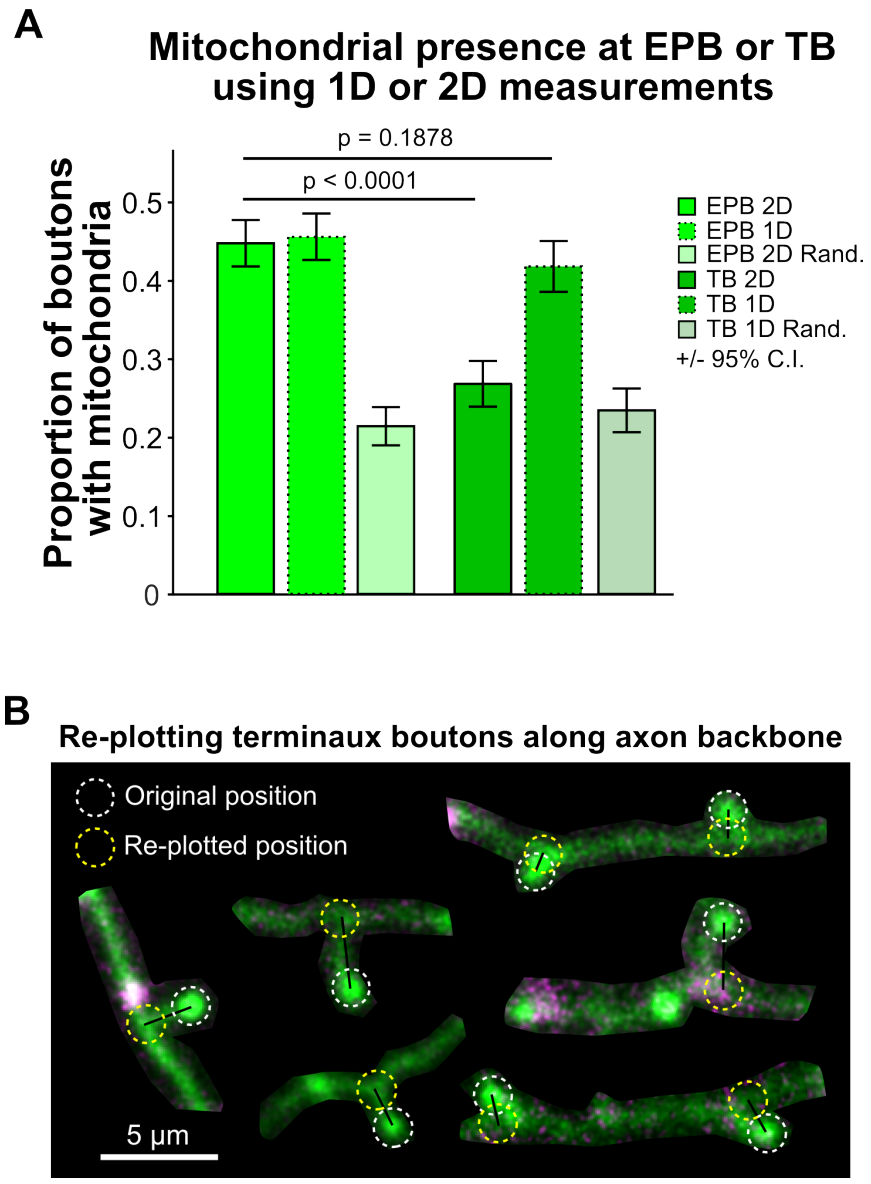

Figure 3.21 Mitochondrial presence was much lower at *terminaux* boutons compared to *en passant* boutons. (**A**): The entire population of boutons was assessed for mitochondrial colocalisation at the first timepoint only to avoid pseudoreplication from pooling data. The population was split by bouton structure (EPB or TB) and by how the mitochondria and boutons were plotted on the axon for distance calculations (1D or 2D). Plotting in 1D along the axon backbone was used during the randomisation procedure to determine that localisation was non-random. The results from randomisation were also measured (*Rand*). (**B**): Example two-photon images and illustrations showing the automated re-plotting of TBs on to the axon backbone for estimation in 1D. The original bouton position (white dashed circle) was translated to the axon backbone (black line) and re-plotted (yellow dashed circle).

Newly-formed boutons are thought to increase the capacity for circuit plasticity in the neocortex (Holtmaat and Svoboda, 2009). A small proportion of newly-formed boutons are long-lived (~30% survive past 1 week; Qiao et al., 2015; Ash et al., 2018; Mostany et al., 2013)

and form synaptic connections (De Paola et al., 2006; Grillo et al., 2013); whereas, the majority of pre-existing boutons are very long-lived (>70% live over 1 month; De Paola et al., 2006; Grillo et al., 2013; Ash et al., 2018; Qiao et al., 2015). Therefore, newly-formed boutons in their first days may not be as active as older (pre-existing), stably-integrated boutons. If this is the case, it may be hypothesised that bouton age is related to mitochondrial presence, to support increased presynaptic activity. To evaluate this hypothesis, bouton age was grouped in to either: new, appeared after day 0; or pre-existing, present on day 0 (Figure 3.22A). Mitochondrial localisation at boutons was assessed on the first day of each of the boutons in these two groups. A significantly higher proportion of pre-existing boutons had mitochondria present than newly-formed boutons (Chi-square test: $X^2(1)$: 25.24, $p < 0.0001$; pre-existing, 38%, newly-formed, 31%; Figure 3.22B). Both newly-formed and pre-existing boutons were still located closer to mitochondria than by chance (18% Pre_{rand}, 19% New_{rand}; Chi-square test: New_{rand} $X^2(1)$: 142.2, $p < 0.0001$; Pre_{rand} $X^2(1)$: 281.2, $p < 0.0001$).

Newly-formed boutons that survive go on to be long-lived boutons, like most of the pre-existing population (Qiao et al., 2015). To see if mitochondrial presence increased with bouton age, mitochondrial presence was measured for the population of boutons that survived for the entire experiment. Newly-formed boutons showed a non-significant trend with time to increasing mitochondrial presence (28% to 40%, Cochran's Q test: $Q(5) = 6.810$, $p = 0.235$; Figure 3.22C). In comparison, the proportion of newly-formed boutons with mitochondria present on their first day was constant over the entire experiment (Figure 3.22D). Therefore, the increase in mitochondrial presence for surviving boutons was not due to a general increase in presynaptic mitochondria. Pre-existing boutons also showed a trend of increasing mitochondrial presence over time, which was statistically significant (42% to 50%, Cochran's Q test: $Q(6) = 51.359$, $p < 0.0005$; Figure 3.22C).

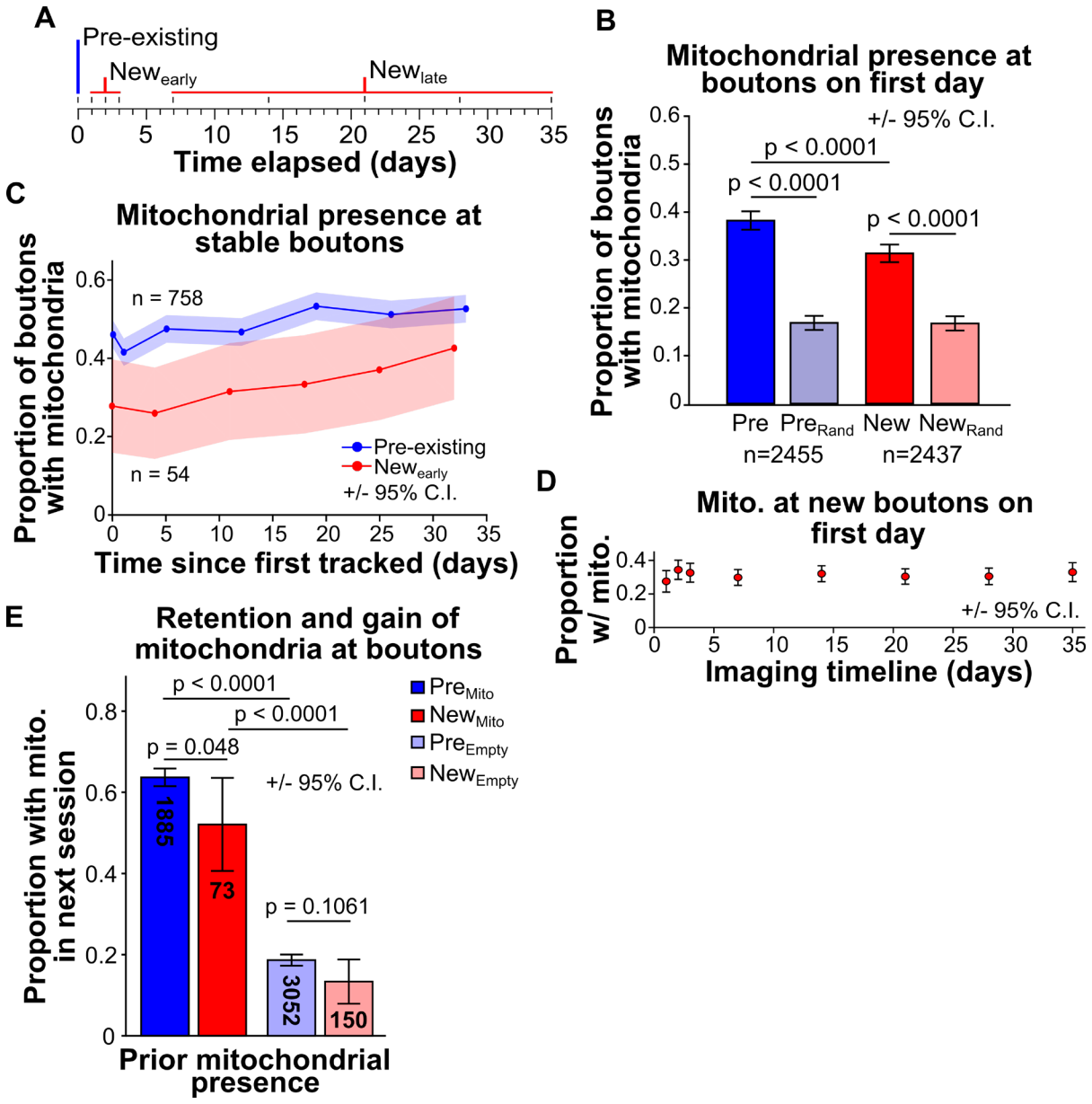

Figure 3.22 Mitochondrial presence at boutons was related to increased maturity and longevity. (**A**): Classification of bouton maturity. Pre-existing boutons were those present on the first day of imaging, New_{early} boutons were those formed in the daily intervals, and New_{late} were those formed in the weekly intervals. (**B**): Populations of newly-formed (New) or pre-existing (Pre) boutons were assessed for mitochondrial presence on the first day they were imaged. The proportion of boutons with mitochondria when mitochondrial positions were randomised was also assessed (Pre_{rand} and New_{rand}). (**C**): Mitochondrial presence was tracked for populations of boutons that persisted for the entire imaging time course. (**D**): The presence of mitochondria at newly-formed boutons on their first day was assessed at each time point individually. (**E**): Boutons were split into groups with (Mito) and without (Empty) mitochondria, and by maturity (New or Pre). Mitochondrial presence was then assessed after 24 h to determine retention and gain. Number of boutons in each group are indicated in the bars.

The increase in mitochondrial presence could have been explained by a retention of mitochondria at boutons. To test this, the number of boutons that retained mitochondria

(New/Pre$_{mito}$) in 24 hours was compared to the number of boutons that were empty and gained a mitochondrion (New/Pre$_{empty}$; Figure 3.22E). Both newly-formed and pre-existing boutons had a significantly higher probability of retaining a mitochondrion than gaining one (Fisher's exact test: 63% to 18% pre-existing, $p < 0.0001$, 50% to 15% newly-formed, $p < 0.0001$). Pre-existing boutons were also significantly more likely to retain a mitochondrion than newly-formed boutons (Fisher's exact test: $p = 0.048$). In summary, the probability of mitochondrial presence at a bouton was greater with increasing bouton age; however, retention of mitochondria alone did not explain the increased presence – those boutons that retain mitochondria must also survive to increase mitochondrial presence in the population.

3.4.10 Bouton survival

As mentioned in the previous section, pre-existing boutons are much more likely to survive than newly-formed boutons (Qiao et al., 2015; Ash et al., 2018; De Paola et al., 2006). To assess this in long-range motor-somatosensory axons, each bouton was tracked until it was lost, or the end of the observational period was reached. The newly-formed bouton population was split further to analyse survival as accurately as possible. Boutons formed in the first three days were identified within 24 h of their formation (days 0-2; New$_{early}$ population; Figure 3.23A). Those formed after that time were less accurate, but still plotted for comparison (days 7–35; New$_{late}$ population). Pre-existing boutons were a mixture of ages; however, the majority were older than newly-formed boutons (10% of pre-existing boutons were probably newly-formed, as daily bouton gain rate was 10% of bouton density; Figure 3.14D and 3.12A).

The two populations of boutons (new and pre-existing) had significantly different survival rates (Log rank test: $X^2(2) = 815.7$, $p = 0.0006$). The median lifetime for newly-formed boutons was 4 and 7 days (New$_{early}$ and New$_{late}$ respectively; Figure 3.23A). Whereas, for pre-existing boutons the median lifetime was 35 days (survival dropped below 50% on the final day of the experiment). The survival curve for New$_{late}$ boutons did not overlay exactly with New$_{early}$ as the precise time of bouton formation was not as accurately estimated (accurate to nearest 7 days rather than nearest 24 hours for New$_{early}$), but it followed a similar trajectory.

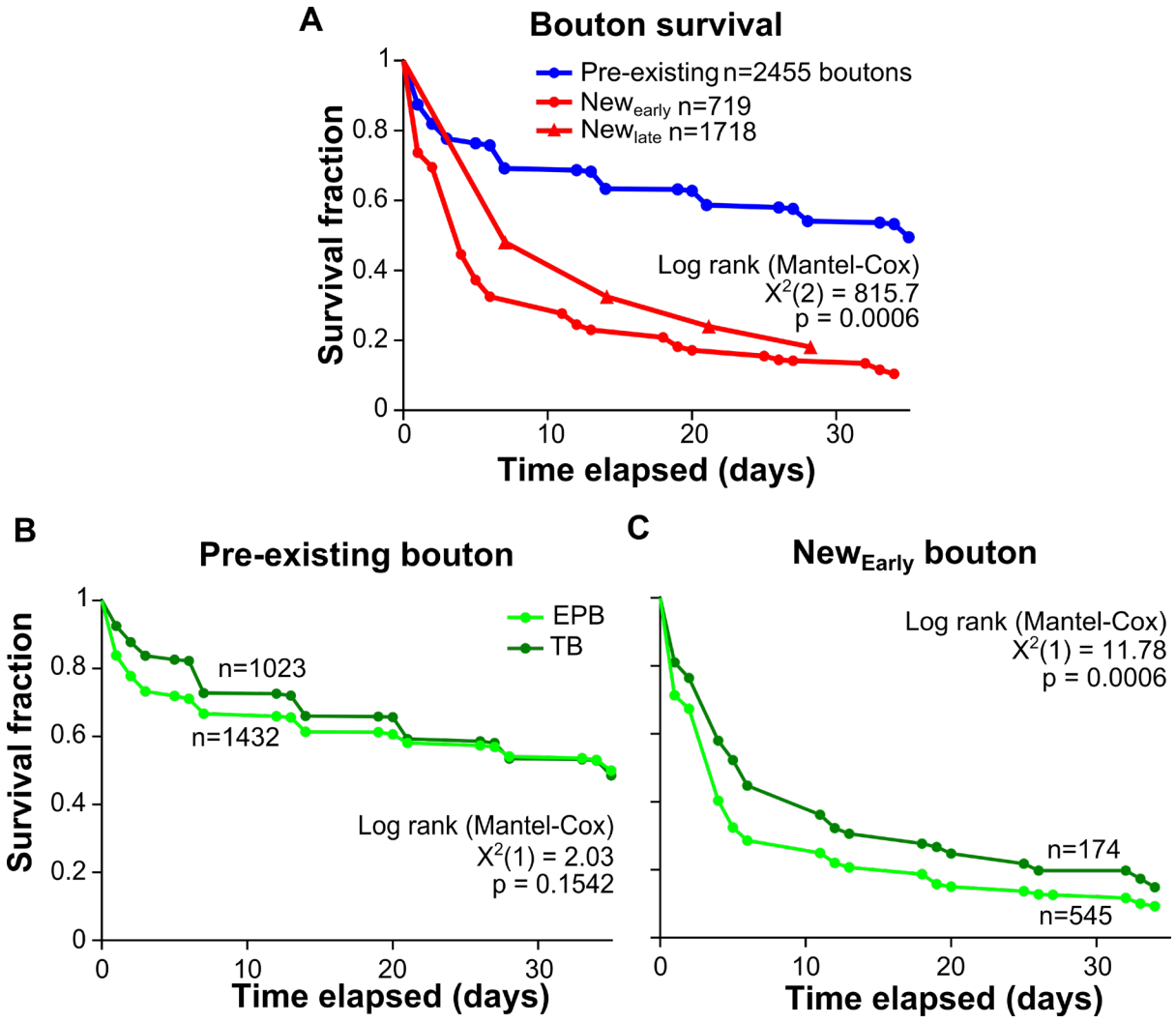

Figure 3.23 Differential survival of newly-formed and pre-existing boutons. (**A**): Bouton survival was measured for the different groups indicated. The first day a bouton was imaged was aligned to day 0. The bouton was scored as lost on the day it was no longer visualised or censored when it was still present on the last day of imaging. Each mark on the line indicates that boutons were lost or censored on that day. (**B** and **C**): Pre-existing boutons (B) or newly-formed boutons from the daily intervals (New_{Early}; C) were split by bouton structure (TB or EPB) and assessed in the same way as (A).

Previous literature has shown that different bouton types on the same axon share similar survival rates (De Paola et al., 2006). To assess this, bouton survival was analysed separately for TBs and EPBs. Bouton survival did not differ between EPBs and TBs in the pre-existing group of boutons (Log rank test: $X^2(1) = 2.03$, $p = 0.1542$; median survival: 35 days, EPB and 35 days, TB; Figure 3.23B). However, there was a significant difference between EPB and TB survival for newly-formed boutons (Log rank test: $X^2(1) = 11.78$, $p = 0.0006$; median survival:

4 days, EPB and 6 days TB; Figure 3.23C). Therefore, it appeared that EPBs were more likely to be lost than TBs in the first few days of their existence.

3.4.11 Relationship between mitochondrial presence and bouton survival

The non-random localisation of mitochondria near to some axonal boutons but not others (Figures 3.20, 3.21 and 3.22) may have been related to bouton survival. Previously, a decrease in pre-existing bouton loss was seen when mitochondria were present (~34% relative decrease; Smit-Rigter et al., 2016). To understand whether the presence of a mitochondrion relates to immediate survival of a new bouton, the loss of newly-formed boutons within their first 24 hours was assessed. There was a significant decrease in bouton loss for newly-formed boutons (New_{early}) with mitochondria present ($p = 0.031$, 35% lost with mitochondria, 45% without; Figure 3.24A). This relationship was also true for pre-existing boutons lost within the first day they were tracked ($p < 0.0005$, 8% with mitochondria, 13% without).

Both relationships were analysed across the entire time course of the study using Cox proportional hazards (PH) regression model with time-varying covariates. Cox proportional hazards regression model takes in to account time-varying covariates (i.e. mitochondrial presence, dichotomous variable) in the assessment of survival. The hazard ratio indicates the fold change (increase or decrease) in bouton loss (see *Methods* for statistics). A significant relationship was not observed for New_{early} boutons across time (Cox PH: hazard ratio = 0.9 +/- 0.24 95% C.I., $p = 0.606$; Figure 3.24B). However, pre-existing boutons with mitochondria present were consistently less likely to be lost (5–10% loss with mitochondria, 10–15% loss without mitochondria; Cox PH: hazard ratio = 0.5 +/- 0.1 95% C.I., $p < 0.0005$; Figure 3.24C). These data indicate that the presence of a mitochondrion at a long-lived bouton approximately halves its likelihood of being removed from the axon.

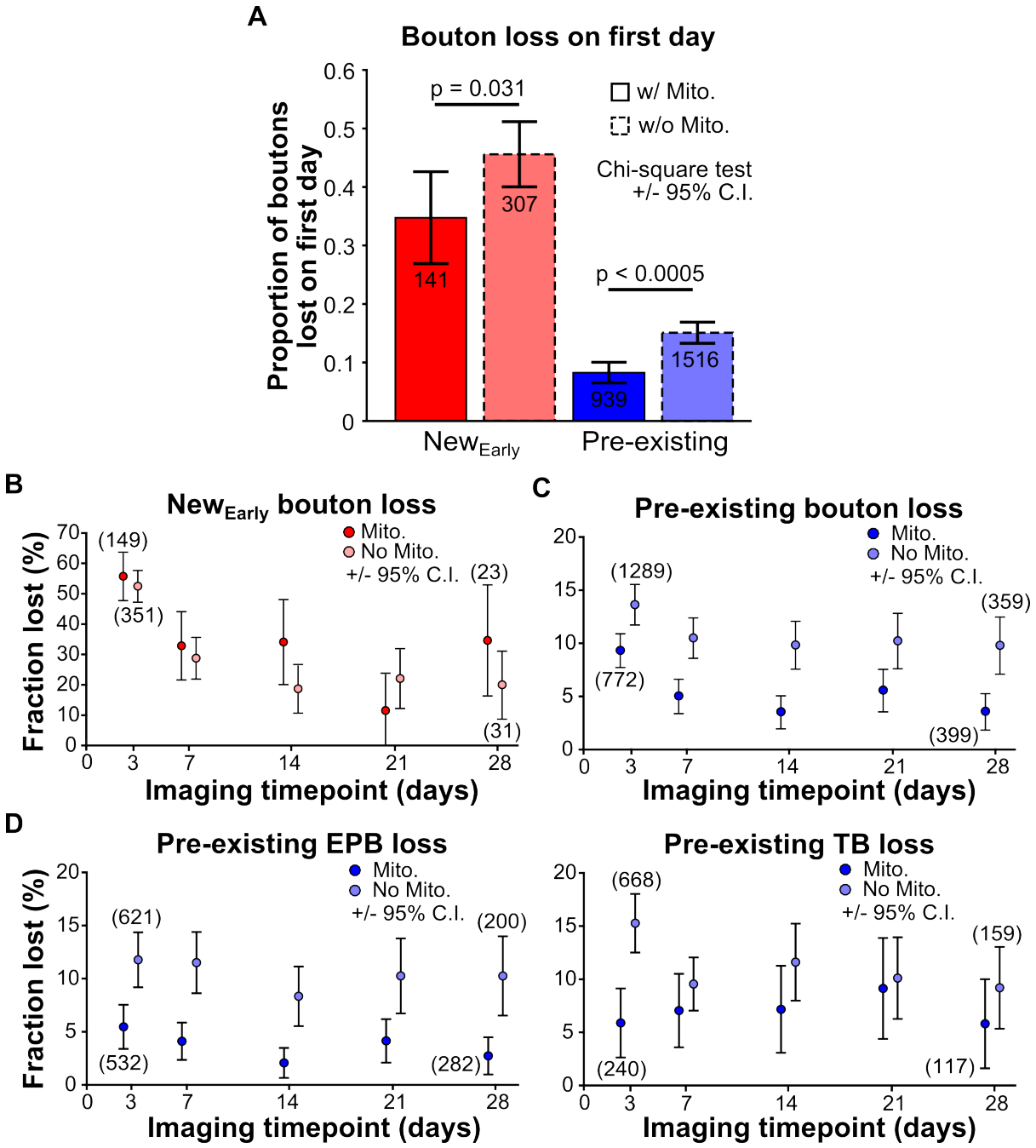

Figure 3.24 Bouton loss was significantly increased when mitochondria were not present. (**A**): The proportion of bouton loss in the first 24 hours was measured for populations with or without mitochondria. Number of boutons in each group is indicated in the bar. (**B** and **C**): The proportion of bouton loss was measured for newly-formed (B) or pre-existing (C) boutons at each timepoint in populations with and without mitochondria. (**D**): Pre-existing boutons were split by bouton structure and assessed in the same way as (B) and (C). The number of boutons in each group is indicated in brackets for the first and last time points. Populations with and without mitochondria are re-evaluated at every time point as mitochondrial localisation changes.

Analysis of pre-existing bouton loss was further split by bouton class, as the probability of mitochondrial presence differed between EPBs and TBs (Figure 3.21A). An even stronger relationship was found for EPBs between mitochondrial presence and survival (hazard ratio = 0.4 +/- 0.1 95% C.I., p = <0.0005; Figure 3.24D). Whereas, TBs had a weaker relationship (hazard ratio = 0.6 +/- 0.2 95% C.I., p = 0.005). Therefore, mitochondrial presence was not as important for explaining the survival rates of TBs than it was for EPBs.

3.5 Discussion

3.5.1 Conclusion

The aim of this study was to determine the relationship between mitochondrial positioning and bouton dynamics in a specific long-range projection of the mouse motor cortex. Previous studies looking at bouton turnover *in vivo* have used transgenic animals with sparse labelling of a mixed population of cells (mostly pyramidal neurons in different neocortical areas of GFP-M or YFP-H mice; Feng et al., 2000) or *in utero* electroporation of DNA plasmids (Saito and Nakatsuji, 2001). These methods result in a mixed population of axonal projections from multiple different areas of the brain being analysed together (De Paola et al., 2006; Grillo et al., 2013; Mostany et al., 2013; Majewska et al., 2006; Morimoto et al., 2018; Ash et al., 2018). In some studies, the origin of these projections was never identified, and in others they were inferred using axonal structure alone (composition and density of EPBs and TBs; De Paola et al., 2006). To reduce the variability in the population of axons analysed, neurons of the motor cortex were specifically targeted using viral injection and their projections imaged in somatosensory cortex (Figure 3.1). The main projection appeared to be from layer 5 neurons (as assessed by histology; Figure 3., 3.5, 3.6 and 3.7), which are mostly excitatory pyramidal neurons (Oswald et al., 2013); however, some inhibitory long-range cortico-cortical neurons are suggested to exist; (Tamamaki and Tomioka, 2010). Within the population, two different subpopulations of axons were identified by their EPB and TB densities; however, the turnover of their boutons was similar (Figure 3.15C).

The average bouton density of all axons was 1.1 per 10 μm, but for EPB-rich axons this dropped to 0.8, and for TB-rich axons it remained at 1.1 (Figure 3.15D). The combined density of EPBs and TBs on these axons appeared to be limited to a maximum of 2–2.5 per 10 μm (Figure 3.15A and 3.12A). In comparison, TB-rich neocortical axons examined previously had densities of 1.5 per 10 μm for TBs alone (Grillo et al., 2013), or a mixture of 1.1 for TBs and 1.4 for EPBs, reaching a total of 2.5 per 10 μm on average (De Paola et al., 2006). EPB-rich neocortical axons had variable densities in the region of 0.6–1.6 per 10 μm (De Paola et al., 2006; Mostany et al., 2013; Grillo et al., 2013; Stettler et al., 2006). Axons of layer 2/3 pyramidal neurons of the visual cortex had bouton density of 1.0 per 10 μm, but TB/EPB densities were not stated (Smit-Rigter et al., 2016). Therefore, the bouton densities seen in this study were at

the lower end of those seen in other studies, but the axonal projections were not comparable to these studies.

Numbers of axonal mitochondria and boutons remained mainly stable over daily and weekly intervals (Figure 3.12 and 3.13), suggesting that repeated anesthetised two-photon imaging was not having a compounded effect on the turnover of boutons or mitochondria. Indeed, bouton loss and gain were correlated over time (Figure 3.14). These results corroborate other findings that bouton density is consistent in neocortical axons of pyramidal neurons *in vivo* due to correlated loss and gain (Stettler et al., 2006; Grillo et al., 2013; De Paola et al., 2006). However, this is the first time that mitochondrial density has been tracked over time *in vivo*. There was a slightly lower average mitochondrial density in axons studied here than in short-range axons of layer 2/3 pyramidal neurons in the visual cortex (0.7 versus 0.9 per 10 μm in Smit-Rigter et al., 2016). In future, it would be interesting to assess mitochondrial distribution in short-range and long-range axonal projections of the same population of neurons to determine if distributing mitochondria over long distances results in lower density (see *General Discussion*). Smith et al. (2016) showed a density of 2 mitochondria per 10 μm in rat hippocampal axons, considerably higher than seen in cortical axons, however Smith et al. used electron microscopy, which is not limited by the diffraction limit of light. This raises an important limitation of this study, that the appearance of a single mitochondrion in light microscopy may be equivalent to multiple mitochondria that can not be resolved. In future, it would be useful to include the intensity of mitochondrial signal (and hence the size of a mitochondrion/mitochondrial pool and their functional capacity) in analyses within individual axons; however, comparison between axons and animals would not be possible due to differential expression levels of AAV.

Regional densities of mitochondria and boutons measured across axonal segments were strongly correlated (Figure 3.16A). Changes in density were correlated more strongly over weeks than days (Figure 3.16B), suggesting that the mitochondrion-to-bouton ratio was equilibrated better over longer time intervals. This is the first time *in vivo* that the relationship between the number of boutons and number of mitochondria has been assessed over time. The origin of cause and effect for these changes remains unresolved but it is most likely to do

with the capture of mitochondria close to boutons. Expression of Miro1, Syntaphilin, or other mitochondrial anchoring proteins is known to mediate mitochondrial anchoring at boutons in a calcium-dependent manner (MacAskill et al., 2009; Kang et al., 2008; Vaccaro et al., 2017); therefore, higher bouton densities may lead to increased concentrations of calcium, elevating the degree of mitochondrial anchoring in the axon.

Previously, mitochondrial distribution was biased towards colocalisation with boutons *in vivo* (Smit-Rigter et al., 2016, Smith et al., 2016), and this was also true in the long-range axons studied here (Figure 3.20). Around 50% of mitochondria were found at boutons in the visual cortex (Smit-Rigter et al., 2016), compared to ~60% in these long-range motor cortical axons (Figure 3.19A). The results in this study suggest that presynaptic mitochondrial presence was related to bouton longevity and age, due to higher retention in older, long-lived boutons (Figure 3.22B, C, E). However, newly-formed boutons did have higher mitochondrial presence on their first day than by chance (Figure 3.22B). Other studies have also shown that mitochondria are retained more strongly at presynaptic sites compared to extrasynaptic sites (Smit-Rigter et al., 2016; Obashi and Okabe, 2013; Chang et al., 2006). The differential probability of mitochondrial presence between newly-formed and long-lived boutons could be due to differences in activity and subsequent calcium transients. Newly-formed boutons are likely to be smaller and therefore functionally weaker (Meyer et al., 2014) than long-lived boutons, as smaller boutons turnover at a much higher rate in layer 5 pyramidal cells of the motor cortex (Ash et al., 2018). Therefore, newly-formed boutons may have reduced calcium influx and calcium-dependent anchoring of mitochondria due to their decreased activity. Previous studies have shown that decreased activity (through pharmacological manipulation) reduces mitochondrial presence at boutons in a calcium-dependent manner (Vaccaro et al., 2017; Obashi and Okabe et al., 2013; Chang et al., 2006).

The structure of boutons was also related to their relationship with mitochondria, as EPBs were more strongly associated with mitochondria than TBs (45% versus 28%; Figure 3.21A). Specifically, mitochondria were less likely to be found at the head of a TB, presumably where the synaptic machinery was localised, than the base of a TB (28% versus 40%; Figure 3.21A). Previously, mitochondrial localisation to EPBs and TBs in saturated EM reconstruction of 0.13

mm^3 somatosensory cortex has made similar findings (Kasthuri et al., 2015), where 40% of EPBs possessed mitochondria and only 14% of TBs. Lower levels of mitochondrial presence would be expected in (<1% of spines; Kasthuri et al. (2015) as they used EM, and mitochondria were only scored within a bouton if they physically resided in the presynaptic terminal, compared to the 1.5 μm threshold used in this study. *Terminaux* boutons possess a structure similar to dendritic spines, which almost never contain mitochondria (Kasthuri et al., 2015). These results suggest that EPBs and TBs may have differential mitochondrial anchoring rates, which could lead to functional differences. Indeed, reduced anchoring of mitochondria at hippocampal boutons is related to decreased PSD area, synaptic vesicle pool size (including docked vesicles), and vesicle pool sizes in response to LTP stimulation (Smith et al., 2016). These functional differences are thought to be related to availability of ATP for vesicle cycling, rather than calcium regulation (Sun et al., 2013; Rangaraju et al., 2014; Smith et al., 2016). This is the first time that differences in EPB and TB mitochondrial anchoring have been explored *in vivo*. Future experiments should be aimed at determining differences in EPB and TB function through identifying cell-types with EPB- or TB-rich axons to correlate with their activity and role in the neocortex.

Newly-formed boutons had a very low survival rate of 10% after 35 days in comparison to pre-existing boutons with a survival fraction of 50% (Figure 3.23A). Very few studies have assessed the daily turnover of presynaptic boutons *in vivo*, instead longer imaging intervals (4-day, weekly or monthly) have led to an underestimation of true turnover and stabilisation rates (Qiao et al., 2015; Ash et al., 2018; Mostany et al., 2013). In this study, newly-formed boutons were lost very quickly, up to 30% in the first few days (Figure 3.23A), however survival plateaued and longevity increased with age, as seen previously (Qiao et al., 2015). This suggests a critical time window for strengthening or regulating new synaptic connections associated with new boutons, so that they persist.

The two bouton classifications of EPB and TB did not differ in their survival in the mature, pre-existing group (Figure 3.23B); however, the newly-formed bouton survival rates did differ between TBs and EPBs (median survival 6 days vs. 4 days, respectively; Figure 3.23C). This may be due to false positive identification of non-synaptic structureswhich are thought to be

about 10% of all axonal swellings along the backbone (Shepherd and Harris, 1998)-as *en passant* boutons. Grillo et al. (2013) have suggested that fluorescence intensity is strongly correlated with presynaptic bouton identification and not non-synaptic swellings, but their sample size was much smaller (~20 boutons). The putative non-synaptic swellings might be expected to be quickly lost again due to their lack of synaptic functionality, which matches the difference in survival seen between EPBs and TBs (Figure 3.23C).

Mitochondria may play a role in the critical window for survival of newly-formed boutons, because their presence decreased the relative number of newly-formed boutons that were lost in their first day by 20% (Figure 3.24A). For pre-existing (older) boutons, the relative decrease in loss was 45%, which was maintained at each later timepoint (Figure 3.24C). The difference in loss for newly-formed boutons could not be detected across time, potentially due to high variance and low numbers surviving (Figure 3.24B). These data show that the risk of a long-lived bouton being lost is doubled if that bouton does not have a resident mitochondrion. This is in line with the only other study, based on visual cortex neurons, that assessed bouton turnover in relation to axonal mitochondria (Smit-Rigter et al., 2016). The situation was further polarised for long-lived boutons upon splitting in to TB and EPB populations (Figure 3.24D). EPBs maintained the positive relationship between mitochondrial presence and survival, whereas for TBs this difference was greatly reduced, but still significant. Thalamocortical axonal projections have a high proportion of mitochondria at presynaptic terminals (80-100%; Bopp et al., 2017; Rollenhagen et al., 2015; Rodriguez-Moreno et al., 2018), and in a separate study have been shown to have a relatively high survival (De Paola et al., 2006). This supports the relationship between prevalence of presynaptic mitochondria and bouton survival in a different cell type, but will require more direct evidence within the same thalamocortical projection.

3.5.2 Limitations

While this study has revealed that mitochondrial localisation at presynaptic boutons is related to their structural plasticity, they are not sufficient for bouton formation, immediate survival or long-term survival alone. Suggestions for future work to address this are outlined in *General Discussion*.

The results in this study may be specific to the model system chosen. The model system chosen was male, adult mice from a wildtype background (C57Bl/6). Mice were used as a model of mammalian structural plasticity due to their similarity in cerebral cortical architecture to humans. They also share properties of structural plasticity with non-human primates (Stettler et al., 2006), with whom humans share a much closer common ancestor. Therefore, observed structural plasticity processes may also be conserved in humans. Male mice were used because of structural plasticity variability seen in females during oestrous cycles (Alexander et al., 2018).

Glass cranial window implantation is a relatively non-invasive technique, allowing chronic observation of the cerebral cortex. It is debated as to whether cranial window implantation causes prolonged inflammation after surgery, affecting the underlying biology (Holtmaat et al., 2009). Here, an anti-inflammatory drug (rimadyl) was given post-operation to reduce inflammation. Skull thinning is another technique also used for chronic long-term imaging (Yang et al., 2010), which is not as invasive and thought to result in less inflammation. However, repeated re-thinning of the skull after regrowth results in scar tissue, limiting the number of repeated observations. Glass cranial windows are very useful for the short-interval repeated imaging used here, whereas skull thinning is appropriate for longer intervals.

The labelling strategy used, viral transduction, may have led to toxicity in some labelled neurons. Virally-infected cells carry on expressing the proteins of interest without balanced turnover, however no apparent cell death has been observed in expression under Synapsin promoters that were used in this study (Watakabe et al., 2008). Steps were taken to avoid analysing cells overexpressing EGFP – axons that had exceptional EGFP intensity (strongest intensity in the volume) at any point were never analysed, and only axons present in all timepoints were tracked. This may have biased analysis of thinner axons. Very few axons were lost in the ROI during imaging, and the ones that were lost most likely retracted, as there was never evidence of blebbing or dystrophy in the images. Mitochondrial and bouton densities remained consistent across time, further suggesting that increased expression over time was not affecting the results.

The relatively small axonal segments (Figure 3.11) might not have been representative of the entire axonal arbor. This may have underestimated the true dynamics of the axon. Axon-centric dynamics were mainly avoided due to this reason, as small segments often resulted in measurements of zero – when they were actually extremely low. Longer axonal samples would solve this issue in the future.

A significant limitation of the study was the lack of additional information to validate the structures identified as boutons and mitochondria. The mitochondrial label (Mito-TagRFP) was tested *in vitro* in neuronal cultures to ensure targeting to mitochondrial structures. However, labelling may have been limited by turnover and trafficking of the protein in long-range axons. For axonal boutons, attempts were made to relocate boutons from two-photon imaging with electron microscopy to reconstruct them and assess reliability of bouton counting (see *Chapter 4*). Successful correlative light and electron microscopy studies have proved that swellings of ~2x the intensity of the axon backbone or more were functional synapses at the ultrastructural level (Grillo et al., 2013). Criteria used in this study were chosen to closely match Grillo et al. (2013), while also being consistent with studies from other groups (Ash et al., 2018; Morimoto et al., 2018; Sammons et al., 2018; Smit-Rigter et al., 2016). Semi-automated counting of boutons is possible and would be more consistent (Gala et al., 2017; Song et al., 2016; Bass et al., 2017); however, this still requires manual refinement to remove false positives and false negatives, re-introducing subjective decisions. A further limitation was the classification of boutons; non-synaptic swellings (Shepherd and Harris, 1998) may have been scored as EPBs, and TBs extending axially may have been falsely scored as EPBs due to poor axial resolution of 2P imaging. Further correlative work, using imaging modalities with increased axial resolution (EM or super-resolution microscopy), will be required to increase the confidence in bouton scoring.

Repeated laser exposure can cause heating of the brain (Podgorski and Ranganathan, 2016), and potentially phototoxicity to cells. However, there was no biologically significant trend seen in bouton dynamics or density with repeated imaging (Figure 3.12 and 3.14). This indicated that there were no compounding effects of repeated imaging but did not rule out a baseline effect. Laser power was kept under 60 mW average power as read from a power

meter at the sample to try to prevent damaging effects seen with higher laser powers (Podgorski and Ranganathan, 2016).

The distance threshold chosen to indicate mitochondrial presence may have been limiting the relationship. The threshold was based on previous studies showing mitochondrial effects close to boutons, at distances from 0 to 3 μm (Sun et al., 2013; Smith et al., 2016; Smit-Rigter et al., 2016). Multiple distances, as used in Smith et al. (2016), may be more appropriate for future work, but are restricted by the limited resolution of the 2P microscope used (~0.7 μm lateral point spread function; Figure 3.18).

The accuracy of bouton lifetime and mitochondrial positioning estimates over time are limited by the interval between imaging time points. For survival analysis, the higher the temporal resolution, the better. However, imaging frequency in this study was limited for ethical and logistical reasons. The daily intervals were still the smallest intervals attempted *in vivo* to study bouton and mitochondrial dynamics (Lewis et al., 2016; Smit-Rigter et al., 2016; Ash et al., 2018). On the other hand, weekly intervals used to track long-term survival led to lifetimes that could be inaccurate by up to seven days. However, both newly-formed and pre-existing boutons had plateaued survival at weekly intervals, suggesting lower rates of loss and subsequently better estimations of survival (Figure 3.23). Estimates of mitochondrial positioning were also based on low temporal resolution; it was assumed that mitochondrial positioning persisted throughout the daily and weekly imaging intervals. Smit-Rigter et al. (2016) used 4-day intervals to track mitochondrial localisation, this led to an estimation that the half-life of positioning was 4 days, although stronger at presynaptic sites. With that half-life, only around 30% of mitochondria would persist in their localisation over a weekly interval in this study – although this would be higher at synaptic sites. Not enough evidence was provided in Smit-Rigter et al. (2016) to confirm relocation of mitochondria or accuracy of alignment over time. Further work is needed *in vivo* with shorter time intervals or photoconvertible tools (Lewis et al., 2016) to make a more convincing estimation of mitochondrial turnover in axons.

CHAPTER 4 CORRELATIVE THREE DIMENSIONAL TWO-PHOTON AND SERIAL BLOCK-FACE SCANNING ELECTRON MICROSCOPY FOR NEURONAL TISSUE

Parts of the content of this chapter have been published previously (Lees et al., 2017). This chapter involved collaborative work. Lucy Collinson and Christopher Peddie at the Francis Crick Institute carried out the final stages of sample preparation (mounting tissue blocks on pins and coating for imaging) and serial block-face scanning electron microscopy. Sarah Hulme carried out all electrophysiology and live imaging of acute slices. Bethany Mulloy, Matthew Shapcott, Ellie Taylor, Thira Chartsakulkanajarn and Sarah Leathem carried out large-scale reconstruction efforts for relocation of *in vivo* imaged axons.

4.1 Introduction

Light microscopy (LM) is invaluable to cell biologists as a tool for obtaining dynamic information about cellular function and structure, especially with the aid of fluorescent reporters or dyes. Multiphoton (MP) fluorescence microscopy allows the

visualisation of these cellular dynamics deeper inside tissue than is possible with conventional fluorescence microscopy (e.g. confocal microscopy; Zipfel et al., 2003). Deeper imaging depths are achieved by employing lower energy, longer wavelength light in the near-infrared part of the spectrum (~700–1400 nm). To excite a fluorophore, near-simultaneous absorptions of multiple, lower-energy photons are required instead of a single, higher-energy photon, as in single-photon fluorescence microscopy. The probability of MP excitation is extremely low in comparison to single-photon excitation. To overcome this, the laser is repeatedly pulsed in ultra-fast (usually femtosecond duration) bursts to increase the photon density. Because photon density falls away with distance from the focal plane, the chance of obtaining MP excitation is effectively zero outside of the focal plane, conferring inherently high three-dimensional resolution (Zipfel et al. 2003). MP microscopy is advantageous to a cell biologist because the near-infrared light is refracted, absorbed and scattered less than visible light as it passes through the tissue. It is possible to routinely achieve imaging depths of around 300 μm with a sample that refracts very little light, with optimisation this raises to more than 1 mm (Helmchen and Denk, 2005; Tischbirek et al., 2015). Although there are other examples of MP excitation, this chapter is focused on two-photon (2P) excitation, the absorption of two photons, using a MP microscope.

Neuroscience research can utilise 2P microscopy to aid in studies of the mammalian brain that were previously limited to smaller, semi-transparent model organisms (Svoboda & Yasuda, 2006). It is possible to image the cortical neurons of mice longitudinally *in vivo* through cranial windows or thinned skull with either genetically-encoded or virally-expressed fluorescent reporters (Holtmaat et al., 2009; Yang et al., 2010). Electrophysiological studies can also be aided in the case of genetically-encoded calcium indicators (GECIs; Akerboom et al., 2012). GECIs are used to look at intracellular Ca^{2+} transients in neurons, which are a proxy measure of membrane depolarisation and hence neuronal cell activity. Another use of 2P microscopy in neuroscience is for the uncaging of neurotransmitter (e.g. glutamate;

Shoham et al., 2005). 2P excitation is used to uncage neurotransmitter with high spatial resolution and the response from the cell is used to map receptors on the neuron, or to induce activity in specific target cells (Ashby & Isaac, 2011). These techniques have contributed to the understanding of both structural and functional neuronal dynamics within the spatial resolution limits of 2P microscopy.

To obtain as much information as possible about the sample, multiple fluorescent proteins or dyes can be used. However, there are technical challenges to labelling and imaging multiple different fluorophores with 2P microscopy in tissue. These include, the lack of fluorophores with sufficiently separate 2P excitation spectra (Drobizhev et al., 2009; Drobizhev et al., 2011) and the difficulty of obtaining a good signal-to-noise ratio deep in tissue (Helmchen and Denk, 2005). Therefore, it has become routine to fix samples and probe for extra information through immunohistochemistry using other forms of LM (often with re-sectioning of the sample). This is especially useful for identifying cell types and protein localisation post-hoc. However, LM becomes limited by spectral and spatial resolution when identifying, quantifying and measuring multiple different subcellular structures that are abundant in the tissue volume (such as synapses and mitochondria). Problems also occur in penetration of the tissue with antibodies and therefore obtaining good signal from greater depths. Although there have been recent advances in this area including the reduction of light scattering in whole tissue samples by clearing (Renier et al., 2014), and serial sectioning of tissue for easier probing, re-probing and imaging by array tomography (Micheva et al., 2010), there are still significant limits to the resolution afforded by LM.

EM can overcome the resolution limits of LM to be able to distinguish subcellular structures that are a few nanometres apart. This resolution allows for the precise measurement of the geometry and organisation of thousands of subcellular structures. Structures can also be identified and have their function inferred using immunogold labelling of proteins (Zhong et al., 2013). However, a limitation to electron microscopy

is that the sample must be fixed to obtain this level of detail, eliminating any chance of obtaining further dynamic data. Processing of tissue for EM can also result in artefacts, depending on the fixation method, altering the true distribution of proteins and membranes (Korogod et al., 2015). As a tool for neuroscience, EM has been used to characterise the ultrastructure of neurons for decades (Palay, 1956; Gray, 1959; Shepherd and Harris, 1998; Kasthuri et al., 2015), resulting in a comprehensive understanding of structural identity, but without correlated dynamic information. Pairing neuronal dynamics from 2P microscopy with the ultrastructural environment provides unprecedented insights in to structure-function relationships (Mostany et al., 2013; Grillo et al., 2013; Meyer et al., 2014; Gala et al., 2017; Drawitsch et al., 2018). However, correlating 3D light and electron microscopy (3D CLEM) in the same tissue sample is not trivial.

Until recently, the only option for reconstructing tissue volumes at ultrastructural resolution was through serial section transmission EM (ssTEM) methods (Harris et al., 2006). This involves highly-trained individuals cutting and staining perfect serial sections, acquiring images and subsequently aligning them in a laborious workflow. However, by automating the sectioning, imaging and alignment simultaneously, time and human error can be mitigated. Both serial block face scanning electron microscopy (SBF SEM) and focused ion beam scanning electron microscopy (FIB SEM) achieve this goal. They work by destructively sectioning or milling off the top layer of the tissue and imaging each serial block face (Peddie & Collinson, 2014). It is conceivable to go from having a fixed brain tissue specimen to a registered 3D ultrastructural volume within two weeks (Karreman et al., 2016). Because FIB SEM and SBF SEM are destructive techniques, they are at a disadvantage in comparison to ssTEM methods (which have also become more automated in recent years; Kasthuri et al., 2015). The choice of technique depends on the volume to be analysed and the resolution required. At present, SBF SEM routinely produces a much larger volume than FIB SEM, albeit with lower axial (Z) resolution. The obtainable voxel size for SBF SEM is currently <20

nm in the Z-axis and <5 nm in lateral (X/Y)-axis, whereas FIB SEM can achieve an isotropic voxel size of 5 nm (Peddie and Collinson, 2014). In comparison, ssTEM reaches a pixel size of <0.5 nm and a reliable slice thickness of only 50 nm. The resolution limits of these systems are sufficient for identification of synaptic structures, making them attractive for use in neuroscience research, especially connectomics (Helmstaedter, 2013).

One of the technical challenges with 3D CLEM is finding a reliable and efficient method for relocating a region of interest (ROI) between imaging modalities. CLEM in tissue cannot benefit from gridded coverslips as in cell culture (Russell et al., 2016). Instead, other methodology has been implemented including immunogold labelling, DAB precipitation and microCT (micro computerised tomography). Immunogold labelling structures of interest (Zhong et al., 2013) can localise probes to proteins of interest, but does not help with relocating a specific LM ROI in large volumes of tissue. DAB precipitation in labelled cells (Knott et al., 2009; Martell et al., 2012; Hirabayashi et al., 2017) can be useful for relocating LM ROIs in thin embedded sections (60 μm), but the DAB precipitate obscures ultrastructural detail inside the cell of interest in EM images. Finally, microCT involves imaging nearby vasculature and using it as a fiducial marker between LM and microCT (Karreman et al., 2016). Blood vessels are highly contrasted in microCT images, which can be used to target the ROI during sectioning of embedded tissue for relocation of an LM ROI.

To circumvent the problems of existing approaches, such as obscuring or compromising ultrastructure or requiring additional imaging modalities, a technique was developed that uses the near-infrared laser of a MP microscope to make fiducial marks in tissue, termed near-infrared branding (NIRB; Bishop et al., 2011; Maco et al., 2014). The branding marks can be used to target relocation by placing them near to the fluorescent ROI. NIRB marks are precisely formed by increasing laser power to the point where damage occurs in the tissue. Cumulative build-up of light exposure

results in microbubbles pushing the tissue apart to form a hole over the area that the laser is scanned (Bishop et al., 2011). The damage caused is restricted to within a few micrometres of the focal plane, for this reason branding appears to be a multiphoton phenomenon. The edges of the branding marks are fluorescent in nature, with an emission spectrum similar to that of tissue autofluorescence, making them perfect for LM and EM correlation.

NIRB was first demonstrated by Bishop et al. (2011) and has been used with ssTEM and FIB SEM in brain tissue (Maco et al., 2014; Blazquez-Llorca et al., 2015). For relocation of a single synapse in a 1 x 10^9 μm^3 piece of brain tissue, NIRB marks can reliably reduce the search area to 1 x 10^3 μm^3; a million-fold decrease. Previously, the use of a single set of NIRB marks in one plane was used to relocate the ROI (Maco et al., 2014). Here, the efficiency and accuracy of relocation are increased by creating a 3D NIRB map. The map is formed of multiple fiducial NIRB marks that aid the relocation of an ROI throughout sectioning (ultramicrotomy). It is therefore possible to target ultramicrotomy efficiently and is especially useful where relocation can take a long time, e.g. larger block faces and ROIs deep in the tissue.

The aim of this study was to further develop the use of NIRB in 3D CLEM to aid in the relocation and ultrastructural reconstruction of axons that had been longitudinally studied *in vivo* (Chapter 3). This would provide additional information to characterise bouton age at the ultrastructural level. Additional applications were used in the development of this technique, which are also included in this chapter.

4.1.1 Key findings

- NIRB marks can be placed at multiple levels in tissue to reduce errors during relocation of an ROI by ultramicrotomy
- SBF SEM imaging is not appropriate for axonal reconstruction of adult mouse brain tissue due to the low axial resolution

- Axonal structure can be more easily traced and segmented in neonatal and juvenile tissue (< 21 days postnatal) from SBF SEM images
- Dendrites and axons appeared densely packed and contorted around a blood vessel in a particular block of adult mouse brain tissue

4.2 Materials

- MP microscope (e.g. Bruker Ultima Intravital, Leica TCS SP8 MP, Scientifica VivoScope etc.)
- Ti:Sapphire laser (e.g. Spectra-Physics Mai Tai DeepSee; Newport Spectra-Physics, UK)
- Low-magnification objective (e.g. 4x, 0.1 N.A.)
- High-magnification objective (1.0+ N.A.)
- Glass microscope slides
- Silicone grease
- Coverslips (# 1.0, rectangular, 22 x 40 mm)
- Plastic Pasteur pipettes
- Perfusion/dissection apparatus (e.g. Fine Science Tools)
- Small hemostats
- Large blunt scissors
- Medium sharp scissors
- Blunt forceps
- Small scoop
- Butterfly cannula with tubing
- 10 mL syringes (for PBS and DiI perfusate)
- 50 mL syringe (for fixative)
- 2/3-way tap
- Small, precision pen-grip drill with drill bit (e.g. dental drill, for drilling implant from cranial window imaging)

- PBS (0.01 M; 137 mM sodium chloride, 2.7 mM potassium chloride, and 10 mM phosphate buffer, pH 7.4)
- Glutaraldehyde (25% EM-grade)
- Paraformaldehyde (16% EM-grade)
- Sodium cacodylate
- Calcium chloride (C3306, Sigma-Aldrich)
- DiI (D282, Invitrogen; OPTIONAL – for labelling vasculature)
- D-Glucose (for DiI diluent)
- Ethanol (for DiI stock)
- Fine paintbrushes
- Glass vials (7–10 mL; e.g. G100, TAAB rolled rim vials)
- ACLAR® sheets (50 and 200 μm thickness; e.g. AGL4458, Agar Scientific)
- Razor blades (single and double-edged)
- Glass (for glass knives e.g. AGG336, Agar Scientific)
- Aluminium pins for SBF SEM specimen mounting (10-006002-50, EM Resolutions, UK)
- Osmium tetroxide
- Potassium ferrocyanide
- Thiocarbohydrazide
- Uranyl acetate
- L-Aspartic acid (A9256, Sigma-Aldrich)
- Lead nitrate
- Potassium hydroxide
- Ethanol (and anhydrous)
- Propylene oxide
- Durcupan ACM epoxy resin kit
- Cyanoacrylate glue
- Toluidine blue

4.3 Methods

4.3.1 Sample preparation

All animal experiments were performed according to the UK Animal (Scientific Procedures) Act, 1986. Sample preparation is outlined below, however this chapter deals with the development of CLEM methodology from the point of fixation onwards, therefore sample preparation steps before this are not discussed in detail.

Sample preparation for imaging used previously published methods for slice electrophysiology or *in vivo* imaging (Edwards et al., 1989; Holtmaat et al., 2009). For slice electrophysiology, brain slices were prepared from young mice pups (postnatal days 1–10) using standard slice preparation protocols. For *in vivo* imaging, animals were implanted with a cranial window (see *Methods* in Chapter 3). Ultimately, the neuronal tissue was fixed after live imaging.

For *ex vivo* slices, immediately after imaging the tissue was briefly washed three times in 2 mL of cold, fresh fixative (2.5% glutaraldehyde, 2% paraformaldehyde, 2 mM $CaCl_2$, 0.15 M sodium cacodylate in ddH_20, pH 7.4) using a fine paintbrush to transfer the tissue. Afterwards, the tissue was post-fixed for at least 2 hours in 2 mL fresh fixative at 4°C.

For adult tissue, after *in vivo* imaging the mouse was put under deep, terminal anaesthesia. Cardiac perfusion was then performed, first with 2-3 mL 0.01 M PBS at 5 mL/min, followed by 20-30 mL fresh, cold fixative (2.5% glutaraldehyde, 2% paraformaldehyde, 2 mM $CaCl_2$, 0.15 M sodium cacodylate in ddH20, pH 7.4) at 5-10 mL/min. Solutions were filtered through a 0.22 μm filter prior to perfusion. After exsanguination, 10 mL DiI (120 μg/mL) was perfused after PBS and prior to the fixative to visualise vasculature. To make DiI working solution, 200 μL of 6 mg/mL DiI in 100% EtOH was diluted in 10 mL of a 1:4 mix of 0.01 M PBS and 5% glucose (wt/vol in dH2O; Li et al., 2008). To obtain tissue under the cranial window, after perfusion and before harvesting tissue the animal was decapitated and the cranial window implant was left on during post-fixation (2 hours in 10 mL fresh fixative at 4°C). Subsequently, the window and skull were removed using a precision hand drill and forceps to expose the imaged brain region, leaving the head bar intact. 0.01 M PBS was continuously applied using

a Pasteur pipette to keep the area from drying. The head was then mounted in the same fixation device used for 2P imaging and a 100–400 μm slice was cut using a vibratome at the same angle as 2P imaging in 0.01 M PBS. The slice was then post-fixed for a further 2 hours in 2 mL fresh fixative at 4°C.

Alternatively, tissue that did not require live imaging was harvested from animals depending on the age. Adult animals were perfusion-fixed (as above for *in vivo* imaging). Juvenile animals that were not old enough for perfusion-fixation were cervically dislocated, decapitated and the brain tissue was incubated in fixative solution (2.5% glutaraldehyde, 2% paraformaldehyde, 2 mM $CaCl_2$, 0.15 M sodium cacodylate in ddH_20, pH 7.4) at 4°C for 2 hours. Afterwards, a 100–400 μm tissue section was cut from the appropriate region of the brain in 0.01 M PBS using a vibratome.

4.3.2 Two-photon microscopy

Different 2P microscopes were used in this study for imaging and NIRB (e.g. Bruker Ultima Intravital, Leica TCS SP8 MP, Scientifica VivoScope). However, all possessed the same essential components. These were: a Titanium:Sapphire (Ti:Saph) laser for NIRB marks and deep imaging, PMTs for emitted light detection, a white light source and camera (e.g. Thorlabs USB-C for brightfield imaging), low magnification objective (e.g. Olympus 4x 0.1 NA for brightfield), high magnification objective (e.g. Olympus 60x 1.1 NA for 2P and NIRB), control software (e.g. Scanimage, SciScan, PrarieView, Leica LAS X) and a motorised stage for ROI relocation and precision placement of NIRB marks.

4.3.3 Imaging of fixed tissue

Tissue sections were left in fixative until required for branding (no more than 24 hours). Each tissue section was washed in 0.01 M PBS and mounted inside a silicone grease well on a glass microscope slide using a few drops of 0.01 M PBS, covered with a large rectangle coverslip. Alternatively, parafilm was used to create a well from spacers with rectangular cut-outs pressed on to a glass microscope slide. The spacers were stacked to create a well that was suitable for the thickness of the slice. An additional sheet of parafilm was placed on top and

pressed gently on to the spacers to seal the tissue inside. Care was taken so that no air bubbles remained, and the tissue could not drift.

Low-magnification (4x objective, 0.1 NA) brightfield images were collected using a camera. If the tissue was larger than the field of view (FOV), a set of images were acquired and stitched together to create a mosaic image of the tissue. If there was no obvious landmark, one was introduced by cutting the tissue on a corner with a scalpel.

High-magnification (40–60x objective, 0.8-1.1 NA) 2P images were acquired using a Ti:Saph laser tuned to 800 nm for Alexa Fluor 594, 910 nm for EGFP, or 1040 nm for TagRFP, tdTomato. Images were taken with the maximum possible FOV of the 2P microscope to maximise correlative information. These images were taken in z-stacks from 10–20 μm below the ROI to the tissue surface at 0.5 μm steps. Subsequently, images with a 50–100 μm FOV were taken at high resolution (100 nm pixel size) with 0.5 μm steps from the ROI to the surface.

4.3.4 Near infrared branding

NIRB was tested in an area of tissue away from the ROI, but at the same depth, to determine the extent of damage caused by chosen settings. Generally, the laser was first set to 800 nm wavelength, 150 mW (average power as read from power meter at the sample) and 20 μs pixel dwell time. Testing was carried out using the segmented or straight linescan function and adjusting the number of lines scanned to increase or decrease the branding volume. If the linescan was not branding, the pixel dwell time or laser power were also increased. Testing was carried out until NIRB marks were reliably made at a size of 2–4 μm in width and 5–10 μm in depth – making them large enough to be re-identified in embedded tissue. Greater branding accuracy was achieved using a higher NA objective which focused the light more tightly.

After determining appropriate settings for reliable branding, an asymmetrical shape of 20 μm along the longest edge was made in the tissue at 5 μm superficial to the structure of interest. Tighter markings could be made, but they were more likely to cause accidental damage to the ROI. Some drifting would occur during imaging, so the ROI was re-centred before branding

each mark. High laser power would damage the PMTs, so they were turned off before commencing the linescan.

Subsequent branding marks were made every 10–15 μm in the Z-axis from the ROI to the surface, with each mark having a progressively longer side length. The final branding mark was in the shape of a cross, <2 μm below the tissue surface. Finally, 2P images were acquired of a large and small FOV around the ROI to document the NIRB marks (as above in *Imaging of fixed tissue*).

4.3.5 Staining, dehydration and flat-embedding

Staining and embedding steps were carried out in a fume hood using personal protective equipment (gloves, goggles, lab coat) as most of the chemicals used were harmful or toxic. All incubation steps at room temperature (RT) or 4°C were done in a tissue rotator (at 2 rpm). All steps were carried out in the same glass vial, transferring chemicals using a plastic Pasteur pipette, unless otherwise noted. A new pipette was used for each chemical. Chemicals were not applied directly on to the tissue and the tissue was not manipulated directly at any stage, as it became extremely brittle after osmication.

After fixation, the tissue was transferred to a small glass vial using a fine paintbrush and washed 5 x 3 min in cold 0.1 M cacodylate buffer containing 2 mM $CaCl_2$. The tissue was then incubated in 2 mL reduced osmium (equal parts of 3% potassium ferrocyanide/0.3 M cacodylate/4 mM $CaCl_2$ to 4% aqueous osmium tetroxide) for 1 hour at 4°C. Afterwards, the tissue was washed for 5 x 3 minutes with ddH_2O at RT then filtered thiocarbohydrazide (TCH) was added and incubated for 20 minutes at RT. TCH solution was made fresh; 0.1 gram of TCH was added to 10 mL ddH_2O and dissolved at 60°C for 1 hour. The solution was agitated gently by hand to aid dissolving. Afterwards, it was filtered through a 0.22 μm syringe filter (Millipore) before use.

After TCH incubation, the tissue was washed for 5 x 3 minutes with ddH_2O at RT. Osmium tetroxide (2% in ddH_2O) was then added and the tissue was incubated for 30 minutes at RT. The tissue was then washed for 5 x 3 minutes with ddH_2O at RT followed by overnight (16 hours) incubation in 1% uranyl acetate (aqueous in ddH_2O; 0.22 μm filtered before use) at 4°C.

The next day the tissue was washed for 5 x 3 minutes with ddH_2O at RT. After the uranyl acetate was washed out, the tissue was incubated in Walton's lead aspartate for 30 minutes at 60°C. To make Walton's lead aspartate, 0.066 g of lead nitrate was added to 9 ml 0.03 M aspartic acid stock and then pH was adjusted to 5.5 using 1 M potassium hydroxide and then incubated at 60°C for 30 minutes. If precipitate formed, the solution was re-made. The tissue was then washed for 5 x 3 minutes with ddH_2O at RT. Afterwards, dehydration of the tissue was carried out through serial incubations with EtOH dilutions of 20%, 50%, 70%, 90% (in ddH2O), 100% and 100% EtOH (anhydrous) for 5 minutes each and finally fresh 100% EtOH (anhydrous) for 10 minutes.

The dehydrated tissue was then incubated in propylene oxide for 10 minutes while Durcupan ACM resin was made. A glass Pasteur pipette was used for propylene oxide, as it corrodes plastic. To make Durcupan ACM resin, 11.4 g part A (epoxy resin), 10 g part B (hardener), 0.3 g part C (accelerator), 0.05-0.1 g part D (dibutyl phthalate) were added sequentially on top of each other, mixing well after each part was added. Tissue was transferred through serial incubations of 25%, 50% and 75% Durcupan in propylene oxide for 2 hours each. Finally, the tissue was incubated in 100% Durcupan overnight and changed to fresh 100% resin in the morning for 2 hours.

The tissue was then carefully removed from the resin using a cocktail stick and transferred to a flat-embedding chamber. The chamber was made on a glass microscope slide from a rectangular sheet of Aclar® as a base and more sheets with rectangular cut-outs in the centre as spacers, all glued together with cyanoacrylate glue. Excess resin was removed from the tissue and a drop of fresh resin added. The resin chamber was sealed with a layer of Aclar® using cyanoacrylate glue and placed in a 60°C oven to polymerise for 72 hours. A relatively heavy metal block was placed on top to keep the specimen flat.

4.3.6 Semi-thin sectioning

After resin polymerisation, the flat-embedding chamber was retrieved from the oven and the layers of Aclar® were removed using a thin razor blade. Each Aclar® layer was peeled away

from the resin and the tissue was imaged using a stereo microscope to determine the correct face to begin sectioning from. Excess resin around the tissue was trimmed using a razor blade.

A thin layer of cyanoacrylate glue was used to attach the resin-embedded tissue to a flat-topped blank resin stub, making sure the tissue face containing the ROI faced upwards. The glue polymerised for at least 2 hours before sectioning. The stub was then mounted in an ultramicrotome and a razor blade was used to outline the rough area (2 x 2 mm square) of the ROI on the block face. The block face was then trimmed to a trapezoid-faced pyramid.

Semithin sections (0.5–1.0 μm) were cut from the block face using a glass knife at 2.0 mm/s (knife speed) until tissue was present in the sections. Each section containing tissue was transferred to a clean glass microscope slide and dried. Every section was imaged using a brightfield microscope until the first branding mark was relocated on the tissue surface. The block face was then roughly trimmed around this region. Semi-thin sections were stained with 1% toluidine blue (in 1% borax) if it was difficult to get contrast in the tissue. Sectioning was continued until each successive NIRB mark was relocated. Once the final NIRB mark was relocated, the block face was trimmed tightly (<1 x 1 mm) around it.

Preservation of ultrastructure was checked by transmission electron microscopy (TEM). A few ultrathin sections (70 nm) were cut using either a diamond histoknife or glass knife, mounted on a copper grid and imaged using a TEM without counterstaining.

4.3.7 Serial block-face scanning electron microscopy

Further sample preparation was required before the block could be imaged. The block was covered with parafilm and the top 2 mm was trimmed off with a razor blade. The trimmed piece was mounted on an aluminium pin using conductive epoxy resin and baked overnight at 60°C. Subsequently, the block was sputter coated with 2 nm platinum to improve conductivity.

The pin was mounted in the 3View attachment for the scanning electron microscope and the block face polished with 100 nm cuts from a diamond knife, before closing the chamber door and pumping to 5-10 Pa of nitrogen gas. The block was imaged during approach cuts to

relocate the ROI. The ROI was then centred in the FOV, and parameters were set for SBF SEM imaging and sectioning. The SEM was operated at an accelerating voltage of 2 kV with high current mode active, a 20 μm aperture, and chamber pressure of ~5 Pa. Pixel dwell time of 2 μs was used with a slice thickness of 50 nm. Images were acquired at the maximum size of 8192 x 8192 pixels, magnification was altered depending on the FOV required (25–50 μm).

4.3.8 Image processing and reconstruction

Individual EM images were large, in the region of 250 MB, and a serial imaging run of 500–1000 images easily reached 250–500 GB. The image stack was batch converted to a .tiff stack in Digital Micrography (Gatan Inc) or in ImageJ (FIJI package; Schindelin, 2012) using the BioFormats importer (Linkert, 2010) for easier handling. Large .tiff stacks were handled in FIJI and other software using a virtual stack to reduce RAM load. Contrast variation was reduced throughout the volume by equalizing the histogram (0.3% pixels saturating) and smoothing the images with a Gaussian filter (2 sigma) to increase contrast.

Large files were down-sampled from 32-bit to 8-bit using the Batch Convert plugin to reduce file size and increase navigation speed by reducing RAM load. This was used when doing rough correlation and tracing of structure without fine subcellular structural detail.

The NIRB mark present in the EM data was used to align the rotation of the 2P images. The high-resolution 2P images of the ROI were used to measure the rough distance between the plane of NIRB and the plane of the structure of interest. The SBF SEM images were then correlated to 2P images using manual (rotational and scale changes in ImageJ) or automated techniques (Icy plugin, eC-CLEM; Paul-Gilloteaux et al., 2017) and fiducials for reference e.g. cell bodies, vasculature and branding marks.

Structures of interest were subsequently manually reconstructed in FIJI software using TrakEM2 (ImageJ plugin; Cardona et al., 2012) or in Amira 6.0.0 software (FEI). Both have guides available online or within the software itself to cover the file import and segmentation followed by reconstruction, display and measurements. For Amira, the software guide was used (https://www.fei.com/software/amira-user-guide/), alternatively the FEI YouTube channel is populated by some video guides (https://www.youtube.com/channel/UC33gA9Z-

FtCccsj29Z-c2gw). For TrakEM2, the tutorials on the ImageJ website were used (http://imagej.net/TrakEM2_tutorials).

4.4 Results

4.4.1 Development and optimisation of techniques for correlating light and electron microscopy in neuronal tissue

Although the total time from live sample to correlated light and electron images has been reduced dramatically, thanks in part to SBF SEM technology (Peddie and Collinson, 2014), the least reliable step is still ROI relocation after tissue staining and embedding. After tissue fixation, both fluorescent and non-fluorescent images of the ROI and surrounding tissue were taken to provide accurate maps to narrow the search for the ROI in the lateral dimension after embedding (Figure 4.1). The highest resolution images (60x 1.1 NA objective, 1024 x 1024 pixels) of the ROI were used for aligning and correlating EM images, whereas images with a larger FOV (300 μm to 3 mm) were used to orient and position the embedded tissue during sectioning.

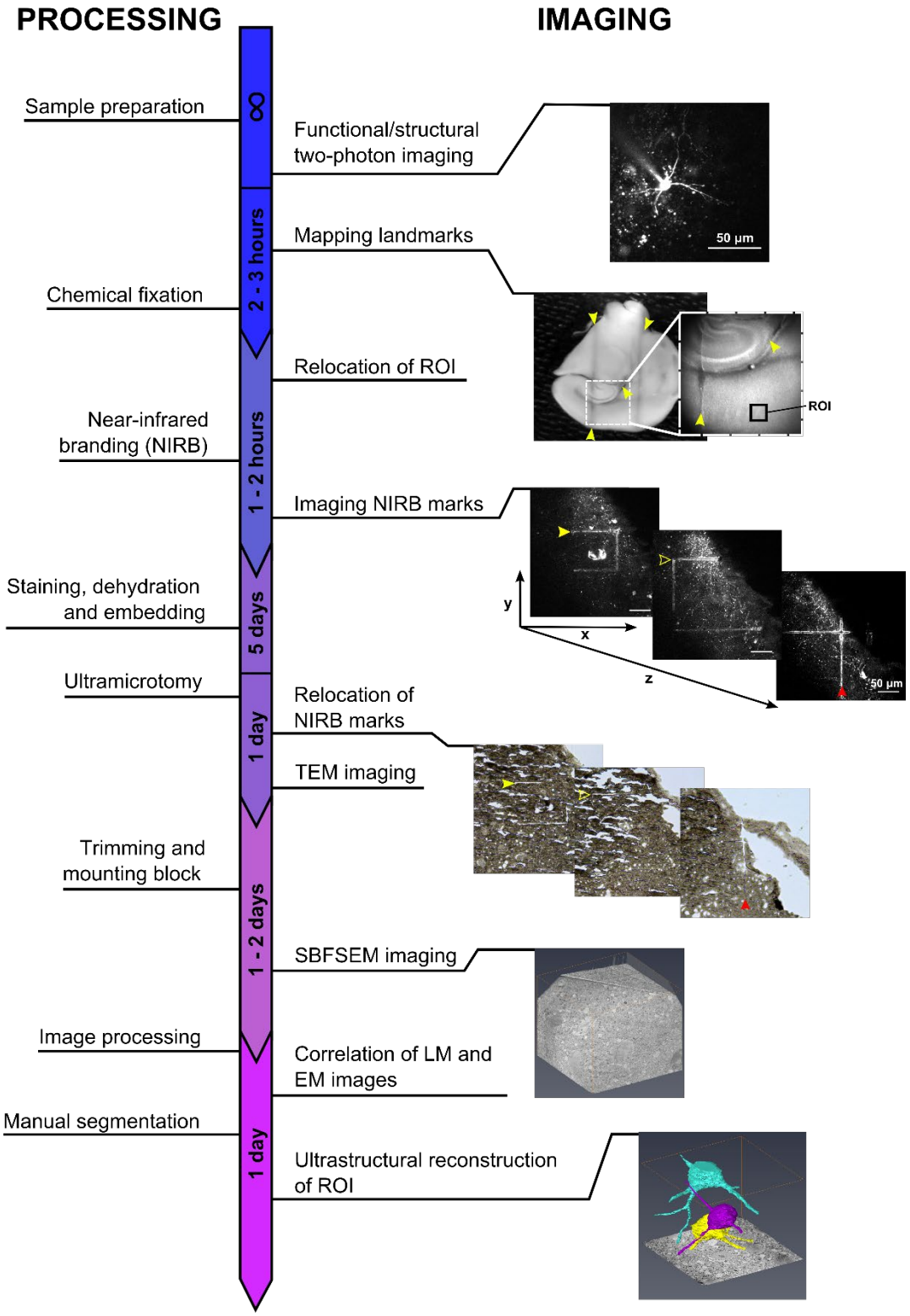

Figure 4.1 Workflow for correlative three-dimensional two-photon and serial block-face scanning electron microscopy. Tissue processing steps are listed on the left of the timeline and imaging steps on the right. The total duration of the workflow is ~10 days, depending on the final segmentation and reconstruction required. The time for each part of the workflow is estimated in the timeline and breaks are allowed between each part of the workflow (see Methods section for details).

Once the tissue had been stained and embedded, all fluorescence was lost, and the tissue appeared mostly homogeneous. Therefore, near-infrared branding marks were made in the fixed tissue before emedding to create fluorescent fiducial marks that could also be resolved in EM images (Figure 4.2). Previously, NIRB marks were made in a single z-plane near the ROI (Bishop et al., 2011; Blazquez-Llorca et al., 2015). Here, multiple marks were made in different z-planes to increase the success of relocating them and provide more fiducial points during sectioning of the embedded tissue (Figure 4.2A). After the tissue was fixed, an ROI was relocated using 2P microscopy, then the same Ti:Saph imaging laser was used at a higher power and with increased pixel dwell time to brand the tissue (Figure 4.2B). NIRB marks were made in a concentric pattern, where larger marks were made closer to the tissue surface. The additional marks added a layer of redundancy during ROI relocation in semi-thin sections (0.5–2 μm) of embedded tissue, where NIRB marks could be missed. Marks were preferably made in a shape with as few axes of symmetry as possible (i.e. not a square; Figure 4.2D) to easily re-orient the tissue in later parts of the workflow. Branding marks closest to the structure of interest were made using relatively low settings, to reduce excess damage, but enough to make a physical hole in the tissue for later relocation (Figure 4.2E, F). Bubbles were a common artefact of NIRB, which could obscure images of the branding marks or ROI (Figure 4.2D), but they mostly disappeared with time (Figure 4.2C).

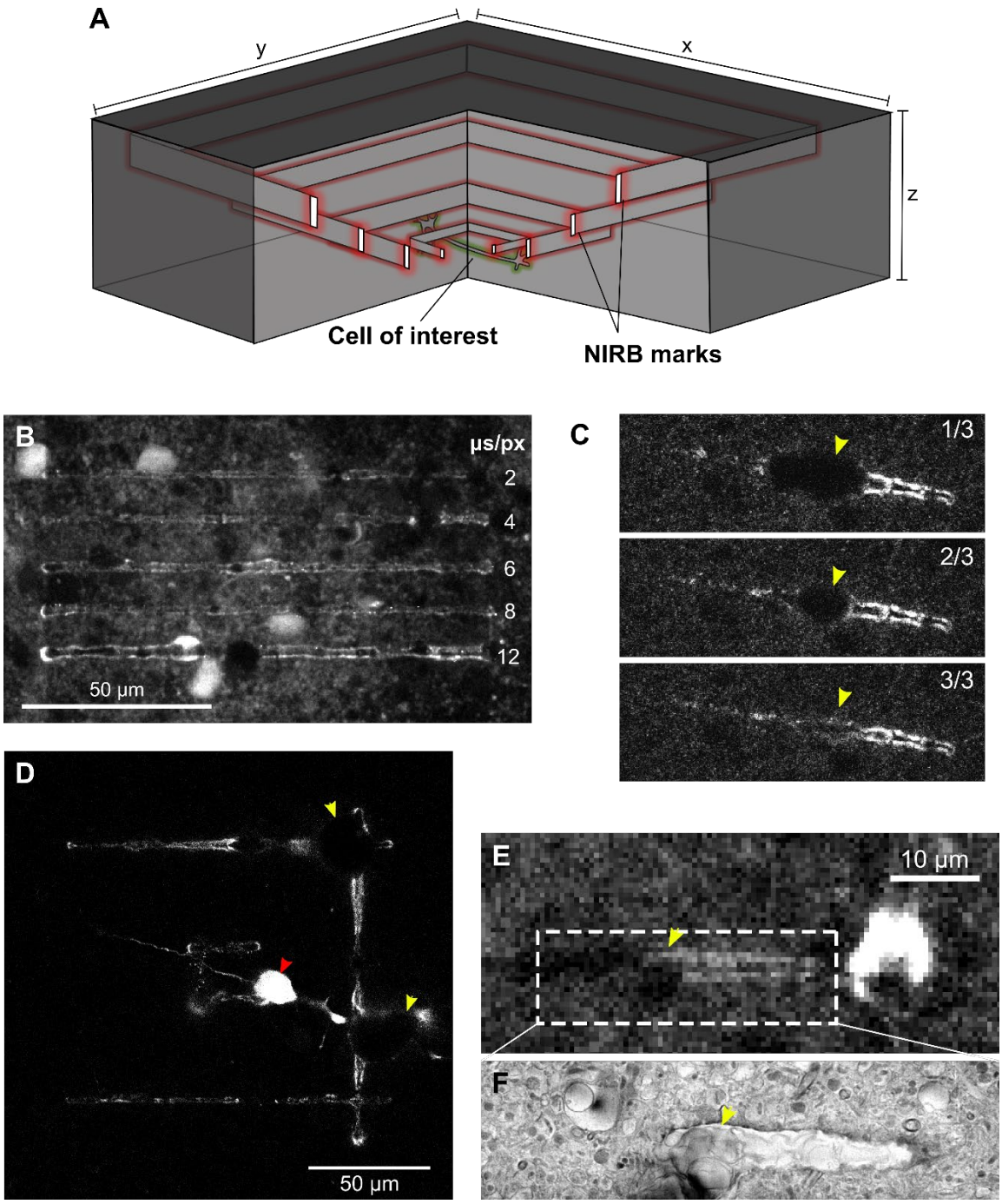

Figure 4.2 Near infrared branding parameter optimisation and artefacts. (**A**): Schematic of near infrared branding (NIRB) strategy showing a cross-section of tissue with a labelled cell of interest. Asymmetric NIRB marks were made in a three-dimensional concentric pattern from the cell to the tissue surface. (**B**): Two-photon image of NIRB marks showing that increased laser pixel dwell time (µs per pixel) resulted in thicker NIRB marks. Notice that NIRB mark outlines were fluorescent. (**C**): Time-lapse of two-photon images after a NIRB mark was made. A bubble is highlighted (*yellow arrowhead*), disappearing over time (~2 min). (**D**): NIRB marks were fluorescent in tissue without any endogenous fluorescence. Bubbles (yellow arrowhead) were undesirable as they obscured imaging. Red arrowhead = neuronal soma. (**E** and **F**): Two-photon (E) and electron micrograph (F) of a NIRB mark. Notice that only the area of the NIRB mark with high fluorescence intensity indicates damage, as shown in the electron micrograph (*yellow arrowhead* = reference point).

An altered reduced osmium-thicocarbohydrazide-osmium (ROTO) *en bloc* method (see *Methods*; Tapia et al., 2012) was used to post-fix and stain the tissue after NIRB. Once embedded, the correct orientation for mounting the stained and embedded tissue was achieved using brightfield images taken before staining (Figure 4.3A-D). The embedded tissue was trimmed to the approximate area of the ROI and then sectioned between 0.5 and 2 μm at a time (Figure 4.3E-G). It was common for the tissue to be extremely brittle at this stage. Initially, a cutting speed of 2.0 mm/s and section thickness of 1 μm for semithin sectioning was used. However, if major artefacts were seen in the semithin sections (e.g. tears and holes), the cutting speed was reduced to 1.5 mm/s and section thickness to 500 nm. Each section was checked for NIRB marks and used to trim the block face closely around the ROI. Two-photon images of the NIRB marks were referred to, to determine the axial distance from the block face to the ROI after relocation of each mark.

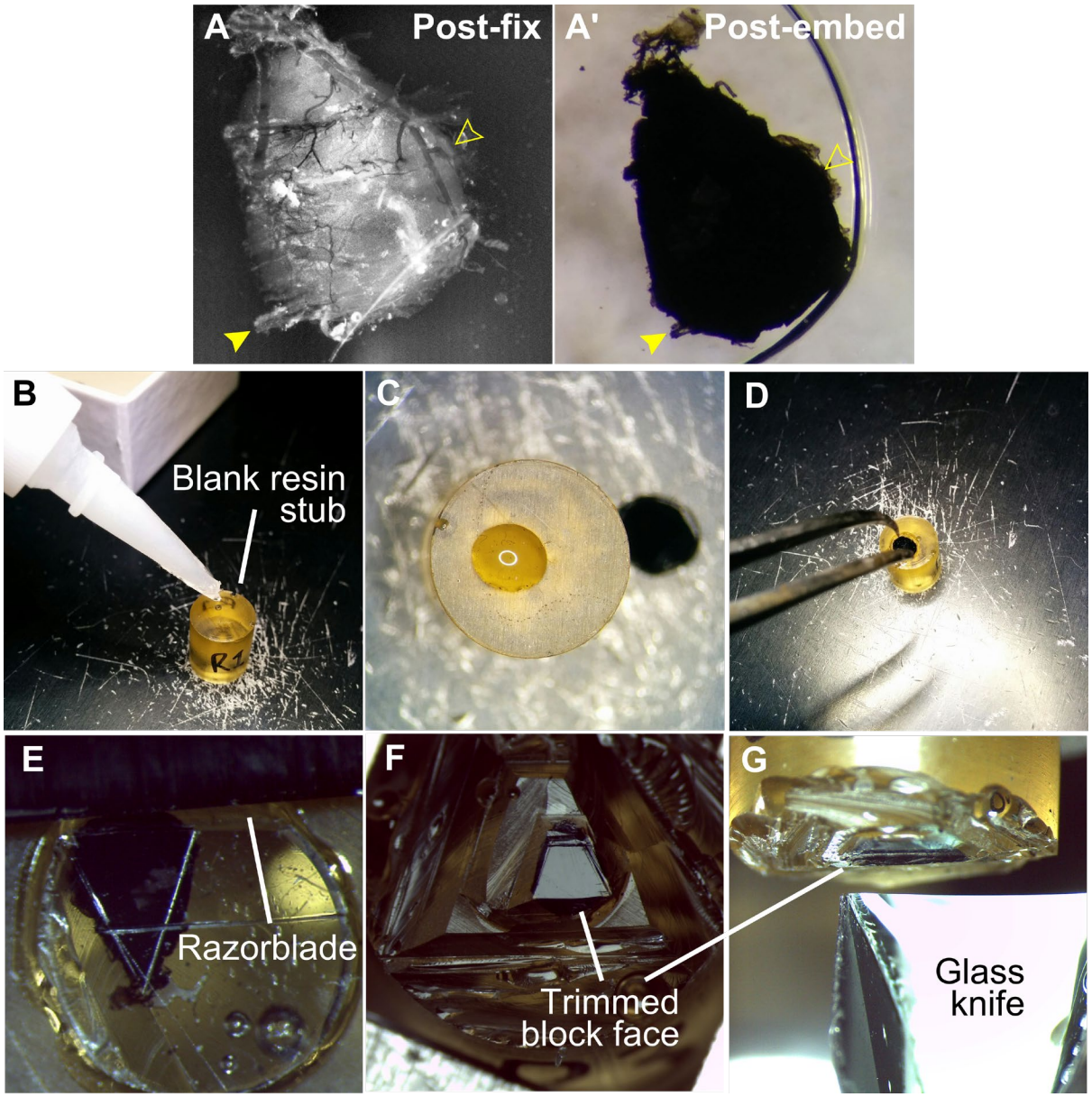

Figure 4.3 Relocation of the ROI on the block face. (**A** and **A'**): Images of the tissue with high contrast after fixation (A) and with no contrast after staining and embedding (A'). Only the outline of the tissue could be used for correct orientation, good documentation was needed to do this. (**B**-**D**): The embedded tissue was secured with cyanoacrylate glue (B) to a flat-faced blank resin stub (C and D). (**E** and **F**): After polymerisation of the glue, the block face was trimmed to an area roughly 2 x 2 mm, centred on the estimated location of the ROI. (**G**): A glass knife was used to cut semi-thin sections for identification of NIRB marks.

Ultimately, the 1 x 1 mm block face centred on the final NIRB mark was cut from the block and mounted for SBF SEM imaging (Figure 4.4A–E). The NIRB mark in the final semi-thin section was correlated to the block face during approach cuts and images (Figure 4.4F, G). SBF SEM images were acquired at a pixel size that was dependent on the resolution and FOV required for the structure being resolved. Resin choice was important for image quality during SBF SEM imaging. Agar 100 Hard resin resulted in many more artefacts, such as flaking or charging (Figure 4.4H), than Durcupan ACM (Figure 4.4I). Before correlation to 2P images, SBF SEM images were processed to remove fluctuations in contrast (Figure 4.4I), the ROTO staining protocol provided good membrane contrast in SBF SEM images. Overall, minor modifications to the workflow resulted in more reliable relocation of the ROI and consistently high quality SBF SEM images.

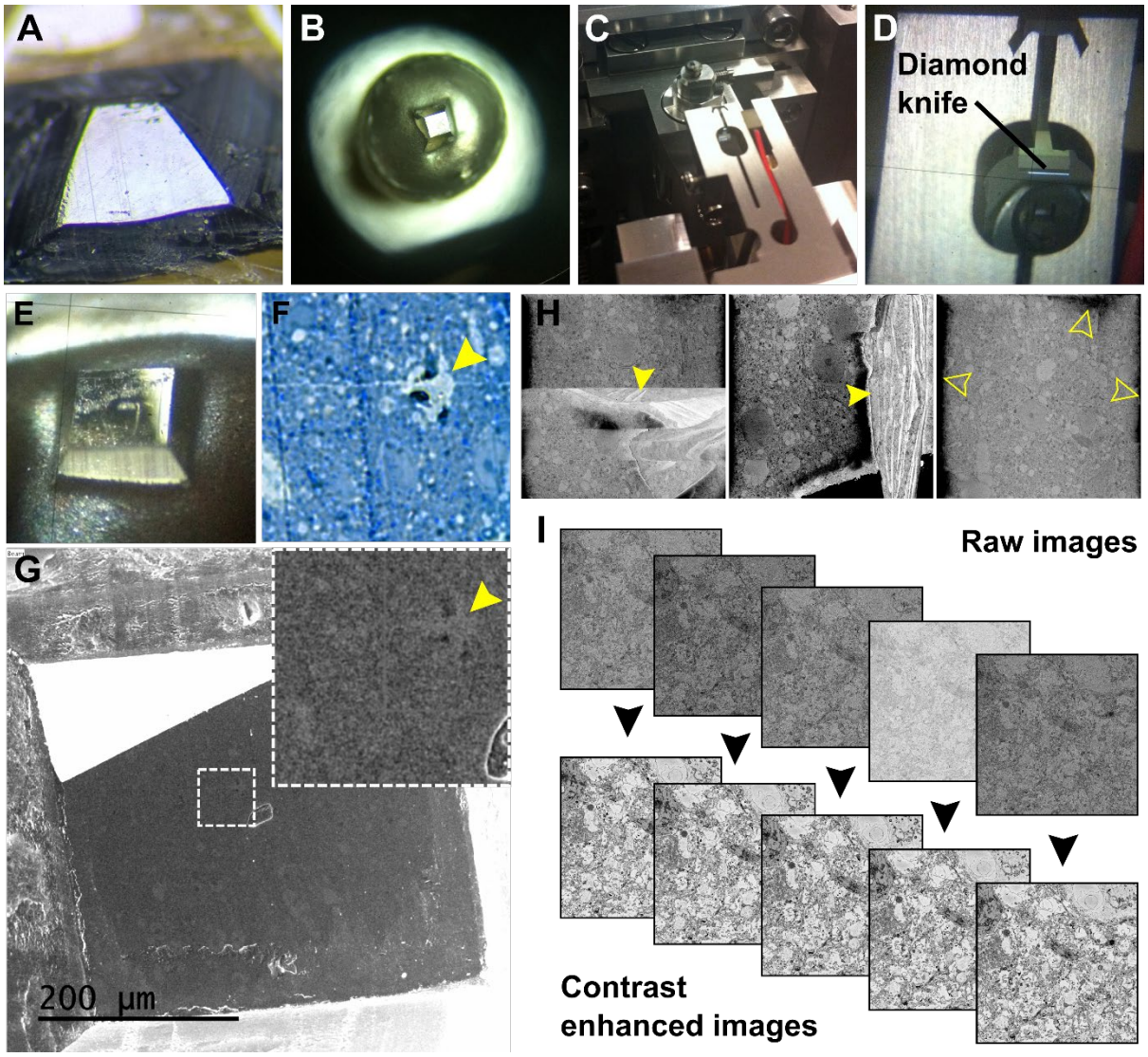

Figure 4.4 Serial block-face scanning electron microscopy sample preparation. (**A-D**): The top 2 mm of the final trimmed block face (1 x 1 mm; A) was cut from the block and stuck to an aluminium pin (B), coated in 2 nm platinum and then mounted in the scanning electron microscope (C and D). (**E**): The top of the block was polished with cuts from a diamond knife. (**F** and **G**): Brightfield image of a stained semi-thin section showing the final NIRB mark in a piece of tissue (F) for comparison with the images taken during approach cuts (G). Yellow arrowhead = reference point. (**H**): Improper resin choice resulted in poor cutting of 50 nm sections. Flaking (left and middle) and charging (right) artefacts were seen when using Agar 100 resin. (**I**): Raw images from SBFSEM contained some noise from nitrogen gas. Noise was easily removed with contrast enhancement and normalisation across the stack. Durcupan ACM resin was also used here to reduce the charging artefacts seen in (H).

4.4.2 Targeted relocation of labelled neurons for ultrastructural characterisation

Neurons differ in their genetic identity and can be classified by these differences (Ascoli et al., 2008). To highlight the use of NIRB for cell-specific 3D CLEM, neurons in layer 4 of the somatosensory cortex were transgenically labelled with the red fluorescent protein, tdTomato. A 400-µm brain slice was fixed and imaged using 2P microscopy (Figure 4.5A, B) and a cell of interest was chosen (50 µm below the surface) to be reconstructed at the ultrastructural level (Figure 4.5D). Branding was completed in multiple z-planes, centred on the cell of interest (Figure 4.5C) and 2P images were acquired of the NIRB marks. After staining the tissue and embedding in resin, semi-thin sections were taken and correlated to 2P images to relocate the cell of interest on the block face (Figure 4.5C). To capture more of the cell of interest, SBF SEM images were acquired with a large FOV but still a suitable pixel size for identification of organelles and some synaptic structures (56 x 56 µm FOV, pixel size of 6.8 nm, 50 nm sections).

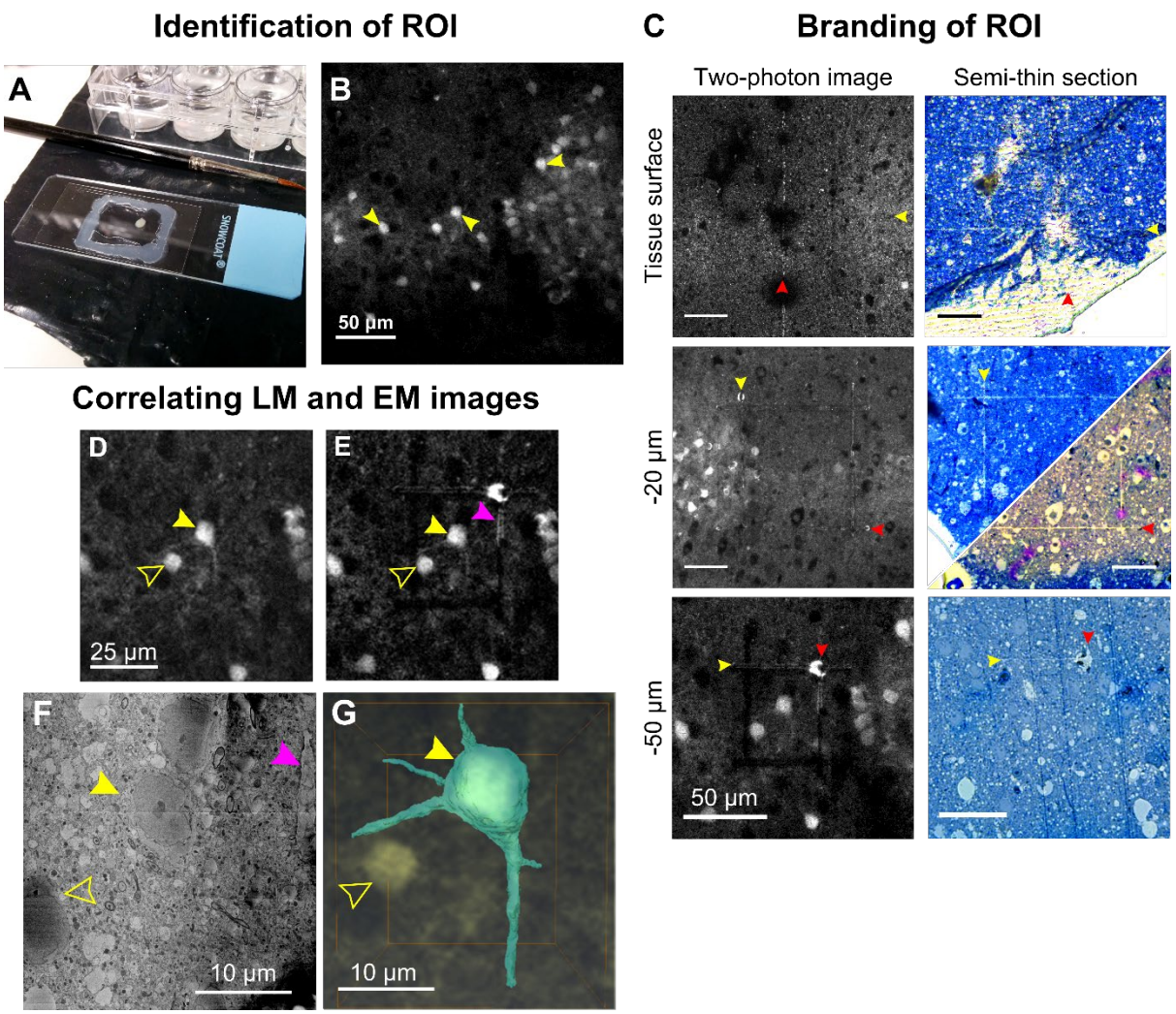

Figure 4.5 Relocation of a neuron from a fixed brain tissue slice. (**A**): The tissue was mounted in PBS inside a well, made from silicon grease, on a glass microscope slide. A coverslip was pressed down on top to secure it in place. (**B**): Tissue from a transgenic mouse expressing tdTomato in layer 4 cells of the somatosensory cortex. Cell bodies are indicated (yellow arrowheads). (**C**): Representative two-photon images, paired with brightfield images of stained semi-thin sections at different levels in the tissue. Reference points are indicated for each pair of images (yellow and red arrowheads). (**D-G**): Two-photon (D and E) and SBF SEM (F) images were correlated by manual comparison for the identification of a single neuronal soma (filled yellow arrowhead). The NIRB mark (magenta arrowhead) acted as a fiducial marker between the light and electron images, additional fiducial markers were also useful, such as an additional labelled cell soma (empty yellow arrowhead). An overlay of the two-photon image with a reconstruction of the cell of interest is shown (G).

Correlation of the 2P images with the SBF SEM images was carried out manually as the SBF SEM volume was only 56 x 56 x 50 µm and contained very few somata (Figure 4.5E-G). Finally, the cell was reconstructed using Amira software and overlaid with the original two-photon image.

This methodology was also successful in relocating cells and specific dendrites filled with fluorescent dye during whole-cell patch clamp electrophysiology recordings (Figure 4.6). Imaging parameters were altered for subsequent SBF SEM runs to increase image resolution (25 x 25 μm FOV, pixel size of 3.1 nm, 50 nm sections) for the identification of individual synaptic vesicles (Figure 4.7), making it possible to do CLEM at the synaptic level.

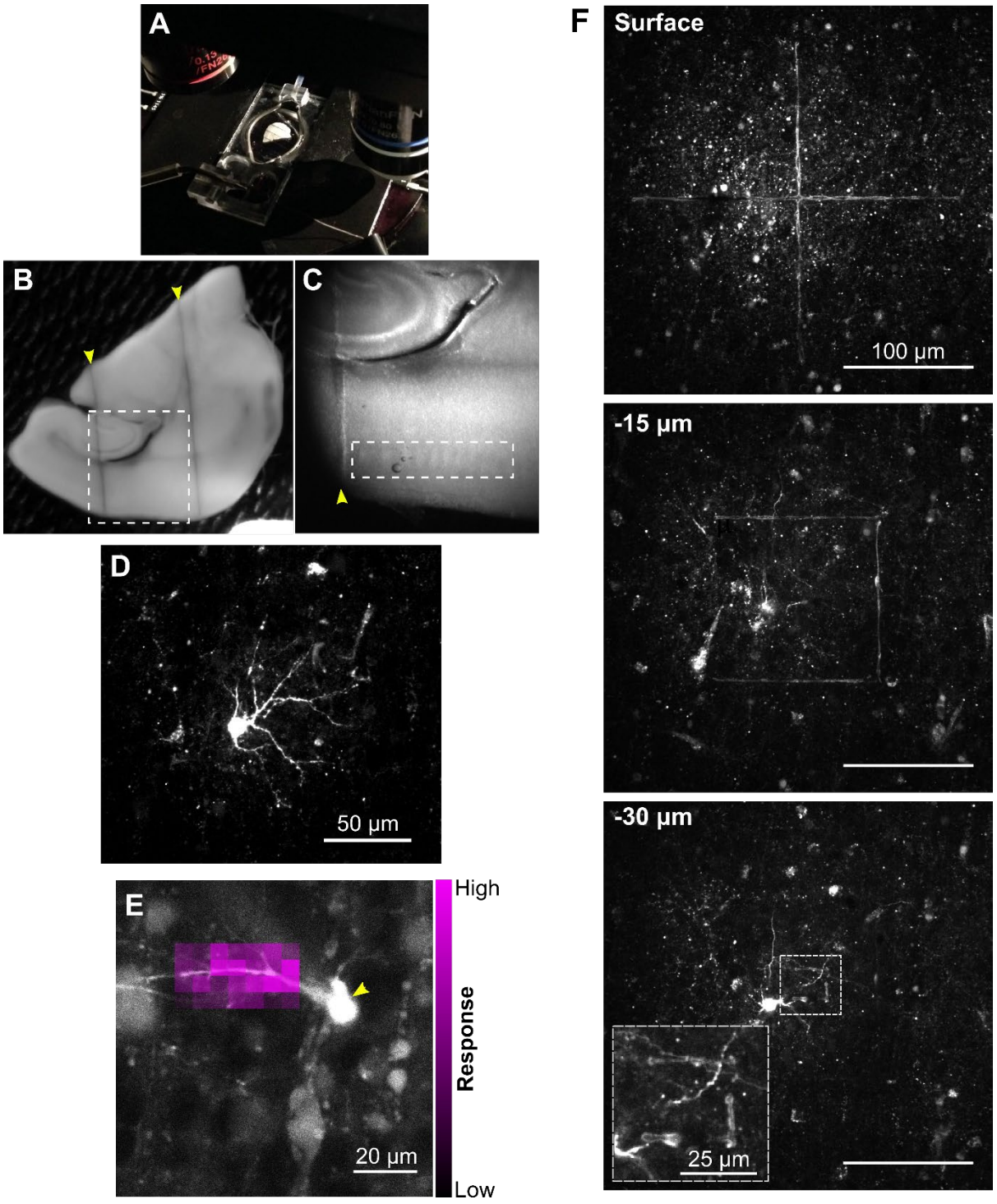

Figure 4.6 Relocation and branding of a dendrite previously imaged during an electrophysiology recording. (**A**): An acute thalamocortical tissue slice was fixed after experimentation and then re-mounted. (**B** and **C**): Landmarks on the slice were used for easy orientation and relocation of the neuron and dendrite of interest (*white dashed box* in B = C; *white dashed box* in C = barrel cortex; a*rrowheads* = slice holder marks). (**D** and **E**): Maximum projection of two-photon images of a cell of interest (D). Previous images taken during uncaging experiments (E) were used to relocate the exact dendrite to be correlated (*Arrowhead* = neuron soma). (**F**): Representative two-photon images show a dendrite targeted with NIRB marks placed at different depths in the tissue (*inset* = zoom of *dashed white box*). A cross was used on the surface of the tissue for identification of the centre of the ROI during semi-thin sectioning. Images are representative of 5 successful relocation attempts.

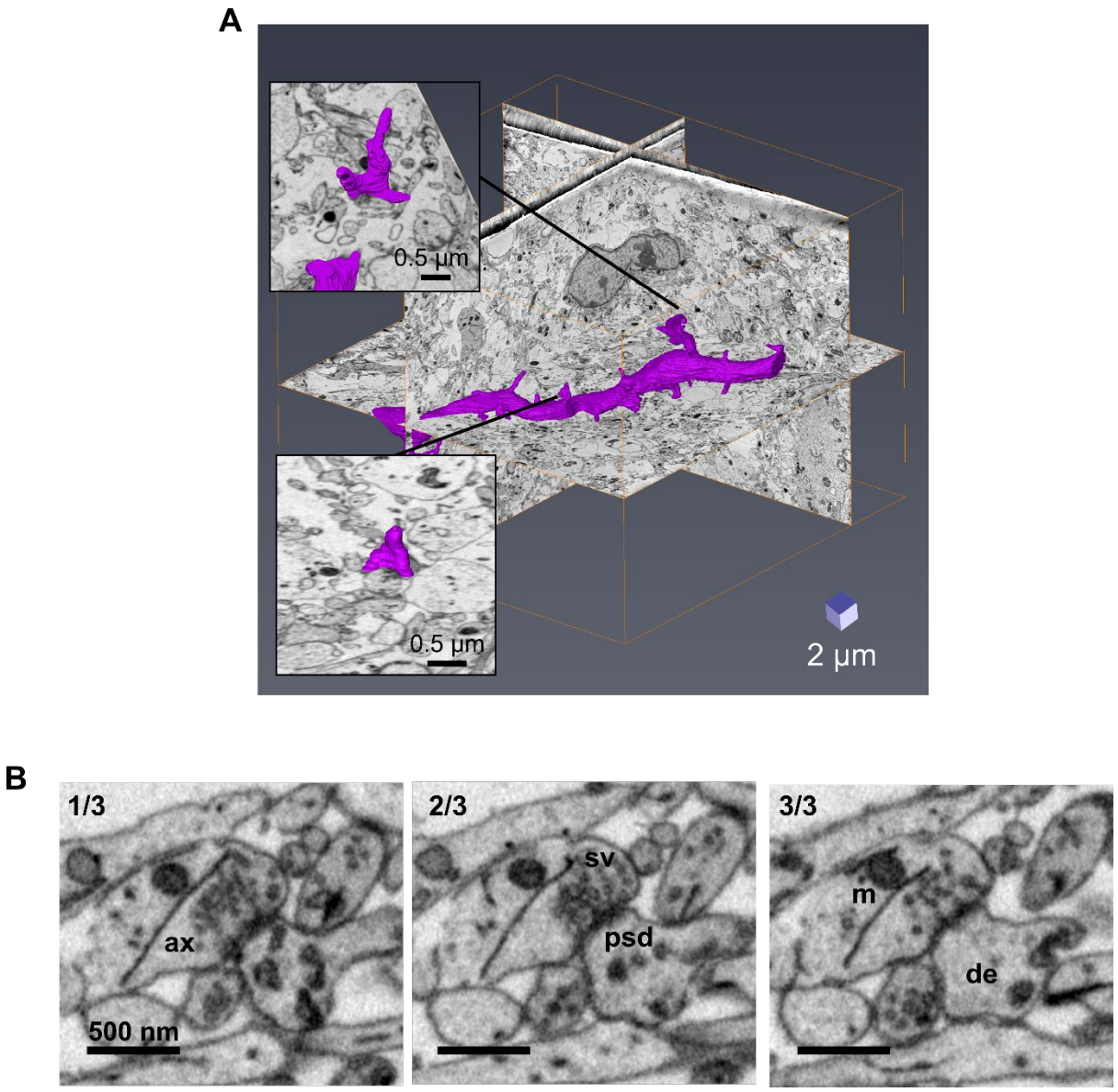

Figure 4.7 Synapses are well resolved in SBF SEM images of neonatal brain. (**A**): Reconstruction of a single dendrite (*magenta*) from a 25 x 25 µm block of neonatal brain tissue. Orthogonal slices are shown of SBF SEM images. Spine-like protrusions were present that could be easily identified as synaptic or non-synaptic depending on their PSD or presynaptic partner (*insets*). (**B**): Consecutive slices from SBF SEM imaging. The resolution of images was good enough to identify individual synaptic vesicles (*sv*), the pixel size for these images was ~3 nm and slice depth was 50 nm. Structures are labelled: *m* = mitochondria, *ax* = axon, *psd* = postsynaptic density, *de* = dendrite.

Overall, the combination of NIRB and SBF SEM can be useful for relocation of specifically labelled cells identified with 2P microscopy for ultrastructural reconstruction at synaptic resolution, and correlation with functional measures from LM.

4.4.3 Targeted relocation of axonal regions for correlating bouton ultrastructure to fluorescence images

Fluorescence intensity of a cell-filling fluorophore is often used to measure the structure of neuronal subcellular compartments *in vivo* (De Paola et al., 2006; Mostany et al., 2013; Grillo et al., 2013). Correlating LM images with ultrastructure provides additional confidence in the identification of pre- or post-synaptic terminal structures (Grillo et al., 2013; Knott et al., 2009; Gala et al., 2017; Drawitsch et al., 2018), and can also provide information to further characterise them (e.g. ultrastructure of newly-formed versus pre-existing boutons in *Chapter 3*). To illustrate the use of NIRB in 3D CLEM of subcellular structures imaged *in vivo*, an ROI containing multiple axons with putative boutons was repeatedly imaged for 35 days *in vivo* (Figure 4.8A). After the final imaging session, the animal was perfused with fixative and a tangential slice taken from the brain under the window (Figure 4.8B). The vasculature usually loses contrast after exsanguination; however, contrast was maintained here using DiI (a lipophilic dye) in the perfusate. Subsequently, the vasculature pattern was used to relocate the ROI imaged *in vivo* (Figure 4.8B) and NIRB marks were used to mark the ROI (Figure 4.8C). A blood vessel was also used as an additional fiducial marker for orientation of the ROI in SBF SEM images (Figure 4.8D).

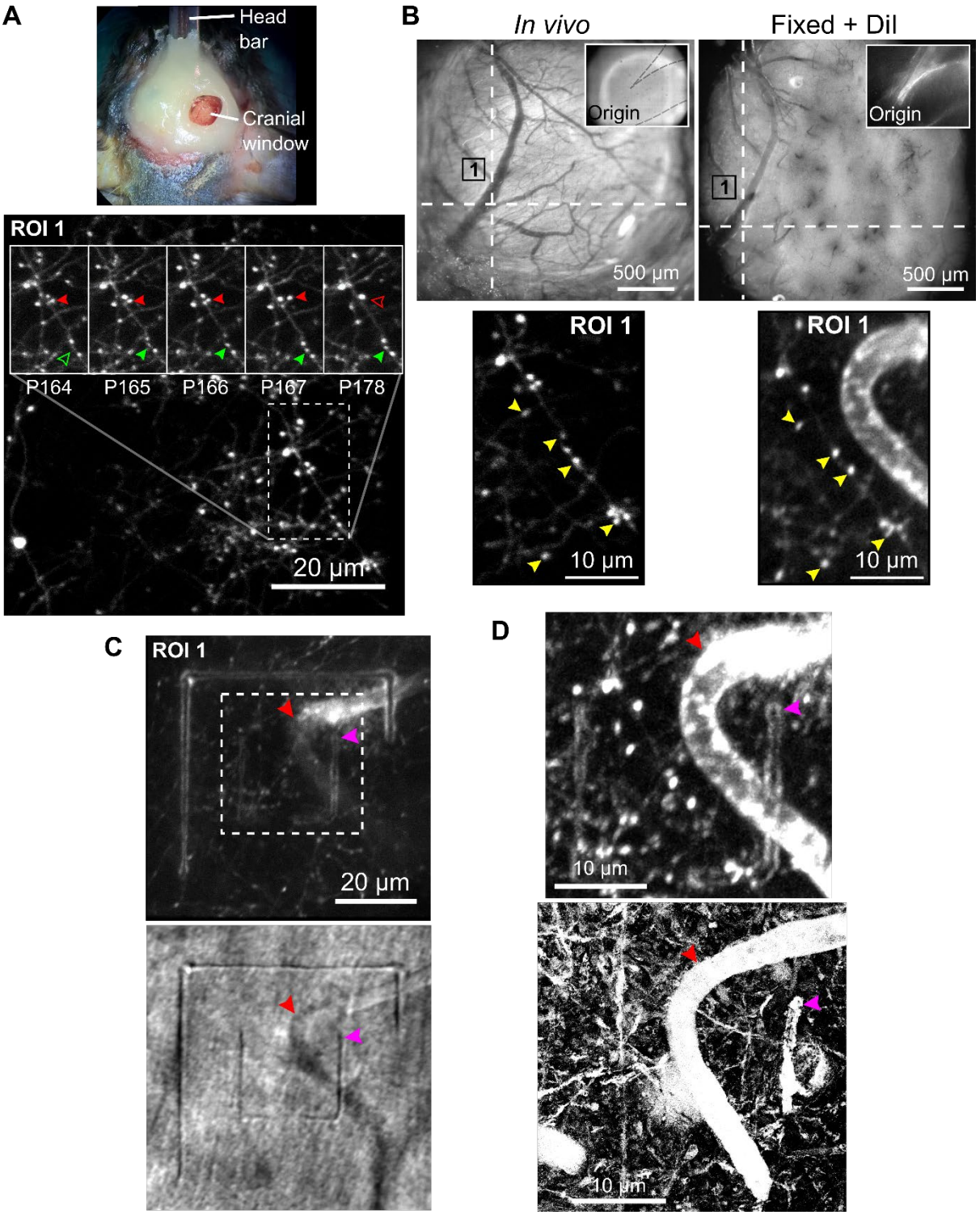

Figure 4.8 Relocation and branding of an axon previously imaged longitudinally *in vivo*. (**A**): (Top) photograph of a cranial window implant immediately after surgery. The head bar was used to angle the head consistently for repeated imaging. (Bottom) representative two-photon image of an ROI. An axon of interest is highlighted (dashed white box) and images from longitudinal observation are shown (inset). Examples of bouton loss (red arrowhead) and gain (green arrowhead) are indicated. (**B**): Relocation of an ROI in fixed tissue (right), with vasculature stained using DiI. Coordinates were used relative to the origin (intersection of dashed white lines and insets) defined during *in vivo* imaging (left). Two-photon images are shown of the ROI before and after fixation (bottom panels). (**C**): Two-photon (top) and brightfield (bottom) images of NIRB marks around the ROI in (A) and (B). Notice marks are

fluorescent as well as physical holes. (**D**): Maximum intensity projections of two-photon (top) and SBFSEM (bottom) images of the final NIRB mark around the axon of interest in (A). The blood vessel (red arrowhead) and NIRB mark (magenta arrowhead) are indicated for reference.

Relocation of the 2P-imaged region appeared to be successful, as an NIRB mark and blood vessel were present in the imaging volume (Figure 8D). However, the fixation, staining and embedding protocol caused changes to the tissue volume between LM and EM imaging (Figure 8D; Korogod et al., 2015). Alignment of the EM and LM volumes was required to relocate specific axons. The Icy plugin eC-CLEM (Paul-Gilloteaux et al., 2017) was used for semi-automated transformation based on fiducial points (blood vessel curvature and NIRB mark) and ImageJ was also used in a separate attempt to adjust rotation and scale manually. Despite this, the axons of interest were not identified in initial attempts to reconstruct the neuropil. One problem was the poor axial resolution of 2P images, individual axons and boutons appeared through 9 slices of the LM image stack, equivalent to 180 EM slices. This made it difficult to align the volumes with high precision. Additionally, axons were densely packed in the neuropil, making segmentation and tracing of individual axons ambiguous in places (Figure 4.9). Synaptic ultrastructure was still clear in adult tissue at this resolution (25 x 25 μm FOV, pixel size of 3.1 nm, 50 nm sections; Figure 4.10).

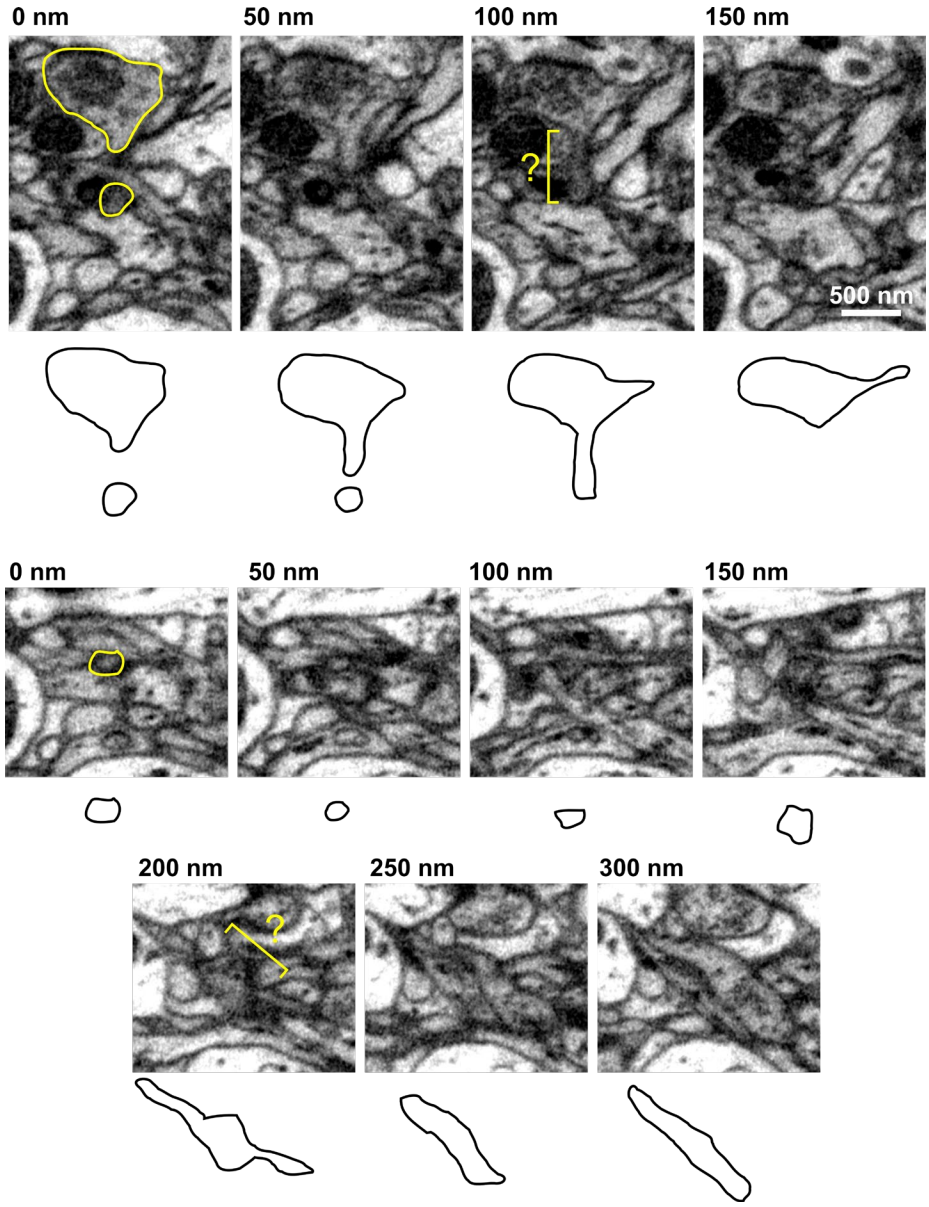

Figure 4.9 Ambiguity in tracing axonal structures. (*Top*): Four panels showing serial sections of an axonal bouton with a very poorly contrasted membrane protrusion coming off (100 nm). The bouton is outlined in yellow at the start (0 nm), along with the candidate membrane that it might be connected to. A manual trace of each section is given below the electron micrograph. (*Bottom*): Seven panels showing serial sections of a tubular membrane, putatively axonal. The membrane disappears in to the poorly contrasted area, and potentially joins a membrane running perpendicular.

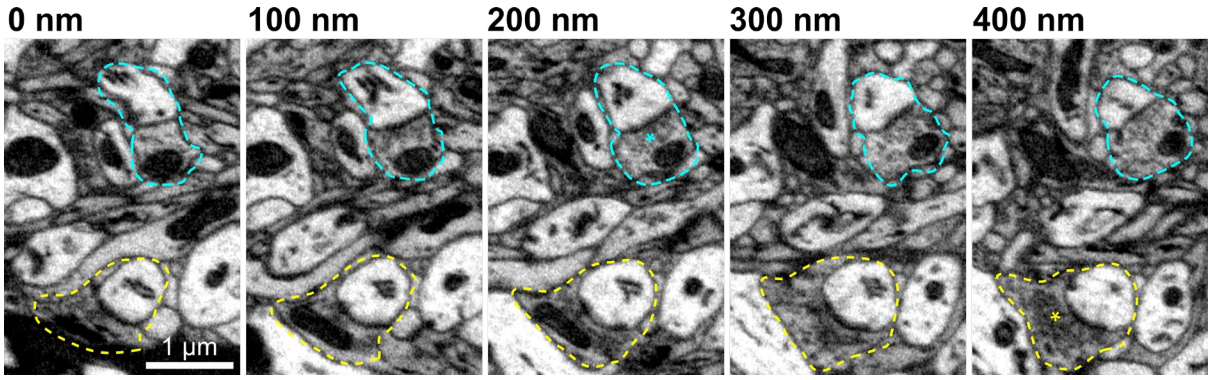

Figure 4.10 Synaptic ultrastructure in SBF SEM images of adult brain. Two synapses are traced in this set of serial 100 nm sections. Dendritic spines (light gray) are clearly identified by their spine apparatus (small dark membrane) and postsynaptic densities. Axonal boutons are identified by their synaptic vesicle pool. Individual vesicles are not resolvable at this resolution (25 x 25 µm FOV, pixel size of 3.1 nm, 50 nm sections). Identifiable synaptic contact is indicated with an asterisk.

4.4.4 Reconstruction of dense neuronal processes in adult mouse brain tissue

Efforts were made to segment and reconstruct the neuropil from the region relocated in Figure 4.8 (Figure 4.11A). Dendritic ultrastructure was easily identified and traced in comparison to axonal structure as dendrites were up to 10 times larger (2 µm-wide dendritic shafts compared to 200 nm-wide axonal shafts). Around 25% of the dendrites present were reconstructed through a cropped portion of the volume (~15 x 15 x 10 µm; Figure 4.11B-D). A large proportion of the reconstructed dendrites were hooked around the blood vessel in the centre of the volume (Figure 4.11B, D), traversing through the tissue in one direction and making a complete 180^{o} turn back to where they originated. Axons were not reconstructed, but also appeared densely packed around the blood vessel along with dendrites. The origin of this phenomenon was undetermined.

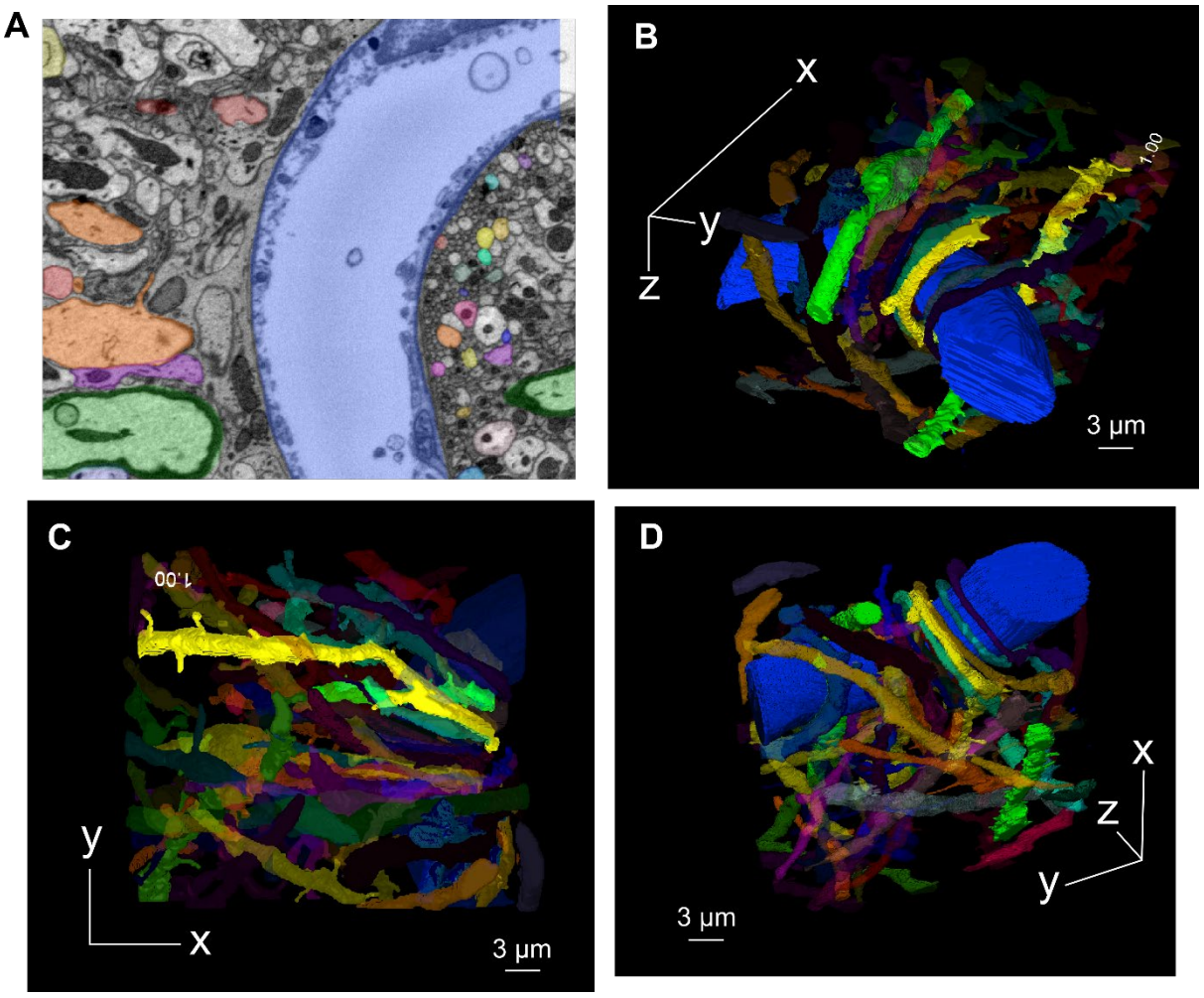

Figure 4.11 Neuronal architecture around a blood vessel in layer 1 of mouse somatosensory cortex. Reconstruction from the ROI in Figure 4.8. (**A**): Screenshot from TrakEM2 (an ImageJ plugin) showing a slice from SBF SEM imaging false-coloured with segmentations of unique axons and dendrites. A blood vessel was present in the centre (*blue*). (**B**): Three-dimensional reconstruction of manual segmentation from ~25% of the dendrites in the field of view. (**C** and **D**): Alternative views of B (see *coordinate references*) showing that some dendrites were hooked around the blood vessel, in most cases turning 180°.

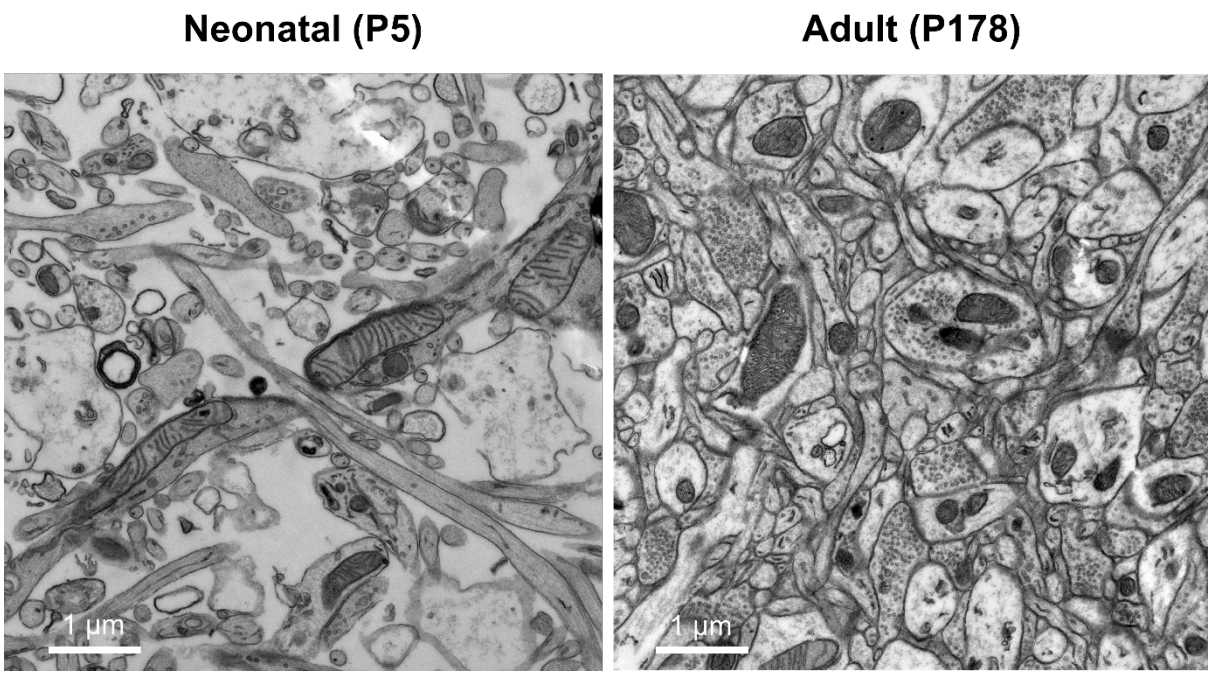

Figure 4.12 Acute *ex vivo* brain tissue from neonatal mice has much greater extracellular space than perfusion-fixed adult tissue. Representative transmission electron micrographs of 70 nm sections taken from tissue stained *en bloc*. There was clearly more extracellular space (*light grey*) in the neonatal tissue than in adult tissue, where there was no visible extracellular space. However, preparations differed in that neonatal tissue was incubated during experimentation at 20–35°C for 5–6 hours before being fixed. Whereas, adult tissue was immediately fixed using cardiac perfusion.

4.4.5 Comparison of extracellular space between neonatal and adult mouse brain tissue

Axonal structure was difficult to segment in adult tissue using SBF SEM. The effect of age on extracellular space was explored here to determine the feasibility of using SBF SEM for axonal relocation in juvenile tissue. The same preparation for SBF SEM imaging was carried out on acute tissue slices taken from neonatal mice (held at 20-35°C for >5 hours; Figure 4.6) alongside adult perfusion-fixed tissue (fixed immediately after exsanguination; Figure 4.8). Electron micrographs from TEM imaging revealed much greater extracellular space in neonatal tissue when compared to adult tissue (Figure 4.12). Extracellular space in adult tissue was almost unresolvable, increasing the chance of inaccurately tracing an axon through the tissue volume. Therefore, the use of SBF SEM seems more appropriate for tracing and correlating axonal structure in juvenile tissue. This increased space may be a result of differences in processing of the tissue, which will require further investigation.

4.5 Discussion

This study aimed to improve the reliability and level of ease with which 3D CLEM could be achieved in neuronal tissue, with the final goal of relocating previously-imaged axons to characterise bouton age at the ultrastructural level. Unambiguously relocating an ROI from LM imaging in a stack of EM images can take considerable time. NIRB marks can reduce the search area for an ROI to a volume of 25 x 25 x 10 μm (Figures 4.5, 4.6 and 4.8; Bishop et al., 2011), in comparison to the size of a whole tissue fragment, which may be up to 5 x 5 mm and 400 μm thick. The marks can also be used as fiducial points for correlation between the LM and EM images (Figures 4.5F,G and 4.8C, D; Maco et al., 2014; Blazquez-Llorca et al., 2015). Here, to increase relocation success, NIRB marks were made in multiple z-planes (Figure 4.2), rather than just a single plane (Bishop et al., 2011; Blazquez-Llorca et al., 2015). The additional marks were not used for correlating EM images, but rather to increase the chance of relocating at least one NIRB mark during sectioning. Overlapping the top and bottom of NIRB marks in the z-axis also meant that there was always a mark present for reference during sectioning. To further decrease ambiguity when orienting the tissue during sectioning, marks with low symmetry were created (e.g. a square has 4 axes of symmetry, removal of 1 side reduces the axes of symmetry to 1; Figures 4.6 and 4.8). Additionally, a cross on the surface of the tissue was useful to identify the centre of the ROI, even when the tissue was not entirely flat (a common problem that was encountered). All the minor improvements mentioned made the relocation of an ROI during sectioning more accurate and reliable.

Tissue thickness was previously limited to 50–100 μm to allow for the visualisation of NIRB marks after embedding (Bishop et al., 2011; Blazquez-Llorca et al., 2015), however thinner tissue is more delicate and harder to handle during processing. Multiple marks allowed for the processing of thick pieces of tissue (e.g. 400 μm acute brain slices), without re-sectioning.

NIRB marks are made by bubbles (formed under high intensity laser light) that expand and push the tissue apart (Bishop et al., 2011); however, large bubbles can also form and persist, obstructing the ROI (Figures 4.2C, D). The success of NIRB relies on choosing settings appropriate for the tissue and depth, so they cause enough damage to accurately outline the ROI but not obscure it. However, heterogeneity within tissue may mean that the detailed

shape of NIRB marks can not be formed accurately, as different parts of the tissue are more susceptible. Indeed, when marks were made along a line, NIRB was only successful at particular locations (Figure 4.2D, 5, 6 and 8). However, this does create unique shapes, reducing ambiguity during relocation and correlation.

Resin choice was also important, because certain resins were more susceptible to charging and beam damage during SEM imaging (e.g. Agar 100 Hard; Figure 4.4H), which affected the stability of ultrathin sectioning and quality of images. Here, Durcupan ACM resin was used to reduce these artefacts (Figure 4.4I).

Other approaches for correlating structures utilise electron dense precipitation of DAB upon excitation of fluorescent proteins (Knott et al., 2009), or activation of modified peroxidase that can be conjugated to a protein of interest (Martell et al., 2012, Hirabayashi et al., 2017). However, these approaches obscure the ultrastructure inside the cell or at the location of the proteins of interest. The advantage of NIRB is that it allows for complete identification of ultrastructure in the ROI, including synaptic structures (Figure 4.7 and 4.10).

NIRB has mostly been limited to neuronal cell biology; marking ROIs from intravital imaging (Blazquez-Llorca et al., 2017; Maco et al., 2014b; Bishop et al., 2011; Karreman et al., 2016; Grillo et al., 2013; Mostany et al., 2013). Three examples of sample preparations from different types of experiments were used in this study to illustrate the scope of applications for NIRB and CLEM in brain tissue. These were: the relocation of a specific cell-type in fixed tissue for ultrastructural characterisation of the intracellular and extracellular environment (Figure 4.5), the relocation of a specific dendrite from an uncaging experiment to correlate receptor distribution to intracellular and membrane ultrastructure (Figure 4.6) and the relocation of a region of axons from longitudinal *in vivo* imaging to correlate fluorescence intensity to synaptic structure (Figure 4.8).

While NIRB marks increased the success of ROI relocation in sectioning and SBF SEM imaging, there were still factors that needed optimisation for complete correlation. The two main factors were segmentation of fine structures in SBF SEM images and alignment of the EM volume for relocation of the exact target structure. Large structures such as cell bodies

(Figure 4.5) or dendrites (Figure 4.7) were unambiguously segmented and correlated with the axial resolution of SBF SEM (50 nm), as they were large in size and few in number. But, smaller structures such as axons were densely packed and difficult to trace through the volume with confidence. SBF SEM may be inappropriate for tracing axons in adult brain tissue due to the low axial resolution and dense packing of axons. Relatively higher axial resolution can be reliably afforded by FIB SEM, where an isotropic voxel size of 5 nm can be achieved, however the size of the block that can be imaged is smaller than SBF SEM (Peddie and Collinson, 2014). While tracing and segmenting axons is useful for the correlation of the LM and EM volumes, many axons must be blindly segmented before alignment can be achieved (Drawitsch et al., 2018).

Without proper alignment prior to segmentation, the search for the target structure is laborious and relatively unguided because of changes in the tissue volume after processing (Korogod et al., 2015). To aid alignment efforts, additional fiducial markers in three dimensions can be used to carry out transformations (Paul-Gilloteaux et al., 2017). NIRB marks are possible to use in three dimensions, but the risk of obscuring the ROI in EM images means other alternatives are required. Nuclear labels, such as Hoechst stain or DAPI would provide additional information to the LM images, and as nuclei are easily identified and segmented in EM images, they can be reliably used as fiducial markers for alignment (Luckner et al., 2018). However, additional labels added after fixation require either: permeabilisation, to increase penetration of stains; or gentle fixation (e.g. PFA only), to increase tissue permeability. Both of these methods would alter the preservation of ultrastructure. Finally, changes in the angle of the tissue between 2P and SBF SEM imaging could be limited by improved flat-embedding techniques (Luckner et al., 2018), reducing the need for alignment and transformation.

Reconstruction of a particular block of adult mouse brain tissue revealed an unexpected and peculiar phenomenon, where many of the neuronal processes were hooked around a blood vessel that had been used as a fiducial marker for CLEM (Figure 4.11). Over one hundred separate but neighbouring axons and dendrites exhibited a looped trajectory around a discrete region of the blood vessel (Figure 4.11B-D). This resulted in a bundle of neurites apposed

directly to the blood vessel wall. This phenomenon has not been reported previously, and therefore may be an artefact, potentially from chemical fixation (Korogod et al., 2015). Further investigation of neuronal architecture around other cortical blood vessels, potentially already available from other datasets (Kasthuri et al., 2015), will be needed to confirm this phenomenon.

Imaging of neonatal and adult mouse brain tissue revealed an obvious difference in extracellular space. Adult brain tissue appeared to have an unresolvable amount of extracellular space, compared to the large degree of space in neonatal tissue, which covered an area roughly equal to the cellular material (Figure 4.12). A reduction in extracellular space has been seen in rat cerebral cortex from postnatal days 1 to 21 (Lehmenkuhler et al., 1993), suggesting this could be a true difference in extracellular space. However, differences in sample preparation may also contribute to the increased extracellular space in neonatal tissue in this study. The neonatal tissue was cut from live brain tissue and kept alive through incubation in solutions that were initially cold (4^{o}C after dissection and during cutting), then warm (21^{o}C before imaging) and finally physiological (35^{o}C for imaging). This harsh preparation may have led to the tissue becoming disconnected and losing integrity, compared to fast perfusion-fixation of the adult tissue. Indeed, electrophysiology preparations can result in dead and dyeing cells on the surface after 3-4 hours (Edwards et al., 1989), which presumably retract their neuronal processes from the tissue. Tissue from young mice (<21 days) with a high proportion of extracellular space may be appropriate for the low axial resolution of SBF SEM imaging as axonal tracing can be done with less ambiguity than in adult mice.

This chapter shows that correlation of 2P microscopy with SBF SEM imaging can be achieved with relative ease using NIRB marks, in comparison to previous techniques. Here, the placement of NIRB marks in three dimensions decreased failure of relocation and made it easier to process thicker tissue specimens. Suggestions were also made to improve the reliability and ease of alignment between the two imaging modalities, reducing the need to segment all structures in the volume.

CHAPTER 5 GENERAL DISCUSSION

The aim of the work in this thesis was to determine the relationship between presynaptic terminal stability, maturity and mitochondrial localisation in mammalian cortical neurons. The results are discussed here with respect to the current literature, indicating original contributions, and outlining ideas for future work.

5.1 Stability of presynaptic terminals in primary cortical culture

Preliminary results in Chapter 2 showed that terminal lifetimes in cultured rat cortical neurons were very short, with a median of 30 minutes, and correlated poorly with duration of mitochondrial colocalisation. These lifetimes did not differ with age in culture from DIV 14 to 21, despite other studies showing continued maturation of synaptic connections (Ichikawa et al., 1993; Chiappalone et al., 2006; Moutaux et al., 2018) and increased proportions of stationary and presynaptic mitochondria in the same period (Lewis et al., 2016; Loss and Stephenson, 2017; Moutaux et al., 2018). The lifetimes of these putative terminals were very short in comparison to cultured hippocampal neurons (Obashi and Okabe, 2013) or *in vivo* as seen in the work presented in Chapter 3 and other published studies (De Paola et al., 2006, Qiao et al., 2015, Ash et al., 2018), where the majority of terminals were stable for periods exceeding 4 days. However, the dynamics did match that of the developing Zebrafish optic tectum (Meyer and Smith, 2006), implying that the cortical culture model at these ages

represents an underdeveloped system for studying terminal dynamics. Further, the poor correlation between mitochondrial colocalisation and terminal lifetime was not corroborated in Chapter 3, where terminal loss in adult mice *in vivo* was significantly reduced with mitochondrial presence.

Mitochondria are the main source of ATP in neurons, and so drawing parallels between *in vivo* and *in vitro* studies of mitochondria relies on the underlying energy homeostasis being similar. Most neuronal culture is not done under similar conditions to *in vivo,* and so it would be interesting to determine if mitochondrial colocalisation with presynaptic terminals, or terminal lifetime, is dependent on nutrient availability, e.g. oxygen and glucose. Culture conditions more closely matching physiological conditions (Kleman et al., 2008) could be compared to pre-existing neuronal culture methodology as seen in Chapter 2.

The work in this thesis assumed that maintaining synaptic efficacy at presynaptic terminals (i.e. release probability) makes them more likely to survive and stabilise. While there is limited evidence to suggest this link (Wiegert and Oertner, 2013), there are other methods of determining it. Munc13 is a presynaptic protein involved in priming glutamatergic synaptic vesicles for fusion and neurotransmission (Augustin et al., 1999). Neuronal cultures from Munc13 knockout mice show no vesicular release, but synaptic ultrastructure and density are normal (Varoqueaux et al., 2002). Using these cultures, it would be possible to determine the relationship between synaptic activity and presynaptic terminal lifetimes in comparison to wildtype neurons. Furthermore, mitochondrial localisation in these axons may be affected due to a lack of requirement for them to regulate presynaptic release, akin to pharmacological inhibition of activity (Vaccaro et al., 2017, Obashi and Okabe, 2013; Chang et al., 2006).

5.2 Relationship between presynaptic mitochondria and bouton aging

Axonal bouton dynamics of long-range motor cortical axons in Chapter 3 shared a similar trajectory to that observed in other studies of cortico-cortical axons and other axons innervating the cortex. Bouton density was similar to previous studies in young adult mice (2.5–3.5 months of age) and remained stable across all axons due to matched loss and gain (Mostany et al., 2013; Qiao et al., 2015; De Paola et al., 2006). Mature (pre-existing) boutons

were much more stable than immature (newly-formed) boutons, at similar rates to previous studies (Grillo et al., 2013; Ash et al., 2018; Qiao et al., 2015).

Bouton density was correlated with mitochondrial density across time in the motor cortical axons studied, and mitochondria were distributed closer to boutons than by chance. Non-random colocalisation of mitochondria and boutons was also previously seen in axons of the visual cortex (Smit-Rigter et al., 2016). Overall, ~40% of boutons had mitochondria within 1.5 μm, which fits with data from other cortical neurons (Kwon et al., 2016; Kasthuri et al., 2015; Chavan et al., 2015; Smit-Rigter et al., 2016). The fact that only a subpopulation of boutons had mitochondria in close proximity may reflect differential expression of anchoring proteins, but could also be explained by an inability to distribute enough mitochondria to these distal axonal regions. See the end of this section for suggestions of future work addressing this question.

Immature boutons were less likely to have mitochondria nearby than mature boutons, and the probability of mitochondrial presence at any bouton increased with bouton age. This was explained by a higher probability of retaining mitochondria at boutons rather than gaining mitochondria at empty boutons, along with decreased loss of boutons where mitochondria were present. Bouton loss was halved for boutons containing mitochondria, whereas short-range axons of the visual cortex had a ~30% relative decrease in loss (Smit-Rigter et al., 2016). The importance of a local, rather than regional presence of mitochondria was evidenced by a poor correlation between regional (axon branch-level) mitochondrial density and bouton turnover. The increased survival of boutons possessing mitochondria supports the idea that presynaptic terminals able to maintain synaptic vesicle release (through calcium homeostasis and ATP production) are more likely to survive (Wiegert and Oertner, 2013). The longitudinal study of mitochondrial localisation at both mature and immature boutons is novel and highlights a relationship between bouton age, longevity and mitochondrial presence.

Ideally, in future experiments, a small proportion of boutons analysed would be relocated using 3D CLEM as developed in Chapter 4. Relocation would increase the reliability of bouton scoring in light microscopy (Grillo et al. 2013; Drawitsch et al., 2018). It would also be possible to determine differences between immature and mature boutons at the ultrastructural level in

terms of size, mitochondrial ultrastructure (where present), ER, synaptic vesicle organisation and number. It is expected that the immature boutons would be smaller than mature boutons (Ash et al., 2018; Grillo et al., 2013), with smaller vesicle pool sizes, which would explain the decreased mitochondrial presence (Smith et al., 2016). The 3D CLEM workflow developed in Chapter 4 has made relocation more reliable due to the addition of more fiducial NIRB marks between the two modalities. Further improvements are required to increase the success of relocating individual axons and boutons by adding more fiducial marks such as nuclei (LM stain) and using these for transformation of image coordinates between the LM and EM imaging volumes.

The increase in mitochondrial presence with bouton age draws parallels with studies of the aging mouse cortex. Bouton density increases in the aging mouse cortex (Grillo et al., 2013; Mostany et al., 2013), which could be explained by increased presynaptic mitochondria with age. However, in aged cortex, boutons are less tenacious in general, especially large boutons (Grillo et al., 2013), which have a high probability of containing mitochondria in young adults (Rollenhagen et al., 2015; Smith et al., 2016). Therefore, it might be expected that mitochondrial presence at presynaptic terminals increases with age and declines again in old age, reflecting an increased and then decreased stabilisation of boutons. Indeed, mitochondria have been related to cognitive decline (Hara et al., 2014; Pickett et al., 2018), especially in neurodegenerative disease (Sheng and Cai, 2012; Devine and Kittler, 2018). To address this, cross-sectional EM studies should be undertaken in juvenile, adult and aged mouse cortex. Analysis of identical axonal projections would be required through viral transduction of a subset of neurons with an APEX(ascorbate peroxidase)-GFP conjugate targeted to cellular membranes (Hirabayashi et al., 2017). Subsequently, fixation and light microscopy imaging of coronal sections would reveal suitable axonal arborisations within the area of interest for analysis and DAB (diamino-benzidine) precipitation used to stain APEX in EM images (Martell et al., 2012).

Using similar methodology, analysis of short-range and long-range axons of the same neurons could be assessed for mitochondrial density and number of presynaptic mitochondria. Layer 5 pyramidal neurons are also known to project locally in superficial layers of the cortex

(Larsen et al., 2008). These projections could be analysed alongside their long-range cortico-cortical projections in the same animal. It would be expected that shorter axons could more easily distribute mitochondria to their presynaptic terminals, due to the shorter distance.

5.3 Relationship between presynaptic mitochondria and bouton survival

The decreased loss of boutons close to mitochondria suggests that there is some advantage to the circuit of keeping them. Boutons of thalamo-cortical axons have a very high presence of mitochondria (Bopp et al., 2017; Rollenhagen et al., 2015; Rodriguez-Moreno et al., 2018) in comparison to other cortical axons (Kasthuri et al., 2015), thought to be due to the high efficacy of thalamocortical synapses. Multi-synaptic boutons are also more likely to possess mitochondria than single-synaptic boutons (Smith et al. 2016; Rollenhagen et al., 2015), potentially to support the multiple release sites. This ultrastructural work is supported by *in vitro* work showing the importance of presynaptic mitochondria in calcium regulation (Vaccaro et al., 2017; Lewis et al., 2018; Kwon et al., 2016; David and Barrett, 2000; Billups and Forsythe, 2002) and synaptic ATP production (Sobieski et al., 2017; Rangaraju et al., 2014; Zhou and Liu, 2015; Ivannikov et al., 2013; Hall et al., 2012). The suggestion from these findings is that highly functional synapses are more likely to possess mitochondria, increasing bouton survival – but is there a causal link between mitochondrial colocalisation and bouton survival?

To address the question of cause and effect, it would be necessary to specifically adjust mitochondrial distribution in a single axon or terminal and monitor bouton turnover. Potential ways to adjust mitochondrial distribution in a cell-specific way would involve the reduction of key mitochondrial trafficking or anchoring proteins, e.g. Miro1 or Syntaphilin. This would require a transgenic mouse line with conditional Cre-dependent knockout of Syntaphilin or Miro1 (Nguyen et al., 2014; Lopez-Domenech et al., 2018). Use of a viral cocktail including low titre Cre virus, high titre Cre-dependent cytosolic BFP (blue fluorescent protein) reporter and high titre bicistronic structural and mitochondrial marker (see Chapter 4) would allow for knockout of a small proportion of neurons (reported by BFP) alongside wildtype neurons not expressing BFP. Mitochondrial and presynaptic structural plasticity could be

compared between knockout and wildtype cells in the same animal and area. An alternative specific intervention for individual mitochondria is the use of light-induced heterodimerisation to mobilise or anchor mitochondria upon light stimulation (van Bergeijk et al., 2015). A light-sensitive protein can be added to mitochondria that binds to an engineered acceptor protein on either syntaphilin or KIF5A upon two-photon light stimulation (van Bergeijk et al., 2015; Kennedy et al., 2010). Mitochondria at specific presynaptic terminals could be targeted for mobilisation (by KIF5A dimerization), and bouton longevity assessed.

It would also be useful to address the strength of the correlation between mitochondrial colocalisation and bouton survival in other projections with different numbers of presynaptic mitochondria and bouton turnover rates. As above, thalamocortical axons projecting in to layer 4 have a high proportion of presynaptic terminals with mitochondria (Bopp et al., 2017; Rollenhagen et al., 2015; Rodriguez-Moreno et al., 2018), assessing bouton turnover in these axons would test the robustness of the correlation in other axonal projections. Separately, olfactory bulb (Cheetham et al., 2016) and some hippocampal-cortical projections (De Paola et al., 2006) have very high turnover and low survival of boutons, measuring numbers of presynaptic mitochondria in these axons would also test the robustness of the correlation.

5.4 Distinguishing *en passant* and *terminaux* boutons

En passant and *terminaux* boutons have unique structures that are postulated to allow for different flexibility in connectivity (Gogolla et al., 2007). The survival of *en passant* or *terminaux* boutons did not differ in the population of pre-existing boutons, but *terminaux* boutons did have slightly increased survival in the newly-formed bouton population (6 days median survival versus 4 days for *en passant*). These data corroborate with previous reports that *en passant* and *terminaux* boutons on the same axon have similar survival (De Paola et al., 2006).

The composition of bouton types on motor-somatosensory axons was variable and the population appeared to arise from two distinct subpopulations with majority *en passant* or majority *terminaux* boutons. However, these subpopulations did not exhibit significantly different turnover. Previously, cell types have been identified in animals with sparse labelling

from cells across the brain by the number and size of *en passant* or *terminaux* boutons on their axons (De Paola et al., 2006). Bouton survival differed between the cell types identified in that study. Bouton size was not measured here, however the population of cells labelled was more specific due to targeted viral injection. The reduced variability of a small, specific population of neurons may be the reason why bouton turnover did not differ significantly. Therefore, these data further support the theory of cell-type specific bouton turnover and suggest that different bouton types do not have inherently different turnover or survival. Rather, something else about cell type is driving turnover, such as activity (Marik et al., 2010; Sammons et al., 2018; Smit-Rigter et al., 2016; Keck et al., 2011; Cheetham et al., 2016), complement of pre- and post-synaptic adhesion molecules (Missler et al., 2012) or mitochondria (Chapter 3; Smit-Rigter et al., 2016).

Without a role in turnover, survival or postsynaptic targeting (Anderson and Martin, 2001), what distinguishes the two bouton types? From the results in Chapter 3, *en passant* boutons were more likely to possess mitochondria and their loss was more strongly related to mitochondrial presence than for *terminaux* boutons. Furthermore, mitochondria were more likely to be present at *en passant* boutons (45%) than *terminaux* boutons (28%). Previous work has drawn parallels between *terminaux* bouton structure and dendritic spine structure, thought to compartmentalise calcium (Yuste et al., 2000). Spines also very rarely contain mitochondria, compared to the dendritic shaft (Kasthuri et al., 2015), although this may be related to steric hindrance. Localisation of mitochondria to the base of *terminaux* boutons is probably too great a distance for effective regulation of calcium, but may still provide adequate ATP (Pathak et al., 2015). The decreased association with mitochondria at *terminaux* boutons, coupled with their compartmentalised structure, suggests that they may function differently to *en passant* boutons.

It may be possible to determine the difference in *terminaux* and *en passant* bouton function by looking at cell types with extreme compositions of each bouton type (e.g. layer 6 axons high *terminaux* density, layer 2/3 and layer 5 high *en passant* density) and relating that to their activity. Subsequently, cell types could be specifically labelled if their genetic identity is known, sorted using FACS (fluorescence-activated cell sorting), and transcriptomics used to

determine RNA levels of cytoskeletal regulators potentially involved in either *terminaux* or *en passant* bouton formation (Okaty et al., 2011). Validation of these candidates could be done using viral delivery of shRNA with a GFP reporter to the neuronal population with high *terminaux/en passant* bouton density. Axonal structure in fixed tissue could then be compared to scrambled shRNA to test whether the cytoskeletal regulator identified is involved in the structure of either of the bouton types.

5.5 Mitochondrial turnover in axons of the central nervous system

While the turnover of mitochondria is something that has not been addressed in the work presented here, it is important to determine the dynamics of mitochondria to ensure the sampling frequency of imaging reliably estimates their location at each timepoint. In neuronal culture, 75% of mitochondria remain within 10 μm of their original position over 12 hours (Lewis et al., 2016). This does not confirm the results of Smit-Rigter et al. (2016) that *in vivo* mitochondria redistribute at a rate of 50% every 4 days (moving >2 μm from their original position). Both studies had comparable rates of mitochondrial motility *in vitro* and *in vivo*, further work is required to determine the redistribution of mitochondria *in vivo* at shorter time scales. To address this gap, the use of photoconvertible mEos2 localised to mitochondria (Lewis et al. 2016) *in vivo* with hourly imaging could be used to track the movement of photoconverted mitochondria in axons.

5.6 Conclusion

In summary, the work in this thesis has provided new evidence supporting the relationship between mitochondria and presynaptic terminals, specifically the positive correlation between presynaptic mitochondrial presence and bouton survival. This work also highlights the importance of accounting for bouton age when studying presynaptic structural dynamics and mitochondrial association. And finally, it makes further attempts to determine the more nuanced differences between *en passant* and *terminaux* boutons. The causality of these relationships is still to be determined and will be the basis of future work.

BIBLIOGRAPHY

Ahmad, T., Aggarwal, K., Pattnaik, B., Mukherjee, S., Sethi, T., Tiwari, B.K., Kumar, M., Micheal, A., Mabalirajan, U., Ghosh, B., et al. (2013). Computational classification of mitochondrial shapes reflects stress and redox state. Cell Death Dis *4*, e461.

Akbik, F.V., Bhagat, S.M., Patel, P.R., Cafferty, W.B.J., and Strittmatter, S.M. (2013). Anatomical plasticity of adult brain is titrated by Nogo Receptor 1. Neuron *77*, 859–866.

Akerboom, J., Chen, T.-W., Wardill, T.J., Tian, L., Marvin, J.S., Mutlu, S., Calderón, N.C., Esposti, F., Borghuis, B.G., Sun, X.R., et al. (2012). Optimization of a GCaMP Calcium Indicator for Neural Activity Imaging. J. Neurosci. *32*, 13819–13840.

Alberts, B., Johnson, A., Lewis, J., Morgan, D., Raff, M., Roberts, K., and Walter, P. (2014). Molecular Biology of the Cell (Garland Science).

Alexander, B.H., Barnes, H.M., Trimmer, E., Davidson, A.M., Ogola, B.O., Lindsey, S.H., and Mostany, R. (2018). Stable Density and Dynamics of Dendritic Spines of Cortical Neurons Across the Estrous Cycle While Expressing Differential Levels of Sensory-Evoked Plasticity. Front. Mol. Neurosci. *11*.

Amunts, K., and Zilles, K. (2015). Architectonic Mapping of the Human Brain beyond Brodmann. Neuron *88*, 1086–1107.

Anderson, J.C., and Martin, K.A.C. (2001). Does bouton morphology optimize axon length? Nature Neuroscience *4*, 1166–1167.

Andreae, L.C., and Burrone, J. (2018). The role of spontaneous neurotransmission in synapse and circuit development. Journal of Neuroscience Research *96*, 354–359.

Ascoli, G., Alonso-Nanclares, L., Anderson, S.A., Barrionuevo, G., Benavides-Piccione, R., Burkhalter, A., Buzsáki, G., Cauli, B., DeFelipe, J., Fairén, A., et al. (2008). Petilla terminology: nomenclature of features of GABAergic interneurons of the cerebral cortex. Nature Reviews Neuroscience *9*, 557–568.

Ash, R.T., Fahey, P.G., Park, J., Zoghbi, H.Y., and Smirnakis, S.M. (2018). Increased Axonal Bouton Stability during Learning in the Mouse Model of MECP2 Duplication Syndrome. ENeuro ENEURO.0056-17.2018.

Ashby, M.C., and Isaac, J.T.R. (2011). Maturation of a Recurrent Excitatory Neocortical Circuit by Experience-Dependent Unsilencing of Newly Formed Dendritic Spines. Neuron *70*, 510–521.

Ashrafi, G., Schlehe, J.S., LaVoie, M.J., and Schwarz, T.L. (2014). Mitophagy of damaged mitochondria occurs locally in distal neuronal axons and requires PINK1 and Parkin. J Cell Biol *206*, 655–670.

Augustin, I., Rosenmund, C., Südhof, T.C., and Brose, N. (1999). Munc13-1 is essential for fusion competence of glutamatergic synaptic vesicles. Nature *400*, 457–461.

Bagkos, G., Koufopoulos, K., and Piperi, C. (2014). A new model for mitochondrial membrane potential production and storage. Medical Hypotheses *83*, 175–181.

Bambrick, L.L., Kostov, Y., and Rao, G. (2011). In vitro cell culture pO2 is significantly different from incubator pO2. Biotechnology Progress *27*, 1185–1189.

Bass, C., Helkkula, P., Paola, V.D., Clopath, C., and Bharath, A.A. (2017). Detection of axonal synapses in 3D two-photon images. PLOS ONE *12*, e0183309.

Bear, M.F., and Kirkwood, A. (1993). Neocortical long-term potentiation. Curr. Opin. Neurobiol. *3*, 197–202.

Bear, M.F., Connors, B.W., and Paradiso, M.A. (2015). Neuroscience: Exploring the brain (Wolters Kluwer).

Bedbrook, C.N., Deverman, B.E., and Gradinaru, V. (2018). Viral Strategies for Targeting the Central and Peripheral Nervous Systems. Annual Review of Neuroscience *41*, 323–348.

van Bergeijk, P., Adrian, M., Hoogenraad, C.C., and Kapitein, L.C. (2015). Optogenetic control of organelle transport and positioning. Nature *518*, 111–114.

Biffi, E., Regalia, G., Menegon, A., Ferrigno, G., and Pedrocchi, A. (2013). The Influence of Neuronal Density and Maturation on Network Activity of Hippocampal Cell Cultures: A Methodological Study. PLOS ONE *8*, e83899.

Billups, B., and Forsythe, I.D. (2002). Presynaptic Mitochondrial Calcium Sequestration Influences Transmission at Mammalian Central Synapses. J. Neurosci. *22*, 5840–5847.

Bishop, D., Nikić, I., Brinkoetter, M., Knecht, S., Potz, S., Kerschensteiner, M., and Misgeld, T. (2011). Near-infrared branding efficiently correlates light and electron microscopy. Nat Meth *8*, 568–570.

Blazquez-Llorca, L., Hummel, E., Zimmerman, H., Zou, C., Burgold, S., Rietdorf, J., and Herms, J. (2015). Correlation of two-photon *in vivo* imaging and FIB/SEM microscopy. Journal of Microscopy *259*, 129–136.

Bliss, T.V.P., and Collingridge, G.L. (1993). A synaptic model of memory: long-term potentiation in the hippocampus. Nature *361*, 31–39.

Bopp, R., Holler-Rickauer, S., Martin, K.A.C., and Schuhknecht, G.F.P. (2017). An ultrastructural study of the thalamic input to layer 4 of primary motor and primary somatosensory cortex in the mouse. J. Neurosci. 2557–16.

Bosch, M., and Hayashi, Y. (2012). Structural plasticity of dendritic spines. Curr Opin Neurobiol *22*, 383–388.

Branco, T., Marra, V., and Staras, K. (2010). Examining size–strength relationships at hippocampal synapses using an ultrastructural measurement of synaptic release probability. Journal of Structural Biology *172*, 203–210.

Brickley, K., and Stephenson, F.A. (2011). Trafficking Kinesin Protein (TRAK)-mediated Transport of Mitochondria in Axons of Hippocampal Neurons. J. Biol. Chem. *286*, 18079–18092.

Briones, T.L., Klintsova, A.Y., and Greenough, W.T. (2004). Stability of synaptic plasticity in the adult rat visual cortex induced by complex environment exposure. Brain Research *1018*, 130–135.

Briones, T.L., Suh, E., Jozsa, L., Rogozinska, M., Woods, J., and Wadowska, M. (2005). Changes in number of synapses and mitochondria in presynaptic terminals in the dentate gyrus following cerebral ischemia and rehabilitation training. Brain Research *1033*, 51–57.

Brose, N., Petrenko, A.G., Südhof, T.C., and Jahn, R. (1992). Synaptotagmin: a calcium sensor on the synaptic vesicle surface. Science *256*, 1021–1025.

Bury, L.A., and Sabo, S.L. (2011). Coordinated trafficking of synaptic vesicle and active zone proteins prior to synapse formation. Neural Dev *6*, 24.

Cagalinec, M., Safiulina, D., Liiv, M., Liiv, J., Choubey, V., Wareski, P., Veksler, V., and Kaasik, A. (2013). Principles of the mitochondrial fusion and fission cycle in neurons. J Cell Sci *126*, 2187–2197.

Calkins, M.J., and Reddy, P.H. (2011). Amyloid beta impairs mitochondrial anterograde transport and degenerates synapses in Alzheimer's disease neurons. Biochimica et Biophysica Acta (BBA) - Molecular Basis of Disease *1812*, 507–513.

Cardona, A., Saalfeld, S., Schindelin, J., Arganda-Carreras, I., Preibisch, S., Longair, M., Tomancak, P., Hartenstein, V., and Douglas, R.J. (2012). TrakEM2 Software for Neural Circuit Reconstruction. PLOS ONE *7*, e38011.

del Castillo, J., and Katz, B. (1954). Quantal components of the end-plate potential. J Physiol *124*, 560–573.

Chang, D.T.W., and Reynolds, I.J. (2006). Differences in mitochondrial movement and morphology in young and mature primary cortical neurons in culture. Neuroscience *141*, 727–736.

Chang, K.T., Niescier, R.F., and Min, K.-T. (2011). Mitochondrial matrix Ca2+ as an intrinsic signal regulating mitochondrial motility in axons. PNAS *108*, 15456–15461.

Chavan, V., Willis, J., Walker, S.K., Clark, H.R., Liu, X., Fox, M.A., Srivastava, S., and Mukherjee, K. (2015). Central Presynaptic Terminals Are Enriched in ATP but the Majority Lack Mitochondria. PLoS One *10*.

Che, D.L., Chowdary, P.D., and Cui, B. (2016). A close look at axonal transport: Cargos slow down when crossing stationary organelles. Neuroscience Letters *610*, 110–116.

Cheetham, C.E.J., Barnes, S.J., Albieri, G., Knott, G.W., and Finnerty, G.T. (2014). Pansynaptic Enlargement at Adult Cortical Connections Strengthened by Experience. Cereb Cortex *24*, 521–531.

Cheetham, C.E.J., Park, U., and Belluscio, L. (2016). Rapid and continuous activity-dependent plasticity of olfactory sensory input. Nature Communications *7*, 10729.

Chen, Y., and Sheng, Z.-H. (2013). Kinesin-1–syntaphilin coupling mediates activity-dependent regulation of axonal mitochondrial transport. J Cell Biol *202*, 351–364.

Chen, X., Nelson, C.D., Li, X., Winters, C.A., Azzam, R., Sousa, A.A., Leapman, R.D., Gainer, H., Sheng, M., and Reese, T.S. (2011). PSD-95 is required to sustain the molecular organization of the postsynaptic density. J Neurosci *31*, 6329–6338.

Chen, Y.-M., Gerwin, C., and Sheng, Z.-H. (2009). Dynein Light Chain LC8 Regulates Syntaphilin-Mediated Mitochondrial Docking in Axons. J. Neurosci. *29*, 9429–9438.

Chi, P., Greengard, P., and Ryan, T.A. (2001). Synapsin dispersion and reclustering during synaptic activity. Nat Neurosci *4*, 1187–1193.

Chiappalone, M., Bove, M., Vato, A., Tedesco, M., and Martinoia, S. (2006). Dissociated cortical networks show spontaneously correlated activity patterns during in vitro development. Brain Research *1093*, 41–53.

Chicka, M.C., Hui, E., Liu, H., and Chapman, E.R. (2008). Synaptotagmin arrests the SNARE complex before triggering fast, efficient membrane fusion in response to Ca2+. Nat Struct Mol Biol *15*, 827–835.

Chklovskii, D.B., Schikorski, T., and Stevens, C.F. (2002). Wiring Optimization in Cortical Circuits. Neuron *34*, 341–347.

Chouhan, A.K., Ivannikov, M.V., Lu, Z., Sugimori, M., Llinas, R.R., and Macleod, G.T. (2012). Cytosolic Calcium Coordinates Mitochondrial Energy Metabolism with Presynaptic Activity. J. Neurosci. *32*, 1233–1243.

Collingridge, G.L., Peineau, S., Howland, J.G., and Wang, Y.T. (2010). Long-term depression in the CNS. Nature Reviews Neuroscience *11*, 459–473.

Costes, S.V., Daelemans, D., Cho, E.H., Dobbin, Z., Pavlakis, G., and Lockett, S. (2004). Automatic and Quantitative Measurement of Protein-Protein Colocalization in Live Cells. Biophys J *86*, 3993–4003.

Courchet, J., Lewis Jr., T.L., Lee, S., Courchet, V., Liou, D.-Y., Aizawa, S., and Polleux, F. (2013). Terminal Axon Branching Is Regulated by the LKB1-NUAK1 Kinase Pathway via Presynaptic Mitochondrial Capture. Cell *153*, 1510–1525.

Cserép, C., Pósfai, B., Schwarcz, A.D., and Dénes, Á. (2018). Mitochondrial Ultrastructure Is Coupled to Synaptic Performance at Axonal Release Sites. ENeuro *5*, ENEURO.0390-17.2018.

David, G., and Barrett, E.F. (2000). Stimulation-Evoked Increases in Cytosolic [Ca2+] in Mouse Motor Nerve Terminals Are Limited by Mitochondrial Uptake and Are Temperature-Dependent. J. Neurosci. *20*, 7290–7296.

David, G., and Barrett, E.F. (2003). Mitochondrial Ca2+ uptake prevents desynchronization of quantal release and minimizes depletion during repetitive stimulation of mouse motor nerve terminals. J Physiol *548*, 425–438.

Denton, R.M., and McCormack, J.G. (1980). On the role of the calcium transport cycle in heart and other mammalian mitochondria. FEBS Letters *119*, 1–8.

De Paola, V., Holtmaat, A., Knott, G., Song, S., Wilbrecht, L., Caroni, P., and Svoboda, K. (2006). Cell Type-Specific Structural Plasticity of Axonal Branches and Boutons in the Adult Neocortex. Neuron *49*, 861–875.

De Stefani, D., Raffaello, A., Teardo, E., Szabò, I., and Rizzuto, R. (2011). A forty-kilodalton protein of the inner membrane is the mitochondrial calcium uniporter. Nature *476*, 336–340.

Devine, M.J., and Kittler, J.T. (2018). Mitochondria at the neuronal presynapse in health and disease. Nature Reviews Neuroscience *19*, 63–80.

Díaz-García, C.M., Mongeon, R., Lahmann, C., Koveal, D., Zucker, H., and Yellen, G. (2017). Neuronal Stimulation Triggers Neuronal Glycolysis and Not Lactate Uptake. Cell Metabolism *26*, 361-374.e4.

Douglas, R.J., and Martin, K.A.C. (2004). Neuronal Circuits of the Neocortex. Annual Review of Neuroscience *27*, 419–451.

Drawitsch, F., Karimi, A., Boergens, K.M., and Helmstaedter, M. (2018). FluoEM, virtual labeling of axons in 3-dimensional electron microscopy data for long-range connectomics. ELife.

Drerup, C.M., Herbert, A.L., Monk, K.R., and Nechiporuk, A.V. (2017). Regulation of mitochondria-dynactin interaction and mitochondrial retrograde transport in axons. ELife *6*, e22234.

Drobizhev, M., Tillo, S., Makarov, N.S., Hughes, T.E., and Rebane, A. (2009). Absolute Two-Photon Absorption Spectra and Two-Photon Brightness of Orange and Red Fluorescent Proteins. J Phys Chem B *113*, 855–859.

Drobizhev, M., Makarov, N.S., Tillo, S.E., Hughes, T.E., and Rebane, A. (2011). Two-photon absorption properties of fluorescent proteins. Nat Methods *8*, 393–399.

Du, H., Guo, L., Yan, S., Sosunov, A.A., McKhann, G.M., and ShiDu Yan, S. (2010). Early deficits in synaptic mitochondria in an Alzheimer's disease mouse model. Proc Natl Acad Sci U S A *107*, 18670–18675.

Dufour, A., Rollenhagen, A., Sätzler, K., and Lübke, J.H.R. (2015). Development of Synaptic Boutons in Layer 4 of the Barrel Field of the Rat Somatosensory Cortex: A Quantitative Analysis. Cereb. Cortex bhv270.

Edelstein, A.D., Tsuchida, M.A., Amodaj, N., Pinkard, H., Vale, R.D., and Stuurman, N. (2014). Advanced methods of microscope control using μManager software. J Biol Methods *1*.

Edwards, F.A., Konnerth, A., Sakmann, B., and Takahashi, T. (1989). A thin slice preparation for patch clamp recordings from neurones of the mammalian central nervous system. Pflugers Arch. *414*, 600–612.

Faits, M.C., Zhang, C., Soto, F., and Kerschensteiner, D. (2016). Dendritic mitochondria reach stable positions during circuit development. ELife *5*.

Faul, F., Erdfelder, E., Lang, A.-G., and Buchner, A. (2007). G*Power 3: a flexible statistical power analysis program for the social, behavioral, and biomedical sciences. Behav Res Methods *39*, 175–191.

Feng, G., Mellor, R.H., Bernstein, M., Keller-Peck, C., Nguyen, Q.T., Wallace, M., Nerbonne, J.M., Lichtman, J.W., and Sanes, J.R. (2000). Imaging Neuronal Subsets in Transgenic Mice Expressing Multiple Spectral Variants of GFP. Neuron *28*, 41–51.

Fletcher, T.L., Cameron, P., Camilli, P.D., and Banker, G. (1991). The distribution of synapsin I and synaptophysin in hippocampal neurons developing in culture. J. Neurosci. *11*, 1617–1626.

Fornasiero, E.F., Raimondi, A., Guarnieri, F.C., Orlando, M., Fesce, R., Benfenati, F., and Valtorta, F. (2012). Synapsins Contribute to the Dynamic Spatial Organization of Synaptic Vesicles in an Activity-Dependent Manner. J. Neurosci. *32*, 12214–12227.

Frank, A.C., Huang, S., Zhou, M., Gdalyahu, A., Kastellakis, G., Silva, T.K., Lu, E., Wen, X., Poirazi, P., Trachtenberg, J.T., et al. (2018). Hotspots of dendritic spine turnover facilitate clustered spine addition and learning and memory. Nature Communications *9*, 422.

Franklin, Keith, and Paxinos, George (2008). The Mouse Brain in Stereotaxic Coordinates (Academic Press).

Frantz, M.G., Kast, R.J., Dorton, H.M., Chapman, K.S., and McGee, A.W. (2016). Nogo Receptor 1 Limits Ocular Dominance Plasticity but not Turnover of Axonal Boutons in a Model of Amblyopia. Cereb Cortex *26*, 1975–1985.

Fu, M., and Zuo, Y. (2011). Experience-dependent structural plasticity in the cortex. Trends in Neurosciences *34*, 177–187.

Gaffield, M.A., and Betz, W.J. (2006). Imaging synaptic vesicle exocytosis and endocytosis with FM dyes. Nat Protoc *1*, 2916–2921.

Gala, R., Lebrecht, D., Sahlender, D.A., Jorstad, A., Knott, G., Holtmaat, A., and Stepanyants, A. (2017). Computer assisted detection of axonal bouton structural plasticity in *in vivo* time-lapse images. Elife *6*.

Gazit, N., Vertkin, I., Shapira, I., Helm, M., Slomowitz, E., Sheiba, M., Mor, Y., Rizzoli, S., and Slutsky, I. (2016). IGF-1 Receptor Differentially Regulates Spontaneous and Evoked Transmission via Mitochondria at Hippocampal Synapses. Neuron *89*, 583–597.

Gincel, D., Zaid, H., and Shoshan-Barmatz, V. (2001). Calcium binding and translocation by the voltage-dependent anion channel: a possible regulatory mechanism in mitochondrial function. Biochem J *358*, 147–155.

Goda, Y., and Davis, G.W. (2003). Mechanisms of Synapse Assembly and Disassembly. Neuron *40*, 243–264.

Gogolla, N., Galimberti, I., and Caroni, P. (2007). Structural plasticity of axon terminals in the adult. Current Opinion in Neurobiology *17*, 516–524.

Graham, L.C., Eaton, S.L., Brunton, P.J., Atrih, A., Smith, C., Lamont, D.J., Gillingwater, T.H., Pennetta, G., Skehel, P., and Wishart, T.M. (2017). Proteomic profiling of neuronal mitochondria reveals modulators of synaptic architecture. Molecular Neurodegeneration *12*.

Gray, E.G. (1959). Axo-somatic and axo-dendritic synapses of the cerebral cortex. J Anat *93*, 420–433.

Grillo, F.W., Song, S., Ruivo, L.M.T.-G., Huang, L., Gao, G., Knott, G.W., Maco, B., Ferretti, V., Thompson, D., Little, G.E., et al. (2013). Increased axonal bouton dynamics in the aging mouse cortex. PNAS *110*, E1514–E1523.

Gundelfinger, E.D., Reissner, C., and Garner, C.C. (2016). Role of Bassoon and Piccolo in Assembly and Molecular Organization of the Active Zone. Front Synaptic Neurosci *7*.

Gunter, T.E., and Sheu, S.-S. (2009). Characteristics and Possible Functions of Mitochondrial Ca2+ Transport Mechanisms. Biochim Biophys Acta *1787*, 1291–1308.

Guo, X., Macleod, G.T., Wellington, A., Hu, F., Panchumarthi, S., Schoenfield, M., Marin, L., Charlton, M.P., Atwood, H.L., and Zinsmaier, K.E. (2005). The GTPase dMiro Is Required for Axonal Transport of Mitochondria to Drosophila Synapses. Neuron *47*, 379–393.

Hafner, A.-S., Donlin-Asp, P., Leitch, B., Herzog, E., and Schuman, E.M. (2018). Local protein synthesis in axon terminals and dendritic spines differentiates plasticity contexts.

Hall, C.N., Klein-Flügge, M.C., Howarth, C., and Attwell, D. (2012). Oxidative phosphorylation, not glycolysis, powers pre- and postsynaptic mechanisms underlying brain information processing. J Neurosci *32*, 8940–8951.

Hara, Y., Yuk, F., Puri, R., Janssen, W.G.M., Rapp, P.R., and Morrison, J.H. (2014). Presynaptic mitochondrial morphology in monkey prefrontal cortex correlates with working memory and is improved with estrogen treatment. Proc Natl Acad Sci U S A *111*, 486–491.

Harms, K.J., Rioult-Pedotti, M.S., Carter, D.R., and Dunaevsky, A. (2008). Transient Spine Expansion and Learning-Induced Plasticity in Layer 1 Primary Motor Cortex. J. Neurosci. *28*, 5686–5690.

Harris, J.J., Jolivet, R., and Attwell, D. (2012). Synaptic Energy Use and Supply. Neuron *75*, 762–777.

Harris, K.M., Perry, E., Bourne, J., Feinberg, M., Ostroff, L., and Hurlburt, J. (2006). Uniform Serial Sectioning for Transmission Electron Microscopy. J. Neurosci. *26*, 12101–12103.

Hedden, T., and Gabrieli, J.D.E. (2004). Insights into the ageing mind: a view from cognitive neuroscience. Nature Reviews Neuroscience *5*, 87–96.

Helmchen, F., and Denk, W. (2005). Deep tissue two-photon microscopy. Nature Methods *2*, 932–940.

Helmstaedter, M. (2013). Cellular-resolution connectomics: challenges of dense neural circuit reconstruction. Nat Meth *10*, 501–507.

Hirabayashi, Y., Tapia, J.C., and Polleux, F. (2017). Correlated Light-Serial Scanning Electron Microscopy (CoLSSEM) for ultrastructural visualization of single neurons *in vivo*. BioRxiv 148585.

Hofer, S.B., Mrsic-Flogel, T.D., Bonhoeffer, T., and Hübener, M. (2009). Experience leaves a lasting structural trace in cortical circuits. Nature *457*, 313–317.

Holderith, N., Lorincz, A., Katona, G., Rózsa, B., Kulik, A., Watanabe, M., and Nusser, Z. (2012). Release probability of hippocampal glutamatergic terminals scales with the size of the active zone. Nature Neuroscience *15*, 988–997.

Holtmaat, A., and Caroni, P. (2016). Functional and structural underpinnings of neuronal assembly formation in learning. Nature Neuroscience *19*, 1553–1562.

Holtmaat, A., and Svoboda, K. (2009). Experience-dependent structural synaptic plasticity in the mammalian brain. Nat Rev Neurosci *10*, 647–658.

Holtmaat, A., Bonhoeffer, T., Chow, D.K., Chuckowree, J., Paola, V.D., Hofer, S.B., Hübener, M., Keck, T., Knott, G., Lee, W.-C.A., et al. (2009). Long-term, high-resolution imaging in the mouse neocortex through a chronic cranial window. Nature Protocols *4*, 1128–1144.

Hopf, F.W., Waters, J., Mehta, S., and Smith, S.J. (2002). Stability and Plasticity of Developing Synapses in Hippocampal Neuronal Cultures. J. Neurosci. *22*, 775–781.

Hurst, J.L., and West, R.S. (2010). Taming anxiety in laboratory mice. Nature Methods *7*, 825–826.

Ichikawa, M., Muramoto, K., Kobayashi, K., Kawahara, M., and Kuroda, Y. (1993). Formation and maturation of synapses in primary cultures of rat cerebral cortical cells: an electron microscopic study. Neuroscience Research *16*, 95–103.

Ivannikov, M.V., Sugimori, M., and Llinás, R.R. (2013). Synaptic Vesicle Exocytosis in Hippocampal Synaptosomes Correlates Directly with Total Mitochondrial Volume. J Mol Neurosci *49*, 223–230.

Jang, S., Nelson, J.C., Bend, E.G., Rodríguez-Laureano, L., Tueros, F.G., Cartagenova, L., Underwood, K., Jorgensen, E.M., and Colón-Ramos, D.A. (2016). Glycolytic Enzymes Localize to Synapses under Energy Stress to Support Synaptic Function. Neuron *90*, 278–291.

Johnson, C.M., Peckler, H., Tai, L.-H., and Wilbrecht, L. (2016). Rule learning enhances structural plasticity of long-range axons in frontal cortex. Nature Communications *7*, 10785.

Joshi, D.C., Zhang, C.-L., Lin, T.-M., Gusain, A., Harris, M.G., Tree, E., Yin, Y., Wu, C., Sheng, Z.-H., Dempsey, R.J., et al. (2015). Deletion of Mitochondrial Anchoring Protects Dysmyelinating Shiverer: Implications for Progressive MS. J. Neurosci. *35*, 5293–5306.

Jouaville, L.S., Pinton, P., Bastianutto, C., Rutter, G.A., and Rizzuto, R. (1999). Regulation of mitochondrial ATP synthesis by calcium: Evidence for a long-term metabolic priming. PNAS *96*, 13807–13812.

de Juan-Sanz, J., Holt, G.T., Schreiter, E.R., de Juan, F., Kim, D.S., and Ryan, T.A. (2017). Axonal Endoplasmic Reticulum Ca2+ Content Controls Release Probability in CNS Nerve Terminals. Neuron *93*, 867-881.e6.

Jung, C.K.E., and Herms, J. (2014). Structural Dynamics of Dendritic Spines are Influenced by an Environmental Enrichment: An *In Vivo* Imaging Study. Cereb Cortex *24*, 377–384.

Kanaan, N.M., Morfini, G.A., LaPointe, N.E., Pigino, G.F., Patterson, K.R., Song, Y., Andreadis, A., Fu, Y., Brady, S.T., and Binder, L.I. (2011). Pathogenic Forms of Tau Inhibit Kinesin-Dependent Axonal Transport through a Mechanism Involving Activation of Axonal Phosphotransferases. J. Neurosci. *31*, 9858–9868.

Kang, J.-S., Tian, J.-H., Pan, P.-Y., Zald, P., Li, C., Deng, C., and Sheng, Z.-H. (2008). Docking of Axonal Mitochondria by Syntaphilin Controls Their Mobility and Affects Short-Term Facilitation. Cell *132*, 137–148.

Kappel, S., Hawkins, P., and Mendl, M.T. (2017). To Group or Not to Group? Good Practice for Housing Male Laboratory Mice. Animals (Basel) *7*.

Kapur, J.N., Sahoo, P.K., and Wong, A.K.C. (1985). A new method for gray-level picture thresholding using the entropy of the histogram. Computer Vision, Graphics, and Image Processing *29*, 273–285.

Karra, D., and Dahm, R. (2010). Transfection Techniques for Neuronal Cells. J. Neurosci. *30*, 6171–6177.

Karreman, M.A., Mercier, L., Schieber, N.L., Solecki, G., Allio, G., Winkler, F., Ruthensteiner, B., Goetz, J.G., and Schwab, Y. (2016). Fast and precise targeting of single tumor cells *in vivo* by multimodal correlative microscopy. J Cell Sci *129*, 444–456.

Kasai, H., Matsuzaki, M., Noguchi, J., Yasumatsu, N., and Nakahara, H. (2003). Structure–stability–function relationships of dendritic spines. Trends in Neurosciences *26*, 360–368.

Kasthuri, N., Hayworth, K.J., Berger, D.R., Schalek, R.L., Conchello, J.A., Knowles-Barley, S., Lee, D., Vázquez-Reina, A., Kaynig, V., Jones, T.R., et al. (2015). Saturated Reconstruction of a Volume of Neocortex. Cell *162*, 648–661.

Keck, T., Scheuss, V., Jacobsen, R.I., Wierenga, C.J., Eysel, U.T., Bonhoeffer, T., and Hübener, M. (2011). Loss of Sensory Input Causes Rapid Structural Changes of Inhibitory Neurons in Adult Mouse Visual Cortex. Neuron *71*, 869–882.

Kennedy, M.J., Hughes, R.M., Peteya, L.A., Schwartz, J.W., Ehlers, M.D., and Tucker, C.L. (2010). Rapid blue-light-mediated induction of protein interactions in living cells. Nat. Methods *7*, 973–975.

Kim, J.H., Lee, S.-R., Li, L.-H., Park, H.-J., Park, J.-H., Lee, K.Y., Kim, M.-K., Shin, B.A., and Choi, S.-Y. (2011). High Cleavage Efficiency of a 2A Peptide Derived from Porcine Teschovirus-1 in Human Cell Lines, Zebrafish and Mice. PLOS ONE *6*, e18556.

Kleman, A.M., Yuan, J.Y., Aja, S., Ronnett, G.V., and Landree, L.E. (2008). Physiological glucose is critical for optimized neuronal viability and AMPK responsiveness in vitro. Journal of Neuroscience Methods *167*, 292–301.

Knott, G.W., Quairiaux, C., Genoud, C., and Welker, E. (2002). Formation of Dendritic Spines with GABAergic Synapses Induced by Whisker Stimulation in Adult Mice. Neuron *34*, 265–273.

Knott, G.W., Holtmaat, A., Wilbrecht, L., Welker, E., and Svoboda, K. (2006). Spine growth precedes synapse formation in the adult neocortex *in vivo*. Nat Neurosci *9*, 1117–1124.

Knott, G.W., Holtmaat, A., Trachtenberg, J.T., Svoboda, K., and Welker, E. (2009). A protocol for preparing GFP-labeled neurons previously imaged *in vivo* and in slice preparations for light and electron microscopic analysis. Nature Protocols *4*, 1145–1156.

Korogod, N., Petersen, C.C., and Knott, G.W. (2015). Ultrastructural analysis of adult mouse neocortex comparing aldehyde perfusion with cryo fixation. ELife *4*.

Krubitzer, L., Campi, K.L., and Cooke, D.F. (2011). All Rodents Are Not the Same: A Modern Synthesis of Cortical Organization. BBE *78*, 51–93.

Kuhlman, S.J., O'Connor, D.H., Fox, K., and Svoboda, K. (2014). Structural Plasticity within the Barrel Cortex during Initial Phases of Whisker-Dependent Learning. J Neurosci *34*, 6078–6083.

Kuromi, H., and Kidokoro, Y. (2000). Tetanic Stimulation Recruits Vesicles from Reserve Pool via a cAMP-Mediated Process in Drosophila Synapses. Neuron *27*, 133–143.

Kwon, H.-B., and Sabatini, B.L. (2011). Glutamate induces de novo growth of functional spines in developing cortex. Nature *474*, 100–104.

Kwon, S.E., and Chapman, E.R. (2011). Synaptophysin Regulates the Kinetics of Synaptic Vesicle Endocytosis in Central Neurons. Neuron *70*, 847–854.

Kwon, S.-K., Iii, R.S., Lewis, T.L., Hirabayashi, Y., Maximov, A., and Polleux, F. (2016). LKB1 Regulates Mitochondria-Dependent Presynaptic Calcium Clearance and Neurotransmitter Release Properties at Excitatory Synapses along Cortical Axons. PLOS Biology *14*, e1002516.

Laar, V.S.V., Arnold, B., Howlett, E.H., Calderon, M.J., Croix, C.M.S., Greenamyre, J.T., Sanders, L.H., and Berman, S.B. (2018). Evidence for Compartmentalized Axonal Mitochondrial Biogenesis: Mitochondrial DNA Replication Increases in Distal Axons As an Early Response to Parkinson's Disease-Relevant Stress. J. Neurosci. *38*, 7505–7515.

Landers, M.S., Knott, G.W., Lipp, H.P., Poletaeva, I., and Welker, E. (2011). Synapse formation in adult barrel cortex following naturalistic environmental enrichment. Neuroscience *199*, 143–152.

Larsen, D.D., Wickersham, I.R., and Callaway, E.M. (2008). Retrograde tracing with recombinant rabies virus reveals correlations between projection targets and dendritic architecture in layer 5 of mouse barrel cortex. Front. Neural Circuits *2*.

Lee, C.W., and Peng, H.B. (2006). Mitochondrial clustering at the vertebrate neuromuscular junction during presynaptic differentiation. J. Neurobiol. *66*, 522–536.

Lee, E., Choi, J., Jo, Y., Kim, J.Y., Jang, Y.J., Lee, H.M., Kim, S.Y., Lee, H.-J., Cho, K., Jung, N., et al. (2016). ACT-PRESTO: Rapid and consistent tissue clearing and labeling method for 3-dimensional (3D) imaging. Scientific Reports *6*, 18631.

Lee, H.-K., Takamiya, K., Han, J.-S., Man, H., Kim, C.-H., Rumbaugh, G., Yu, S., Ding, L., He, C., Petralia, R.S., et al. (2003). Phosphorylation of the AMPA receptor GluR1 subunit is required for synaptic plasticity and retention of spatial memory. Cell *112*, 631–643.

Lees, R., Peddie, C., Collinson, L., Verkade, P., and Ashby, M. (2017). Correlative two-photon and serial block face scanning electron microscopy in neuronal tissue using 3D near-infrared branding maps. In Methods in Cell Biology: Correlative Light and Electron Microscopy III, (Elsevier), pp. 245–276.

Lehmenkühler, A., Syková, E., Svoboda, J., Zilles, K., and Nicholson, C. (1993). Extracellular space parameters in the rat neocortex and subcortical white matter during postnatal development determined by diffusion analysis. Neuroscience *55*, 339–351.

Lein, E.S., Hawrylycz, M.J., Ao, N., Ayres, M., Bensinger, A., Bernard, A., Boe, A.F., Boguski, M.S., Brockway, K.S., Byrnes, E.J., et al. (2007). Genome-wide atlas of gene expression in the adult mouse brain. Nature *445*, 168–176.

Lendvai, B., Stern, E.A., Chen, B., and Svoboda, K. (2000). Experience-dependent plasticity of dendritic spines in the developing rat barrel cortex *in vivo*. Nature *404*, 876–881.

Lewis, T.L., Turi, G.F., Kwon, S.-K., Losonczy, A., and Polleux, F. (2016). Progressive Decrease of Mitochondrial Motility during Maturation of Cortical Axons In Vitro and *In Vivo*. Current Biology *26*, 2602–2608.

Lewis, T.L., Kwon, S.-K., Lee, A., Shaw, R., and Polleux, F. (2018). MFF-dependent mitochondrial fission regulates presynaptic release and axon branching by limiting axonal mitochondria size. BioRxiv 276691.

Li, Y., Song, Y., Zhao, L., Gaidosh, G., Laties, A.M., and Wen, R. (2008). Direct labeling and visualization of blood vessels with lipophilic carbocyanine dye DiI. Nature Protocols *3*, 1703–1708.

Li, Z., Okamoto, K.-I., Hayashi, Y., and Sheng, M. (2004). The Importance of Dendritic Mitochondria in the Morphogenesis and Plasticity of Spines and Synapses. Cell *119*, 873–887.

Ligon, L.A., and Steward, O. (2000). Movement of mitochondria in the axons and dendrites of cultured hippocampal neurons. J. Comp. Neurol. *427*, 340–350.

Lin, M.-Y., Cheng, X.-T., Tammineni, P., Xie, Y., Zhou, B., Cai, Q., and Sheng, Z.-H. (2017). Releasing Syntaphilin Removes Stressed Mitochondria from Axons Independent of Mitophagy under Pathophysiological Conditions. Neuron *94*, 595-610.e6.

Linkert, M., Rueden, C.T., Allan, C., Burel, J.-M., Moore, W., Patterson, A., Loranger, B., Moore, J., Neves, C., MacDonald, D., et al. (2010). Metadata matters: access to image data in the real world. The Journal of Cell Biology *189*, 777–782.

London, M., and Häusser, M. (2005). Dendritic Computation. Annual Review of Neuroscience *28*, 503–532.

López-Doménech, G., Higgs, N.F., Vaccaro, V., Roš, H., Arancibia-Cárcamo, I.L., MacAskill, A.F., and Kittler, J.T. (2016). Loss of Dendritic Complexity Precedes Neurodegeneration in a Mouse Model with Disrupted Mitochondrial Distribution in Mature Dendrites. Cell Reports *17*, 317–327.

López-Doménech, G., Covill-Cooke, C., Ivankovic, D., Halff, E.F., Sheehan, D.F., Norkett, R., Birsa, N., and Kittler, J.T. (2018). Miro proteins coordinate microtubule- and actin-dependent mitochondrial transport and distribution. The EMBO Journal e96380.

Loss, O., and Stephenson, F.A. (2017). Developmental changes in trak-mediated mitochondrial transport in neurons. Molecular and Cellular Neuroscience *80*, 134–147.

Luckner, M., Burgold, S., Filser, S., Scheungrab, M., Niyaz, Y., Hummel, E., Wanner, G., and Herms, J. (2018). Label-free 3D-CLEM Using Endogenous Tissue Landmarks. IScience *6*, 92–101.

MacAskill, A.F., and Kittler, J.T. (2010). Control of mitochondrial transport and localization in neurons. Trends in Cell Biology *20*, 102–112.

MacAskill, A.F., Rinholm, J.E., Twelvetrees, A.E., Arancibia-Carcamo, I.L., Muir, J., Fransson, A., Aspenstrom, P., Attwell, D., and Kittler, J.T. (2009). Miro1 Is a Calcium Sensor for Glutamate Receptor-Dependent Localization of Mitochondria at Synapses. Neuron *61*, 541–555.

Maco, B., Cantoni, M., Holtmaat, A., Kreshuk, A., Hamprecht, F.A., and Knott, G.W. (2014). Semiautomated correlative 3D electron microscopy of *in vivo*–imaged axons and dendrites. Nat. Protocols *9*, 1354–1366.

Magistretti, P.J., and Allaman, I. (2015). A Cellular Perspective on Brain Energy Metabolism and Functional Imaging. Neuron *86*, 883–901.

Majewska, A.K., Newton, J.R., and Sur, M. (2006). Remodeling of Synaptic Structure in Sensory Cortical Areas *In Vivo*. J. Neurosci. *26*, 3021–3029.

Malenka, R.C., Kauer, J.A., Zucker, R.S., and Nicoll, R.A. (1988). Postsynaptic calcium is sufficient for potentiation of hippocampal synaptic transmission. Science *242*, 81–84.

Manders, E.M.M., Verbeek, F.J., and Aten, J.A. (1993). Measurement of co-localization of objects in dual-colour confocal images. Journal of Microscopy *169*, 375–382.

Marik, S.A., Yamahachi, H., McManus, J.N.J., Szabo, G., and Gilbert, C.D. (2010). Axonal Dynamics of Excitatory and Inhibitory Neurons in Somatosensory Cortex. PLOS Biology *8*, e1000395.

Marland, J.R.K., Hasel, P., Bonnycastle, K., and Cousin, M.A. (2016). Mitochondrial Calcium Uptake Modulates Synaptic Vesicle Endocytosis in Central Nerve Terminals. J. Biol. Chem. *291*, 2080–2086.

Martell, J.D., Deerinck, T.J., Sancak, Y., Poulos, T.L., Mootha, V.K., Sosinsky, G.E., Ellisman, M.H., and Ting, A.Y. (2012). Engineered ascorbate peroxidase as a genetically-encoded reporter for electron microscopy. Nat Biotechnol *30*, 1143–1148.

Martin, S.J., Grimwood, P.D., and Morris, R.G.M. (2000). Synaptic Plasticity and Memory: An Evaluation of the Hypothesis. Annual Review of Neuroscience *23*, 649–711.

Mazzoni, A., Broccard, F.D., Garcia-Perez, E., Bonifazi, P., Ruaro, M.E., and Torre, V. (2007). On the Dynamics of the Spontaneous Activity in Neuronal Networks. PLOS ONE *2*, e439.

McAllister, A.K. (2007). Dynamic Aspects of Synapse Formation. Annu Rev Neurosci *30*, 425–450.

McFarland, N.R., Lee, J.-S., Hyman, B.T., and McLean, P.J. (2009). Comparison of transduction efficiency of recombinant AAV serotypes 1, 2, 5, and 8 in the rat nigrostriatal system. Journal of Neurochemistry *109*, 838–845.

Meyer, M.P., and Smith, S.J. (2006). Evidence from *In Vivo* Imaging That Synaptogenesis Guides the Growth and Branching of Axonal Arbors by Two Distinct Mechanisms. J. Neurosci. *26*, 3604–3614.

Meyer, D., Bonhoeffer, T., and Scheuss, V. (2014). Balance and Stability of Synaptic Structures during Synaptic Plasticity. Neuron *82*, 430–443.

Micheva, K.D., O'Rourke, N., Busse, B., and Smith, S.J. (2010). Array Tomography: High-Resolution Three-Dimensional Immunofluorescence. Cold Spring Harb Protoc *2010*, pdb.top 89.

Miller, K.E., and Sheetz, M.P. (2004). Axonal mitochondrial transport and potential are correlated. J Cell Sci *117*, 2791–2804.

Minerbi, A., Kahana, R., Goldfeld, L., Kaufman, M., Marom, S., and Ziv, N.E. (2009). Long-Term Relationships between Synaptic Tenacity, Synaptic Remodeling, and Network Activity. PLOS Biology *7*, e1000136.

Mironov, S.L. (2007). ADP Regulates Movements of Mitochondria in Neurons. Biophys J *92*, 2944–2952.

Misgeld, T., and Schwarz, T.L. (2017). Mitostasis in Neurons: Maintaining Mitochondria in an Extended Cellular Architecture. Neuron *96*, 651–666.

Missler, M., Südhof, T.C., and Biederer, T. (2012). Synaptic Cell Adhesion. Cold Spring Harb Perspect Biol *4*.

Morimoto, M.M., Tanaka, S., Mizutani, S., Urata, S., Kobayashi, K., and Okabe, S. (2018). *In Vivo* Observation of Structural Changes in Neocortical Catecholaminergic Projections in Response to Drugs of Abuse. ENeuro *5*.

Mostany, R., Anstey, J.E., Crump, K.L., Maco, B., Knott, G., and Portera-Cailliau, C. (2013). Altered Synaptic Dynamics during Normal Brain Aging. J. Neurosci. *33*, 4094–4104.

Moutaux, E., Christaller, W., Scaramuzzino, C., Genoux, A., Charlot, B., Cazorla, M., and Saudou, F. (2018). Neuronal network maturation differently affects secretory vesicles and mitochondria transport in axons. Scientific Reports *8*, 13429.

Murley, A., and Nunnari, J. (2016). The emerging network of mitochondria-organelle contacts. Mol Cell *61*, 648–653.

Narendra, D., Tanaka, A., Suen, D.-F., and Youle, R.J. (2008). Parkin is recruited selectively to impaired mitochondria and promotes their autophagy. J. Cell Biol. *183*, 795–803.

Nguyen, T.T., Oh, S.S., Weaver, D., Lewandowska, A., Maxfield, D., Schuler, M.-H., Smith, N.K., Macfarlane, J., Saunders, G., Palmer, C.A., et al. (2014). Loss of Miro1-directed mitochondrial movement results in a novel murine model for neuron disease. PNAS *111*, E3631–E3640.

Nikonenko, I., Jourdain, P., and Muller, D. (2003). Presynaptic Remodeling Contributes to Activity-Dependent Synaptogenesis. J. Neurosci. *23*, 8498–8505.

Nimchinsky, E.A., Sabatini, B.L., and Svoboda, K. (2002). Structure and Function of Dendritic Spines. Annual Review of Physiology *64*, 313–353.

Nishiyama, H., Fukaya, M., Watanabe, M., and Linden, D.J. (2007). Axonal Motility and Its Modulation by Activity Are Branch-Type Specific in the Intact Adult Cerebellum. Neuron *56*, 472–487.

Nithianantharajah, J., Levis, H., and Murphy, M. (2004). Environmental enrichment results in cortical and subcortical changes in levels of synaptophysin and PSD-95 proteins. Neurobiology of Learning and Memory *81*, 200–210.

Norkett, R., Modi, S., Birsa, N., Atkin, T.A., Ivankovic, D., Pathania, M., Trossbach, S.V., Korth, C., Hirst, W.D., and Kittler, J.T. (2016). DISC1-dependent Regulation of Mitochondrial Dynamics Controls the Morphogenesis of Complex Neuronal Dendrites. J Biol Chem *291*, 613–629.

Obashi, K., and Okabe, S. (2013). Regulation of mitochondrial dynamics and distribution by synapse position and neuronal activity in the axon. Eur J Neurosci *38*, 2350–2363.

Oeding, S.J., Majstrowicz, K., Hu, X.-P., Schwarz, V., Freitag, A., Honnert, U., Nikolaus, P., and Bähler, M. (2018). Identification of Miro as a mitochondrial receptor for myosin XIX. J Cell Sci jcs.219469.

Ohno, N., Chiang, H., Mahad, D.J., Kidd, G.J., Liu, L., Ransohoff, R.M., Sheng, Z.-H., Komuro, H., and Trapp, B.D. (2014). Mitochondrial immobilization mediated by syntaphilin facilitates survival of demyelinated axons. PNAS *111*, 9953–9958.

Okabe, S., Miwa, A., and Okado, H. (2001). Spine Formation and Correlated Assembly of Presynaptic and Postsynaptic Molecules. J. Neurosci. *21*, 6105–6114.

Okaty, B.W., Sugino, K., and Nelson, S.B. (2011). Cell-type-specific transcriptomics in the brain. J Neurosci *31*, 6939–6943.

Orenbuch, A., Shalev, L., Marra, V., Sinai, I., Lavy, Y., Kahn, J., Burden, J.J., Staras, K., and Gitler, D. (2012). Synapsin Selectively Controls the Mobility of Resting Pool Vesicles at Hippocampal Terminals. J. Neurosci. *32*, 3969–3980.

Oswald, M.J., Tantirigama, M.L.S., Sonntag, I., Hughes, S.M., and Empson, R.M. (2013). Diversity of layer 5 projection neurons in the mouse motor cortex. Front Cell Neurosci *7*.

Pakkenberg, B., Pelvig, D., Marner, L., Bundgaard, M.J., Gundersen, H.J.G., Nyengaard, J.R., and Regeur, L. (2003). Aging and the human neocortex. Experimental Gerontology *38*, 95–99.

Palay, S.L. (1956). SYNAPSES IN THE CENTRAL NERVOUS SYSTEM. J Biophys Biochem Cytol *2*, 193–202.

Park, C., Lee, S.-A., Hong, J.-H., Suh, Y., Park, S.J., Suh, B.K., Woo, Y., Choi, J., Huh, J.-W., Kim, Y.-M., et al. (2016). Disrupted-in-schizophrenia 1 (DISC1) and Syntaphilin collaborate to modulate axonal mitochondrial anchoring. Molecular Brain *9*, 69.

Pathak, D., Shields, L.Y., Mendelsohn, B.A., Haddad, D., Lin, W., Gerencser, A.A., Kim, H., Brand, M.D., Edwards, R.H., and Nakamura, K. (2015). The Role of Mitochondrially Derived ATP in Synaptic Vesicle Recycling. J. Biol. Chem. *290*, 22325–22336.

Patron, M., Checchetto, V., Raffaello, A., Teardo, E., Vecellio Reane, D., Mantoan, M., Granatiero, V., Szabò, I., De Stefani, D., and Rizzuto, R. (2014). MICU1 and MICU2 Finely Tune the Mitochondrial Ca2+ Uniporter by Exerting Opposite Effects on MCU Activity. Mol Cell *53*, 726–737.

Paul-Gilloteaux, P., Heiligenstein, X., Belle, M., Domart, M.-C., Larijani, B., Collinson, L., Raposo, G., and Salamero, J. (2017). eC-CLEM: flexible multidimensional registration software for correlative microscopies. Nature Methods *14*, 102–103.

Peddie, C.J., and Collinson, L.M. (2014). Exploring the third dimension: Volume electron microscopy comes of age. Micron *61*, 9–19.

Perkins, G.A., Tjong, J., Brown, J.M., Poquiz, P.H., Scott, R.T., Kolson, D.R., Ellisman, M.H., and Spirou, G.A. (2010). The Micro-Architecture of Mitochondria at Active Zones: Electron Tomography Reveals Novel Anchoring Scaffolds and Cristae Structured for High-Rate Metabolism. J Neurosci *30*, 1015–1026.

Petreanu, L., Mao, T., Sternson, S.M., and Svoboda, K. (2009). The subcellular organization of neocortical excitatory connections. Nature *457*, 1142–1145.

Petreanu, L., Gutnisky, D.A., Huber, D., Xu, N., O'Connor, D.H., Tian, L., Looger, L., and Svoboda, K. (2012). Activity in motor–sensory projections reveals distributed coding in somatosensation. Nature *489*, 299–303.

Pickett, E.K., Rose, J., McCrory, C., McKenzie, C.-A., King, D., Smith, C., Gillingwater, T.H., Henstridge, C.M., and Spires-Jones, T.L. (2018). Region-specific depletion of synaptic mitochondria in the brains of patients with Alzheimer's disease. Acta Neuropathol.

Podgorski, K., and Ranganathan, G. (2016). Brain heating induced by near-infrared lasers during multiphoton microscopy. J Neurophysiol *116*, 1012–1023.

Pologruto, T.A., Sabatini, B.L., and Svoboda, K. (2003). ScanImage: Flexible software for operating laser scanning microscopes. Biomed Eng Online *2*, 13.

Qiao, Q., Ma, L., Li, W., Tsai, J.-W., Yang, G., and Gan, W.-B. (2015). Long-term stability of axonal boutons in the mouse barrel cortex. Devel Neurobio n/a-n/a.

Rangaraju, V., Calloway, N., and Ryan, T.A. (2014). Activity-Driven Local ATP Synthesis Is Required for Synaptic Function. Cell *156*, 825–835.

Reeve, A.K., Grady, J.P., Cosgrave, E.M., Bennison, E., Chen, C., Hepplewhite, P.D., and Morris, C.M. (2018). Mitochondrial dysfunction within the synapses of substantia nigra neurons in Parkinson's disease. Npj Parkinson's Disease 4, 9.

Regehr, W.G. (2012). Short-Term Presynaptic Plasticity. Cold Spring Harb Perspect Biol *4*.

Reilly, J.E., Hanson, H.H., Fernández-Monreal, M., Wearne, S.L., Hof, P.R., and Phillips, G.R. (2011). Characterization of MSB Synapses in Dissociated Hippocampal Culture with Simultaneous Pre- and Postsynaptic Live Microscopy. PLOS ONE *6*, e26478.

Renier, N., Wu, Z., Simon, D.J., Yang, J., Ariel, P., and Tessier-Lavigne, M. (2014). iDISCO: A Simple, Rapid Method to Immunolabel Large Tissue Samples for Volume Imaging. Cell *159*, 896–910.

Rizzuto, R., De Stefani, D., Raffaello, A., and Mammucari, C. (2012). Mitochondria as sensors and regulators of calcium signalling. Nat. Rev. Mol. Cell Biol. *13*, 566–578.

Robert, F., Cloix, J.-F., and Hevor, T. (2012). Ultrastructural characterization of rat neurons in primary culture. Neuroscience *200*, 248–260.

Rodriguez-Moreno, J., Rollenhagen, A., Arlandis, J., Santuy, A., Merchan-Pérez, A., DeFelipe, J., Lübke, J.H.R., and Clasca, F. (2018). Quantitative 3D Ultrastructure of Thalamocortical Synapses from the "Lemniscal" Ventral Posteromedial Nucleus in Mouse Barrel Cortex. Cereb Cortex *28*, 3159–3175.

Rollenhagen, A., Klook, K., Sätzler, K., Qi, G., Anstötz, M., Feldmeyer, D., and Lübke, J.H.R. (2015). Structural determinants underlying the high efficacy of synaptic transmission and plasticity at synaptic boutons in layer 4 of the adult rat 'barrel cortex.' Brain Struct Funct *220*, 3185–3209.

Romanov, R.A., Lasher, R.S., High, B., Savidge, L.E., Lawson, A., Rogachevskaja, O.A., Zhao, H., Rogachevsky, V.V., Bystrova, M.F., Churbanov, G.D., et al. (2018). Chemical

synapses without synaptic vesicles: Purinergic neurotransmission through a CALHM1 channel-mitochondrial signaling complex. Sci Signal *11*.

Roome, C.J., and Kuhn, B. (2014). Chronic cranial window with access port for repeated cellular manipulations, drug application, and electrophysiology. Front Cell Neurosci *8*.

Russell, M.R.G., Lerner, T.R., Burden, J.J., Nkwe, D.O., Pelchen-Matthews, A., Domart, M.-C., Durgan, J., Weston, A., Jones, M.L., Peddie, C.J., et al. (2016). 3D correlative light and electron microscopy of cultured cells using serial blockface scanning electron microscopy. J Cell Sci jcs.188433.

Ruthazer, E.S., Li, J., and Cline, H.T. (2006). Stabilization of Axon Branch Dynamics by Synaptic Maturation. J. Neurosci. *26*, 3594–3603.

Sabo, S.L., Gomes, R.A., and McAllister, A.K. (2006). Formation of Presynaptic Terminals at Predefined Sites along Axons. J. Neurosci. *26*, 10813–10825.

Saheki, Y., and De Camilli, P. (2012). Synaptic Vesicle Endocytosis. Cold Spring Harb Perspect Biol *4*.

Saito, T., and Nakatsuji, N. (2001). Efficient gene transfer into the embryonic mouse brain using *in vivo* electroporation. Dev. Biol. *240*, 237–246.

Sammons, R.P., Clopath, C., and Barnes, S.J. (2018). Size-Dependent Axonal Bouton Dynamics following Visual Deprivation *In Vivo*. Cell Reports *22*, 576–584.

Saotome, M., Safiulina, D., Szabadkai, G., Das, S., Fransson, Å., Aspenstrom, P., Rizzuto, R., and Hajnóczky, G. (2008). Bidirectional Ca2+-dependent control of mitochondrial dynamics by the Miro GTPase. Proc Natl Acad Sci U S A *105*, 20728–20733.

Sarzi, E., Seveno, M., Angebault, C., Milea, D., Rönnbäck, C., Quilès, M., Adrian, M., Grenier, J., Caignard, A., Lacroux, A., et al. (2016). Increased steroidogenesis promotes early-onset and severe vision loss in females with OPA1 dominant optic atrophy. Hum Mol Genet *25*, 2539–2551.

Schindelin, J., Arganda-Carreras, I., Frise, E., Kaynig, V., Longair, M., Pietzsch, T., Preibisch, S., Rueden, C., Saalfeld, S., Schmid, B., et al. (2012). Fiji: an open-source platform for biological-image analysis. Nature Methods *9*, 676–682.

Schnell, U., Dijk, F., Sjollema, K.A., and Giepmans, B.N.G. (2012). Immunolabeling artifacts and the need for live-cell imaging. Nature Methods *9*, 152–158.

Schroeder, A., and Wit, J. de (2018). Leucine-rich repeat-containing synaptic adhesion molecules as organizers of synaptic specificity and diversity. Experimental & Molecular Medicine *50*, 10.

Sheng, Z.-H., and Cai, Q. (2012). Mitochondrial transport in neurons: impact on synaptic homeostasis and neurodegeneration. Nat Rev Neurosci *13*, 77–93.

Shepherd, G.M.G., and Harris, K.M. (1998). Three-Dimensional Structure and Composition of CA3→CA1 Axons in Rat Hippocampal Slices: Implications for Presynaptic Connectivity and Compartmentalization. J. Neurosci. *18*, 8300–8310.

Shidara, Y., and Hollenbeck, P.J. (2010). Defects in Mitochondrial Axonal Transport and Membrane Potential without Increased Reactive Oxygen Species Production in a Drosophila Model of Friedreich Ataxia. J. Neurosci. *30*, 11369–11378.

Shoham, S., O'Connor, D.H., Sarkisov, D.V., and Wang, S.S.-H. (2005). Rapid neurotransmitter uncaging in spatially defined patterns. Nat Meth *2*, 837–843.

Silver, I.A., and Erecinska, M. (1994). Extracellular glucose concentration in mammalian brain: continuous monitoring of changes during increased neuronal activity and upon limitation in oxygen supply in normo-, hypo-, and hyperglycemic animals. J. Neurosci. *14*, 5068–5076.

Sirevaag, A.M., and Greenough, W.T. (1987). Differential rearing effects on rat visual cortex synapses.: III. Neuronal and glial nuclei, boutons, dendrites, and capillaries. Brain Research *424*, 320–332.

Slater, A.M., and Cao, L. (2015). A Protocol for Housing Mice in an Enriched Environment. J Vis Exp.

Smith, H.L., Bourne, J.N., Cao, G., Chirillo, M.A., Ostroff, L.E., Watson, D.J., and Harris, K.M. (2016). Mitochondrial support of persistent presynaptic vesicle mobilization with age-dependent synaptic growth after LTP. ELife *5*, e15275.

Smit-Rigter, L., Rajendran, R., Silva, C.A.P., Spierenburg, L., Groeneweg, F., Ruimschotel, E.M., van Versendaal, D., van der Togt, C., Eysel, U.T., Heimel, J.A., et al. (2016). Mitochondrial Dynamics in Visual Cortex Are Limited *In Vivo* and Not Affected by Axonal Structural Plasticity. Current Biology *26*, 2609–2616.

Sobieski, C., Fitzpatrick, M.J., and Mennerick, S.J. (2017). Differential Presynaptic ATP Supply for Basal and High-Demand Transmission. J. Neurosci. *37*, 1888–1899.

Song, S., Grillo, F.W., Xi, J., Ferretti, V., Gao, G., and De Paola, V. (2016). EPBscore: a Novel Method for Computer-Assisted Analysis of Axonal Structure and Dynamics. Neuroinformatics *14*, 121–127.

Spillane, M., Ketschek, A., Merianda, T.T., Twiss, J.L., and Gallo, G. (2013). Mitochondria Coordinate Sites of Axon Branching through Localized Intra-Axonal Protein Synthesis. Cell Rep *5*, 1564–1575.

van Spronsen, M., Mikhaylova, M., Lipka, J., Schlager, M.A., van den Heuvel, D.J., Kuijpers, M., Wulf, P.S., Keijzer, N., Demmers, J., Kapitein, L.C., et al. (2013). TRAK/Milton Motor-Adaptor Proteins Steer Mitochondrial Trafficking to Axons and Dendrites. Neuron *77*, 485–502.

Stettler, D.D., Yamahachi, H., Li, W., Denk, W., and Gilbert, C.D. (2006). Axons and synaptic boutons are highly dynamic in adult visual cortex. Neuron *49*, 877–887.

Stowers, R.S., Megeath, L.J., Górska-Andrzejak, J., Meinertzhagen, I.A., and Schwarz, T.L. (2002). Axonal Transport of Mitochondria to Synapses Depends on Milton, a Novel Drosophila Protein. Neuron *36*, 1063–1077.

Südhof, T.C. (2012). Calcium Control of Neurotransmitter Release. Cold Spring Harb Perspect Biol *4*.

Sun, T., Qiao, H., Pan, P.-Y., Chen, Y., and Sheng, Z.-H. (2013). Motile Axonal Mitochondria Contribute to the Variability of Presynaptic Strength. Cell Reports *4*, 413–419.

Sung, H., Tandarich, L.C., Nguyen, K., and Hollenbeck, P.J. (2016). Compartmentalized Regulation of Parkin-Mediated Mitochondrial Quality Control in the Drosophila Nervous System *In Vivo*. J. Neurosci. *36*, 7375–7391.

Svoboda, K., and Yasuda, R. (2006). Principles of Two-Photon Excitation Microscopy and Its Applications to Neuroscience. Neuron *50*, 823–839.

Sztainberg, Y., and Chen, A. (2010). An environmental enrichment model for mice. Nature Protocols *5*, 1535–1539.

Takahashi, T., Svoboda, K., and Malinow, R. (2003). Experience strengthening transmission by driving AMPA receptors into synapses. Science *299*, 1585–1588.

Tamamaki, N., and Tomioka, R. (2010). Long-Range GABAergic Connections Distributed throughout the Neocortex and their Possible Function. Front. Neurosci. *4*.

Tang, Y., and Zucker, R.S. (1997). Mitochondrial Involvement in Post-Tetanic Potentiation of Synaptic Transmission. Neuron *18*, 483–491.

Tang, L.T.-H., Craig, T.J., and Henley, J.M. (2015). SUMOylation of synapsin Ia maintains synaptic vesicle availability and is reduced in an autism mutation. Nature Communications *6*, 7728.

Tang, Y., Scott, D., Das, U., Gitler, D., Ganguly, A., and Roy, S. (2013). Fast Vesicle Transport Is Required for the Slow Axonal Transport of Synapsin. J Neurosci *33*, 15362–15375.

Tapia, J.C., Kasthuri, N., Hayworth, K.J., Schalek, R., Lichtman, J.W., Smith, S.J., and Buchanan, J. (2012). High-contrast en bloc staining of neuronal tissue for field emission scanning electron microscopy. Nat. Protocols *7*, 193–206.

Therneau, T., Crowson, C., and Atkinson, E. (2018). Using Time Dependent Covariates and Time Dependent Coefficients in the Cox Model.

Tinevez, J.-Y., Perry, N., Schindelin, J., Hoopes, G.M., Reynolds, G.D., Laplantine, E., Bednarek, S.Y., Shorte, S.L., and Eliceiri, K.W. (2017). TrackMate: An open and extensible platform for single-particle tracking. Methods *115*, 80–90.

Tischbirek, C., Birkner, A., Jia, H., Sakmann, B., and Konnerth, A. (2015). Deep two-photon brain imaging with a red-shifted fluorometric Ca2+ indicator. Proc Natl Acad Sci U S A *112*, 11377–11382.

Trachtenberg, J.T., Chen, B.E., Knott, G.W., Feng, G., Sanes, J.R., Welker, E., and Svoboda, K. (2002). Long-term *in vivo* imaging of experience-dependent synaptic plasticity in adult cortex. Nature *420*, 788–794.

Traynelis, S.F., Wollmuth, L.P., McBain, C.J., Menniti, F.S., Vance, K.M., Ogden, K.K., Hansen, K.B., Yuan, H., Myers, S.J., and Dingledine, R. (2010). Glutamate Receptor Ion Channels: Structure, Regulation, and Function. Pharmacol Rev *62*, 405–496.

Tyurina, Y.Y., Poloyac, S.M., Tyurin, V.A., Kapralov, A.A., Jiang, J., Anthonymuthu, T.S., Kapralova, V.I., Vikulina, A.S., Jung, M.-Y., Epperly, M.W., et al. (2014). A mitochondrial pathway for biosynthesis of lipid mediators. Nature Chemistry *6*, 542–552.

Vaccaro, V., Devine, M.J., Higgs, N.F., and Kittler, J.T. (2017). Miro1-dependent mitochondrial positioning drives the rescaling of presynaptic Ca2+ signals during homeostatic plasticity. EMBO Reports *18*, 231–240.

Varoqueaux, F., Sigler, A., Rhee, J.-S., Brose, N., Enk, C., Reim, K., and Rosenmund, C. (2002). Total arrest of spontaneous and evoked synaptic transmission but normal synaptogenesis in the absence of Munc13-mediated vesicle priming. PNAS *99*, 9037–9042.

Veinante, P., and Deschênes, M. (2003). Single-cell study of motor cortex projections to the barrel field in rats. Journal of Comparative Neurology *464*, 98–103.

Verstegen, A.M.J., Tagliatti, E., Lignani, G., Marte, A., Stolero, T., Atias, M., Corradi, A., Valtorta, F., Gitler, D., Onofri, F., et al. (2014). Phosphorylation of Synapsin I by Cyclin-Dependent Kinase-5 Sets the Ratio between the Resting and Recycling Pools of Synaptic Vesicles at Hippocampal Synapses. J. Neurosci. *34*, 7266–7280.

Verstreken, P., Ly, C.V., Venken, K.J.T., Koh, T.-W., Zhou, Y., and Bellen, H.J. (2005). Synaptic Mitochondria Are Critical for Mobilization of Reserve Pool Vesicles at Drosophila Neuromuscular Junctions. Neuron *47*, 365–378.

Villa, K.L., Berry, K.P., Subramanian, J., Cha, J.W., Oh, W.C., Kwon, H.-B., Kubota, Y., So, P.T.C., and Nedivi, E. (2016). Inhibitory Synapses Are Repeatedly Assembled and Removed at Persistent Sites *In Vivo*. Neuron *89*, 756–769.

Vogt, C., and Vogt, O. (1919). Allgemeinere Ergebnisse unserer Hirnforschung (English Translation: Results of our brain research in a broader context). J. Psychol. Neurol. *25*, 292–398.

Wang, X., and Schwarz, T.L. (2009). Imaging Axonal Transport of Mitochondria. Methods Enzymol *457*, 319–333.

Watakabe, A., Ohtsuka, M., Kinoshita, M., Takaji, M., Isa, K., Mizukami, H., Ozawa, K., Isa, T., and Yamamori, T. (2015). Comparative analyses of adeno-associated viral vector serotypes 1, 2, 5, 8 and 9 in marmoset, mouse and macaque cerebral cortex. Neuroscience Research *93*, 144–157.

Welzel, O., Henkel, A.W., Stroebel, A.M., Jung, J., Tischbirek, C.H., Ebert, K., Kornhuber, J., Rizzoli, S.O., and Groemer, T.W. (2011). Systematic Heterogeneity of Fractional Vesicle Pool Sizes and Release Rates of Hippocampal Synapses. Biophys J *100*, 593–601.

Wiegert, J.S., and Oertner, T.G. (2013). Long-term depression triggers the selective elimination of weakly integrated synapses. PNAS *110*, E4510–E4519.

Yang, G., Pan, F., Parkhurst, C.N., Grutzendler, J., and Gan, W.-B. (2010). Thinned-skull cranial window technique for long-term imaging of the cortex in live mice. Nature Protocols *5*, 201–208.

Yang, G., Lai, C.S.W., Cichon, J., Ma, L., Li, W., and Gan, W.-B. (2014). Sleep promotes branch-specific formation of dendritic spines after learning. Science *344*, 1173–1178.

Youle, R.J., and van der Bliek, A.M. (2012). Mitochondrial Fission, Fusion, and Stress. Science *337*, 1062–1065.

Yuste, R. (2013). Electrical Compartmentalization in Dendritic Spines. Annual Review of Neuroscience *36*, 429–449.

Yuste, R., Majewska, A., and Holthoff, K. (2000). From form to function: calcium compartmentalization in dendritic spines. Nat. Neurosci. *3*, 653–659.

Zenisek, D., and Matthews, G. (2000). The Role of Mitochondria in Presynaptic Calcium Handling at a Ribbon Synapse. Neuron *25*, 229–237.

Zhong, L., Brown, J.C., Wells, C., and Gerges, N.Z. (2013). Post-embedding Immunogold Labeling of Synaptic Proteins in Hippocampal Slice Cultures. J Vis Exp.

Zhou, H., and Liu, G. (2015). Regulation of density of functional presynaptic terminals by local energy supply. Molecular Brain *8*, 42.

Zhou, B., Yu, P., Lin, M.-Y., Sun, T., Chen, Y., and Sheng, Z.-H. (2016). Facilitation of axon regeneration by enhancing mitochondrial transport and rescuing energy deficits. J Cell Biol *214*, 103–119.

Zipfel, W.R., Williams, R.M., and Webb, W.W. (2003). Nonlinear magic: multiphoton microscopy in the biosciences. Nat Biotech *21*, 1369–1377.

Züchner, S., Mersiyanova, I.V., Muglia, M., Bissar-Tadmouri, N., Rochelle, J., Dadali, E.L., Zappia, M., Nelis, E., Patitucci, A., Senderek, J., et al. (2004). Mutations in the mitochondrial GTPase mitofusin 2 cause Charcot-Marie-Tooth neuropathy type 2A. Nature Genetics *36*, 449–451.

Zufferey, R., Donello, J.E., Trono, D., and Hope, T.J. (1999). Woodchuck Hepatitis Virus Posttranscriptional Regulatory Element Enhances Expression of Transgenes Delivered by Retroviral Vectors. J Virol *73*, 2886–2892.